Nuclear Fuels & Materials SPOTLIGHT 2010

Idaho National Laboratory

Nuclear Fuels & Materials SPOTLIGHT

October 2010

Idaho National Laboratory
P.O.Box 1625
Mailstop 3878
Idaho Falls, ID 83415-3878

INLNFMSpotlight@inl.gov

Tel: 208-526-1950
Fax: 208-526-2930

www.inl.gov/nuclearfuels

Nuclear Fuels and Materials Spotlight Second Volume

K. O. Passamehmetoglu

Idaho National Laboratory's (INL's) Nuclear Fuels and Materials Division is happy to issue the second volume of the Nuclear Fuels and Materials Spotlight, which is our division's yearly publication. As with the first volume, the Spotlight continues to highlight the research areas, capabilities, and expertise of our young division, established in 2007. The division's research portfolio remains strong and continues to grow steadily in support of the various nuclear energy research and development (R&D) programs. In 2010, a new department was established to focus on fuel performance modeling and simulation in close coordination with our steadily growing experimental departments specializing in fabrication, characterization, design and analysis, and irradiation testing.

In April 2010, the Department of Energy (DOE) issued its Nuclear Energy Roadmap. The roadmap contains the major R&D objectives, and the development of advanced fuels and materials is a key element to achieve the proposed objectives. The Nuclear Energy Roadmap also outlines a "goal-oriented science-based approach" to the development of the nuclear energy technologies. The "science-based approach," with its elements illustrated in the figure, is aimed at a fundamental understanding, with reduced reliance on large-scale prototyping during the development phase. This approach is particularly suitable for the development of advanced fuels that has historically relied on a heavily empirical approach (Edisonian approach), which is lengthy and expensive.

To support the Nuclear Energy Roadmap, the Nuclear Fuels and Materials division is enhancing its experimental and analytical fuel development capabilities, with emphasis on micro-structural understanding of fuel behavior. In addition, we continue to increase our collaborations across, INL, other national laboratories, universities, and industry to support the nuclear energy R&D objectives.

This spotlight provides a sample set of articles in R&D areas that are currently ongoing within the Nuclear Fuels and Materials division. We hope that you find the selected articles interesting. As always, we are looking forward to your feedback on this and the previous volume for future improvements.

KEMAL O. PASAMEHMETOGLU received the PhD in Mechanical Engineering – with the sponsorship of the U.S. Nuclear Regulatory Commission – from the University of Central Florida in 1986, specializing in nuclear reactor technology. He then joined Los Alamos National Laboratory where he worked and served in leadership positions for multiple projects, including the Transient Reactor Analysis Code development, restart analysis for Savannah River K-Reactors, flammable gas mitigation in high-level nuclear waste storage tanks at Hanford, Accelerator Production of Tritium, Accelerator Transmutation of Waste, and Advanced Accelerator Application. While serving as national technical director for advanced fuel development in the Advanced Fuel Cycle Initiative (AFCI), he joined the INL in October 2004. He continues to serve as the national director of advanced fuel development activities, which involves participation by multiple national laboratories and universities. Kemal became the first director of the Nuclear Fuels and Materials Division at the INL in April 2007.

Disclaimer

This information was prepared as an account of work sponsored by an agency of the U.S. Government. Neither the U.S. Government nor any agency thereof, nor any of their employees, makes any warranty, express or implied, or assumes any legal liability or responsibility for the accuracy, completeness, or usefulness of any information, apparatus, product, or process disclosed, or represents that its use would not infringe privately owned rights. References herein to any specific commercial product, process, or service by trade name, trademark, manufacturer, or otherwise, does not necessarily constitute or imply its endorsement, recommendation, or favoring by the U.S. Government or any agency thereof. The views and opinions of authors expressed herein do not necessarily state or reflect those of the U.S. Government or any agency thereof.

Table of Contents

Multidimensional Multiscale Fuels Modeling and Simulation 1

New In-pile Instrumentation for the ATR 27

Irradiation Testing and Post-irradiation Examination of Very High Temperature Reactor (VHTR) Fuel 51

TEM Characterization of the Irradiated Dispersion Fuel 75

The Steady State Swelling Rate of Ferritic And Ferritic/ Martensitic Alloys 83

Microstructural Evolution of an HT9 Fuel Assembly Duct Irradiated in FFTF to 155 Dpa at 443ºC 99

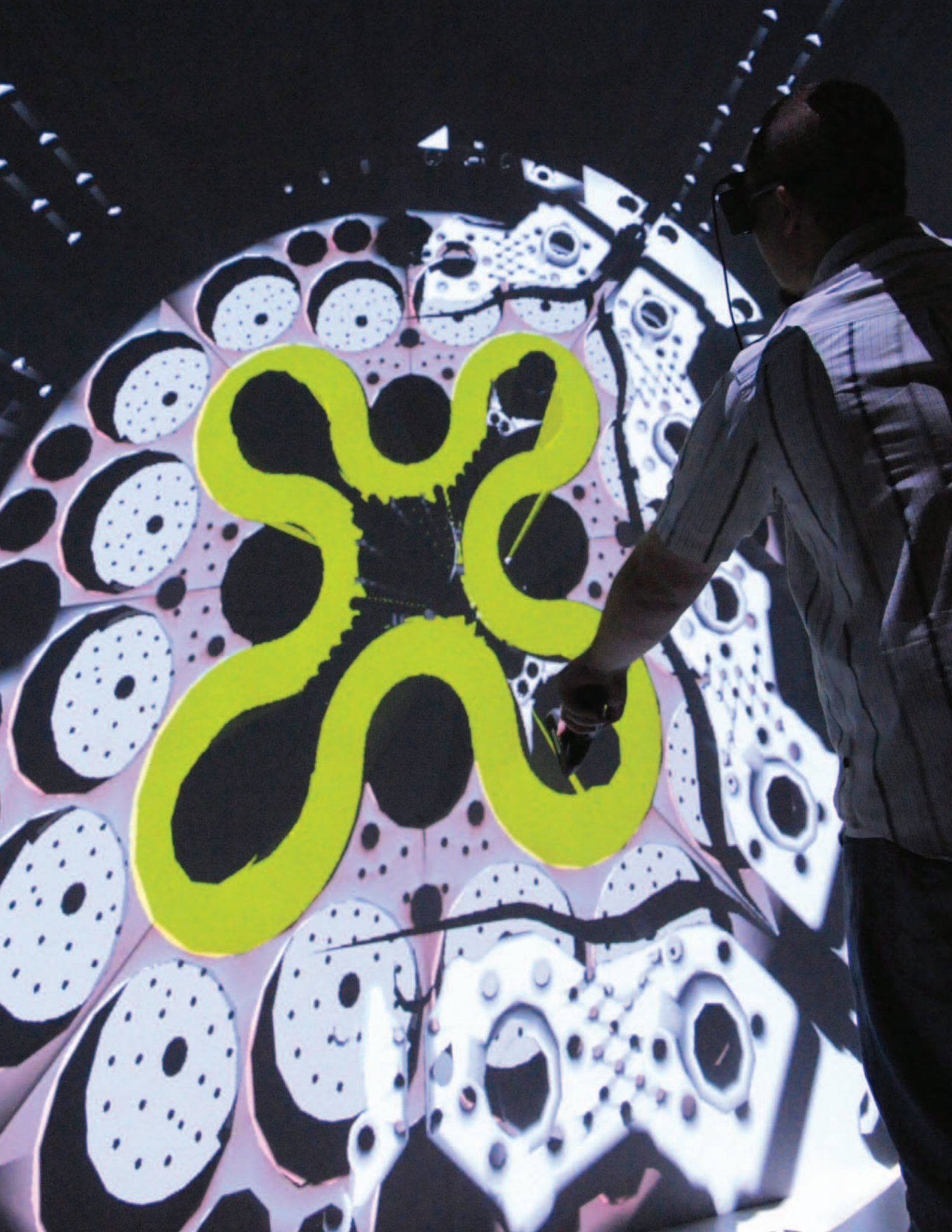

Multidimensional Multiscale Fuels Modeling and Simulation

C. J. Permann, M. R. Tonks, D. R. Gaston, R. L. Williamson, P. Millet, G. A. Hansen, R. C. Martineau

Abstract

The Fuels Modeling and Simulation Department at Idaho National Laboratory (INL) was recently created to develop state-of-the-art numerical methods, algorithms, and analysis tools that support scientists and engineers in performing high-fidelity computer simulations of the strongly-coupled, complex nuclear reactor fuels phenomena. Methods development, multiphysics simulation, and the development of computational science algorithms and applications, where the complexity and diversity in length and time scales have previously been numerically intractable, are the cornerstones of the department's efforts. A multidisciplinary staff, consisting of physicists, engineers, mathematicians, and computer scientists, enables an integrated research environment combining the vast supply of empirical data gathered from years of experimentation and state-of-the-art numerical capabilities utilizing the high-performance computing systems available at INL. The resulting efforts have yielded a number of high quality simulation applications that are providing cutting-edge contributions to the scientific community. This same effort has also produced a solid software development team employing rigorous development practices and a mature multiphysics application framework that is cross cutting the laboratory as a new core laboratory capability. The computational framework, its derivative fuels performance applications, and ongoing efforts in experimental integration are presented in this work.

Introduction

The Fuels Modeling and Simulation Department (FMSD) at Idaho National Laboratory (INL) develops state-of-the-art numerical methods, algorithms, and analysis tools that support scientists and engineers in performing high-fidelity computer simulations of the strongly-coupled, complex nuclear reactor fuels phenomena. Methods development, multiphysics simulation, and the development of computational science algorithms and applications, where the complexity and diversity in length and time scales have previously been numerically intractable, are the cornerstones of the departments' efforts. Experts in material and fuels sciences, fluid dynamics, heat transfer, neutronics, computational physics, nuclear engineering, computer science, and mathematics collaborate to simulate the challenging materials environment of an operating reactor, where the complexity and diversity in length and time scales have previously been numerically intractable. Combining simulation efforts with the extensive nuclear experimental facilities and scientists of INL's Materials and Fuels Complex (MFC) is another key focus of the department to aid in developing mathematical models and further validating computational results.

Formed in 2009 by refocusing researchers from a number of diverse programs throughout INL, the members of the FMSD have developed a national reputation in the field of fuels performance and analysis. This national recognition is resulting in growing programmatic support and the ability to draw top talent from various universities and research laboratories across the country. The mission of the FMSD is to directly support the INL goal to advance the U.S. nuclear energy endeavor by furthering the state of computational nuclear engineering in developing a robust technical basis in multidimensional multiscale fuels performance. This mission is met using computing facilities at INL and leadership-class supercomputers across the Department of Energy Complex. Thus, the FMSD applies the evolving computational nuclear science capabilities to both reduce the cost and uncertainty of new reactor design and construction and increase the safety and efficiency of new and currently operating reactors.

This document provides an overview of the modeling and simulation work being conducted within the FMSD. In Part 1, the common framework approach taken by the FMSD is summarized, including a summary of INL's MOOSE framework. In Part 2, the various fuels performance applications to which MOOSE has been applied are discussed. The efforts being taken in experimental integration are detailed in Part 3.

Part I
Common Framework Approach

MOOSE

MOOSE: *Multiphysics Object Oriented Simulation Environment* is a specialized software development framework for building applications that solve real world problems consisting of multiple interacting physical phenomena. This framework is flexible enough to run on portable laptops, yet powerful enough to run on large-scale high-performance computing hardware in a scalable, efficient manner. The main goal of the MOOSE framework is a focus on "ease of use," creating a common underlying base layer to hide the many complexities of modern computational software. This design principle naturally supports a rapid application development cycle that allows researchers to focus on science instead of software development. Rapid development is made possible through the use of object-oriented design and efficient utilization of existing open-source libraries. Researchers designing new applications are boosted into a productive work environment with a complete application template, revision control repository, test suite, and an editable wiki containing a plethora of relevant information. Careful design of the framework allows researchers to build comprehensive, feature-rich applications in just weeks instead of the years common to other computational development efforts.

MOOSE is designed to support the development of *engineering analysis applications*. Unlike a "research code," the architecture and development methodology of MOOSE must focus on more than sheer performance. MOOSE was developed with the following in mind:

Massively parallel performance and scalability is needed for large problems, but economics mandate that MOOSE applications also perform well on desktop computers and modestly parallel machines. Further, MOOSE applications must be robust and "easy to use" by engineering analysis staff, independent of the machine they are run on. Thus, the implementation of implicit strongly convergent methods is as important to MOOSE as is parallel scalability.

MOOSE must be developed using modern software engineering principles, as its value as a framework is directly related to the cost of maintaining and extending applications based on it. Further, decisions will be based on MOOSE application results; thus, the software must meet accepted QA requirements.

MOOSE is a component of an engineering analysis system that includes domain geometry construction, mesh generation, mesh quality and adaptation, and visualization and analysis of the final results. As such, the usability of MOOSE applications depends on the efficacy of the entire simulation system, including the robustness of system-wide uncertainty quantification and the ability to assess the propagation of uncertainty throughout.

MOOSE applications must meet rigorous validation and verification specifications. This mandates a robust, repeatable, and transparent verification of the MOOSE framework. Clearly, no amount of validation of the ultimate application is sufficient to justify an inadequate verification of the host framework.

The Jacobian-Free Newton-Krylov (JFNK) method forms the robust numerical core of MOOSE. JFNK is a state-of-the-art numerical algorithm that is uniquely suited to solving coupled systems of nonlinear equations. JFNK differs from Newton's method in that a Jacobian matrix never needs to be formed. Instead, the residual function is utilized to form a finite-difference operation for the matrix-vector product needed by the Krylov linear solver. This leads to a nonlinear solution method that requires very little information about the nonlinear system to be solved: only a residual. This ability to solve large nonlinear coupled systems of equations with little information from the developer leads to the rapid application development observed by development teams utilizing MOOSE.

MOOSE was also developed to leverage as much existing software as possible, which significantly reduces its development cost and minimizes maintenance expenses. The core mesh framework for MOOSE is libMesh, developed and maintained by the University of Texas at Austin. The parallel data structures, tools, linear and nonlinear solver libraries, and support tools are from the PETSCc toolkit from Argonne National Laboratory and the Trilinos toolkit from Sandia National Laboratories. Thus, MOOSE leverages the investment of DOE's ASC and SciDAC programs extensively.

Structure

The design of MOOSE capitalizes on the fact that JFNK requires only residual evaluations of the discrete system. Strategic use of this fact results in a modular, pluggable architecture that greatly simplifies adding and coupling new physics

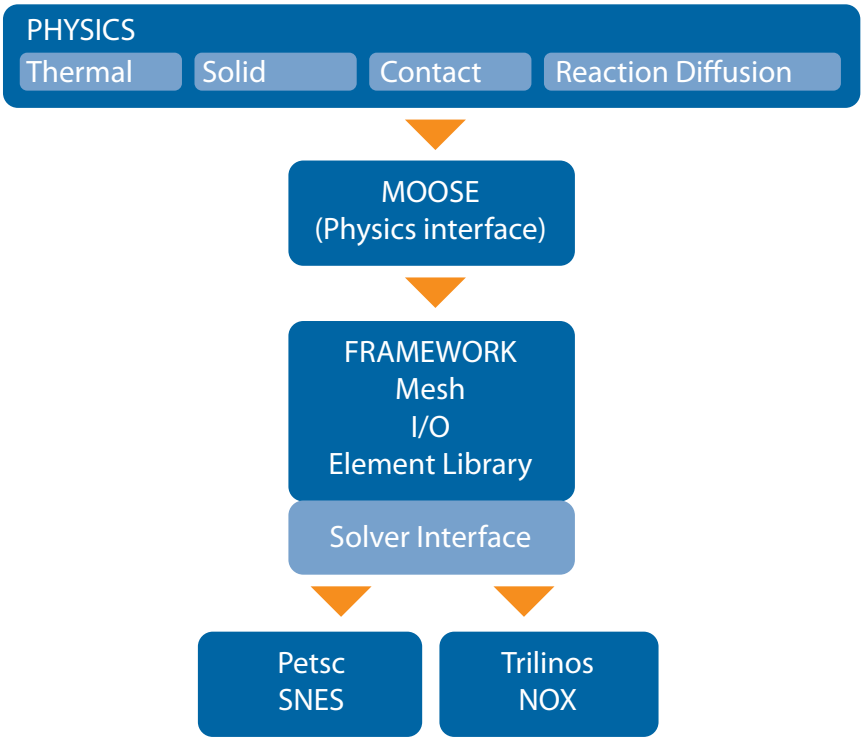

Figure 1. *MOOSE structure.*

together. Further, nonlinear material properties and boundary conditions are handled consistently.

As shown in Figure 1, MOOSE is based on a layered approach providing the core services in support of multiphysics simulations. The physics modules shown at the top of Figure 1 are called kernels and can be added, removed, and coupled together easily. MOOSE resides below the kernel level, providing a set of core functionality. Underneath MOOSE is the libMesh finite-element framework developed by the CFDLab at the University of Texas in Austin [1]. LibMesh provides a set of utilities for massively parallel finite-element based computations, including mesh I/O, a finite-element library, and interfaces to solver packages. Utilizing the interfaces in libMesh provides MOOSE, and, subsequently, the applications built using MOOSE, a considerable amount of flexibility, including the ability to swap out solver libraries and to utilize diverse large scale parallel computing resources.

Kernels

The heart of MOOSE is the kernel. A kernel is a "piece" of physics or a residual. To add new physics to an application built using MOOSE, all that is required is to supply a new kernel that describes the discrete form of the equation. It's usually convenient to think of a kernel as a mathematical operator, such as a Laplacian or a convection term in a PDE. Kernels may be swapped or coupled together to achieve different application goals.

All kernels are required to supply a residual. This residual usually involves summing products of finite-element shape functions (which MOOSE provides from libMesh). Alternatively, the residual could be calculated by calling a third party application and/or involve bridging calculations from a computation on a different scale (e.g., a mesoscale calculation for thermal conductivity) to form the "engineering scale" residual.

Kernels may also optionally provide a Jacobian, or some loose approximation thereof, which is subsequently used for physics-based preconditioning of the matrix-free calculation. In practice, one typically supplies the diagonal block of the Jacobian in the kernel, which is sufficient for effective preconditioning in many cases. In particular, if the diagonal block of the Jacobian contains a large elliptic component, then the system may respond well to multigrid preconditioning [2, 3].

Boundary Conditions

Boundary conditions are treated similarly to kernels, with their residuals and Jacobians evaluated on boundaries. Care is taken to evaluate only what is necessary on problem boundaries for efficiency. Several typical boundary conditions are provided by MOOSE itself, such as Dirichlet- and Neumann-type boundary conditions. These represent constraints on the value and gradient (respectively) of a variable. Special boundary conditions may also be created in an application built on MOOSE such as coupling two variables together or forming Robin-type boundary conditions.

Materials

Material characterization is extremely important in nuclear processes; therefore, the material system built into MOOSE is designed to be flexible and powerful. The material system allows an application to create material objects that calculate the material properties necessary for the simulation. Material objects have few restrictions on the calculations they can employ to evaluate a material property.

Before kernels compute residuals, MOOSE computes values of all materials at locations coinciding to where kernels need material information. During this step a material can call a third party library such as MATPRO [4] to evaluate itself or it can perform its own internal (possibly nonlinear) calculation. Different materials can be applied to different subsets of the domain. This plays an important role in the ability to perform calculations on complex domains, such as fuel rods with pellets and cladding in a reactor core assembly containing hundreds of different materials.

Advanced Capabilities

MOOSE provides applications with many advanced simulation capabilities, including dimension-independent physics, massively parallel computation, higher order discretization methods, and adaptive methods.

Dimension independent physics. Physics are written in a dimension independent manner, allowing for the same code to be run in one, two or three dimensions.

Massively parallel computation. All programs built using MOOSE are inherently parallel. The same code can be run on one processor or thousands. Figure 2 shows a three dimensional UO_2 fuel pellet mesh that has been decomposed for running on 1,024 processors. The decomposition can either be performed manually prior to the start of the simulation or automatically at the onset of computation. Further, many different mesh formats are supported including: exodusII [5], GMV [6], UNV [7], UCD [8], and Tecplot [9]. Parallel I/O is handled using the nemesis [10] file format from Sandia National Laboratories.

Figure 2. *Parallel mesh decomposition.*

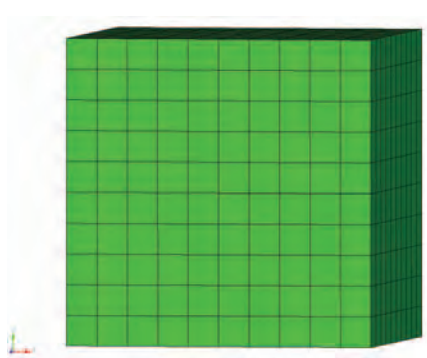

Figure 3. *Three-dimensional mesh on a cube domain.*

Meshing. In addition to the wide mesh file support available, MOOSE is capable of generating meshes for many simple geometries on the fly. This on-demand capability supports many 2-D and 3-D geometries with options to generate varying numbers and kinds of elements for these geometries. Rapid scaling and testing is simplified, leaving out manual mesh generation for many prototyping activities. Figure 3 shows a simple mesh generated by Cubit, the meshing package produced by Sandia National Laboratory. Simple geometric figures like this, however, can be created and meshed on the fly automatically through MOOSE, and need not be generated in advance. More advanced automated mesh generation techniques are being studied within the department as well. Figure 4 shows a complex stacked dished fuel pellet assembly generated from a Cubit file produced by a parameterized python script. The various dimensions of the pellet, gap, and cladding can all be specified and regenerated on demand. This capability also gives us the ability to generate the mesh for a full fuel pin or could be easily scaled up to a full reactor core in the future. The meshing is also automated, even for the difficult "saucer" and pinched toroidal geometries present between the pins due to the dishing and chamfering of the individual pellets.

Higher order methods. MOOSE utilizes a semidiscrete method in which the problem is discretized spatially using the finite-element method and temporally using traditional finite-difference methods. The finite-element discretization can be realized in MOOSE via first and second order La-grange, arbitrary order C^0 hierarchic, C^1 continuous and discontinuous finite-element families. Element types consist of the standard geometric types: triangles,

quadrilaterals, tetrahedrals, hexahedrals, prisms and pyramids. Specific details for finite-element methods can be found in [11, 12]. These elements are accessible to the application developer without the need to modify the underlying kernel code. Time integration methods include implicit Euler, Crank–Nicolson, and second order backward difference. For descriptions of time integration methods see [13].

Adaptive methods. Accuracy and cost of the simulation are determined by mesh size. Regions with discontinuities, shocks, steep gradients, and variation in spatial scale require greater mesh resolution. MOOSE utilizes the following spatial adaptive methods: *h* (cell subdivision), *p* (order elevation), and *r* (mesh redistribution) [14, 15]. Figure 5 shows a neutron flux simulation of a simple reactor model.

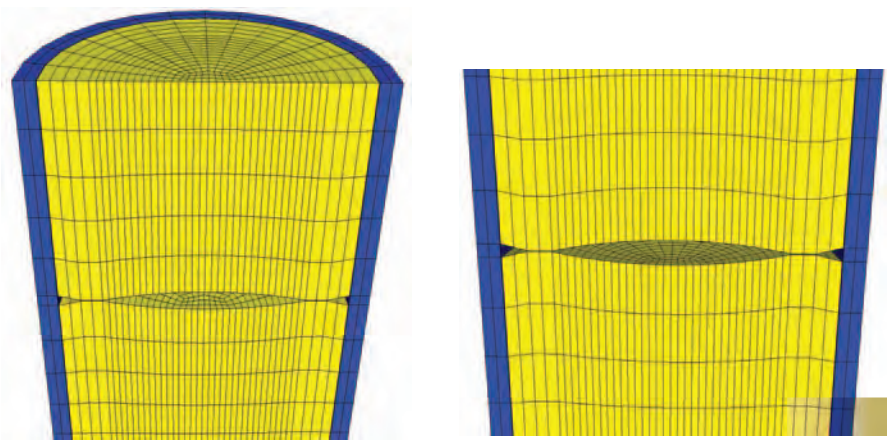

(a) Dished pellets in stacked configuration. (b) Gap detail.

Figure 4. *Three-dimensional stacked dished pellet configuration auto-generated and auto-meshed from a parameterized python script.*

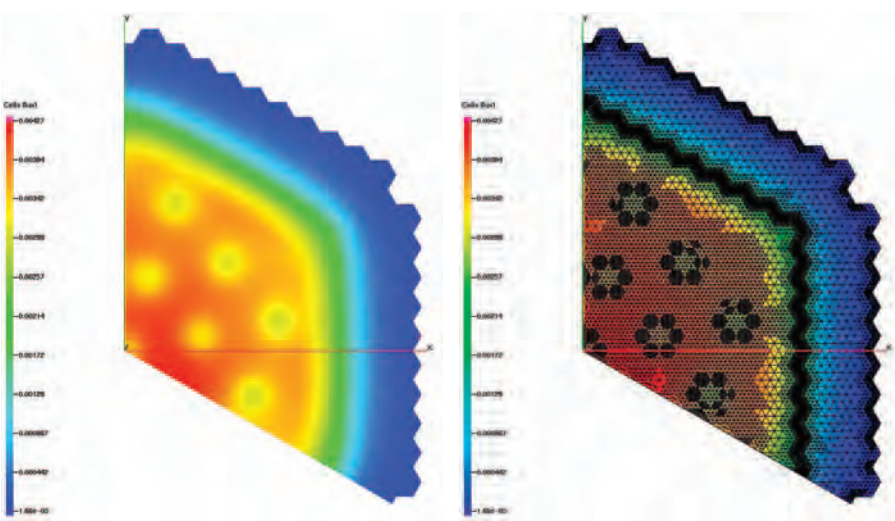

Figure 5. *Neutron flux simulation of a simple reactor configuration showing* h*–adaptation driven by a flux gradient jump indicator (see text). Note mesh subdivision in areas of high flux gradient, around fuel pins and near component boundaries.*

The color shown in the left image shows the magnitude of neutron flux, and the right image shows the computational mesh. Rapid color changes correspond to large gradients in the flux near fuel pins (the circular features at the lower left of the image). The mesh employs the *h*–adaptation capabilities within MOOSE on a triangular mesh. Mesh adaptivity is typically driven by some local estimation of error; the mesh is enriched where the local estimated error is high and coarsened where the local estimated error is low. MOOSE includes the capability for physics independent and physics dependent error estimation [16]. For the results in Figure 5, a gradient jump error indicator is used that is derived from [17]. Like spatial adaptivity, MOOSE has the capability for adaptive time-step control, where the time-step size is adjusted to control temporal error [13].

These capabilities work together seamlessly from the application developers' perspective. The necessary input from the physics application developer is a residual in the form of a kernel.

ELK

With a growing set of applications built upon MOOSE, the opportunity to share common physics code became a logical step in the maturation of the common framework. ELK: *Extended Library of Kernels* was devised to fill this role and serves as an optional shared add-on repository for all MOOSE based applications. Users of ELK benefit by using validated pluggable code modules developed by fellow researchers for otherwise separate applications. ELK is a shared add-on repository of kernels, boundary conditions, and materials compatible with the common framework. Sets of complimentary modules are available for use together, representing generic cohesive sets of physics. This library allows end users to share common physics operators with other MOOSE application developers, maximizing code reuse and increasing productivity of the entire community. Furthermore, the use of common components reduces the likelihood of human error and inconsistencies in code development while simplifying the verification and validation of these modules. Other advantages to this approach include centralized testing and better developer training through example as developers are offered a rich code base before they begin development on new applications. The final feature of ELK that makes it a useful tool at a mixed lab like the INL is that all modules placed in this repository are required to pass export compliance so that these modules can be freely used by foreign national researchers as well as U.S. citizens and permanent lawful residents, which was difficult prior to the creation of ELK.

Software Development Methodology

The FMSD recognizes the importance of sensible modern development practices not only to maximize the effectiveness of our developers, but to minimize software maintenance as well. To support this commitment, each member of the core development team is working toward obtaining Certified Software Development Professional (CSDP) certifications, an industry standard recognized throughout the professional software development community recognizing quality developers. All of the software development taking place on the common framework follows sensible modern development practices despite the rapidly changing research environment. While existing projects and funded research generally have explicit objectives and goals, the ever present need for growth and new opportunities can often change priorities and development directions. To cope with this dynamic environment, the group employs agile development methods. Key to this effort is a flexible documentation and wiki website, *Trac*, which all researchers, developers, and collaborators are encouraged to use on a daily basis to track their progress, record work directions, and augment verbal communication. *Trac* is fully editable by MOOSE developers and serves as a great collaboration area, removing the need for alternative communication paths such as email. Developers consistently document platform tips, build instructions, submit bug reports, and track task time on the wiki.

Subversion is an industry standard software version control system adopted by the FMSD. Trac natively supports Subversion which serves as the central repository for all framework and application source code. Version control aims to virtually eliminate the risks associated with any distributed development model. The *Trac* wiki also enables the idea of *continuous integration* through the use of *Bitten* for doing up-to-the-minute code integration and testing. All source changes checked into the repository are built against a number of different system architectures and compilers, assuring compatibility on all target platforms at all times. Developers are notified automatically via email when changes they make fail to build or pass verification testing. *Bitten* also provides a summary page of the current build status which allows all developers a glimpse of the overall health of the common framework and all derivative applications at any point in time. This feature is especially important to the framework developers as changes made to the underlying framework always risk causing adverse effects to the applications built on top of the framework.

Part II
Fuels Performance Applications

BISON: Multidimensional Fuel Analysis

BISON is the most mature application in the MOOSE family. It was developed simultaneously with the MOOSE framework and, consequently, informed many of the design choices made in MOOSE. Its primary purpose has been to study the physical properties of individual nuclear fuel pellets of a typical light water reactor over the entire lifespan of those fuel elements. The fully implicit, fully coupled methods of BISON's parent framework allow it to capture a wide range of interesting physical phenomena from reactor startup through latter stages of fuel burnup. Extensive studies of thermomechanical behavior of reactor fuel pellets have been performed with the BISON code, including swelling due to thermal expansion and oxygen diffusion [18], material cracking due to strain, burnup through spatially and temporarily varying fission modules, nonlinear mechanics, and lower-length scale coupling. All are important phenomena to understand in extending fuel life and improving the predictive capability of fuel failure. These various studies are easily assembled in BISON due to the modular design techniques and a growing set of pluggable physics available through the common framework and shared kernel library previously discussed. The lower-length scale studies spawned another MOOSE-based application called MARMOT. which is discussed later. A small sample of these studies is overviewed here.

Figure 6 illustrates the thermomechanical behavior of a cracked pellet during reactor startup. This result is from a simplified geometry, but shows the three-dimensional evolution of the crack as the pellet heats up. This simplified geometry and physics model is ideal for running on smaller workstations or laptops, which contrasts with some of the higher fidelity models presented next. In either case the code base, problem setup, and execution procedure remain constant as one scales from serial laptops to parallel super computers.

Figure 7 shows simulation results for a parallel, three-dimensional, fully-coupled thermomechanics simulation of a cracked dished-pellet. The presence of the predefined crack in the mesh and boundary conditions on the top and bottom of the pellet create a true three-dimensional result. This particular result was run on 512 processors of INL's ICESTORM

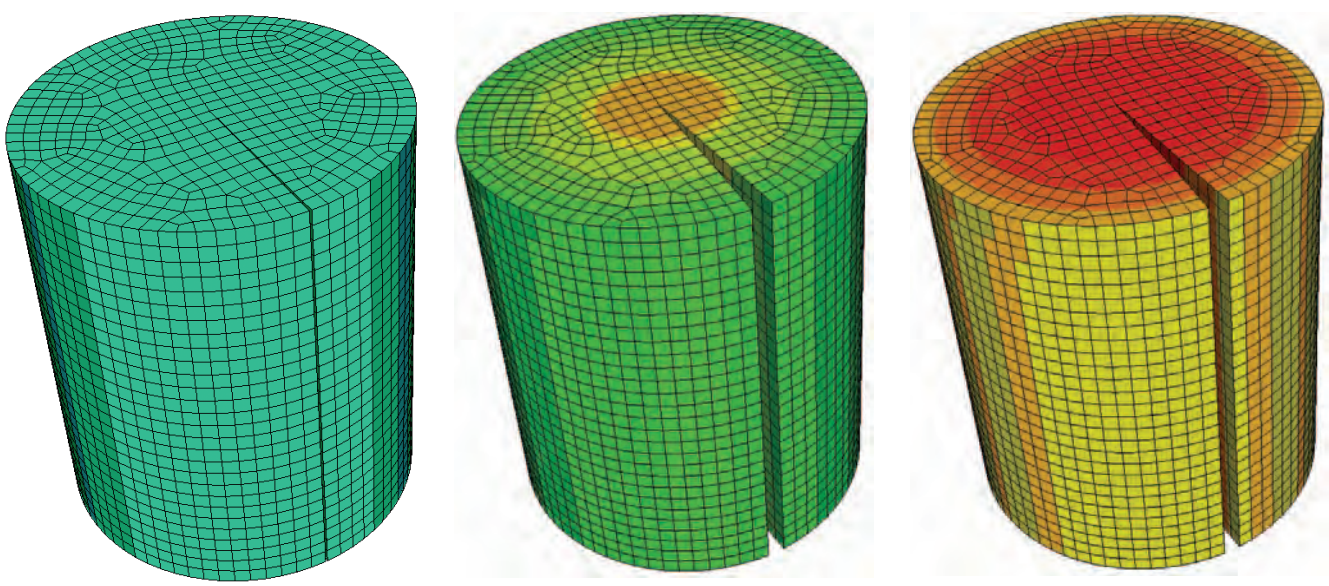

(a) Initial. (b) 1 min. (c) 2.5 min.

Figure 6. *Transient UO_2 fuel pellet under power-up conditions. Note the presence of an idealized crack, which makes the simulation three-dimensional.*

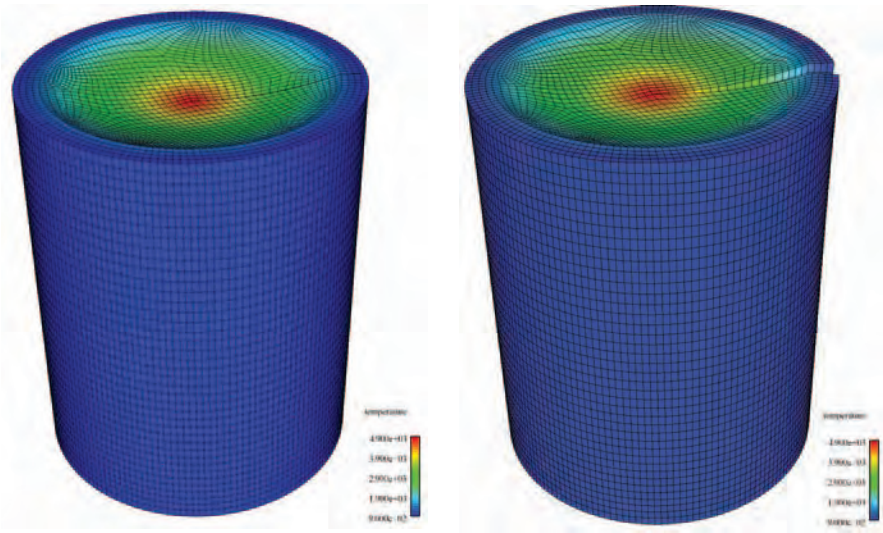

a) Initial cracked pellet. (b) Cracked pellet in thermal equilibrium.

Figure 7. *Parallel three-dimensional representative simulation of a dished pellet; showing a crack extending from the center of the pellet to the right outer edge, where (a) shows pellet at the onset of thermal expansion and (b) shows pellet in thermal and mechanical equilibrium. Note how crack opens due to thermal expansion of the pellet.*

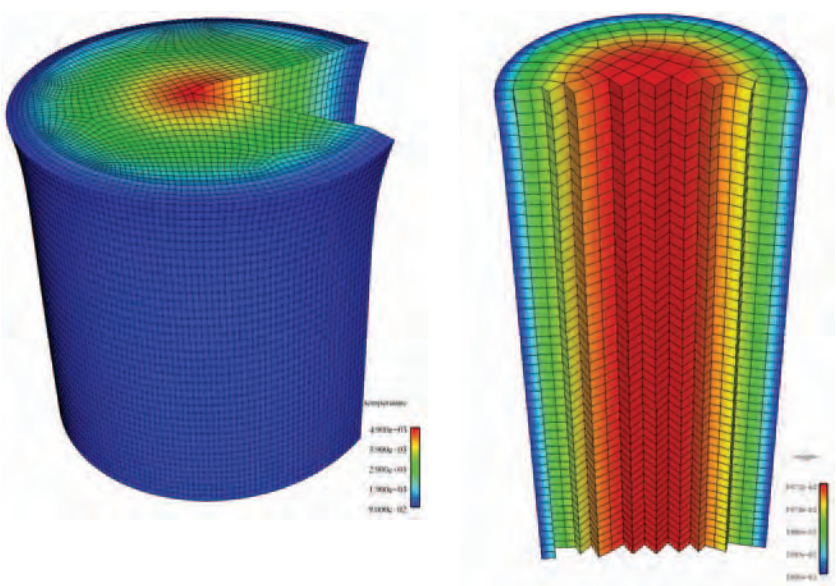

(a) Displacement magnified by factor of 9. (b) Degree of hyperstoichiometry in the pellet.

Figure 8. *Representative simulation of UO_2 pellet showing oxygen diffusion coupled to thermomechanics. Figure (a) shows the thermomechanical equilibrium results from Figure 7 with the displacement magnified by a factor of ten to illustrate complex deformation near the "root" of the crack. In (b), the coloration indicates the degree of hyperstoichiometry (x) in the pellet, or $UO_{(2+x)}$.*

computer. The initial condition was a constant heat generation term to mimic a constant energy generation rate across the pellet. Thermal heating of the pellet then ensues, directly leading to deformation of the pellet.

Figure 8(a) illustrates an exaggerated view of the cracked pellet, where the displacement was magnified by a factor of ten to highlight the deformation local to the crack. The strong three-dimensional behavior of the cracked pellet is apparent in this diagram; note the raised edge near the root of the crack on top of the pellet. This raised area quickly decays to the mean elevation of the dished pellet a short distance away from the crack. Also note the strong deformation toward the cladding near the outer edge of the crack. It is clear, even with this simple model, that this local deformation near cracks will significantly alter the geometry of the pellet in these areas and the mechanics of its interaction with the cladding. Figure 8(b) depicts an oxygen diffusion simulation of similar, but un-cracked, pellet geometry. The legend in the diagram corresponds to the degree of hyperstoichiometry x in the oxide [18].

Work on pellet cladding interaction is an ongoing research area in BISON. Initial studies have been conducted to test the mechanical interaction of pellet contact with cladding by meshing the pellet, gap, and cladding of a partial light water reactor fuel pin. Figure 9(a) shows the initial configuration of the pellet prior to the gap being closed due to thermal expansion. Note the radial displacement of the cladding in Figure 9(b) after the pellet has swelled and made contact with the cladding. Also note the vertical displacement of the pellet mesh relative to the cladding mesh as the pellet

swells and expands axially. Studies in pellet cladding interaction are an important area of research as a higher confidence in predicting cladding failure can greatly improve the operating costs of the reactor fuel cycle and improve overall reactor safety.

Some of the current and future goals of BISON include modeling full reactor pins and potentially complete reactor cores. Preliminary work to scale our single pellet models up to significant fractions of a full pin have already been performed (Figure 10). Plans to incorporate mesoscale-informed fission-gas release and pressures in the plenum are forthcoming. Additionally, work to accurately model additional physics, such as plastic deformation, spatially accurate fission models, burnup, and various contact methods, are currently being implemented to increase our model fidelity.

TRISO Fuel Simulation Using BISON

Although early BISON development has been principally directed toward the analysis of fuel for light water reactors, much of the code's current capability can be readily applied to other fuel types. This section demonstrates this versatility, as BISON is used to investigate TRISO-coated particle fuel which is being developed for use in the Next Generation Nuclear Plant. For initial TRISO-fuel studies, BISON was used to investigate three-dimensional fully-coupled heat transfer and cesium fission-product transport. Fission reactions are assumed to generate energy at a uniformly distributed constant rate, and cesium transport is modeled assuming Fickian diffusion and radioactive decay, including diffusion coefficients which are strongly temperature dependent. Although only a single fission product is considered here, the modular structure of BISON permits easy and rapid application to multiple chemical species in a fuel particle.

The TRISO particle geometry is shown in Figure 11. The fuel kernel is surrounded by a porous pyrocarbon layer (Buffer), a dense inner pyrocarbon layer (IPyC), a SiC layer, and an outer pyrocarbon layer (OPyC). Assuming symmetry along three perpendicular planes, a finite element mesh of a one-eighth section of the particle was generated, as shown in Figure 12. Initial simulations were run with power at 50 mW and the outer radius set to a temperature of 1500 K and cesium

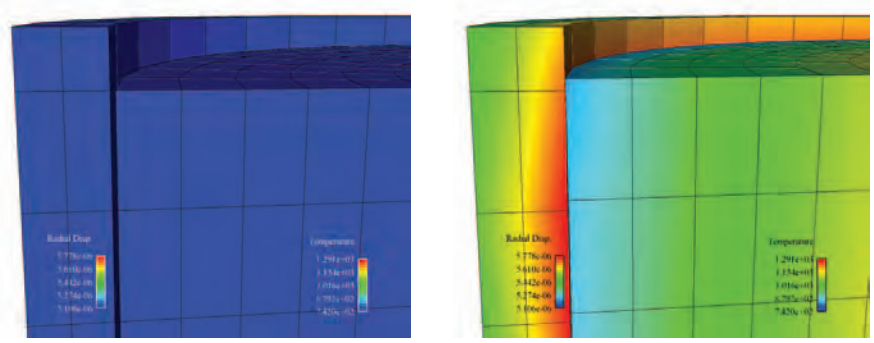

(a) Initial pellet cladding configuration. (b) Pellet cladding after power up.

Figure 9. *Parallel three-dimensional representative simulation of a pellet and cladding thermo-mechanical interaction at (a) initial condition and immediately after contact; (b) the cladding is colored by radial displacement while the pellet is colored by temperature.*

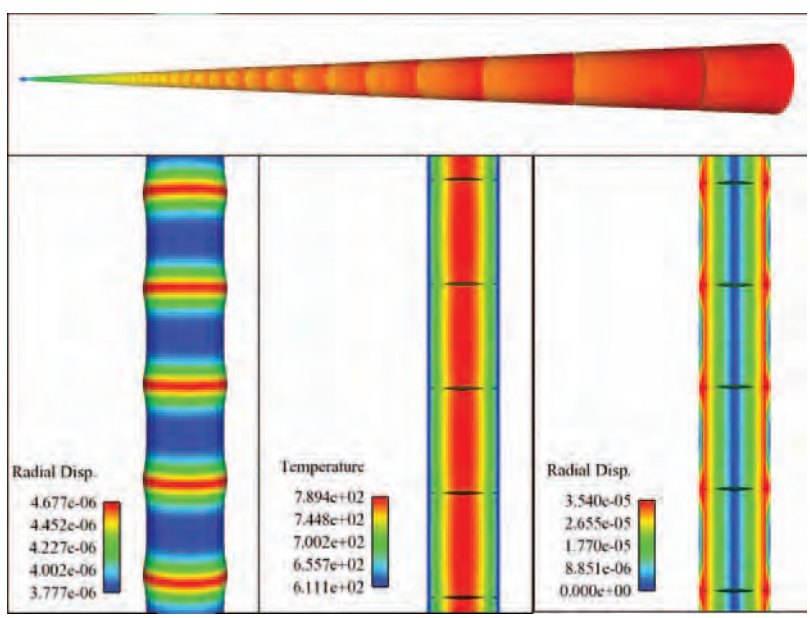

Figure 10. *One hundred UO_2 pellets and cladding modeled with thermo-mechanics. Top pane: pellets colored by position relative to stack.*

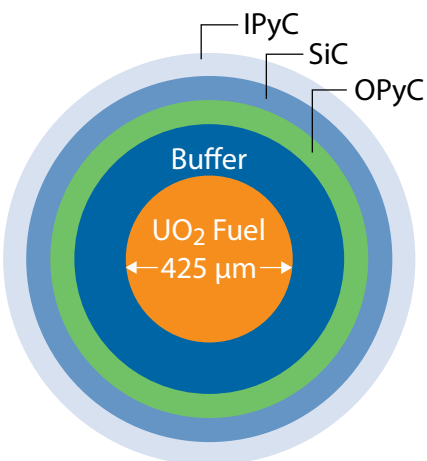

Figure 11. *TRISO fuel-particle geometry.*

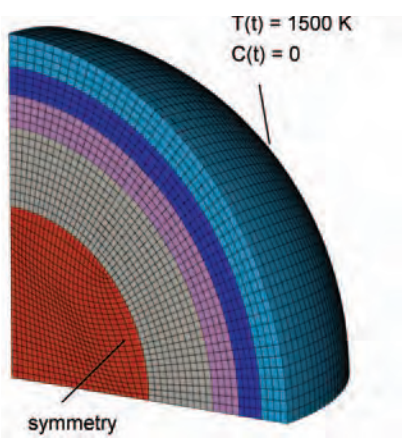

Figure 12. *TRISO fuel-particle geometry.*

concentration held at zero.

Thermal and mass diffusion in TRISO fuel occurs on very different time scales. Assuming instantaneous power-up, a steady thermal profile is established in less than a second due to the small particle size. A steady temperature profile thus exists after the first computational time increment, and is shown in Figure 13(a). This disparity in time scales justifies the use of a fully implicit solution strategy such as the one in BISON. An explicit scheme would need to follow the fastest timescale of the problem where the implicit scheme can follow the dynamical timescale of interest, allowing for long burnup calculations.

The largest temperature drop occurs across the porous buffer layer due to a low thermal conductivity. Predicted cesium concentration profiles at four times during irradiation are shown in Figure 13(b). The profile has widely varying slopes, with a steep gradient occurring across the SiC layer because of a low diffusion coefficient. These results demonstrate the effectiveness of the SiC layer in preventing cesium escape from the particle.

During irradiation, the buffer layer shrinks and can debond from the IPyC layer. A second simulation explores the effects of this phenomenon by including a xenon-filled gas gap between the buffer and IPyC layers. As shown in Figure 14(a), the gap was assumed to exist over only one-third of the interlayer surface, resulting in multi-dimensional behavior. Figure 14(b) shows a temperature contour plot at thermal steady-state. Comparing thermal profiles along the X and Z axes, it is clear that the low thermal conductivity of the gas layer results in a steep gradient over the layer thickness. Because of the gap's small thickness in this simulation, it does not have a strong effect on the peak fuel temperature. The effect of the gap on the cesium concentration is also insignificant because the cesium profile is dominated by the low diffusion coefficient of the SiC layer.

In a final simulation, flaws were placed in the SiC layer to investigate their effect on cesium release from the particle. Figure 15(a) shows the basic geometry and the coarse finite-element mesh used for initial calculations. Simulations were performed for four different geometries by first considering a single flaw (#1 in Figure 15(a) and then successively adding the second, third, and fourth flaws identified in the figure). Figure 15(b) shows the effect of the flaws by comparing the cesium fractional-release histories for the four flaw geometries, and that for a standard particle. Because SiC is the only TRISO material that effectively prevents cesium diffusion, the small holes become local vents which release substantial amounts of fission gas. Even a single flaw results in significant cesium release early in fuel life, with the four-flaw simulation predicting over 10% release at the end of irradiation.

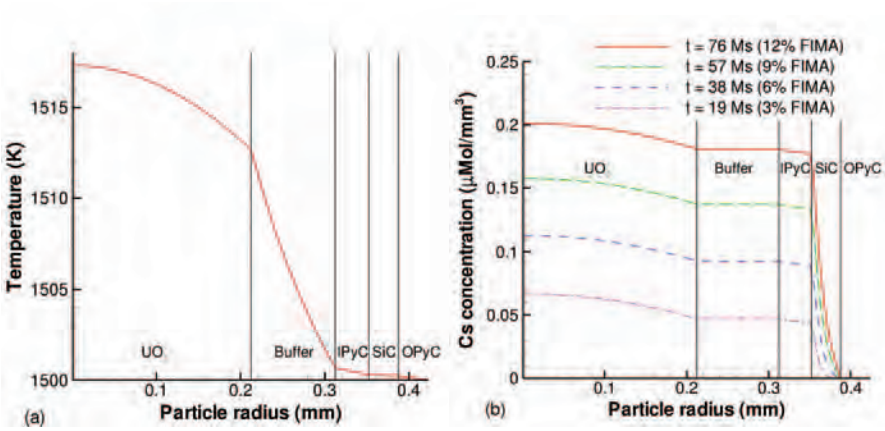

Figure 13. *(a) Predicted steady-state predicted profile, and (b) cesium concentration profiles at four times during irradiation.*

A useful BISON feature is the ability to easily perform a uniform mesh refinement on the entire particle geometry. To demonstrate this capability, a single uniform mesh refinement was specified, which simply subdivides a brick element in half along each dimension, thus replacing each coarse-mesh element with eight elements. For the mesh shown in Figure 15(a), this uniform refinement increases the number of elements from 53,568 to 428,544, and the degrees of freedom from 114,096 to 884,542. This significant increase in elements can result in much longer simulation times; thus, this problem was run on the INL ICESTORM computer cluster using 16 processors. Figure 8 provides a comparison of the cesium concentration contours in the vicinity of the flaws for the coarse and refined meshes at the end of irradiation. The local "venting" of cesium through the flaws is evident, with the refined mesh providing improved resolution of the large concentration gradients.

Even a single uniform mesh refinement results in an 8-fold increase in the number of elements and a significantly larger computational problem. In many cases, mesh refinement is only necessary in local regions of the domain, such as in the vicinity of flaws, fractures, or debonding. To address this issue, BISON utilizes the MOOSE framework's capability to perform local mesh refinement, also known as h-refinement. This approach has the significant advantages that, (1) mesh refinement is based on estimates of numerical error (thus, new elements are only generated in areas where they are most needed) and (2) mesh refinement is dynamic, such that the mesh can be locally refined and then coarsened, if needed, as the solution evolves. Figure 17 shows a series of combined mesh and cesium concentration contour plots, demonstrating the localized mesh resolution as the solution develops. The mesh is significantly refined to resolve the more complex behavior in the vicinity of the SiC flaws and the IPyC/SiC interface, with limited or no refinement throughout the rest of the domain. The result is a solution having better fidelity than that with the uniform refinement shown in Figure 8 while still utilizing fewer total elements and less computational time.

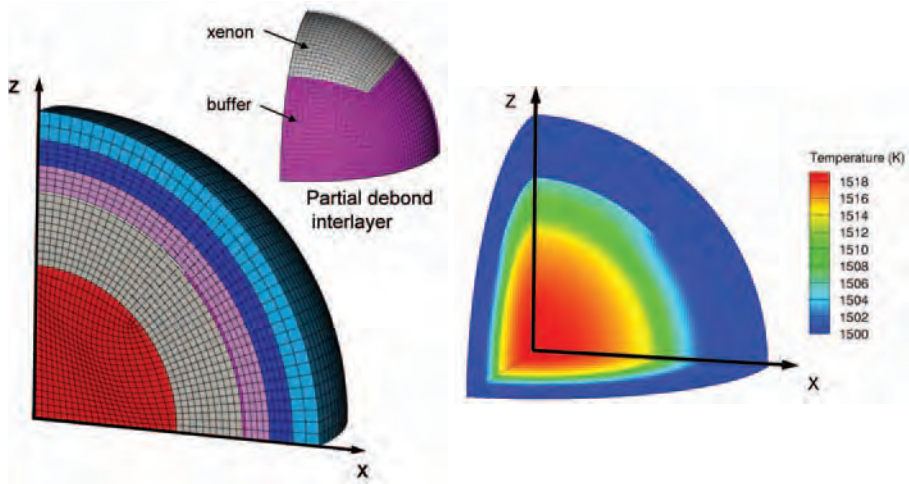

(a) (b)

Figure 14. *(a) Geometry and mesh for partial-debond simulation, and (b) temperature contours at steady state.*

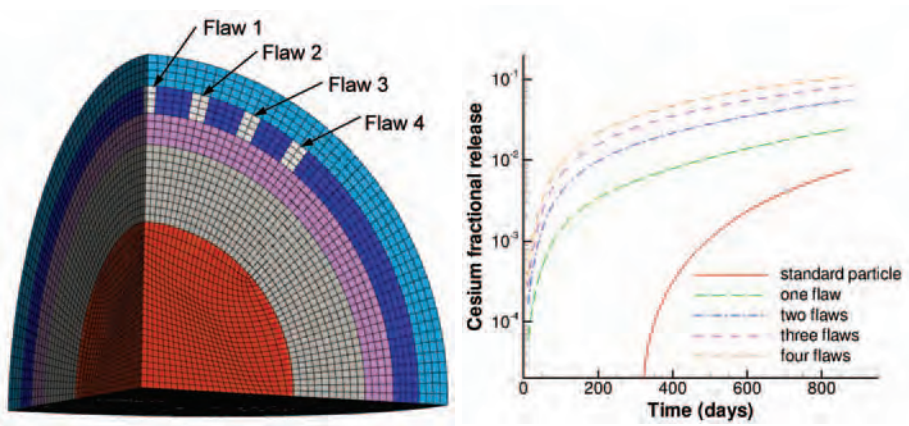

(a) (b)

Figure 15. *(a) Geometry and initial coarse mesh with flaws, and (b) comparison of cesium fractional-release histories.*

Robust high-fidelity models play an important role in understanding the complex multiphysics processes that occur in nuclear fuel during steady operation and accident conditions. Such understanding leads to improvements in fuel design or operating conditions, resulting in longer fuel life, improved reactor efficiencies, and increased safety margins. Models also play a critical role in investigating and better understanding experimental observations. For example, the BISON TRISO model described here is currently being extended to investigate the significant reductions in fuel swelling which have been experimentally observed when a thin ZrC layer is included between the fuel kernel and buffer. Such reductions in swelling lead to extended fuel life, but are currently not well understood. Modeling will provide a reasonably inexpensive and rapid investigation of the important physical processes involved and likely lead to a clear understanding of the phenomena. Finally, it is important to point out that high-quality mechanistic models are predictive, meaning they can be used to explore new fuel-related concepts, such as new and untested fuel materials, design modifications, or fuel behavior at extended burnup.

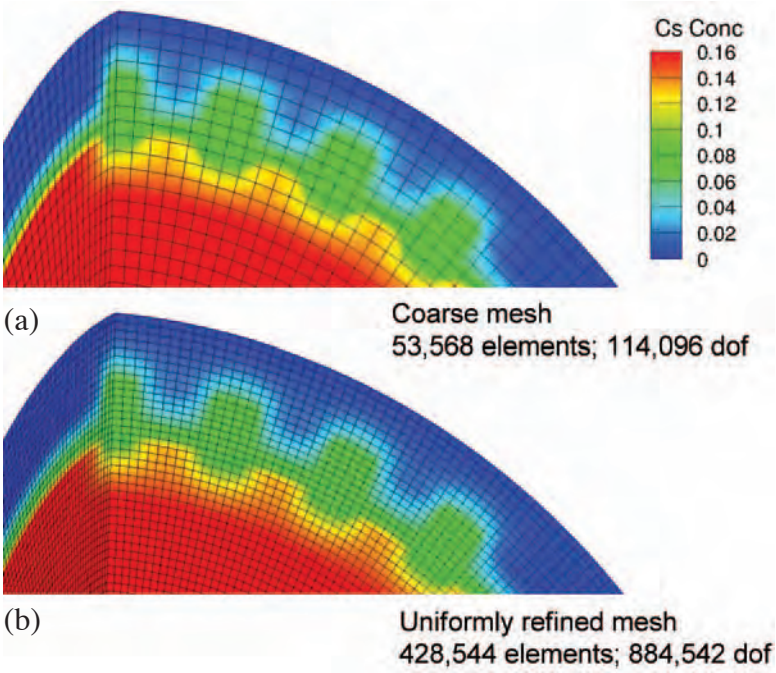

Figure 16: *Comparison of the cesium-concentration contours in the vicinity of the flaws for the (a) coarse; and (b) refined meshes at a time of 880 days.*

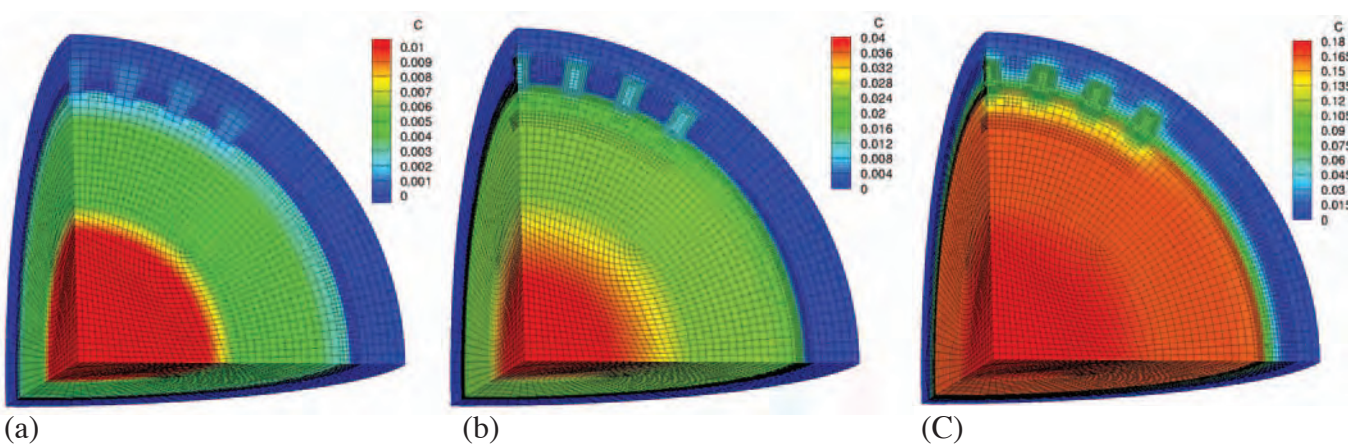

Figure 17. *Combined mesh and cesium-concentration contour plots at times of (a) 23 days, (b) 116 days; and (c) 880 days, demonstrating automatic mesh refinement as the solution develops.*

Mesoscale Fuel Analysis.

Continuum scale modeling such as that performed with BISON often requires so-called "closure models" that represent bulk properties of the material. In heat conduction, these usually take the form of thermal-conductivity models while, in solid mechanics, it might be an elasticity tensor. Often it is the case that closure models are either informed by or derived from experimental data forming an empirical model. An alternative to experimentally informed models is to perform lower length-scale simulations to compute properties needed by the continuum-scale solution process. This process, known as mesoscale modeling, aims to allow simulation of new materials before they are ever fabricated in the laboratory, providing material scientists an efficient way to shrink their search space before ever doing an experiment.

Within the FMSD, mesoscale modeling efforts are underway to incorporate microstructure-scale physics into the continuum-level MOOSE framework to generate a more comprehensive, science-based understanding of fuel performance and processing. These mesoscale models seek to capture the complex interplay between defects, such as vacancies, dislocations, voids, and fission-gas bubbles, in fuel and cladding materials in the crystal lattice. The set of equations that is utilized is known as a phase-field model, which is a powerful modeling approach that combines thermodynamics of multi-component, multi-phase materials systems with kinetic transport equations. Computational simulations using this phase-field model can capture the simultaneous processes of microstructural evolution including nucleation, growth, and coarsening phenomena (see Figure 18).

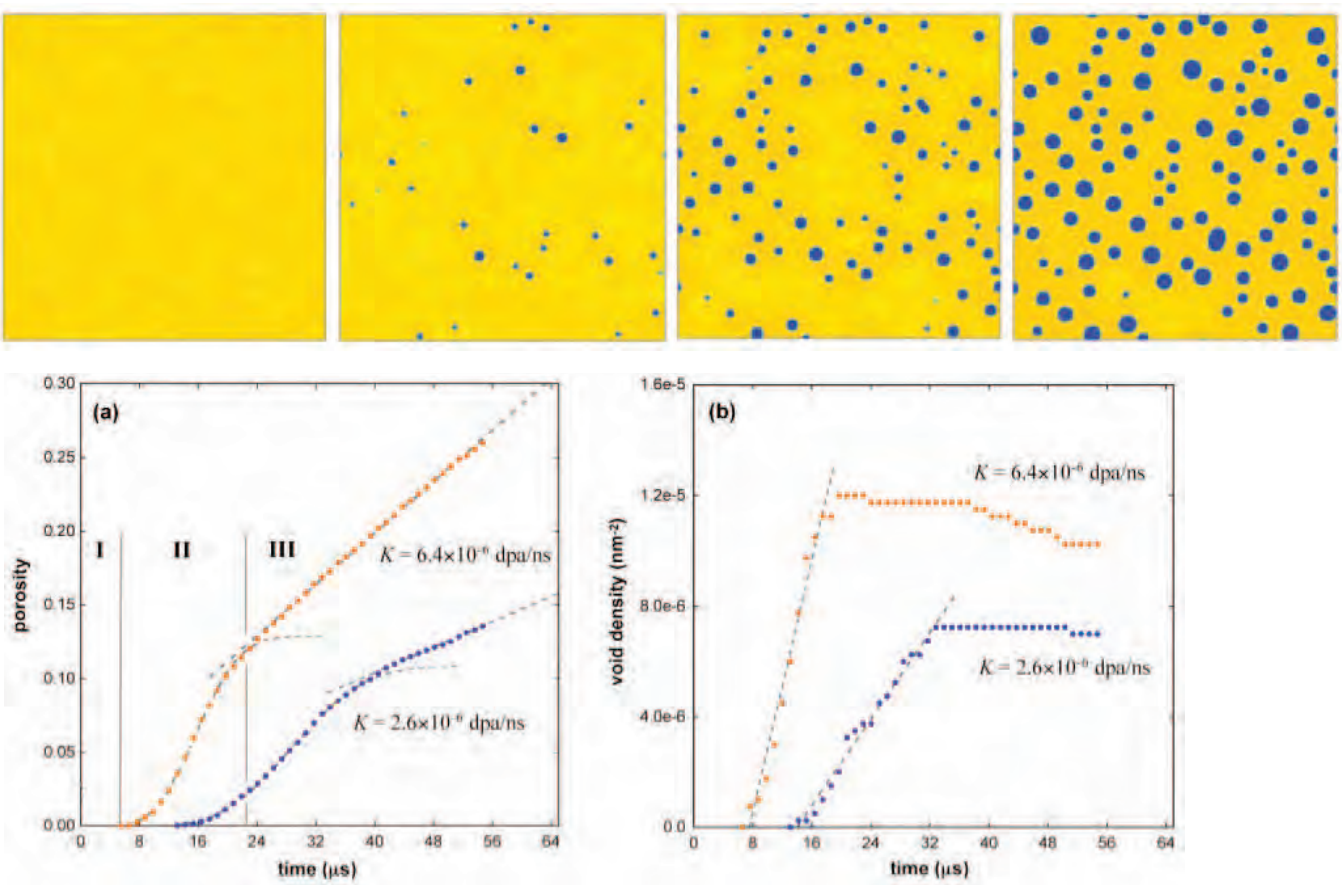

Figure 18. *Phase-field simulation of nucleation and growth of voids showing the evolution of porosity and void density throughout time.*

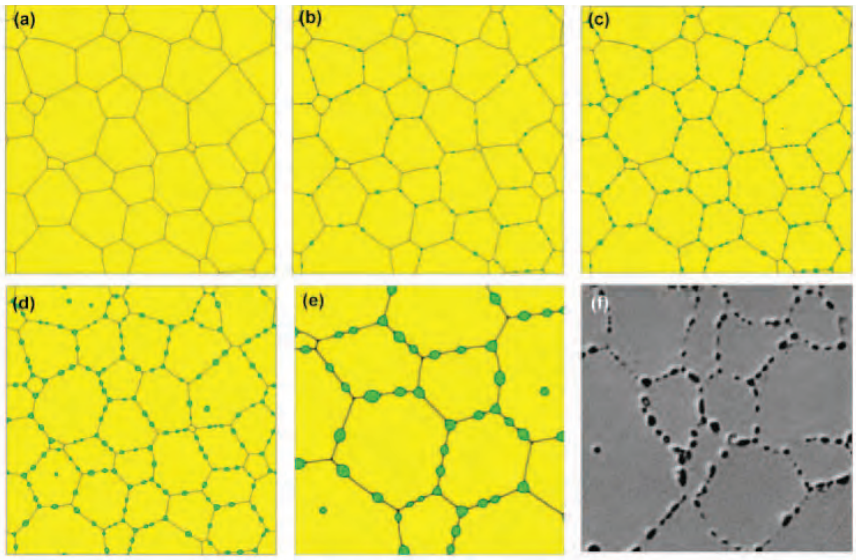

Figure 19. *Snapshots throughout time of the nucleation and growth of intergranular gas bubbles a polycrystalline grain structure.*

In nuclear fuel materials, like many other material systems, microstructure evolution at the mesoscale leads to significant changes in macroscale processes, including thermal transport, mechanical deformation, and dimensional changes such as swelling. In particular, the precipitation of fission-gas species into gas-filled bubbles leads to high-temperature embrittlement, loss of thermal conductivity, and volumetric swelling. Furthermore, fission-gas bubbles that exist on grain boundaries grow to much larger dimensions than those on grain interiors. These intergranular bubbles coalesce and develop an interconnected porosity that leads to fission gas release to the plenum regions of the fuel pin. As seen in Figure 19, the phase-field model developed by Millett et al. [19] can simulate evolution of gas bubbles along grain boundaries in polycrystalline fuel materials, and good qualitative agreement exists with experimentally-observed bubble structure.

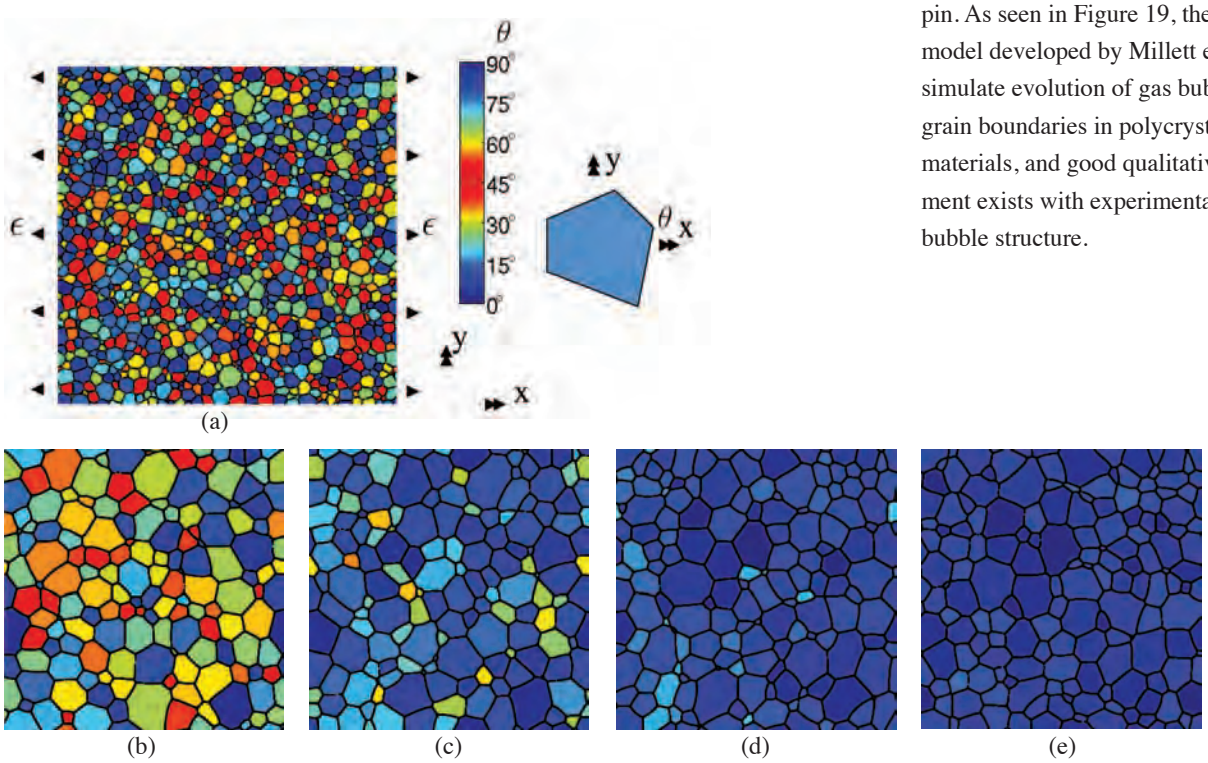

Figure 20. *Deformation-induced grain growth in an 1156 grain 2-D copper polycrystal with a random initial orientation distribution, where the colors represent the initial grain orientations, with a) a diagram of the initial polycrystal, showing the elongation in the x-direction. Also, the copper polycrystal with 150 remaining grains for (b) no applied elongation, (c) 0.5% elongation, (d) 1.0% elongation; and (e) 2.0% elongation. Note that a distinct texture forms with applied load, where grains oriented near 0° tend to grow.*

While microstructure evolution influences thermal transport and mechanical deformation, stress and temperature gradients also influence defect migration and grain boundary migration. This can have a large impact on the evolving microstructure and must be considered to accurately describe the changes that occur in irradiated fuel. For example, an applied strain drives grain growth due to the anisotropic elastic response of each grain. With a phase-field grain-growth model coupled with a spectral stress calculation, the FMSD has investigated the effect of an applied elongation on grain growth. The grain growth model was first validated by comparison with molecular dynamics (MD) results for a deformed copper bicrystal from [20], and all the material parameters were taken from their MD calculations. The model was then used to investigate the effect of elongation on grain growth in a 2-D copper polycrystal with 1156 grains and a random initial orientation distribution. As shown in Figure 20, no orientation was preferred in the grain growth when the polycrystal was not elongated. However, with increasing elongation, grains oriented near 0 degrees, which are softer with respect to the applied strain, tend to grow at the expense of grains oriented near 45 degrees.

In the initial development of the phase-field model, the system of equations was solved in 2-D using finite difference and explicit time integration. An initial implementation of the model using MOOSE solves the equation system in either 2-D or 3-D with FEM and implicit time integration. The MOOSE-based phase field model is called MARMOT. As a proof-of-concept, the basic model presented in [21] was initially implemented in MARMOT and was found to predict similar results to the finite difference model. In addition, due to implicit time integration, MARMOT takes time steps four orders of magnitude larger than is possible using the explicit finite difference solution. Computation time is reduced in MARMOT by taking advantage of time step and mesh adaptivity capabilities found within MOOSE. By adapting the time step, the solution follows the intrinsic time scale of the current physical phenomena being simulated. For example, in a simulation of void nucleation during irradiation, as

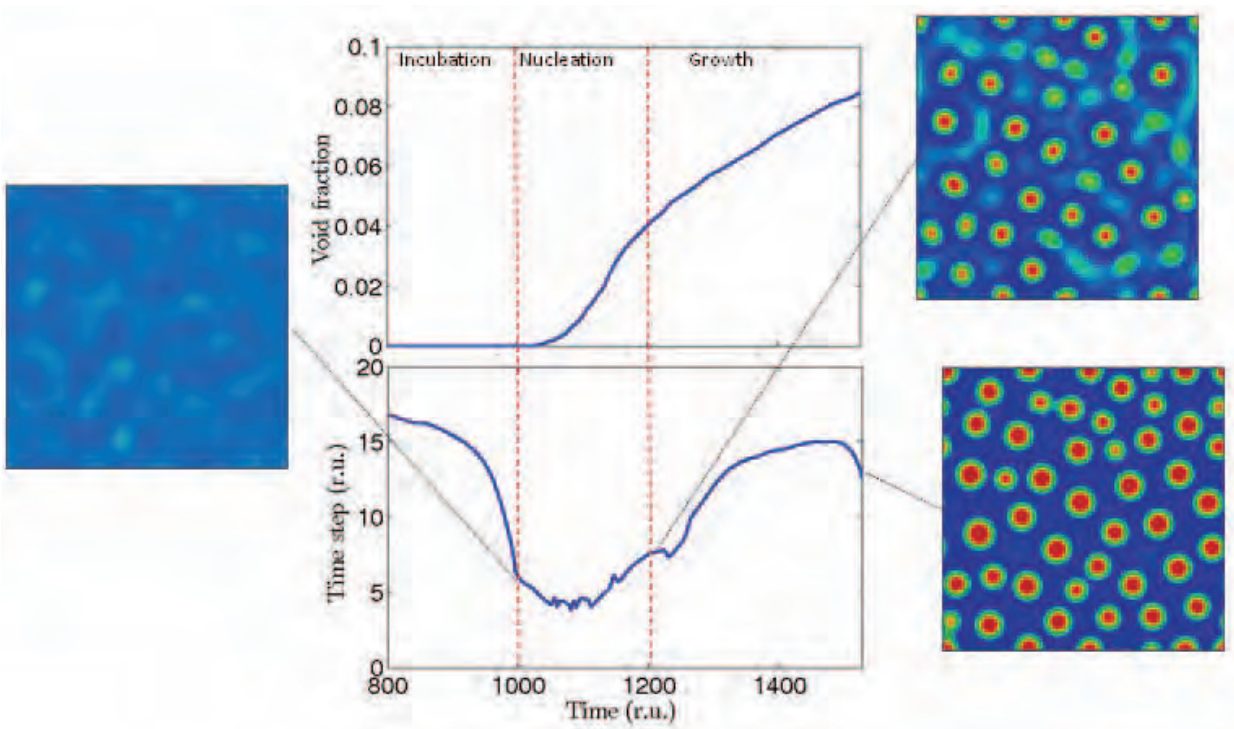

Figure 21. *Comparison between the void fraction and computational time step in a MARMOT simulation of void nucleation during irradiation with adaptive time stepping. The inset plots show the vacancy concentration at three points during the simulation. The time step adapts to the intrinsic time scale of the current physical phenomenon.*

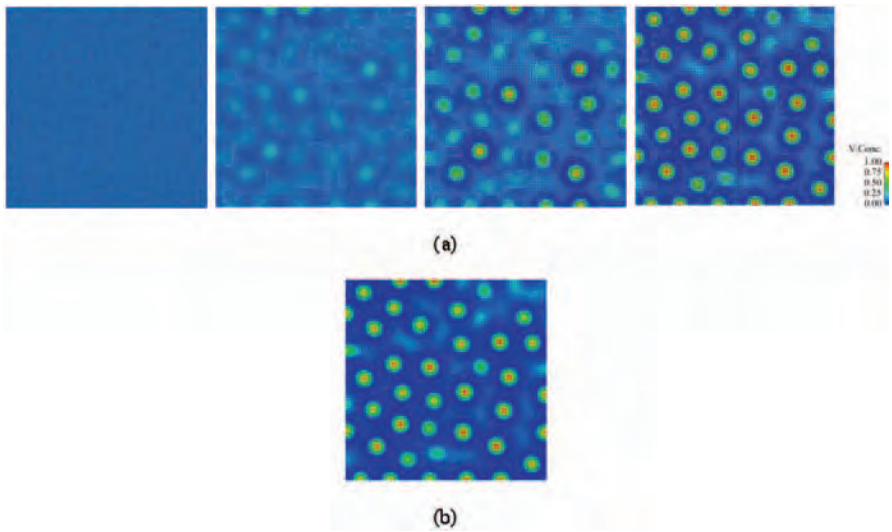

Figure 22. *The benefits of mesh adaptivity (a) void nucleation with adaptive mesh refinement. As voids nucleate, the mesh is coarsened where no voids have formed. (b) Final microstructure without mesh adaptivity. The adaptive mesh predicts the same evolved microstructure with a 25% reduction in computation cost.*

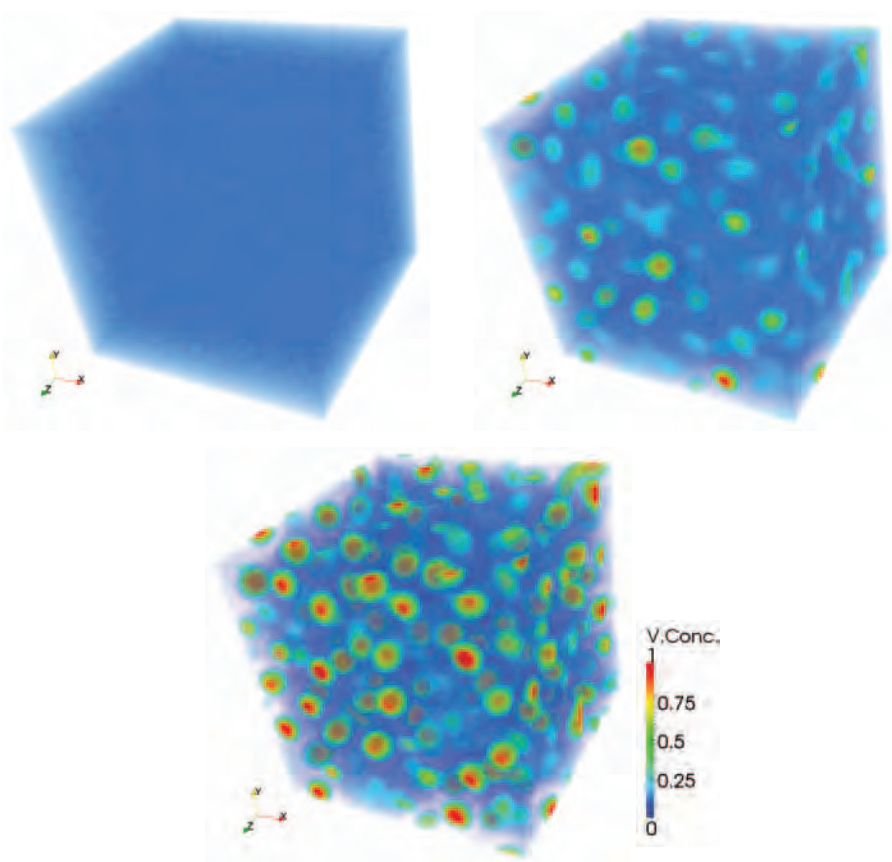

Figure 23. *3-D void nucleation in an irradiated solid simulated using MARMOT.*

shown in Figure 21, a larger time step can be taken during incubation and void growth than during void nucleation. Similarly, by adapting the mesh, the elements are focused in the areas that require the highest spatial resolution, e.g. Figure 22 shows adaptive mesh refinement in a simulation of void nucleation within an irradiated material. As the voids nucleate, the mesh is coarsened in the areas with no voids, resulting in a 25% reduction in the computation cost with no effect on the predicted microstructure. Finally, the modeling capabilities of MARMOT allow void nucleation to be simulated in 3-D for the first time (see Figure 23).

Multiscale Fuel Analysis via Scale Bridging.

BISON primarily includes irradiation effects due to microstructure evolution using empirically-developed closure models. While these models accurately interpolate within known conditions, they cannot extrapolate to new conditions or new materials. The mesoscale phase-field model captures irradiation-induced microstructure evolution; however, it is not feasible to use for simulation of macroscale bodies, such as a fuel pellet, due to the large number of degrees of freedom involved. The effect of radiation-induced microstructural evolution can be considered at the macroscale by coupling the phase field model to BISON. Because FE discretizations only consider the material behavior at discrete points, a coupled model need only resolve the microstructure at these specific points, thus reducing the computational cost of the simulation significantly.

In the multiscale model, a fuel pellet is represented with BISON. During the nonlinear solution of the equation system

within BISON, the mesoscale model evolves the microstructure. Various material properties of the evolved microstructure, such as thermal conductivity, are then measured and passed to BISON for the macroscale calculation. Random noise in the computed properties is eliminated by fitting the computed values with a polynomial surface. See Figure 24 for a schematic of the multiscale model.

A simple simulation of an irradiated fuel pellet has been used to investigate the validity of the multiscale model. In the simulation, steady-state heat conduction in a fuel pellet is modeled, such that the effect of irradiation on thermal conductivity is determined using a mesoscale phase-field model. Further details on this simple simulation can be found in [22, 23]. Figure 25 shows both the temperature profile within the fuel pellet and plots of the mesoscale vacancy concentration at three radial positions as found through simulation. From these results, it is evident that the void formation has a strong radial dependence; at the pellet center, many large voids surrounded by vacancy-depleted zones have formed; at mid-radius, a larger number of small voids have formed; on the outer circumference, only a few small voids are present. Thus, the multiscale model explicitly determines the microstructure throughout the fuel pellet.

Radial variation in void formation results in variation in thermal conductivity. The effect of void formation on thermal conductivity and pellet temperature is demonstrated by comparing the results to an unirradiated pellet. Thermal conductivity and the temperature at various radii for irradiated and pure, unirradiated pellets are shown in Figures 26(a) and 26(b), respectively. Due to large voids in the center of

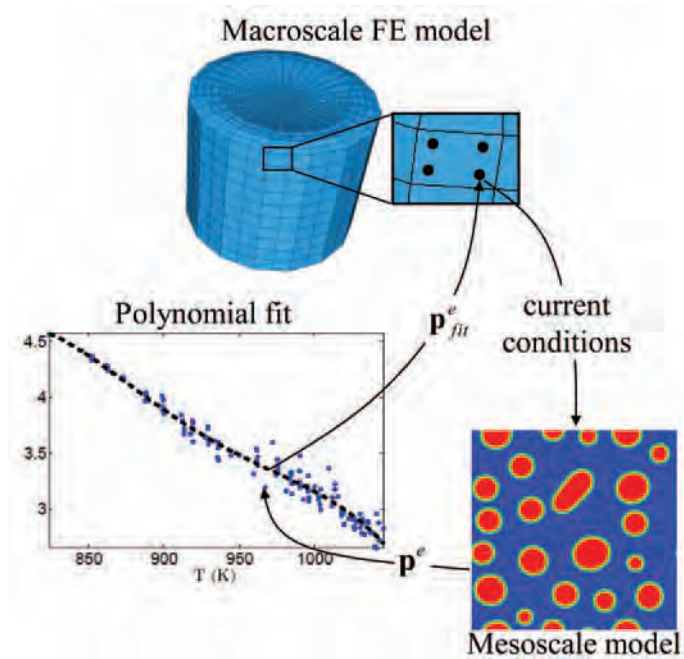

Figure 24. *Schematic of the proposed multiscale methodology. At the current conditions, the mesoscale model determines effective parameter values p^e which are fit with a polynomial surface at each nonlinear iteration. The macroscale FE model obtains values of p^e from the latest fit.*

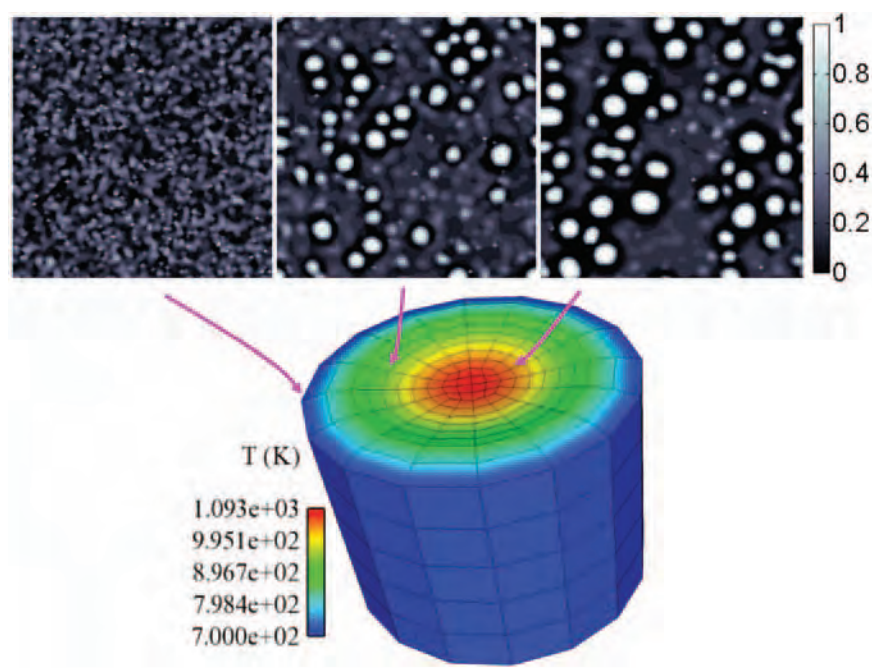

Figure 25. *Computed fuel-pellet temperature profile, where color corresponds to temperature. Snapshots above the pellet show vacancy concentration in the microstructure computed by the mesoscale model at the indicated radial positions.*

the irradiated pellet, thermal conductivity is significantly lower than that in the pure pellet. On the cooler outer edge, where only a few small voids have formed, thermal conductivity is only slightly lower than that in the pure pellet. Low internal thermal conductivity reduces transfer of heat to the pellet surface and, therefore, the center temperature is 27 K hotter in the irradiated pellet than in the pure pellet. While quite simple due to the elementary models employed at both scales, these results reflect general behavior observed in fission reactors.

Most critical behaviors of fuel that impact the performance and safety of reactors are caused by phenomena that occur at the mesoscale. By coupling the powerful simulation capability of our mesoscale phase-field model to our advanced fuel-performance code, the behavior of a fuel pellet or fuel rod assembly is predicted, as is the microstructural cause of that behavior. Thus, the multiscale model provides a truly predictive capability that will assist in the design of revolutionary new fuels that may impact the energy security of the US for many years.

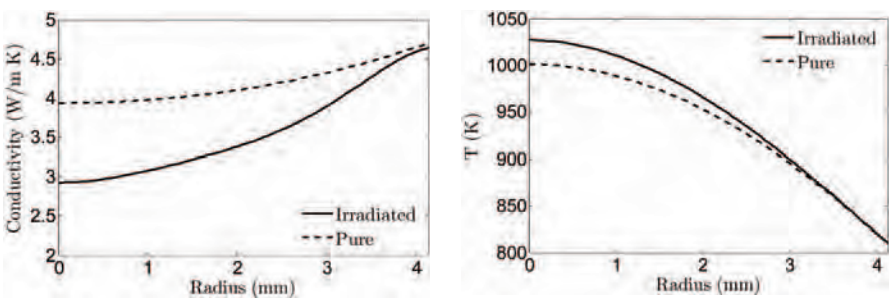

Figure 26. *Comparison between (a) the thermal conductivity; and (b) the temperature profile at various radii in an irradiated fuel pellet and in a pure pellet. Values are measured at a height z = 3:825 mm from the base of the pellet.*

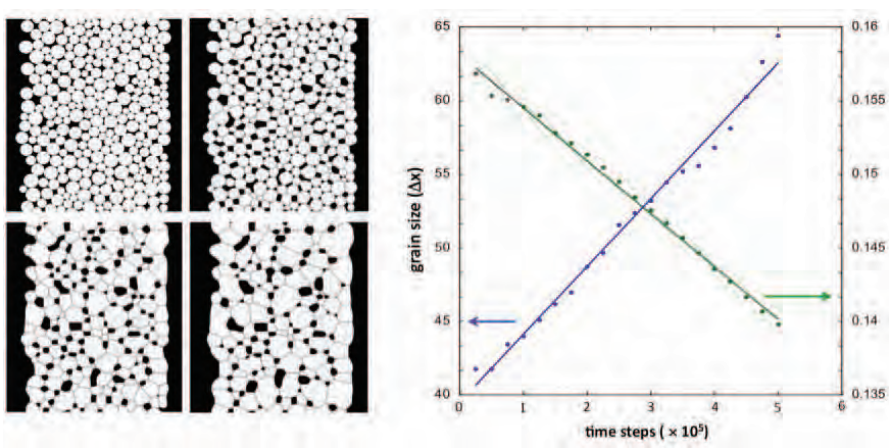

Figure 27. *Phase-field simulation of particle sintering showing the evolution of the average grain size and porosity versus time.*

Fuel Fabrication

The fabrication of ceramic fuels such as UO_2 is accomplished through the sintering process, in which a powder compact is annealed at high temperature, with or without stress, allowing densification of the material. In fuel materials, the process is stopped short of complete densification due to the desire for a certain porosity that can accommodate some of the fission products generated during service, and thereby minimize volumetric swelling. An understanding of how to design the initial porosity and pore size distribution for a given material is therefore highly desirable for optimized fuel performance. A mesoscale phase-field model has been implemented to study the sintering process by capturing the relevant diffusional processes, i.e., bulk diffusion, grain boundary diffusion, and surface diffusion, within a multi-particle system. Figure 27 shows the resultant microstructure during sintering, as simulated by the phase-field model, as well as the grain size and porosity behavior with time.

With mesoscale modeling, a better fundamental understanding of the fabrication process will improve fuel processing times and yields. This insight will lead to better management and use of fissile material within the nuclear energy ecosystem. The outcome will be more seamless transitions across the fuel cycle from reprocessing to fabrication to use.

Part III
Experimental Integration

One of the objectives of the FMSD is to bring people of various disciplines in the computational sciences, essentially under one roof, to form a focused, concerted effort to model and simulate advanced nuclear systems with sufficiently detailed physics in terms of quantifiable spatial and temporal accuracy. Executing on this plan will greatly enhance the Nuclear Science and Technology (NS&T) division's ability to successfully compete inside and outside the DOE complex by allowing the physics to drive experiments. It is not the intent of deploying and executing this plan to replace experiment and experience with advanced numerical simulation, but to expand and enhance them in a much more cost-effective and timely manner. The best possible outcome for accomplishing NS&T missions will occur with the blending of modeling and simulation, experiment/empirical data collection, and an expanding knowledge base (experience). An advanced simulation capability will provide a simulation-based confidence in the experimental programs so that neither simulation nor experimental efforts should be considered or treated as stand-alone efforts, but as combining both in a unified approach to our R&D and engineering analysis efforts.

Model Verification and Validation

While the magnitude of the advances in simulation capability have been staggering, verification and validation (V&V) of the software applications are necessary to provide for a simulation-based confidence. Without V&V, simulation of multiphysics phenomena becomes an academic exercise in mathematics and computer science. Simply stated, verification is a mathematical and software quality-control process designed to provide confidence that a chosen set of partial differential equations numerically approximated to represent a set of phenomena are solved in a mathematically correct fashion. Validation is largely a process to determine the degree to which the chosen set of partial differential equations actually replicate the real world phenomena being observed and measured, i.e., conducting experiments from which empirical validation can be generated. In other words, are we employing the correct mathematical models and property coefficients? Typically, this is an ongoing process as the physical models are tuned and optimized to better replicate the phenomena being observed. In some instances, conducting experiments result in discovering unknown phenomena for which mathematical models must be developed and then incorporated into software applications to provide a predictive capability. Quite often in nuclear systems, the physics of some systems, such as irradiated nuclear fuel, are so complex that simplification of the physics in the form a single mathematical representation is required. Employing new models or physical simplifications can only be accomplished through the validation process. And finally, verification and validation are not separable processes. Heavily verified yet un-validated software does not inspire any confidence that simulations of conceptual experiments will predict representative behavior. Conversely, it makes no sense to validate unverified software as matching of empirical data to numerical solution may be purely coincidental or the result of tuning equation coefficients.

Currently, models developed in the FMSD are validated against published results whenever possible. For example, BISON was initially verified against results reported in [24] and against commercial simulators. Preliminary models have also been implemented in BISON to simulate the annealing stage of the fuel fabrication process [25]. The extreme temperature ranges applied to the heterogenous fuel forms cause deformations and warping throughout the material. BISON results were compared to independent studies run using commercial codes. Non-uniform cooling and deformation of the materials were observed and can be seen in the exaggerated view in Figure 28. The mesoscale phase field model has been qualitatively verified by comparison to micrographs of irradiated materials (see Figure 19). Other codes built using MOOSE such as PRONGHORN (a pebble-bed reactor simulation tool) have also undergone rigorous verification against both benchmark problems and experimental data. For some simulations, however, particularly at the mesoscale, relevant data is not available. Therefore, experiments are currently being planned with the staff from the Basic Fuel Properties Department and the Fuel Performance and Design Department to provide the necessary

data. These experiments will involve the examination of irradiated samples of pure metals, focusing on quantifiable measures of microstructure evolution such as void fraction, void/grain boundary interaction, and void size distributions. This data will provide a quantifiable measure of the model accuracy.

Simulation-Assisted Experiments

Combining modeling and simulation with experiments into a unified approach to NS&T R&D and engineering analysis efforts will enhance both simulation and experiment while providing the nuclear engineering community with valuable experience. As discussed above, validation data is critical to the quality and usefulness of scientific software. Benefits provided to experimental (empirical) data collection through modeling and simulation can be extensive. In many fields of science, conducting experiments and obtaining meaningful measurements can be extremely difficult. The test apparatus or prototype of an engineered system may contain domains of interest that are too big, too small, or exist in hostile environments, such as in the case of an operating nuclear reactor core. Performing high-resolution simulations before the experiment is conducted gives the experimentalists insight as to where and what measurements need to be performed and possibly how they are to be performed. Greater intuition of how a system will react for a given set of initial conditions and boundary conditions (operating parameters) can be obtained cheaply and efficiently by detailed numerical simulation where comparable data would be nearly impossible to measure. Insight and intuition become critically important when performing the experiment more than once is prohibitively expensive. In fact, simulating conceptual experiments can and should be used to justify (and fund) an expensive physical experiment. Even if the physics of the conceptual experiment are not well understood, valuable intuition can be obtained by identifying certain phenomena trends of the experiment.

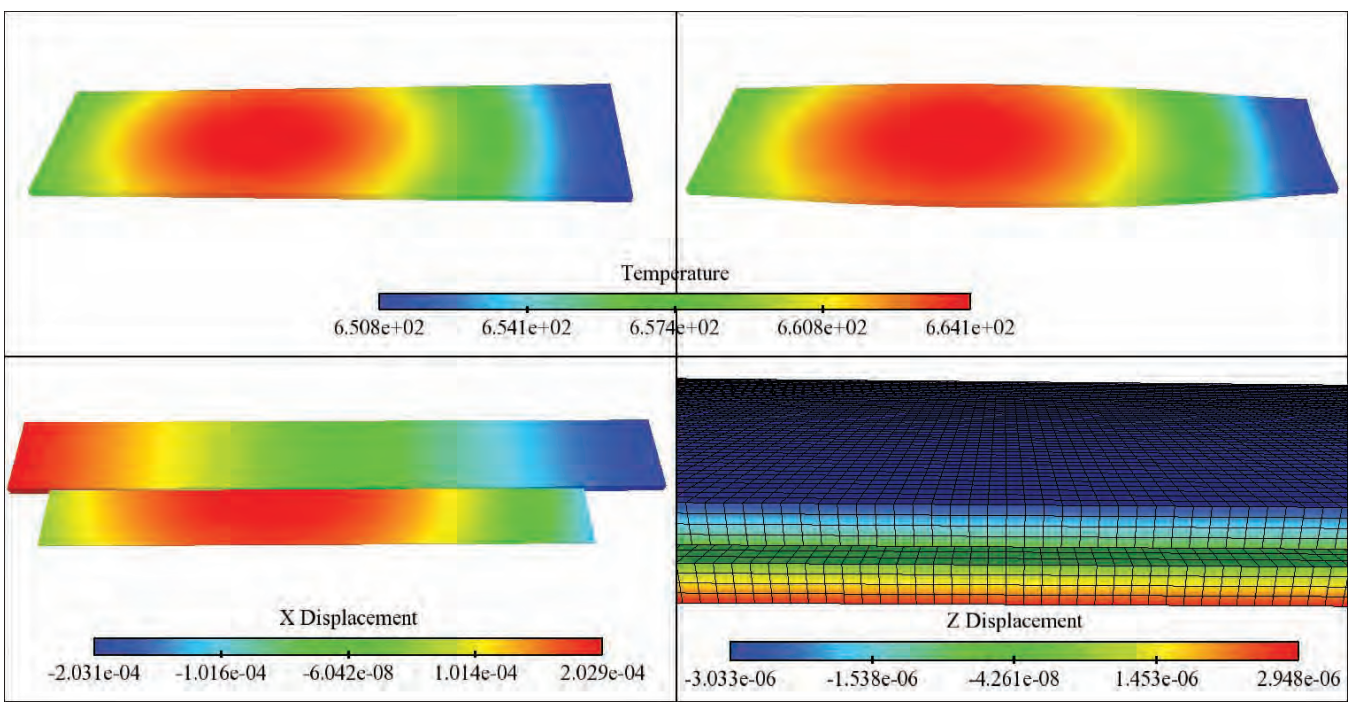

Figure 28. *Exaggerated displacements and temperature profiles after partially cooling a fuel plate during the annealing process. .*

Computational Post-Irradiation Examination (PIE)

Through collaboration with experimentalists, a computational PIE capability is one of the early targets of experimental integration being planned that will allow simulation results to be directly compared with irradiated fuel samples. For example the qualitative distribution of U-Pu-Zr is shown in Figure 29. This tool will allow manipulation of the irradiation and reactor conditions as they are integrated through time as well as giving insight into how the physics inside the fuel interrelate. If manipulation of the parameters results in a duplication of the PIE result, one has a plausible explanation for the processes that created it. The FMSD is well positioned to interact with the Advanced Test Reactor (ATR) National User Facility located here at the INL and the results generated from the numerous experiments performed there. Plans for developing a capability to calculate parameters like cladding temperatures based on coolant temperatures and the neutronics environment are currently under consideration.

Bibliography

1. Kirk, B. S., J. W. Peterson, R. H. Stogner, and G. F. Carey, 2006, "LibMesh: A C++ library for parallel adaptive mesh refinement/coarsening simulations," Eng Comput-Germany, 22(3-4), 237–254, Jan. 2006.
2. Berndt, M., J. D. Moulton, and G. Hansen, 2008, "Efficient nonlinear solvers for Laplace-Beltrami smoothing of three-dimensional unstructured grids," Comput. Math. Appl., 55(12), 2791–2806.
3. Mousseau, V. A., D. A. Knoll, and W. J. Rider, 2000, "Physics-based preconditioning and the Newton-Krylov method for nonequilibrium radiation diffusion," J. Comput. Phys., 160, 743–765.
4. Hohorst, K., 1990, "SCDAP/RELAP5/MOD2 Code Manual, Vol. 4: MATPRO – A Library of Materials Properties for Light-water Reactor Accident Analysis," NUREG/CR-5273, EGG-2555, U. S. Nuclear Regulatory Commission, Washington, D. C.
5. Schoof, L., and V. Yarberry, 1996, "EXODUS II: A Finite Element Data Model," SAND92-2137, Sandia National Laboratories, Sep. 1996.
6. Ortega, F. A., 2008, "General Mesh Viewer User's Manual," LA-UR-95-2986, Los Alamos National Laboratory (http://www.xdiv.lanl.gov/XCM/gmv/GMVHome.html).
7. I-deas NX (http://www.plm.automation.siemens.com/en us/products/nx/).
8. Advanced Visual Systems (AVS) (http://www.avs.com).
9. Tecplot (http://www.tecplot.com).
10. Hennigan, G., and J. Shadid, 1997, "NEMESIS I: A Set of Functions for Describing Unstructured Finite-element Data on Parallel Computers," Sandia Report, July 1997.
11. Braess, D., 2001, Finite Elements: Theory, Fast Solvers, and Applications in Solid Mechanics, Cambridge University Press, Cambridge.
12. Brenner, S. C., and L. R. Scott, 2002, The Mathematical Theory of Finite Element Methods, Springer, New York, Berlin, Heidelberg.
13. Ascher, U. M., and L. R. Petzold, 1998, Computer Methods for Ordinary Differential Equations and Differential-Algebraic Equations, SIAM, Philadelphia, PA.
14. Babuška, I., and M. Suri, 1994, "The 'p' and 'h - p' Versions of the Finite Element Method, Basic Principles, and Properties," SIAM Rev., 36 (4), 578–632, Dec. 1994.

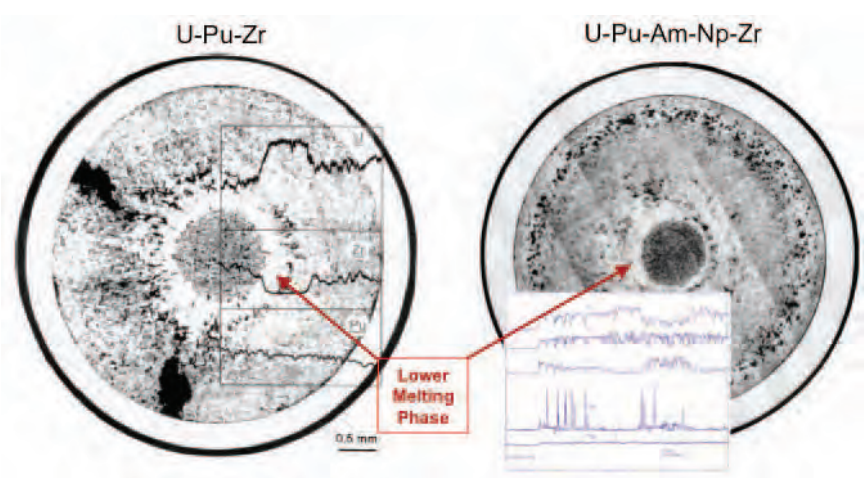

Figure 29. *Post-irradiation examination (PIE) of a metallic fuel showing the redistribution of constituents within the fuel as it undergoes irradiation.*

15. Carey, G. F., 1997, Computational Grids: Generation, Adaptation, and Solution Strategies, Taylor & Francis, Washington, D. C.

16. Ainsworth, M., and J. T. Oden, 2000, A Posteriori Error Estimation in Finite Element Analysis, Wiley Interscience, John Wiley & Sons, New York.

17. Kelly, D. W., J. P. De SR Gago, O. C. Zienkiewicz, and I. Babuska, 1983, "A posteriori error analysis and adaptive processes in the finite element method: Part I – Error Analysis," Internat. J. Numer. Methods Engrg., 19(11), 1593–1619.

18. Newman, C., G. Hansen, and D. Gaston, 2009, "Three-dimensional Coupled Simulation of Thermomechanics, Heat, and Oxygen Diffusion in UO_2 Nuclear Fuel Rods," J. Nucl. Mater., 392(1), 6–15.

19. Millett, P. C., A. El-Azab, and D. Wolf, 2010, "Phase Field Model of Gas Bubble Kinetics in Irradiated Metals," Phys. Rev. B., submitted.

20. Schönfelder, B., D. Wolf, S. R. Phillpot, and M. Furtkamp, 1997, "Molecular-dynamics Method for the Simulation of Grain-boundary Migration," Interf. Sci., 5, 245–262.

21. Rokkam, S. K., A. El-Azab, P. C. Millet, and D. Wolf, 2009, "Phase Field Modeling of Void Nucleation and Growth in Irradiated Metals," Modeling Simul. Mater. Sci. Eng., 17, 064002.

22. Tonks, M. R., D. Gaston, C. Permann, P. Millet, G. Hansen, and D. Wolf, 2010, "A Coupling Methodology for Mesoscale-informed Nuclear Fuel Performance Codes," Nucl. Engrg. Des., In press.

23. Tonks, M. R., G. Hansen, D. Gaston, C. Permann, P. Millett, and D. Wolf, 2009, "Fully-coupled Engineering and Mesoscale Simulations of Thermal Conductivity in UO_2 Fuel Using an Implicit Multiscale Approach," J. of Phys.: Conf. Ser., 180(1), 012078.

24. Ramirez, J. C., M. Stan, and P. Cristea, 2006, "Simulations of Heat and Oxygen Diffusion in UO_2 Nuclear Fuel Rods," J. Nucl. Mater., 359(3), 174–184.

25. Clark, C., G. Moore, D. Keiser, Jr., J. Jue, and B. Park, 2009, "Fabrication of Monolithic RERTR Fuels by Hot Isostatic Pressing," Nucl. Tech., submitted.

CODY PERMANN is currently a high-performance computing software engineer in the Nuclear Fuels and Material Division at the Idaho National Laboratory. He is an accomplished computer scientist with experience in multiple application areas. His research interests include optimization, specialized acceleration hardware, and software frameworks. He is serving a joint appointment with the Center for Advanced Modeling and Simulation (CAMS). He will receive his masters degree in computer science in December 2010.

MICHAEL TONKS has a Ph.D. in Mechanical Engineering from the University of Illinois, Urbana-Champaign. His research background is in multiscale modeling of material behavior, including computational materials science and computational mechanics. He is developing 3-D mesoscale models of irradiation-induced microstructure evolution using finite element phase field models. He is also investigating methods for coupling the mesoscale models to fuel performance codes. He has been at Idaho National Laboratory for two years.

DEREK GASTON holds advanced degrees in Computational Applied Mathematics and Computer Science. His background is in enabling large scale, parallel, scientific simulation with a particular interest in software frameworks. Areas of research include generic frameworks for mesh adaptivity, error estimation, code verification and validation, scale bridging, fluid simulation and fully implicit contact. Derek has previously held a position at Sandia National Laboratory developing simulation frameworks and is currently leading the Computational Frameworks group within the Fuel Modeling and Simulation department at Idaho National Laboratory.

RICHARD L. WILLIAMSON (BS, 1977, MS, 1978, Mechanical Engineering, Brigham Young University; PhD, 1989, Mechanical Engineering, University of Idaho) is a member of the Fuel Modeling and Simulation Department at the INL. He has over 32 years experience in computational methods research and model development. His current research relates to developing models to simulate nuclear fuel behavior with specific emphasis on complex multiphysics phenomena including: fully-coupled nonlinear thermomechanics, fission product behavior, fuel-pellet clad interaction, material property degradation due to irradiation, and propagating fractures.

DR. PAUL MILLETT is currently a research staff member in the Nuclear Fuels and Materials Division in Idaho National Laboratory (since 2009). He received his doctoral degree in Civil Engineering from the University of Arkansas in 2006 with support from the Distinguished Doctoral Fellowship. His research interests involve the development and application of multiscale materials modeling capabilities that provide new insight and prediction of material behavior on multiple length and time scales. Dr. Millett has applied atomistic as well as mesoscale simulation techniques to study the behavior of micro- and nano-structured materials subjected to severe environments. Dr. Millett has access to and vast experience with highly-parallel MD computer codes executed on INL's High Performance Computing (HPC) cluster.

GLEN HANSEN, Ph.D. is recognized for his work in multiphysics methods and software development performed at Idaho and Los Alamos National Laboratories. He currently leads development of various multiphysics capabilities at INL and was a PI of a major Accelerated Strategic Computing Initiative (ASCI) effort and also a Deputy Group Leader at Los Alamos. He holds a Ph.D. in computer science from the University of Idaho, an M.S. in mechanical engineering from the University of Nebraska and a B.S. in petroleum engineering from the University of Wyoming. He is a certified Project Management Professional and is an IEEE Certified Software Development Professional (CSDP). Dr. Hansen is a member of the Idaho Section of the American Nuclear Society and the Society for Industrial and Applied Mathematics. He is an adjunct professor at the University of Nevada-Reno and has authored or co-authored over 40 peer reviewed publications in the field of computational science.

DR. RICHARD MARTINEAU began employment at the INL in July of 1989. He is manager of the Fuels Modeling and Simulation Department within the INL Nuclear Fuels and Materials Division. The department is responsible for those aspects of developing advanced numerical methods, scientific numerical packages, high-performance computing frameworks, and multiphysics analysis tools for nuclear fuel performance modeling and simulation. The work performed in this department is in direct support of DOE Nuclear Energy programs as well as supporting internal programs within the INL's Nuclear Science & Technology Directorate. Dr. Martineau's background includes expertise in computational fluid dynamics, multiphysics simulation of coupled-fluid flow and solid-state heat transfer, gas dynamics and thermodynamics.

DC POWER SUPPLY
RAPID

New In-pile Instrumentation for the ATR

J. L. Rempe, D. L. Knudson, B. G. Kim, K. G. Condie, J. E. Daw, D. W. Nigg, S. C. Taylor, and T. Unruh

Abstract

A key component of the Advanced Test Reactor (ATR) National Scientific User Facility (NSUF) effort is to enhance instrumentation techniques available to users conducting irradiation tests in this unique facility. In particular, development of sensors capable of providing 'real-time' measurements of key irradiation parameters is emphasized because of their potential to increase data fidelity and reduce post-test examination costs. This section describes the strategy for identifying new instrumentation needed for ATR irradiations and the program underway to develop and evaluate new sensors to address these needs. Accomplishments from this program are illustrated by describing new sensors now available to users of the ATR NSUF. In addition, progress is reported on current research efforts to provide users improved in-pile instrumentation.

Introduction

The U.S. Department of Energy (DOE) designated the Advanced Test Reactor (ATR) as a National Scientific User Facility (NSUF) in April 2007 to further U.S. nuclear science and technology research. By supporting users from universities, laboratories, and industry, the ATR conducts basic and applied nuclear research and development that advances the nation's energy security needs. A major component of the ATR NSUF effort is to develop and implement in-pile instrumentation that is capable of providing real-time measurements of key parameters during irradiation. As discussed below, significant progress has been made toward obtaining new sensors to address these needs.

ATR and Test Location Descriptions

The ATR and its associated Advanced Test Reactor Critical (ATR-C) facility are premier facilities for scientific investigation of nuclear fuel and materials [1]. Designed to allow simulation of long neutron radiation exposures in a short time period, the reactor has a maximum power rating of 250 MW_{th}, with a maximum unperturbed thermal neutron flux of 1 $x10^{15}$ n/cm^2-s and a maximum fast neutron flux of 5 x 10^{14} n/cm^2-s. The ATR-C facility is a nuclear mock-up of the ATR core that allows researchers to characterize in advance, with precision and accuracy, the expected changes in core reactivity of the ATR of a proposed test.

The ATR is cooled by pressurized (2.5 MPa/360 psig) water that enters the reactor vessel bottom at an average temperature of 52°C (126°F), flows up outside cylindrical tanks that support and contain the core, passes through concentric thermal shields into the open part of the vessel, then flows down through the core to a flow distribution tank below the core. When the reactor is operating at full power, the primary coolant exits the vessel at 71°C (160°F).

As shown in Figure 1, the ATR core consists of 40 curved plate fuel elements in a serpentine arrangement around a 3 x 3 array of primary testing locations, or nine large high intensity neutron flux traps. The unique ATR control device design permits power variations among its nine flux traps using a combination of control cylinders (drums) and neck shim rods. The beryllium control cylinders contain hafnium plates that can be rotated toward and away from the core. Hafnium shim rods, which withdraw vertically, are inserted or withdrawn for minor power adjustments. Within bounds, the power level in each corner lobe of the reactor can be controlled independently to allow for different power and flux levels in the four corner lobes during the same operating cycle. The ratio of fast to thermal flux can be varied from 0.1 to 1.0. In addition to the nine large volume (up to 122 cm/48" long and up to 13 cm/5.0" diameter) high-intensity neutron flux traps, there are 66 irradiation positions inside the reactor core reflector tank, and there are two capsule irradiation tanks outside the core with 34 low-flux irradiation positions. A Hydraulic Shuttle Irradiation System (HSIS), more commonly referred to as a "Rabbit," testing capability was also recently installed in the ATR to restore the reactor's capability to perform irradiations of small capsules in selected "B" positions of the reactor for materials research, rapid activations, and isotope production. This system will become available to ATR users in 2011.

There are three basic types of test assembly configurations used in the ATR:

- **Static Capsule Experiment** – These capsules may contain a number of small sample or engineered components. Static capsule experiments may be sealed or contain material that can come in contact with the primary coolant (such capsules are in an open configuration without being sealed). Capsules may be any length up to 122 cm (48 in.) and be irradiated in any core position, including the flux traps. Irradiation temperature may be controlled (within limits) by providing a gas gap in the capsule with a known thermal conductance. Peak temperatures may be measured using a series of melt wires, temperature-sensitive paint spots, or silicon carbide temperature monitors. Accumulated neutron fluences may be verified using flux wires.

- **Instrumented Lead Experiment** – Active control of experiments and data from test capsules during irradiation is achieved using core positions with instrumentation cables and temperature control gases in instrumented lead experiments. Such experiments can have instrumentation (i.e., sensors for in-pile detection of parameters such as temperature, pressure, elongation, etc.) connected to individual capsules or single specimens. This instrumentation can be used to control and sample conditions within the capsule. For example, temperature control in individual zones is performed by varying the gas mixture (typically helium and neon) in the gas gap that thermally links the capsule to the water-cooled reactor structure. In addition to temperature, instrumented lead experiments have been used to monitor the gas around the test specimen. In a fueled experiment, the presence of fission gases due to fuel failures or oxidation can be detected via gas chromatography. Instrument leads allow real time display of experimental parameters in the control room.

- **Pressurized Water Loop Experiment** – Five of the nine flux traps used for materials and fuels testing are equipped with pressurized water loops (at the NW, N, SE, SW, and W locations). A sixth loop will be operational in 2011. Each of the water loops can be operated independently at different temperatures, pressures, flow rates, or water chemistry requirements. These loops can operate above the standard temperatures and pressure of a commercial PWR power plant. The great advantage of loop tests is the ease in which a variety of samples can be subjected to conditions specified for any PWR design. Each pressurized loop in the ATR is instrumented to measure and control (both helium and water) coolant flows, temperatures, pressures, and sample test data. Figure 1 provides a cross section of the ATR core.

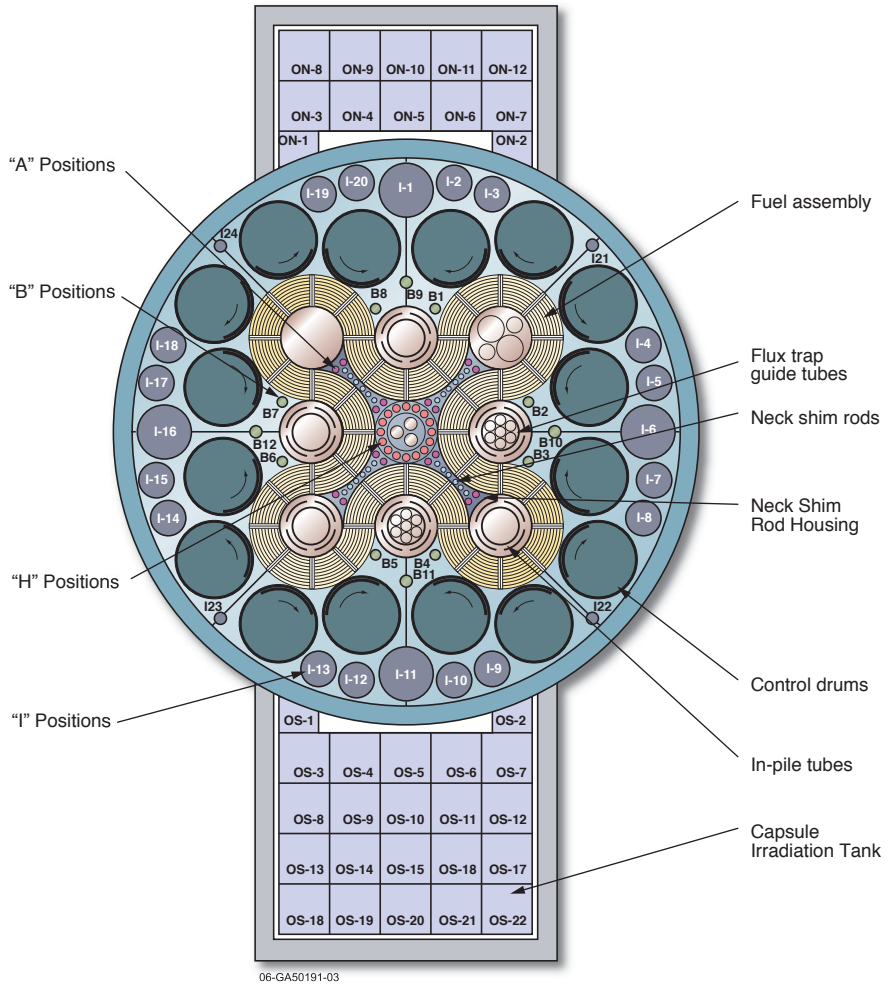

Figure 1. *ATR core cross section identifying irradiation locations.*

The ATR-C core is a nuclear mock-up of the ATR core that generally operates at thermal power of less than 5 kW. The primary difference between the ATR-C and ATR is that the highly-enriched uranium (HEU) fuel in the ATR-C is uniformly loaded with boron, while the ATR fuel is not. A second difference of note is that the ATR-C uses five cadmium-plated safety rods, while the ATR uses six hafnium-plated safety rods. During operation, this difference is insignificant. ATR-C criticality is normally attained at a power greater than 0.25 mW. However, this pool-type reactor (see Figure 2) usually operates at a power level of about 600 W and provides useful physics data for evaluating:

- worth and calibration of control elements
- excess reactivities and charge lifetimes
- thermal and fast neutron distributions
- gamma heat generation rates
- fuel-loading requirements
- effects of inserting and removing experiments and experiment void reactivities
- temperature and void reactivity coefficients.

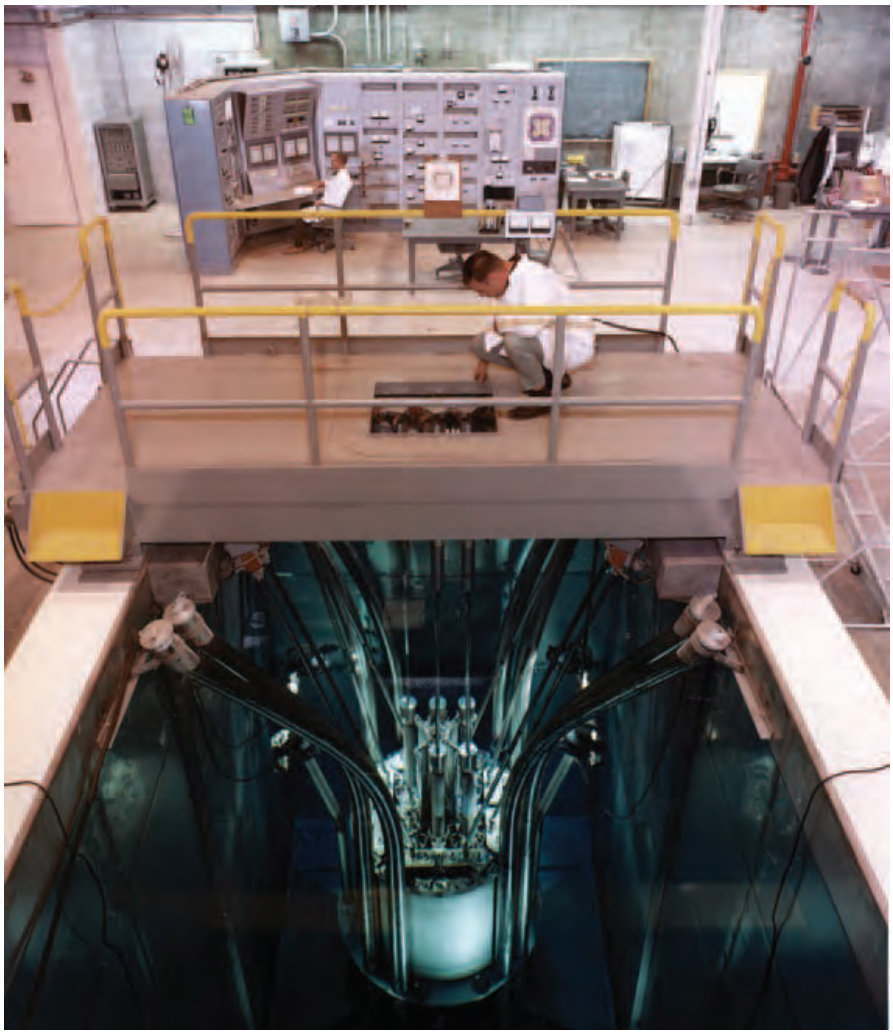

Figure 2. *ATR-C facility layout.*

Clearly, the ATR and ATR-C offer unique advantages for testing. With additional in-pile instrumentation to support these testing capabilities, the features offered by these facilities can be even more fully utilized.

Strategy to Address ATR User Needs for Enhanced Instrumentation

Despite its long history for developing highly specialized instrumentation to meet the demands of customers conducting unique tests in one-of-a-kind test facilities, INL instrumentation research funding decreased significantly in the 1980s when large nuclear test facility programs ended. In 2004, an effort was initiated that now allows INL to explore obtaining unique new instrumentation required for ATR irradiations. Because much of the sensor fabrication and evaluation equipment and expertise were still available, INL's High Temperature Test Laboratory (HTTL) staff quickly developed high temperature thermocouples requested by ATR customers for fuel irradiations. Today, INL instrumentation development staff is involved in the development of several types of enhanced sensors for ATR users.

As discussed in [2], INL efforts to enhance ATR instrumentation began by first completing a review to identify instrumentation available to users at other test reactors located in the U.S. and abroad, including OSIRIS (France), HBWR (Norway), BR-2 (Belgium), HFR (Netherlands), HANARO (Republic of Korea), JMTR (Japan), HFIR (US), and MITR (US). Table 1 summarizes results from this review. The column labeled

"ATR Technology" indicates the types of sensors currently available to ATR users. The column, "Proposed Advanced Technology," includes two categories: "Available at Other Reactors," which identifies several technologies employed at other test reactors that could be adapted to enhance ATR instrumentation capabilities, while the "Developmental" category identifies developmental or non-nuclear technologies that could be used in irradiation tests. Technologies listed in this last column are considered to be less "ready" for implementation. The blue text in Table 1 denotes the instrumentation

Table 1. *Review of instrumentation available at ATR and other test reactors[a].*

Parameter	Parameter			ATR Technology	Proposed Advanced Technology	
	Static Capsule	Instr. Lead	PWR Loop		Available at Other Reactors	Developmental
Temperature	√	√	√	- Melt wires (peak) - Paint spots (peak) - SiC temperature monitors (range)		- Wireless (range) - Ultrasonic thermometers
		√	√	- Thermocouples (Type N, K, C, and HTIR-TCs)[b]		- Fiber optics - Ultrasonic thermometers
Thermal Conductivity		√	√	- Out-of-pile examinations	- Degradation using signal changes in thermocouples	- Hot wire needle probe techniques
Flux/Fluence (neutron)	√	√	√	- Flux wires (Fe, Ni, Nb)	- Activating foil dosimeters	
		√	√		- Self-powered neutron detectors (SPNDs) - Subminiature /miniature fission chambers	- Moveable SPNDs
Gamma Heating		√	√		- Degradation using signal changes in thermocouples	
Dimensional		√	√		- LVDTs (stressed and unstressed) - Diameter gauge - Hyper-frequency resonant cavities	- Ultrasonic transducers - Fiber optics
Fission Gas (Amount, Composition)		√	√	- Gas chromatography - Pressure sensors - Gamma detectors - Sampling	- LVDT-based pressure gauge	- Acoustic measurements with high-frequency echography
Loop Pressure			√	- Differential pressure transmitters - Pressure gauges with impulse lines		
Loop Flowrate			√	- Flow venturis - Orifice plates		
Loop Water Chemistry			√	- Off-line sampling /analysis		
Crud Deposition			√		- Diameter gauge with neutron detectors and thermocouples	
Crack Growth Rate			√		- Direct current potential drop technique	

a Blue text denotes instrumentation being investigated for ATR applications; red text denotes new instrumentation currently deployed at the ATR.
b Type C thermocouple use requires a "correction factor " to correct for decalibration during irradiation.

currently being pursued as a part of ATR NSUF research activities, while the red text denotes new instrumentation developed by INL and deployed in the ATR. Instrumentation currently being evaluated for the ATR NSUF was selected based on anticipated user needs and 'technology readiness' (allowing this effort to provide ATR users requested instrumentation as soon as possible).

It should be noted that adapting instrumentation used at other test reactors often requires laboratory demonstrations because of ATR-specific irradiation conditions (e.g., higher neutron fluxes, higher temperatures, etc.) and test capsule geometries. To maximize the benefit from instrumentation development activities, many efforts are in collaboration with other organizations that are experienced with such instrumentation and that have similar interests in obtaining enhanced versions of these sensors for their test facility.

Sensor Development/ Deployment Highlights

As a result of this new instrumentation development and evaluation effort, several new sensors are now available to ATR and ATR-C users. In addition, as discussed in this section, efforts are underway to explore the viability of several other technologies for detecting key parameters during irradiation.

Temperature

Because of the importance of this key parameter, new methods for detecting sample temperature during irradiation were initially emphasized in this program. As discussed in this section, HTTL research has led to several new temperature sensors, and efforts continue to explore the potential for more compact and accurate temperature detectors.

High Temperature Irradiation Resistant Thermocouples (HTIR-TCs)

Commercially-available thermocouples drift due to degradation at high temperatures (above 1100°C) or due to transmutation of thermocouple components. Hence, thermocouples were needed that could withstand both high temperature and high radiation environments. To address this need, INL developed a High Temperature Irradiation Resistant ThermoCouple (HTIR-TC) design that contains commercially-available doped molybdenum paired with a niobium alloy. Battelle Energy Alliance (BEA), the operating contractor for INL, has filed a patent application for this technology, and INL now offers the sensors to ATR and other test reactor customers. HTIR-TC component materials were selected based on data obtained from materials interaction tests, ductility investigations, and resolution evaluations [2,3,4,5,6,7].

To demonstrate HTIR-TC long duration performance, long-term testing, in which thermocouples were held at elevated temperatures (from 1200°C to 1800°C) for up to six months, was performed at the HTTL. The 1200°C test included nineteen commercially-available Type N thermocouples, three commercially-available Type K thermocouples, and nine INL-developed swaged HTIR-TCs (see Figure 3). As indicated in Figure 3, some Type K and N thermocouples drifted by over 100°C or 8%. Much smaller drifts (typically less than 20°C or 2%) were observed in the INL-developed HTIR-TCs. As documented in [3], similar drifts (2%) were observed in HTIR-TCs in a long duration (4000 hour) test completed at 1400°C.

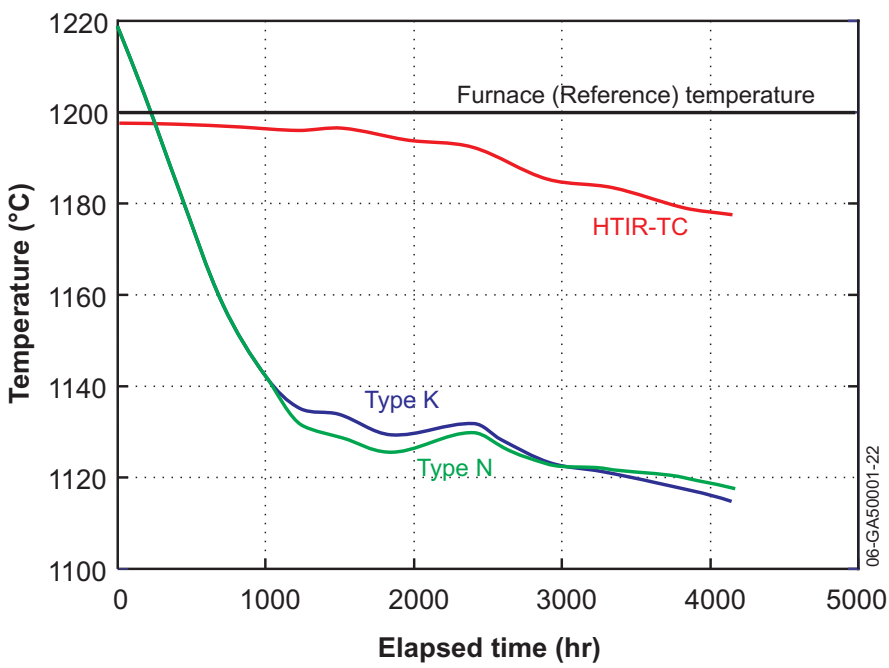

Figure 3. *Representative thermocouple response in HTTL 1200°C tests .*

HTIR-TCs were installed in the AGR-1 multi-capsule experiment that irradiated gas reactor fuel samples at temperatures up to 1200°C in INL's ATR. The test started in February 2007 and concluded in October 2009. Figure 4 shows signals from two INL-developed HTIR-TCs and one Type N thermocouple located within one of the test capsules. Signal variations are due to ATR power fluctuations and outages. As shown in this figure, the HTIR-TC (TC-4-1) located near the Type N thermocouple (TC-4-3) is giving a signal consistent with the signal from this Type N thermocouple at the beginning of this irradiation. In addition, the HTIR-TC located at a higher temperature region within the capsule (TC-4-2) is yielding a consistent, but higher temperature, signal. However, in October 2008, the Type N thermocouple failed; and its signal ceased.

HTTL staff also explored options to reduce fabrication costs and enhance the reliability of HTIR-TCs for higher temperature in-pile testing, allowing their use in applications up to 1800°C. For example, initially deployed HTIR-TCs rely on swaging fabrication techniques because of their simplicity and durability. However, INL also recently explored alternate fabrication techniques that could enhance HTIR-TC high temperature performance. As shown in Figure 5a, a swaged TC is fabricated by loading pre-formed, crushable insulator beads onto thermoelement wires and placing the insulated thermoelements in a sheath (tube) that is then swaged (compacted) to form a single, cohesive component. If desired, the thermocouple may be joined to hard extension cable using a splice sleeve as shown in Figure 5a. INL also developed fabrication processes for drawn and loose assembly HTIR-TC designs. Drawn thermocouples are prepared similarly to swaged thermocouples in that crushable insulator beads are loaded onto thermoelement wires that are placed in a sheath. However, the assembly is passed through a stationary die to form a drawn thermocouple. In a loose assembly thermocouple (see Figure 5b), preformed hard-fired insulators are loaded onto thermoelement wires. After being placed in a sheath, a splice sleeve is used to join the thermocouple assembly to the hard extension cable. To preclude any oxidation of thermocouple components, the assembly is vacuum purged and backfilled with inert gas through this splice sleeve.

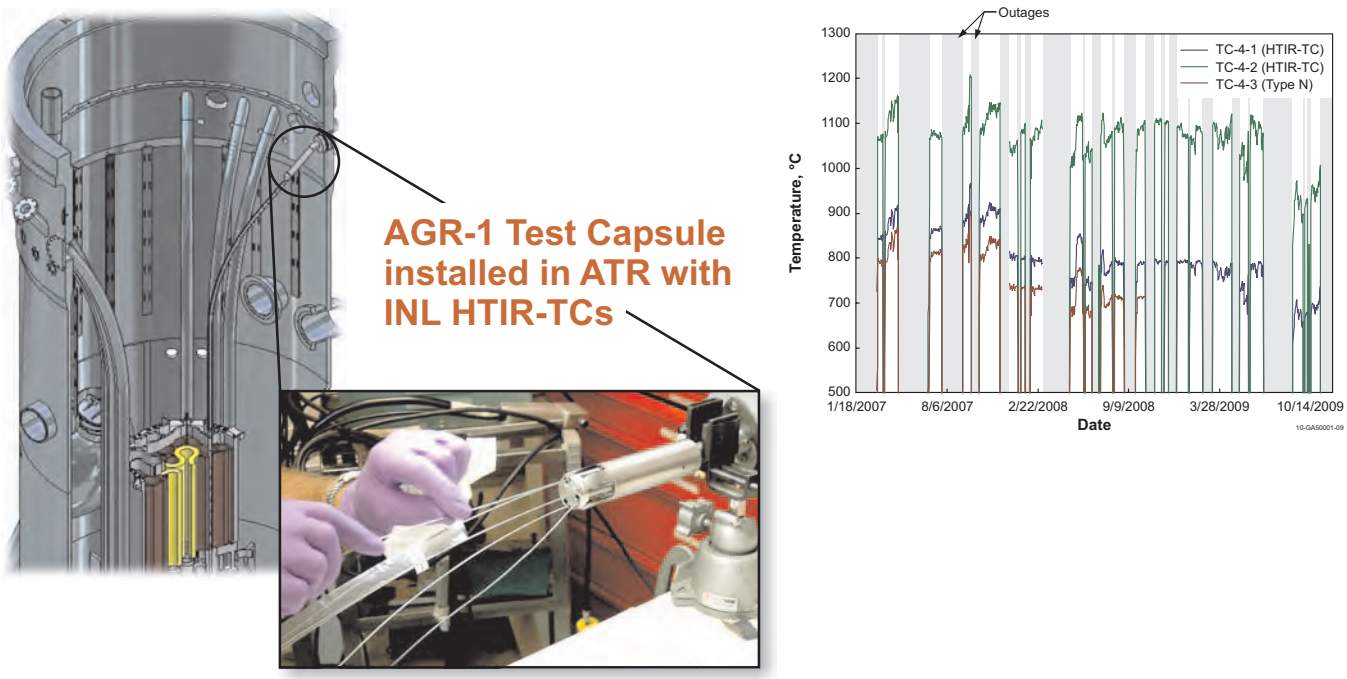

Figure 4. *HTIR-TCs installed in AGR-1 test capsule and representative HTIR-TC and Type N data during ATR irradiation.*

A long duration (1000 hour) test was completed to compare the performance of swaged, drawn, and loose assembly HTIR-TCs at 1500°C. Figure 6(a) provides the results from that test. The signals from the swaged and drawn HTIR-TCs decreased by 2.3%, primarily during the first 600 hours of the test, whereas the loose assembly thermocouple displayed greater stability and resolution than either the swaged or drawn thermocouples. Although the observed swaged HTIR TC response is consistent with the drift observed in prior 1200 and 1400°C four thousand hour tests, the fact that most of the drift occurred during initial portions of this test suggests that longer duration heat treatments may be needed to stabilize the distortion associated with swaging or drawing processes when larger diameter thermoelement wires are used (prior HTTL efforts to optimize heat treatment processes had focused on thermocouples with smaller diameter wires). Selected thermocouples from this test were then operated at 1800°C without any additional heat treatment. Results, shown in Figure 6(b), suggest that HTIR-TCs are also capable of functioning at this temperature. Although a furnace malfunction led to this test being terminated prematurely at 170 hours, the loose assembly and drawn HTIR-TCs exhibited less than 1% drift, and the swaged HTIR-TC exhibited approximately 8% drift. Note that fabrication processes for HTIR TCs expected to operate at 1800°C would include heat treatment above this temperature. Although better stability would be expected from all three HTIR-TC designs if they had been heat-treated for operation at 1800°C, the performance of all three HTIR-TC designs in this test suggests that they are viable for this temperature.

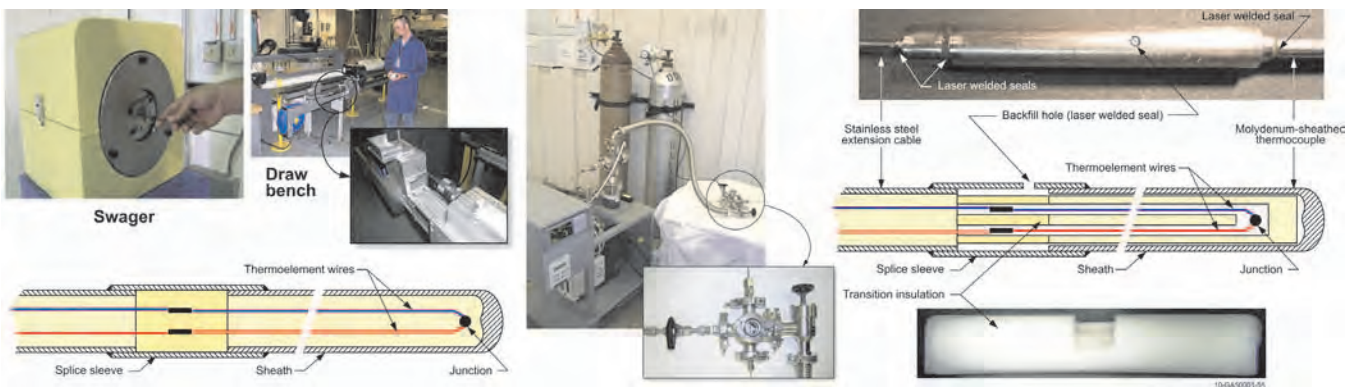

(a) Swaged and drawn HTIR-TCs

(b) Loose-assembly HTIR-TCs

Figure 5. *Possible HTIR-TC configurations.*

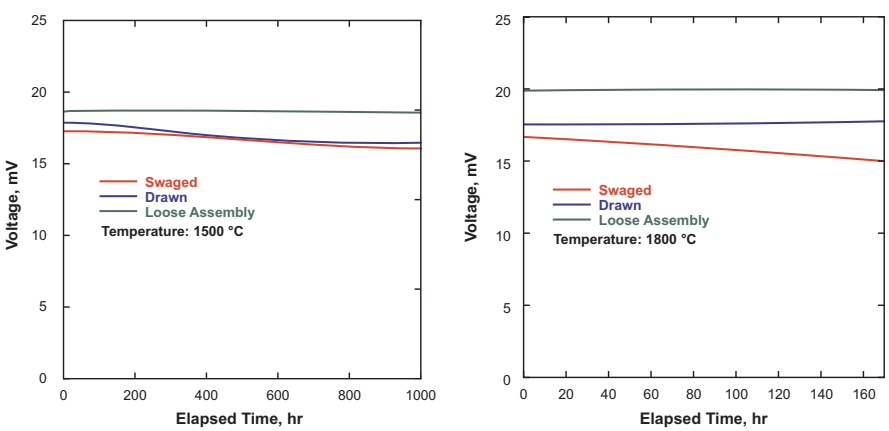

Figure 6. *HTIR-TC performance at (a) 1500°C and (b) 1800°C.*

Silicon Carbide Temperature Monitors

Silicon carbide (SiC) temperature monitors are now available for use as temperature sensors in ATR static capsules. Melt wires or paint spots, which are the standard temperature sensors available for ATR static capsules, are limited in that they can only detect whether a single temperature was exceeded or not. SiC monitors are advantageous because a single monitor can be used to detect for a range of temperatures that may have occurred during irradiation. For decades, the use of these temperature monitors was based on the phenomenon that irradiation-induced defects in SiC experience annealing at temperatures exceeding its peak irradiation temperature. Researchers relied on changes in length, density, thermal conductivity, and electrical resistivity to infer irradiation temperature from SiC monitors. However, recent research [8] recommends using changes in resistivity because of improved accuracy, ease of measurement, and reduced costs. Experimental data indicate that accuracies of approximately 20°C are possible with this technique for dose ranges of 1 to 8 dpa and temperatures from 200 to 800°C. Absolute limits for this approach are 150°C (an amorphorous threshold) and 875°C (due to recrystallization).

Specialized equipment at INL's HTTL (see Figure 7) has been configured to measure SiC samples after heating at various temperatures in a furnace located within a stainless steel enclosure at the HTTL. After heating, cooled samples are placed into a constant temperature environmental test chamber to insure electrical resistivity measurements are taken within 0.2°C of a predetermined temperature, 30°C. A high accuracy (nine-digit) multimeter, which is placed outside the stainless steel enclosure, is used to obtain resistance measurements.

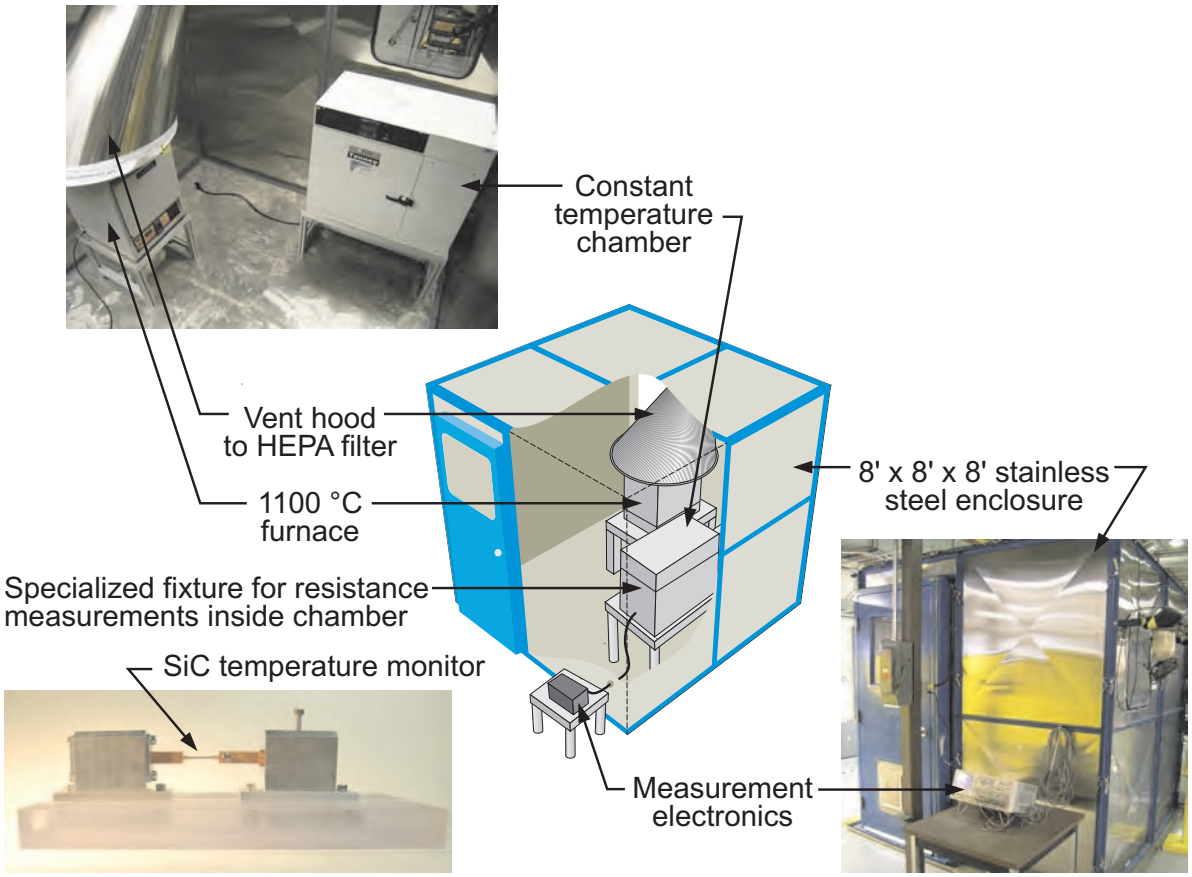

Figure 7. *Setup for annealing and measuring electrical resistivity of SiC temperature monitors.*

To assess INL's capability to accurately perform SiC temperature monitor measurements, a comparison effort was completed with Oak Ridge National Laboratory (ORNL). In these comparisons, identical SiC monitors that had been subjected to identical irradiation conditions were measured by ORNL and INL [9]. As indicated in Figure 8, results from one of the four sets of samples evaluated in this effort show that INL and ORNL estimate similar peak irradiation temperatures from SiC monitors (e.g., the normalized resistivity increased at similar temperatures for both organizations). ORNL/INL comparisons for samples tested at other temperatures and fluences all yielded similar temperature estimates.

Ultrasonic Thermometry

Ultrasonic thermometry has the potential to improve upon temperature sensors currently used for in-pile fuel temperature measurements. Even though the HTIR-TCs developed by INL have overcome most of the difficulties associated with thermocouples, the resistivity of electrical insulators can degrade if subjected for long durations to high temperatures (> 1800°C), causing shunting errors. Furthermore, thermocouples typically allow one measurement at a single location, and examination of melt wires or silicon carbide monitors only allow estimation of the maximum test temperatures at the point of installation. Ultrasonic thermometry offers the potential for real-time in-pile measurement of a temperature profile using a single multi-segment sensor.

Prior applications of ultrasonic thermometers have demonstrated the viability of this technology, but in-pile applications were primarily limited to high-temperature fuel damage tests, which ceased several decades ago. INL recently initiated a new effort to investigate the use of ultrasonic thermometry for measuring a temperature profile using a single, small diameter (typical diameters range from 0.25 mm to 1 mm) multi-segment sensor [10,11,12]. Tests are underway at INL's HTTL to demonstrate the viability of and optimize ultrasonic techniques using the setup shown in Figure 9.

Initial testing is focusing on a simplified, single segment probe. As part of this optimization effort, various design alternatives are being explored. Alternate wave guide, sensor, and sheath materials with high melting temperatures and insensitivity to neutron radiation, such as molybdenum, are under evaluation. Also, different methods of generating ultrasonic pulses (i.e., magnetostrictive and piezoelectric materials) as well as different pulse modes (i.e., longitudinal and torsional) are being considered. Ultimately, evaluations will focus on multiple segment probes, as a key feature of the ultrasonic thermometry system is the ability to measure a temperature profile. However, these sensors will also require development of a signal conditioning and processing system for the complicated signals generated by a multi-segment sensor. Ultimately, it is planned that the optimized UT design for in-pile temperature detection will be evaluated in an ATR NSUF test.

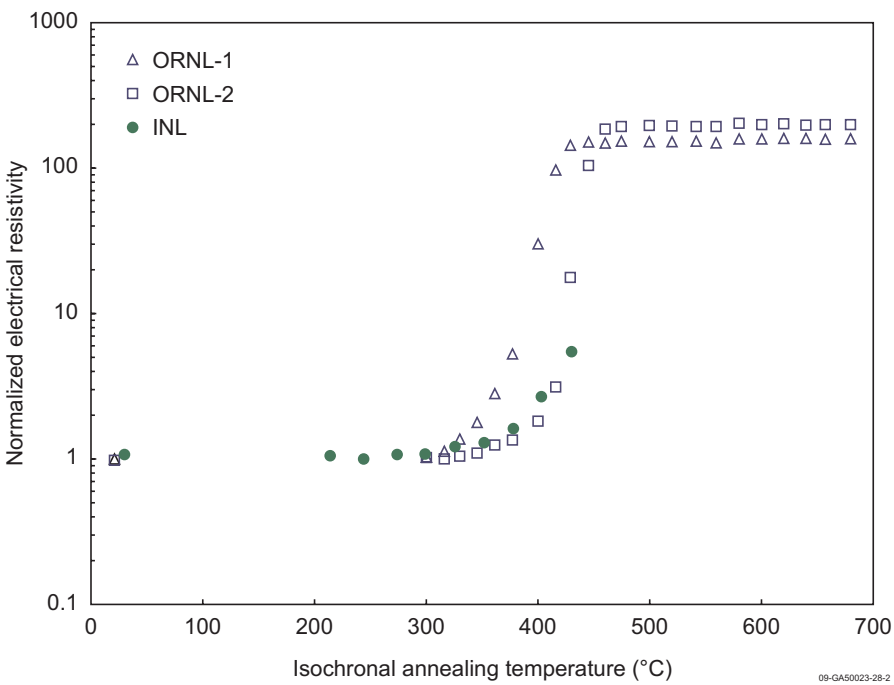

Figure 8. *Electrical resistivity measurement comparison on SiC monitors irradiated at 300°C.*

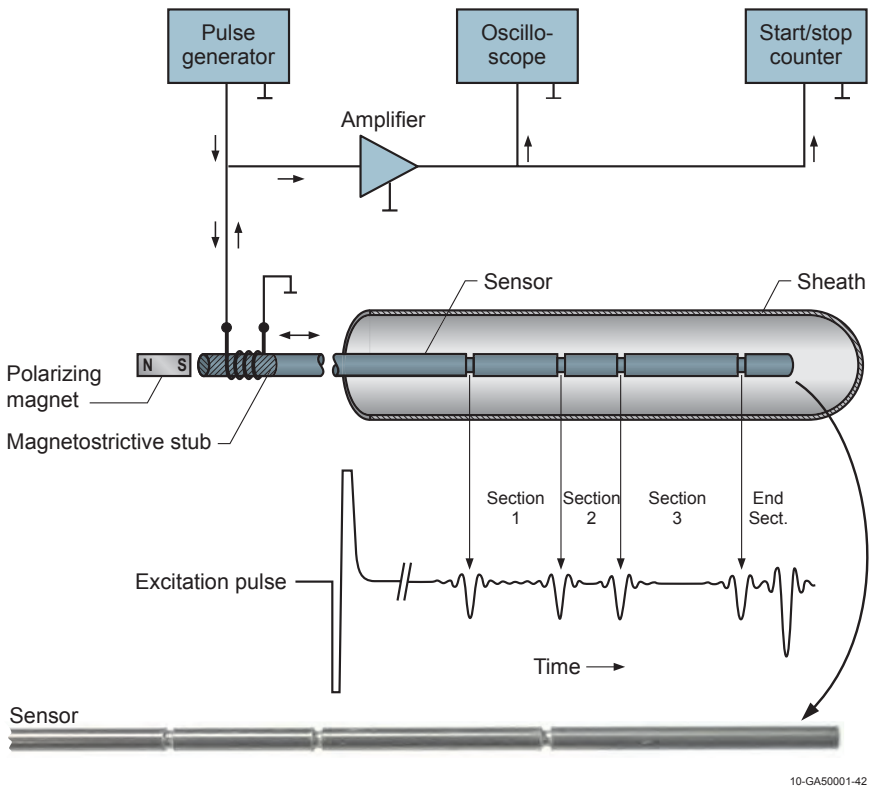

Figure 9. *A typical multi-sensor pulse/echo ultrasonic thermometry system and 'notched' sensor.*

Thermal conductivity detection

Thermal conductivity is another key property that must be known during irradiation testing of fuels or structural materials. Thermal conductivity is highly dependent on the physical structure, chemical composition, and the state of the material. Currently, changes in fuel or material thermal conductivity during ATR irradiations are evaluated out-of-pile. However, as part of a collaborative effort with Utah State University (USU) and the Institute for Energy Technology at the Halden Reactor Project (IFE/HRP), HTTL staff are evaluating a two-thermocouple steady-state thermal conductivity approach and a transient hot wire thermal conductivity method as candidate in-pile effective thermal conductivity measurement techniques (see Figure 10). Details about the setup for each approach, definitions of the variables shown in figure equations, and the status of evaluations are summarized in this section. Additional details may be found in [13,14,15].

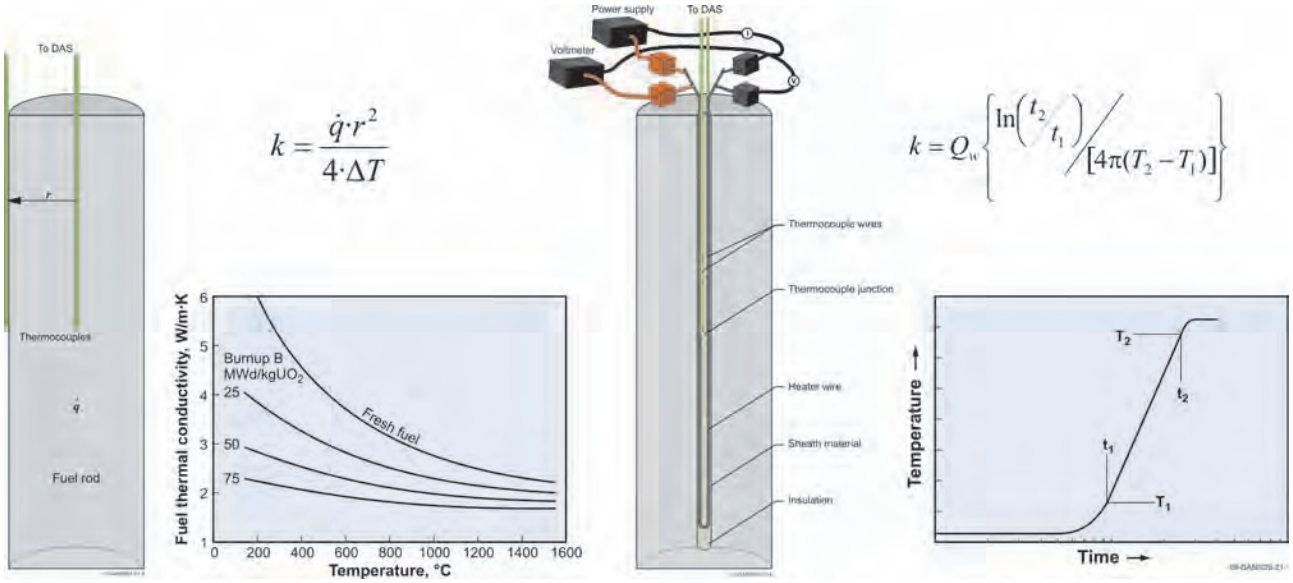

(a) Steady-State Method

(b) Transient Method

Figure 10. *In-pile thermal conductivity methods under evaluation (see text for equation variable definitions).*

Steady-state multiple thermocouple method

The first method, the steady state radial heat flow method, calculates fuel rod thermal conductivity using two thermocouples inserted into the surrogate fuel rod with volumetric heat generation simulated by Joule heating. One thermocouple monitors fuel centerline temperature, while the other monitors temperature at a measured radial position within the rod. As shown in Figure 10a, the thermal conductivity, k, is calculated from the radial temperature drop, ΔT, the radial distance between the thermocouples, r, and volumetric heat generation, $\dot{q}$. Often, this approach is implemented in-pile, with one thermocouple in the center of the fuel and one located outside the fuel cladding (in the coolant). Hence, as indicated in Figure 10a, in-pile degradation of fuel during irradiation (due to swelling, cracking, etc.) typically leads to results being presented as simply an indication of thermal conductivity degradation (because the 'effective' thermal conductivity of the fuel, cladding, and gap is measured; and one is really just detecting changes in the fuel that impact its thermal conductivity).

For this approach, USU/INL evaluations focused on estimating the thermal conductivity of a surrogate fuel rod using two thermocouples inserted into a surrogate material rod—one to monitor centerline temperature and the other to monitor temperature—at a measured radial position within the rod. Although initial USU/INL evaluations were performed using Type K thermocouples, in-pile applications would incorporate the use of INL-developed HTIR-TCs. A high temperature carbon structural foam was selected as the surrogate material in these evaluations. Several candidate surrogate materials were initially explored; but investigations indicated that this structural foam was the only viable surrogate material with appropriate electrical resistivity, low thermal conductivity, and high temperature resistance to oxidation and melting. Although the limited room-temperature data from its manufacturer were sufficient to select this material as a surrogate, temperature-dependent material property data were needed for this USU/INL effort. Temperature-dependent data were obtained using standard material property measurement systems (e.g., laser flash diffusivity, pushrod dilatometry, and differential scanning calorimetry) available at INL's HTTL.

Figure 11 shows the test setup used to evaluate the two-thermocouple method. Surrogate rods containing two thermocouples were positioned inside a tube furnace with an argon cover gas to provide a controlled sample test temperature. Voltage and current from the power supply were supplied to the rod using Inconel electrodes connected to Inconel clamps. Leads attached to Inconel clamps at each end of the rod were used to measure the voltage drop across the rod. A precision current shunt was used to measure current within the experimental test loop. Volumetric heat generation was calculated using the measured current, I and the sample voltage drop, V, sample dimensions, and the fact that power is the product of the current and voltage. Flow rates were adjusted using valves to vary fluid conditions within the

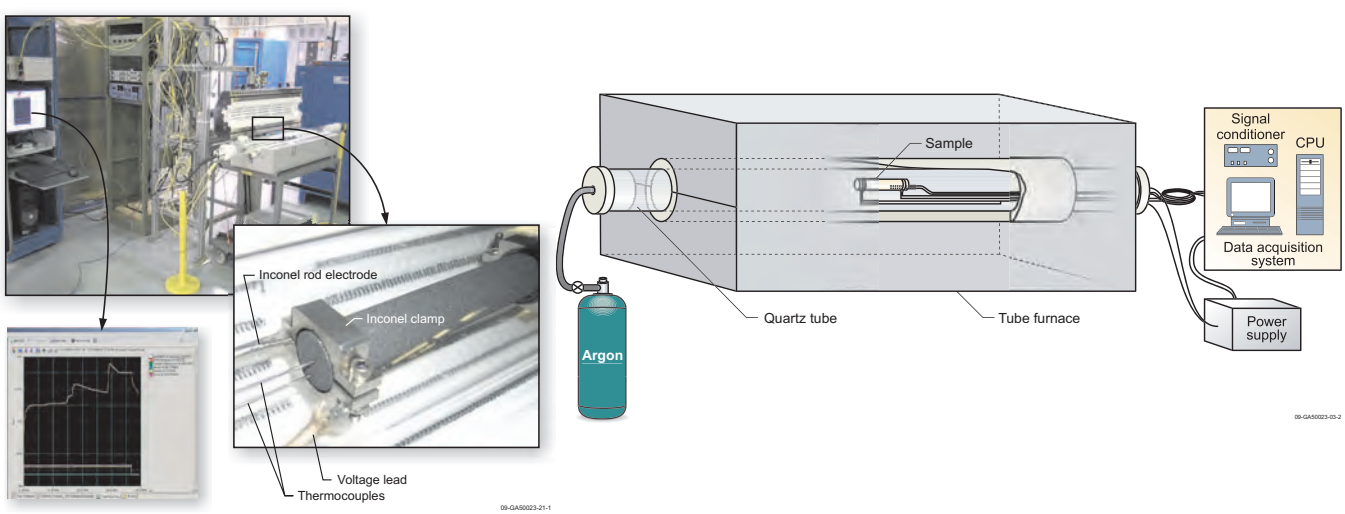

Figure 11. *Setup for evaluating the two-thermocouple method.*

tube. The fluid inside the tube can either be air or an inert gas, such as argon. Signals were processed by a data acquisition system to give temperatures from thermocouples and power in the sample.

As indicated in Figure 12, experimental results show that the two-thermocouple method can detect thermal conductivity of the selected surrogate rod material with 14% accuracy from 500 to 600°C and 33% from 600 to 700°C. Note that measurement uncertainty for 'Property data average k' in Figure 12, which was obtained with HTTL material property measurement systems, was estimated as ±14%. Hence, lower temperature thermal conductivity values were consistent with values obtained from standard laboratory techniques. Increased differences in thermal conductivity values obtained at higher temperatures are suspected to be due to the selected surrogate material porosity and the experimental setup (e.g., radiation/convection enhanced heat transfer associated with the porous material led to increased heat transfer).

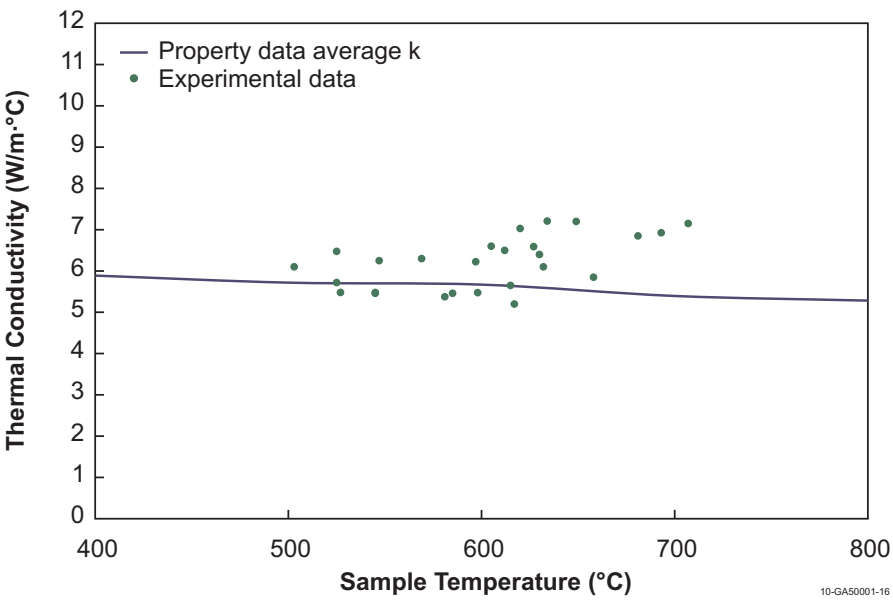

Figure 12. *Comparison of two-thermocouple and material property measurement system thermal conductivity data.*

Hot wire method

The second method evaluated by USU/INL is a needle probe method based on Transient Hot Wire Methods (THWM). As shown in Figure 10b, the probe contains a heat source element and a temperature sensor inserted into a material whose thermal conductivity is to be measured. As indicated in this figure, the fuel rod thermal conductivity, k, is derived from a relation that includes Q_w, the linear power dissipated by the heater and the measured increase in temperature, T_2 and T_1, between times, t_2 and t_1. The surrogate nuclear fuel rod thermal conductivity is determined from the temperature rise measurement of the sample. Needle probes were designed and fabricated at INL's High Temperature Test Laboratory (HTTL) for both room temperature proof-of-concept evaluations and high temperature testing. Using the

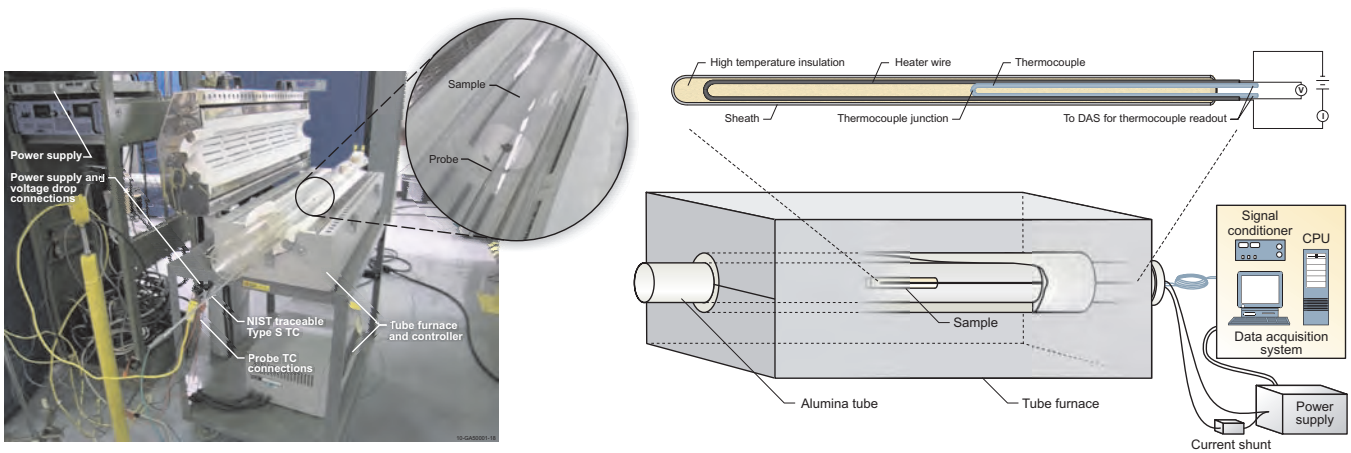

Figure 13. *Setup for evaluating transient hot wire needle probe.*

setup shown in Figure 13, transient method experimental results show that the INL/USU designed needle probes can measure the American Society for Testing and Materials (ASTM)-recommended thermal conductivity of the reference material, fused silica, within 2% at room temperature, 250°C, and 400°C. In these evaluations, the probe design was selected such that materials and geometry were optimized to improve accuracy for the proposed test temperature and surrogate rod material (e.g., the diameter and materials used for probes would differ to optimize their heating in the surrogate fuel rod and reduce losses between a surrogate rod and the data acquisition equipment). These optimization techniques will also be implemented for irradiation testing, where the distance from the fuel rod to the data acquisition equipment is even longer with more dramatic temperature differences.

INL/USU evaluations are continuing to gain insights about the limitations and benefits of each method and its respective viability for in-pile applications. Initial results suggest that the transient method reduces the impact on the sample because it only requires a single small centerline sensor. Furthermore, the transient method requires shorter measurement times, and it eliminates the need to quantify 'uncertain' parameters (such as fuel to cladding contact resistance or coolant convective heat transfer coefficients) that are required for two-thermocouple approaches. However, additional evaluations are underway to gain insights about the limitations of this approach with respect to substrate thermal conductivity, material size, and long-term reliability of these needle probes.

Geometry

Geometry changes of samples irradiated in the ATR are currently evaluated out-of-pile after specified lengths of irradiation time. However, efforts are underway to evaluate several options that offer the potential to obtain real-time length and diameter data from samples irradiated in the ATR. For lower temperature (up to 500°C) applications, commercially available Linear Variable Differential Transducers (LVDTs) are being evaluated as a near-term option for detecting geometry changes in ATR irradiations. In addition, ultrasonic transducers are being explored as a more compact sensor that can detect geometry changes and crack growth with higher precision in multiple dimensions.

Linear Variable Differential Transformers (LVDTs)

LVDTs are electrical transformers with three coils placed end-to-end around a tube, as shown in Figure 14a. The center coil is the primary, and the two outer coils are known as the secondaries. A cylindrical magnetically-permeable core, attached to the object whose position is to be measured, slides along the axis of the tube. An alternating current is driven through the primary, causing a voltage to be induced in each secondary, which is proportional to its mutual inductance in the primary. As the core moves, these mutual inductances change, causing the voltages induced in the secondaries to change. The coils are

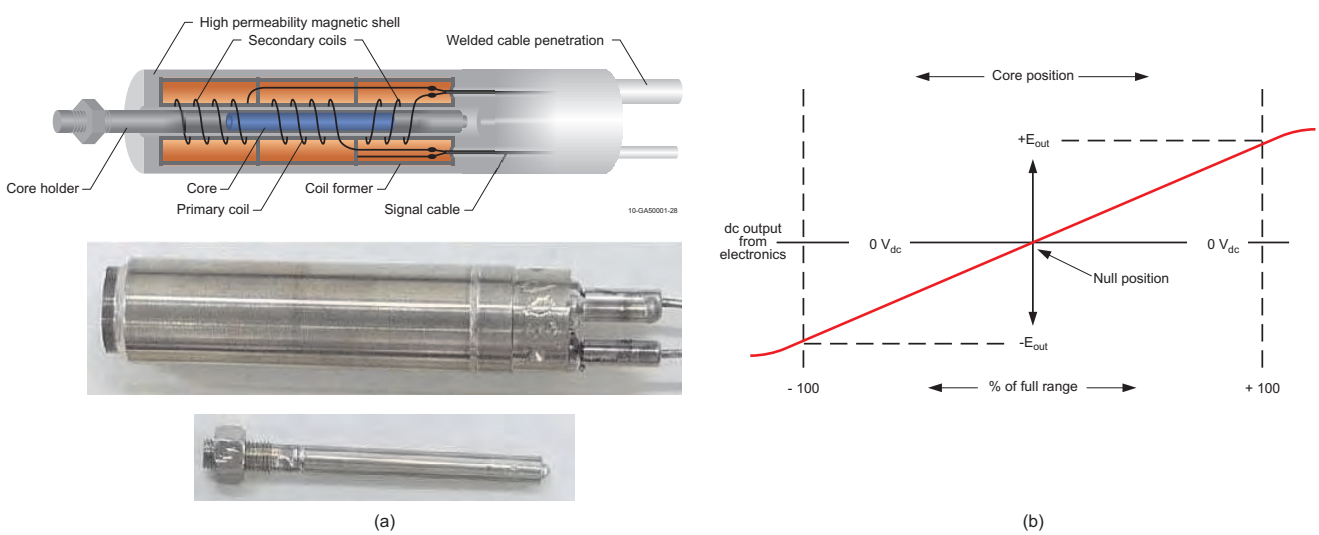

Figure 14. *LVDTs (a) key components and (b) operation.*

connected in reverse series so that the output voltage is the difference between the two secondary voltages. When the core is in its central position, equidistant between the two secondaries, equal but opposite voltages are induced in these two coils, so the output voltage is zero (see Figure 14b).

Prior to deployment in ATR's high flux and temperature test conditions, LVDT designs made by vendors offering nuclear grade LVDTs for irradiations were evaluated at the HTTL [16,17]. The objective of this effort was to evaluate (and enhance, as needed) the viability of applying commercially-available LVDTs as in-pile sensors for detecting dimensional changes of specimens during high temperature (up to 500°C) irradiations in ATR instrumented lead capsules and PWR loop tests.

Nuclear-grade commercial LVDTs produced by two vendors were identified as having the potential to meet anticipated ATR test conditions if minor modifications were incorporated into their design. The first supplier, identified as Vendor A, could provide LVDTs qualified to a maximum operating temperature of only 350°C; the second supplier, identified as Vendor B, could only provide LVDTs with diameters that exceeded ATR design requirements, but indicated that they could meet ATR design requirements of 500°C. (Note that Vendor A's temperature limitation was established primarily because of instabilities associated with the sensor response as its coils pass through a material-specific Curie temperature at approximately 360°C. Hence, including Vendor A's LVDT was deemed appropriate because alternate materials, that are not susceptible to Curie temperature effects, could be incorporated into their sensor design. Likewise, Vendor B indicated that alternate components could be used in their sensor design so that it was smaller in

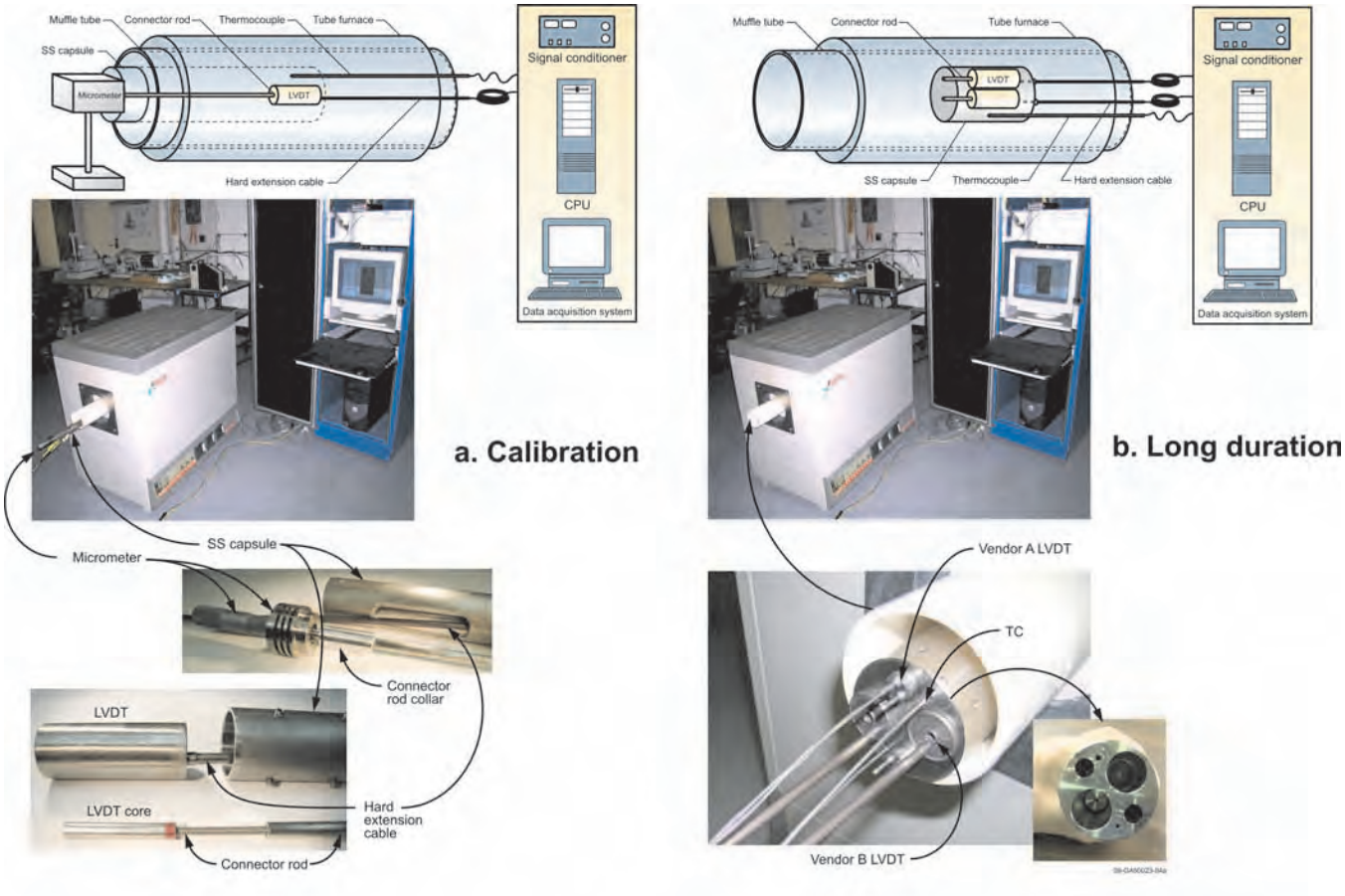

Figure 15. *Setup for evaluating LVDT performance.*

diameter). In both cases, limited data were available to verify either manufacturer's claims regarding their LVDT performance at high temperature. Hence, INL evaluated LVDTs made by each vendor at the HTTL using test setups shown in Figure 15. To verify the accuracy for the range of elongations anticipated, calibration tests were completed between room temperature and 500°C. Long duration performance evaluations were then completed to monitor signal stability at 500°C for 1000 hours.

For the long duration test, all four LVDTs were configured in the test fixture with cores set as close as possible to the zero displacement, or 'null,' positions. Consequently, output for all four LVDTs would be expected to remain near 0 Vdc throughout the test (if they remained stable). For comparison purposes, 500°C calibration data for each LVDT were used to convert measured output voltage to an indicated displacement. Figure 16 presents the deviation of the indicated displacement (relative to the time 0 output) as a percentage of the maximum linear travel, which is ± 2.5 mm for all the sensors tested.

As indicated in Figure 16a, Vendor A's LVDTs were found to be superior to Vendor B's LVDTs. Their maximum deviation was equivalent to a displacement of ~7×10^{-6} m, relative to their time 0, position. (Approximately 25 h were set aside for stabilization at 500°C before marking time 0.) Results for Vendor B's LVDTs are quite different. These LVDTs show substantial oscillation in addition to dramatic step changes in indicated deviations (near 130 h for LVDT B1 and near 210 h for LVDT B2). In fact, LVDT B1 shows a maximum deviation equivalent to a displacement of ~700×10^{-6} m, indicating a reduction in stability by a factor of ~100 compared to Vendor A's LVDTs. These results, along with calibration evaluations documented in [16,17], clearly favor the Vendor A's LVDT design for use in ATR irradiation experiments. Several options are being pursued to enhance Vendor A's LVDT designs. INL evaluations of developmental nuclear grade LVDTs that include these components demonstrate that their response is very stable for the entire 1000 hours that they were tested (see Figure 16b).

Test results from evaluations of developmental and commercially available nuclear grade LVDTs were used to select an optimized LVDT design for ATR irradiations. Initial ATR irradiations with LVDTs will be completed in a PWR loop containing a creep test rig, similar to the design shown in Figure 17. As discussed in [18,19], a prototype of this creep test rig is currently being evaluated in an autoclave at INL's HTTL. As shown in Figure 18, initial evaluations with a 2 mm diameter stainless steel tensile specimen in the elastic region yield data that are consistent with results obtained from a load frame for this material.

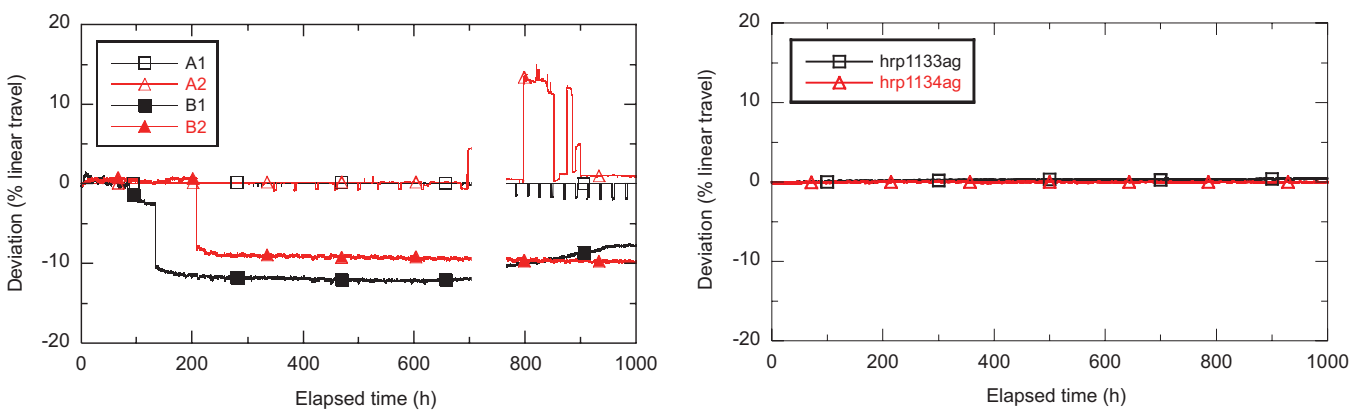

Figure 16. *LVDT response during long duration testing.*

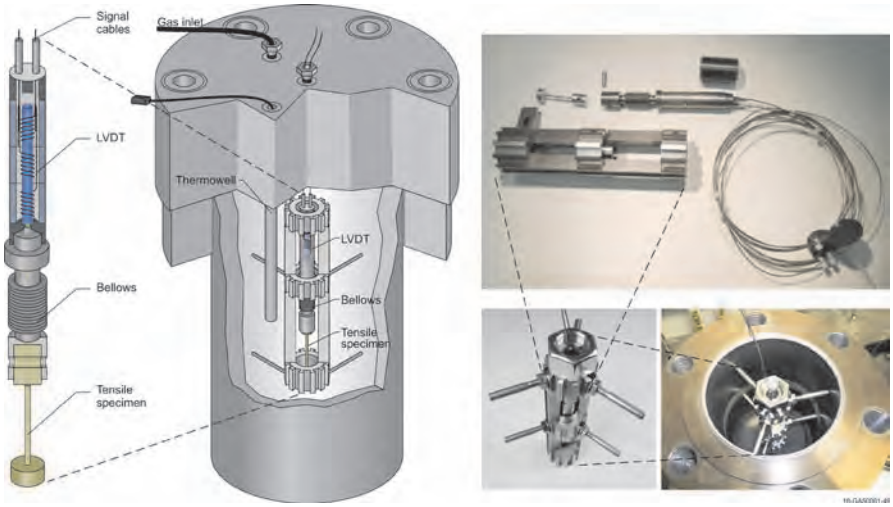

***Figure 17**. Creep test rig positioned in autoclave for testing.*

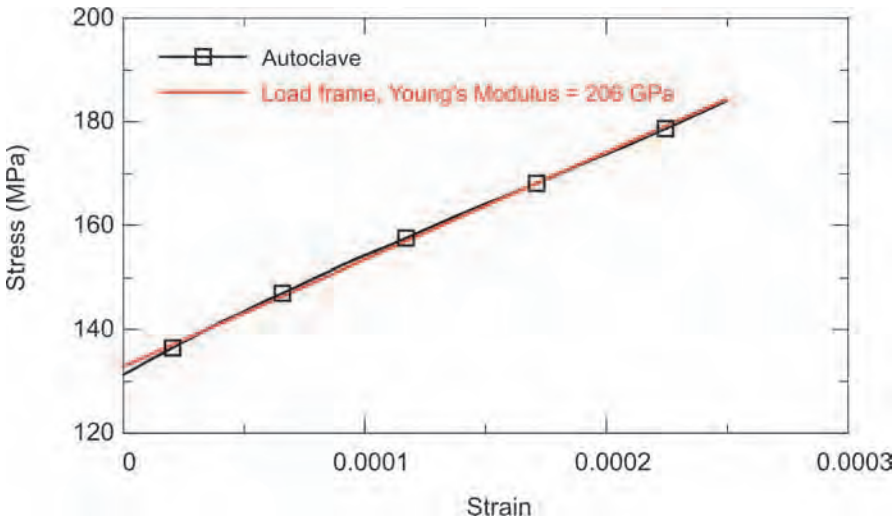

***Figure 18.** Initial autoclave data obtained for a 304 stainless steel 2 mm diameter specimen.*

Ultrasonic Transducers (UTs)

Ultrasonic Transducers (UTs) offer the potential for a more compact, more accurate, higher temperature, and multi-dimensional real-time sensor for detecting geometry changes or crack growth during irradiation. In collaboration with Pennsylvania State University (PSU), INL is investigating UT feasibility for detecting geometry changes.

UT utilizes high-frequency sound waves to examine a given specimen. A transducer is used to convert an electrical signal to mechanical vibrations, which transmit the ultrasonic waves into the specimen. After propagating through the specimen, the ultrasonic waves are either reflected back to the transmitter (pulse-echo mode) or are picked up by a second transducer (through-transmission mode). The received signal is then converted back into an electrical signal by one of the transducers. The recorded waveform is then analyzed to determine various properties of the structure. For example, the time-of-flight in a creep specimen will increase due to specimen elongation. Also, the plastic deformation associated with creep can alter the frequency spectrum of the received signal.

The use of ultrasonic inspection techniques as an in-pile sensor is challenging for two reasons. First, typical operating conditions (350°C) are well above the Curie temperature of conventional transducer materials, and the transducer will stop functioning. Second, conventional transducers are typically not suitable for radiation exposure. Radiation can damage transducer materials and degrade their performance. Furthermore, conventional transducers often contain elements, such

as lead, lithium, and gold, which transmute into toxic substances.

One possible solution explored by INL/PSU is to locate the transducer outside of the radiation environment and transmit the ultrasonic waves to the specimen via a wire waveguide. This is possible because of guided wave phenomena. Guided waves occur when the ultrasonic waves interact with the boundaries (surfaces) of a specimen and constructive interference leads to a unique wave structure. Because the boundaries of the specimen contain the ultrasonic energy, a specimen can be interrogated at the end of a very long waveguide. Using the equipment shown in Figure 19, bench-top tests were completed to investigate this design. The setup includes five components: the magnetostrictive transducer (e.g., driver coil), a Remendur (or similar other magnetostrictive material) guide, a coupling, the stainless steel wave guide, and the sample. Initial evaluations considered the sample geometry shown in Figure 19 because this acoustic horn enhances the signal. Evaluations included several different sets of electronics to optimize the signal.

Initial testing by INL and PSU demonstrated that energy can be transmitted into the sample and can be received in both pulse-echo and through-transmission mode. (A through-transmission signal was monitored using a contact Pizeo 1.5 MHz broadband transducer). Testing also demonstrated that the use of a magnetostrictive sleeve eliminated the need for a brass joint to connect magnetostrictive material to stainless steel. However, results suggest that the laser weld used to join the acoustic horn to the 30-foot wave guide hinders transmission and reception of the signal. In fact, additional optimization efforts are needed for most of the components shown in Figure 19. For example, alternate coupling methods should be explored in which the magnetostrictive transducer is directly coupled to a stainless steel wave guide. Alternate wave guide materials, such as molybdenum or Inconel, are being explored that have higher temperature and better repeatability characteristics. In addition, efforts are underway to optimize the design of the acoustic horn for specimens of interest to ATR customers. Efforts will be completed to quantify the accuracy possible from this technology. Ultimately, prior to ATR testing, this technology will be evaluated at PWR temperatures and pressures in an autoclave.

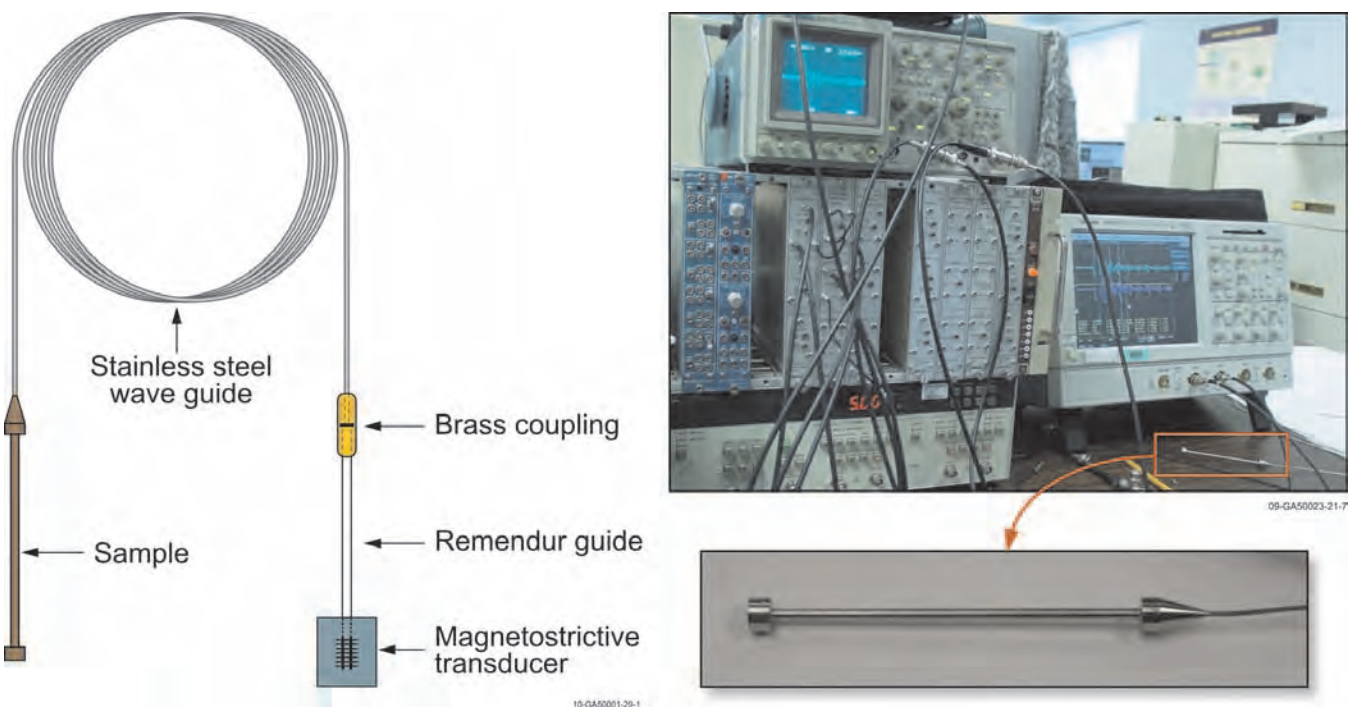

Figure 19. *UT testing equipment evaluating specimen attached to acoustic horn and 30 ft wave guide.*

Flux

The ATR and ATR-C facilities currently lack real-time methods for directly detecting thermal neutron flux and fission reaction rates for irradiation capsules. However, recent technological developments offer the possibility for such direct measurements without resorting to complicated correction factors. In addition, it is possible to directly measure minor actinide fission-reaction rates and to provide time-dependent monitoring of the fission-reaction rate or fast/thermal flux during transient testing.

A three-year Idaho State University (ISU)/INL project was recently initiated to evaluate new real-time state-of-the-art in-pile flux detection sensors [20]. Initially, the project is comparing the accuracy, response time, and long duration performance of several flux and fluence detectors (see Figure 20), including French Atomic Energy Commission (CEA)-developed miniature fission chambers, specialized self-powered neutron detectors (SPNDs) developed by the Argentinean National Energy Commission (CNEA), specially developed commercial SPNDs, and back-to-back fission (BTB) chambers developed by Argonne National Laboratory (ANL).

As shown in Figure 21, specialized instrument positioning hardware and associated software has been developed by INL to facilitate these evaluations, which were initiated in Summer 2010. In initial tests, the response and accuracy of specially developed real-time flux detectors, such as fission chambers and SPNDS, are compared using experimental guide tubes that can axially position the detectors at up to six radial positions in the ATR-C core. Software has been developed to process data obtained from these detectors and provide a real time ATR-C flux map. Data are benchmarked with activation wire and foil measurements and modeled with reactor physics codes.

Results of this effort will be used to select the detector that can provide the best online regional ATR-C power measurement. It is anticipated that this may offer the potential to increase the ATR-C's current power limit and its ability to perform low-level irradiation experiments. In addition, the data should provide insights about the viability of using these detectors in the ATR. Hence, this effort complements current activities to improve ATR software tools, computational protocols, and in-core instrumentation under the ATR Modeling, Simulation, and V&V Upgrade initiative, as well as the work to replace nuclear instrumentation under the ATR Life Extension Project (LEP) and provide support to the ATR NSUF.

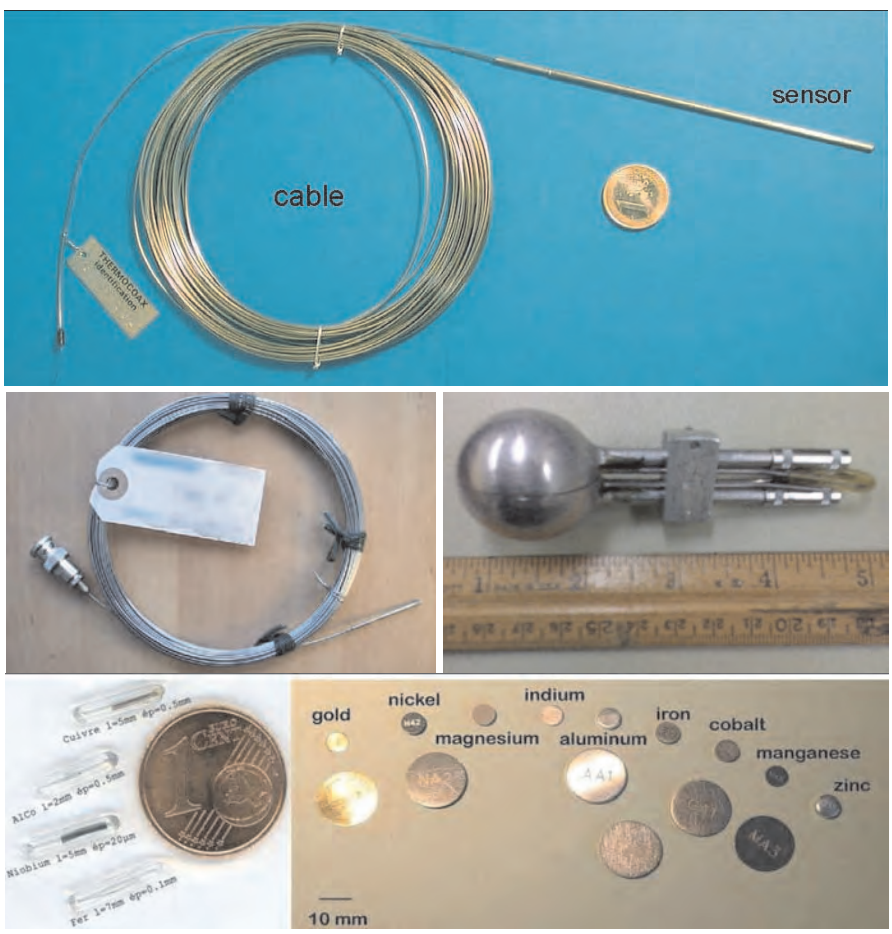

10-GA50001-50

Figure 20. *Representative flux and fluence detectors under evaluation.*

Summary and Future Directions

A key component of the ATR NSUF is to enhance instrumentation techniques available to users conducting irradiation. As discussed in this section, this effort has already led to several new sensors now available to ATR users for detecting temperature. In addition, it is anticipated that ongoing investigations will soon lead to new sensors for in-pile detection of thermal conductivity, elongation, and neutron flux for ATR users. In addition, several new research efforts in this area offer the promise of new detectors being available to ATR users that are not available at other test reactors. In particular, future efforts are focusing on sensor technologies that can detect multiple parameters with a single probe.

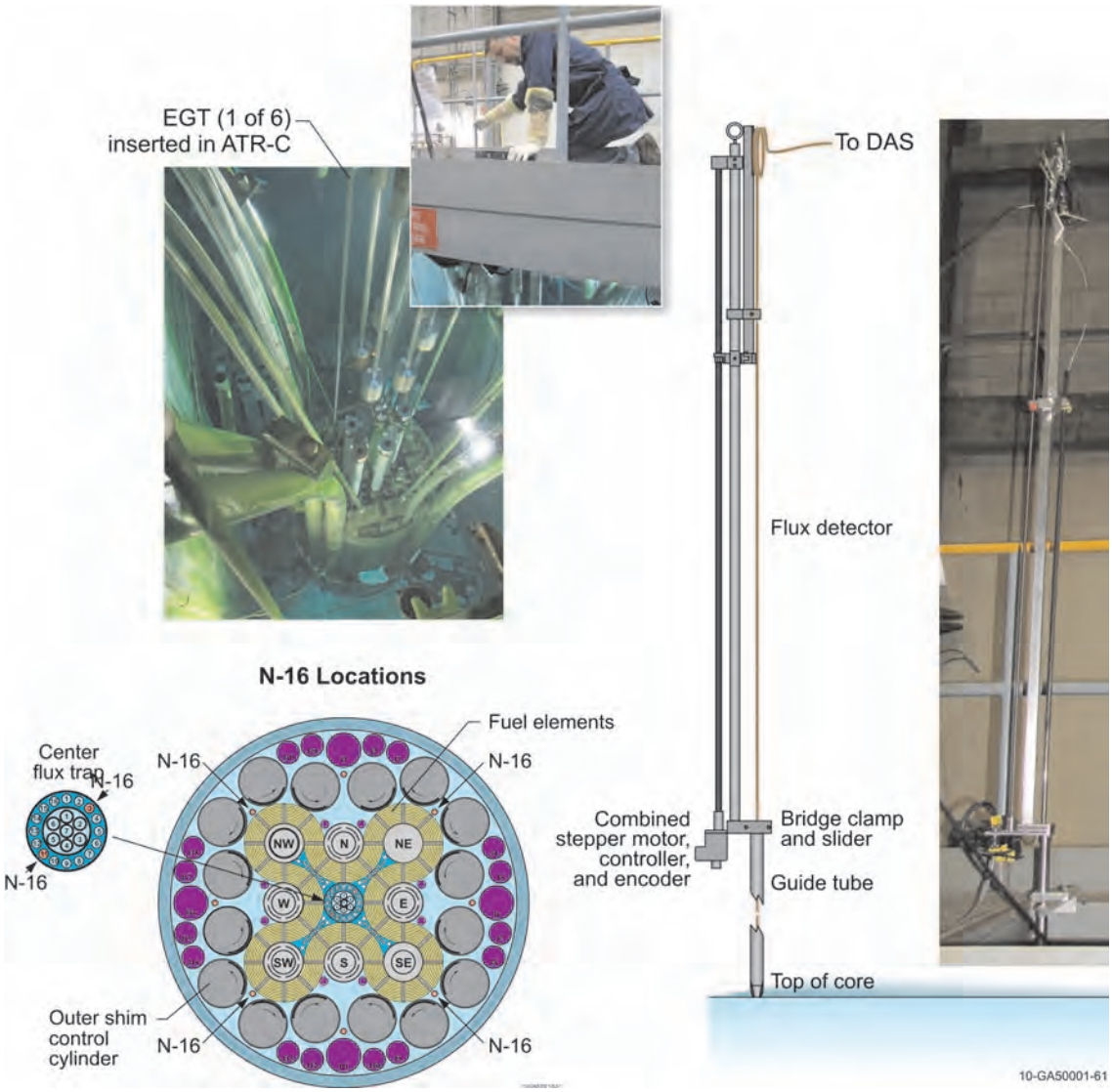

Figure 21. *Positioning equipment and insertion ATR-C insertion locations.*

References

1. "FY2009 Advanced Test Reactor National Scientific User Facility Users' Guide," INL/EXT-07-13577, Idaho National Laboratory, 2009.

2. J. L. Rempe, D. L. Knudson, K. G. Condie, J. E. Daw, H. Ban, B. S. Fox, and G. E. Kohse, "New Sensors for the Advanced Test Reactor National Scientific User Facility," *invited paper for ANIMMA Special Edition, IEEE Transactions on Nuclear Science*, accepted January 2010, to be published October 2010.

3. J. L. Rempe, D. L. Knudson, K. G. Condie, S. C. Wilkins, J. C. Crepeau, and J. E. Daw, "Options Extending the Applicability of High Temperature Irradiation Resistant Thermocouples," *invited paper for NURETH12 Special Edition, Nuclear Technology,* **167**, July 2009, pp 169-177.

4. J. E. Daw, J. L. Rempe, D. L. Knudson, S. C. Wilkins, and J. C. Crepeau, "High Temperature Irradiation-Resistant Thermocouple Performance Improvements," *Proceedings of the ANS NPIC HMIT 2009 Topical Meeting on Nuclear Plant Instrumentation, Controls, and Human Machine Interface Technology,* Knoxville, TN, April 2009.

5. D. L. Knudson, J. L. Rempe, K. G. Condie, S. C. Wilkins, J. E. Daw, and J. C. Crepeau, "High Temperature Irradiation Resistant Thermocouples – A Low Cost Sensor for In-Pile Testing at High Temperatures," Paper 8222, *2008 International Congress on Advances in Nuclear Power Plants (ICAPP '08)*, Anaheim, CA, June 8-12, 2008.

6. J. E. Daw, J. L. Rempe, D. Knudson, S. C. Wilkins, and J. C. Crepeau, "Extension Wire for High Temperature Irradiation Resistant Thermocouples," *Measurement Science and Technology,* **19**, February 2008 (045206).

7. J. L. Rempe, D. L. Knudson, K. G. Condie, and S. C. Wilkins, "Thermocouples for High-Temperature In-Pile Testing," *Nuclear Technology,* **156**, No. 3, December 2006, 320-331.

8. L. L. Snead, A. M. Williams, and A. L. Qualls, "Revisiting the use of SiC as a post-irradiation temperature monitor," Effects of Radiation on Materials, ASTM STP 1447, M. L. Grossbeck, Ed, ASTM International, West Conshohocken, PA, 2003.

9. J. L. Rempe, K. G. Condie, D. L. Knudson, and L. L. Snead, "Comparison Measurements of Silicon Carbide Temperature Monitors," *IEEE Transactions on Nuclear Science,* **57**, No. 3, June 2010.

10. M. Laurie, D. Magallon, J. Rempe, S. Wilkins, J. Pierre, C. Marquié, S. Eymery, and R. Morice, "Ultrasonic High Temperature Sensors: Past Experiments and Prospective for Future Use," *submitted to the International Journal of Thermophysics,* April 2010.

11. J. Daw, J. Rempe, and S. C. Wilkins, "Ultrasonic Thermometry for In-Pile Temperature Detection," *7th International Topical Meeting on Nuclear Plant Instrumentation, Control, and Human Machine Interface Technologies (NPIC&HMIT 2010),* Las Vegas, NV, November 7–11, 2010.

12. M. Laurie, D. Magallon, J. Rempe, S. Wilkins, J. Pierre, C. Marquié, S. Eymery, and R. Morice, "Ultrasonic High Temperature Sensors: Past Experiments and Prospective for Future Use," *Joint International Symposium on Temperature, Humidity, and Moisture and Thermal Measurements in Industry and Science,* Portorož, Slovenia, May 31–June 4, 2010.

13. B. Fox, H. Ban, J. Rempe, D. Knudson, and J. Daw, "Development of an in-pile technique for fuel thermal conductivity measurement," Proc. *ANS NPIC HMIT 2009 Topical Meeting,* Knoxville, TN, April 2009.

14. B. Fox, H. Ban, J. Rempe, J. Daw, K. Condie, and D. Knudson, "In-Pile Thermal Conductivity Measurement Method for Nuclear Fuels," *Thermal Conductivity 29,* M. A. White (Editor), DEStech Publications Inc., to be published 2010.

15. B. Fox, H. Ban, J. Rempe, J. Daw, K. Condie, and D. Knudson, "In-Pile Thermal Conductivity Measurement Method for Nuclear Fuels," *30th International Thermal Conductivity Conference and 18th International Thermal Expansion Symposium,* Pittsburgh, PA, August 29–September 2, 2009.

16. D. L. Knudson and J. L. Rempe, "Recommendations for use of LVDTs in ATR High Temperature Irradiation Testing," *7th International Topical Meeting on Nuclear Plant Instrumentation, Control, and Human Machine Interface Technologies (NPIC&HMIT 2010),* Las Vegas, NV, November 7–11, 2010.

17. D. L. Knudson and J. L. Rempe, "LVDT evaluations for ATR irradiations," *Proc. ANS NPIC HMIT 2009 Topical Meeting,* Knoxville, TN, April 2009.

18. B. G. Kim, J. Rempe, D. Knudson, K. Condie, and B. Sencer, "An In-situ Creep Testing Capability for the Advanced Test Reactor," *submitted to Nuclear Technology,* MS 10-58, April 2010.

19. B. G. Kim, J. L. Rempe, D. L. Knudson, K. G. Condie, and B. H. Sencer, "Development of an In-situ Creep Testing Capability for the Advanced Test Reactor," *7th International Topical Meeting on Nuclear Plant Instrumentation, Control, and Human Machine Interface Technologies (NPIC&HMIT 2010),* Las Vegas, NV, November 7–11, 2010.

20. T. Unruh, J. Rempe, D. Nigg, P. Hart, G. Imel, J. Harris, and E. Bonebrake, "Flux Sensor Evaluations at the ATR Critical Facility," *7th International Topical Meeting on Nuclear Plant Instrumentation, Control, and Human Machine Interface Technologies (NPIC&HMIT 2010),* Las Vegas, NV, November 7–11, 2010.

JOY REMPE (B.S., 1981, Nuclear Engineering, University of Missouri–Rolla; M.S., 1983 and PhD., 1986; Massachusetts Institute of Technology) is a Directorate Fellow and Group Leader at the Idaho National Laboratory (INL) where she leads in-pile instrumentation development efforts for INL's Advanced Test Reactor National Scientific User Facility. She also serves on several advisory groups reviewing the U.S. Department of Energy's Office of Nuclear Energy Research and Development programs, and she provides consulting assistance to vendors, utilities, and regulators on severe accident issues. With over 25 years of research experience, Dr. Rempe has authored or co-authored 35 archival peer reviewed journal publications and over 80 peer-reviewed conference papers on reactor safety, severe accident phenomena, high temperature testing, and in-pile instrumentation. She is an inventor/co-inventor on three patents (pending). In 2005, Dr. Rempe was elected a Fellow in the American Nuclear Society (ANS); in 2009, she was elected to the ANS Board of Directors; and in 2010, she was appointed to the U.S. Nuclear Regularly Commission's Advisory Committee on Reactor Safeguards.

DARRELL KNUDSON (B.S., 1979, and M.S., 1981, Mechanical Engineering, Utah State University) has over 30 years of experience in ATR safety analysis, fuel performance modeling, and in-pile instrumentation fabrication and testing. Mr. Knudson is currently working at the Idaho National Laboratory's High Temperature Test Laboratory to develop advanced in-core instrumentation, where he leads INL efforts to evaluate and deploy LVDTs in the ATR. He has authored or co-authored numerous peer reviewed journal publications and conference papers on high temperature testing and in-pile instrumentation. He is also an inventor/co-inventor of several patents (pending) in this area.

BONG GOO KIM (B.S., 1979, Material Engineering, Ulsan University–Korea; M.S., 1993 and PhD., 2000; Chungnam National University–Korea) has worked more than 30 years at the Korea Atomic Energy Research Institute (KAERI) with experience in the fields of nuclear fuel development and irradiation technology development. For the last ten years, he led efforts to develop in-pile instrumentation and irradiation devices for irradiation tests of nuclear fuel and materials in the HANARO test reactor at KAERI. With over 30 years of research experience, Dr. Kim has authored or co-authored 32 archival peer-reviewed journal publications and over 60 peer-reviewed conference papers on nuclear fuel development, evaluation of fuel performance, irradiation testing, and in-pile instrumentation. He is an inventor/co-inventor on 17 patents. In September 2009, Dr. Kim began a one-year assignment working at the HTTL/ATR NSUF..

KEITH CONDIE (B.S., 1968, and M.S., 1970; Mechanical Engineering, Utah State University) Mr. Keith Condie has more than 35 years of experience in experimental test programs. He was a key technical contributor to several INL programs, including the Loss of Fluid Test facility, Semiscale, Savannah River Restart programs, the INL Matched Index-of-Refraction experimental research loop, and a Prototypic Materials Test Program funded by Japan's Nuclear Power Engineering Corporation. He has authored or co-authored numerous peer reviewed journal publications and conference papers on high temperature testing and in-pile instrumentation. He is also an inventor/co-inventor of several patents (pending) in this area.

JOSHUA DAW (B.S., 2006, Mechanical Engineering, Idaho State University; M.S., 2008, University of Idaho) is a researcher at the Idaho National Laboratory (INL) where he works on in-pile instrumentation development efforts for INL's Advanced Test Reactor National Scientific User Facility and conducts high-temperature thermal property testing. As a University of Idaho graduate student, he was recognized for outstanding research in high-temperature in-pile instrumentation. Mr. Daw has authored or co-authored 6 peer reviewed journal publications and 11 peer-reviewed conference papers on high temperature testing and in-pile instrumentation. In 2009, Mr. Daw completed a six-month assignment with the Institute for Energy at the Halden Reactor Project.

DAVID NIGG (B.S., 1972, Engineering Physics, University of Kansas; M.S., 1974, Nuclear Engineering, Texas A&M; Ph.D., 1977, Engineering Sciences, University of Kansas) has over 30 years of experience in computational and experimental reactor and radiation physics, research reactor applications, medical applications of nuclear and radiological sciences, radiobiology and radiation biophysics, and technical management. He is a registered Professional Engineer by Examination in the State of Idaho. In 2006, he received the Hatanaka Memorial Award, the highest honor bestowed by the International Society for Neutron Capture Therapy (ISNCT) in recognition of sustained excellence and leadership in NCT research and development. He currently leads the INL ATR Modeling, Simulation, and V&V Upgrade initiative.

STEVEN TAYLOR (B.S., 1993, Industrial Technology, University of Idaho) has over 32 years of experience in developing unique state-of-the-art, one-of-a-kind nondestructive test and evaluation systems in support of INL's nuclear programs. His expertise has led to requests that he become involved in nondestructive examination of production fuels for ATR & universities, development of fuels for the RERTR Program, examination of irradiated fuels prior to reinsertion in to the ATR, and spent fuel evaluation of FERMI and EBR-II fuels. Mr. Taylor has developed over a dozen systems that have had national and international impact, and he has served or is serving as principal investigator of numerous major projects (from $.5M to over $3M). Mr. Taylor holds five patents in the area of non-destructive evaluation of materials, and he has published numerous international peer-reviewed papers.

TROY UNRUH (B.S., 2004, and M.S., 2010, Nuclear Engineering, Kansas State University) has over eight years of experience with reactor operations and experiments. He is currently the ATR Reactor Project Engineer who leads ATR NSUF flux evaluation activities. Mr. Unruh earned an R&D 100 award for research he completed on semiconductor neutron detection at Kansas State University, and he has authored several archival peer-reviewed journal publications and peer-reviewed conference papers. In 2010, Mr. Unruh began a six month assignment at the French Atomic Energy Agency in Cadarche, France.

EU01-46T-Z05

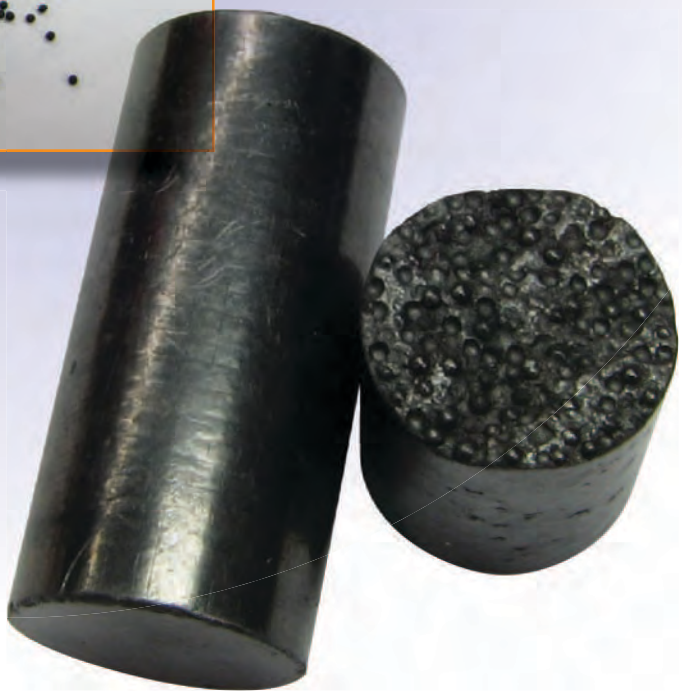

Irradiation Testing and Post-irradiation Examination of Very High Temperature Reactor (VHTR) Fuel

P. A. Demkowicz, B. Grover

Introduction

The Next Generation Nuclear Plant (NGNP) Fuel Development and Qualification Program was established to perform the requisite research and development on tri-isotropic (TRISO) coated particle high-temperature gas reactor fuel to support deployment of a very high temperature reactor (VHTR), which has been selected as the reactor concept for the NGNP project. The overarching goal of the program is to provide a baseline fuel qualification data set to support licensing and operation of a VHTR. To achieve these goals, the program includes the elements of fuel fabrication, irradiation, post-irradiation examination (PIE) and accident testing, fuel performance, and fission product transport [1].

Up to nine fuel irradiation experiments are planned in the Advanced Test Reactor (ATR) at Idaho National Laboratory (INL). These experiments are intended to provide data on fuel performance under irradiation, support fuel process development, qualify the fuel for operating and accident conditions, provide irradiated fuel for accident testing, and support the development of fuel performance and fission product transport models. The first of these irradiation tests, designated AGR-1 (Advanced Gas Reactor-1), began in the ATR in December 2006 and ended in November 2009, with zero particle failures observed out of approximately 300,000 particles in the experiment. This experiment was primarily to act as a shakedown test of the multicapsule design and provide early data on fuel performance that will be used in fuel fabrication process development. This test will also provide samples for post-irradiation accident testing, where fission product retention of the fuel at high temperatures will be experimentally measured. The second irradiation experiment (AGR-2) was inserted in the ATR in June 2010.

The AGR-1 fuel consists of 350 μm diameter uranium oxycarbide kernels coated with a pyrocarbon buffer (100 μm), inner pyrolytic carbon (40 μm), silicon carbide (35 μm), and outer pyrolytic carbon (40 μm) layers. Uranium enrichment in the kernels is 19.8% [2]. The particles were pressed into right cylindrical compacts using a thermosetting carbonaceous material. The fuel compacts are nominally 25 mm in length and 12.3 mm in diameter (Figure 1). The compacts have ~1.5-mm-thick fuel-free end caps at the top and bottom, as shown in Figure 1. A baseline fuel type and three fuel variants were included in the AGR-1 irradiation, with each variant fabricated by varying one step of the coating process to produce slightly different IPyC or SiC coating properties. One key objective of the experiment is to identify any fuel performance differences between the fuel types, either during the irradiation or during post-irradiation high temperature accident tests, to support optimization of the fuel fabrication process and eventual selection of a reference fuel for qualification.

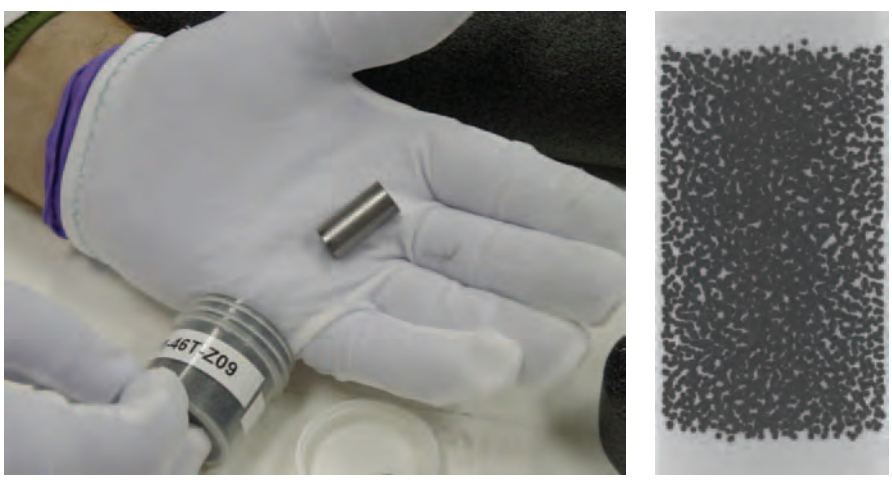

Figure 1. *Photograph (left) and x-radiograph (right) of an unirradiated Baseline AGR-1 fuel compact. Uranium oxycarbide kernels and non-fueled end caps are clearly visible in the x-radiograph.*

This article presents an overview of the coated particle fuel irradiation and post-irradiation examination capabilities and activities at INL. The AGR-1 and AGR-2 experiment designs will be discussed, as well as the results of the AGR-1 irradiation. Also presented are the plans for the AGR-1 PIE and early results of ongoing PIE experiments.

Fuel Irradiation

The goals of the NGNP irradiation experiments are to provide irradiation performance data to support fuel process development, to qualify fuel for normal operating conditions, to support development and validation of fuel performance and fission product transport models and codes, and to provide irradiated fuel and materials for PIE and safety testing [1,2]. The experiments, which will each consist of multiple separate capsules, will be irradiated in an inert sweep-gas atmosphere with individual online temperature monitoring and control of each capsule. The sweep gas will also have online fission product monitoring on its effluent to track performance of the fuel in each individual capsule during irradiation. The experiments are specifically designed for the irradiation position location and size, irradiation parameters (temperature, fluence, etc.) and with an umbilical tube routing necessary to connect the experiment capsules to the monitoring, control, and data collection systems.

Experiment Capsules

The experiment test trains for both AGR-1 and AGR-2 consist of six separate stacked capsules vertically centered in the ATR core. Each capsule has its own custom blended gas supply and exhaust for independent temperature control and fission product monitoring. An AGR-1 capsule horizontal cross-section is shown in Figure 2, and a vertical section is shown in Figure 3. The majority of the test train and fuel details are identical for these two experiments, so this section is focused on the commonalities and similarities. The differences in both configuration and purpose/mission will be discussed in a later section.

The experiment capsules are approximately 35 mm in diameter and 150 mm in height, including the plenums between adjacent capsules. Each capsule contains 12 prototypical right circular cylinder fuel compacts nominally 12.4 mm in diameter and 25 mm long. The AGR fuel is comprised of Low Enriched Uranium (LEU) fuel kernels, which are covered with a layer of silicon carbide, sandwiched between two pyrolytic carbon layers to make up the TRISO-coated fuel particles. The fuel particles are over-coated with a thermo-set resin and pressed into fuel compacts that are then sintered to remove the volatile compounds in the resin. The compacts are arranged in four layers in each capsule with three compacts per layer nested in a triad configuration. A nuclear grade graphite holder surrounds and separates the three fuel compact stacks in each capsule to prevent any fuel particles on adjacent compacts from touching each other, which could possibly cause a premature particle failure. Very thin (1.5 mm or less) graphite top and bottom end caps on the compacts prevent particle-to-particle contact between adjacent axial compacts. The graphite holder also provides the inner boundary of the insulating gas jacket (approximately 0.25 mm to 1.0 mm thick, depending on vertical location within the reactor core) for temperature control of the fuel during irradiation, and contains boron carbide to serve as a consumable neutron poison.

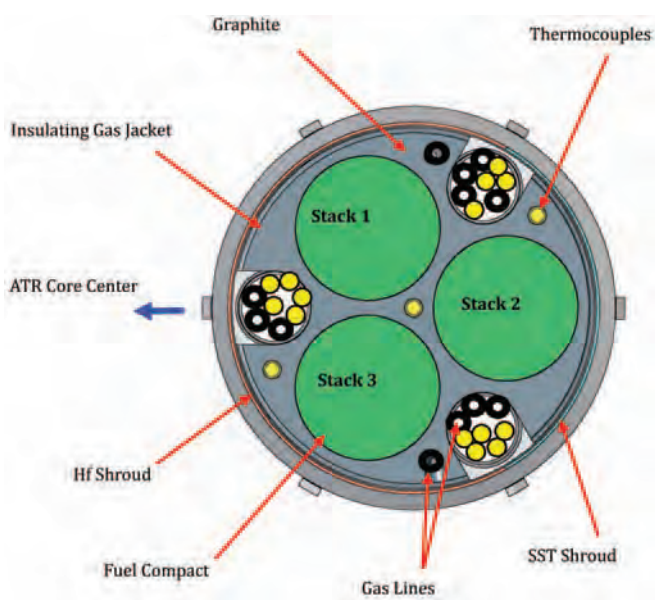

Figure 2. *AGR-1 experiment cross-section.*

In addition to the boron carbide, a thin (0.25 mm thick) hafnium shield next to the outside capsule wall surrounds the two fuel compact stacks facing toward the center of the ATR core (Stacks 1 and 3 shown in Figure 2 for AGR-1). A thin (0.25 mm thick) stainless steel shield next to the outside capsule wall blankets the other fuel compact stack (Stack 2 shown in Figure 2) located on the side of the capsule facing away from the ATR core. A stainless steel shield versus hafnium was used on this side of the capsule to minimize the effects on the neutron flux to these already lower-powered fuel compacts while retaining the same insulating gas jacket to maintain the proper irradiation temperature. The neutron poisons are necessary to limit the initial fission rate in the fuel and thereby provide a more consistent fission rate/power production during irradiation. As the boron carbide is consumed in the graphite holder, the fission rate in the fuel reaches a peak at about the mid-point of the irradiation and then slowly decreases as the fuel continues to burnup. Reducing and controlling the initial fission rate in this manner decreases the ratio of the maximum-to-minimum heat generation rates in the fuel, which provides better temperature control in the fuel during the rather long irradiations that are in excess of 2 years. In addition to protecting the fuel, the graphite holder has features machined to accommodate the thermocouples for measuring temperature within the capsule and the three through tubes containing the gas lines and thermocouples for adjacent capsules. The through tubes are positioned very precisely in the top and bottom heads of the capsules so they can also be utilized to center the graphite in the capsule and provide the necessary gas jacket for temperature control.

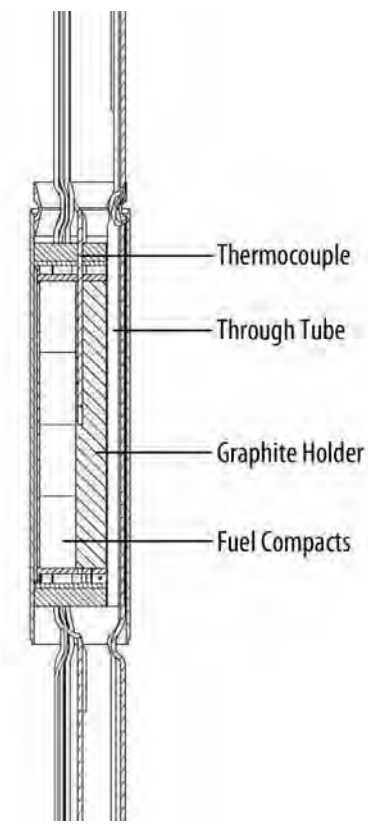

Figure 3. *AGR experiment vertical section.*

There are nominally three thermocouples in each AGR-1 capsule (the top and bottom capsules have five and two thermocouples, respectively, for different reasons) located in the top, middle, and bottom areas of the graphite holder. The size of the thermocouples being used in AGR-2 was increased, which resulted in only two thermocouples per capsule with the exception of the top capsule, which has five thermocouples as did AGR-1. Since no metal could touch the fuel particles, the thermocouples measure the graphite temperature and the corresponding fuel temperatures are calculated. Flux wires are also installed in the graphite to measure both the thermal and fast neutron fluence. Since the outside diameter of the graphite establishes the inner boundary of the insulating gas jacket, the graphite diameter varies among the capsules depending on the neutron flux rate at the vertical location of the specific capsule within the ATR core. The vertical location of the capsule also determined the boron carbide content in the graphite holder in the capsules as well due to the chopped cosine-shaped vertical neutron flux profile in the ATR core.

An umbilical tube (termed a lead-out) houses and protects the gas lines and thermocouple leads from the experiment capsules to the reactor vessel wall penetration. Outside the reactor vessel wall, the gas lines and thermocouple leads are connected to their facility counterparts in the temperature monitoring, control, and data collection system. The lead-out also vertically locates the experiment within the applicable Large B irradiation position (shown in Figure 4) in the ATR core. The Large B positions (38 mm diameter) were chosen for these two AGR fuel irradiations due to the rate of fuel burnup and fast neutron fluence accumulation in these positions, providing an acceleration factor of between one and three times that expected in the VHTR. This acceleration factor was high enough to accomplish the irradiation within a reasonable time, but low enough to avoid possible premature fuel-particle failures similar to those experienced in past highly accelerated particle fuel tests.

In addition to limiting the acceleration factor, avoiding contact between fuel particles as well as limiting the materials contacting the fuel compacts/particles to only graphite and the inert temperature-control gas was done to prevent possible premature fuel particle failures. In essence, limiting the acceleration factor also determined the irradiation time for these AGR experiments since the neutron flux rate is one of the major controlling factors for the irradiation time. The AGR-1 and AGR-2 irradiations each have their own Fissions per Initial Metal Atom (FIMA) burnup requirements, which in conjunction with the fuel enrichments and the Large B neutron flux rate resulted in the rather long irradiation times in excess of 2 years. Along with the long irradiation times, these requirements also resulted in a significantly reduced heat-generation rate toward the end of the irradiation. As indicated earlier, every effort was made to flatten the heat-generation rate curve as much as possible to increase the controllability of the temperatures at the end of the irradiation. This controllability was necessary to meet the time-average volume-average temperature requirements during irradiation while staying below the time-average and the instantaneous peak temperatures. The combination of these requirements provided some significant challenges in the design of the AGR experiments and their control systems.

The next six AGR experiments are currently planned to be irradiated in a different, larger ATR irradiation position with a higher neutron flux in order to achieve their burnup and fast fluence requirements in a shorter period of time. However, the acceleration factor between these ATR experiments and the VHTR for fuel burnup and fast neutron fluence rates will remain at or below three to prevent premature fuel particle failures. The test trains for these later experiments will be different in size and shape and are currently planned to be doubled up (with essentially twice as many capsules) to reduce the time required by half to obtain the necessary irradiation data. Nonetheless, the same type of temperature control system and fission product monitors will be used, along with a lot other similarities in the capsule configurations and design (e.g., graphite specimen holders, insulating gas jackets, individual capsule temperature control and fission product monitoring, etc.). The need for the last experiment is still being debated, but if it is approved, then it will be irradiated in the west Large B position used by the second experiment. This experiment will again utilize the same type of temperature control and fission-product monitoring systems used by the first two experiments and is anticipated to be irradiated in parallel with the doubled up experiments in the larger ATR flux trap irradiation position.

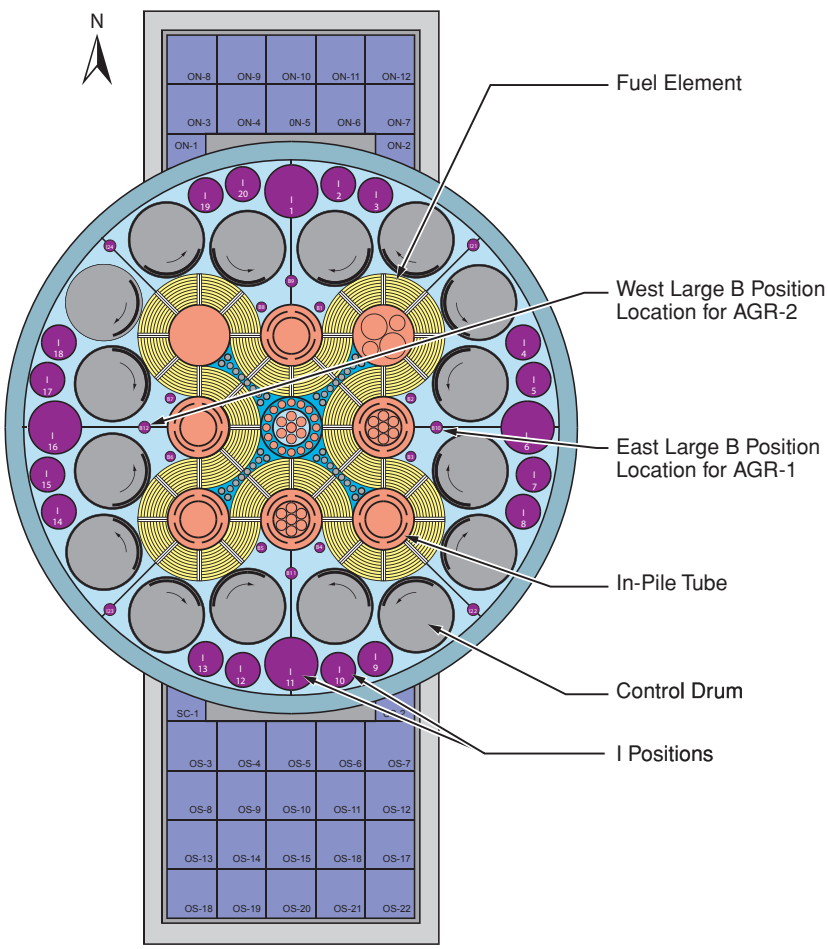

Figure 4. *ATR Core cross-section showing AGR experiment locations.*

Experiment Temperature Control

The desired temperatures in the capsules are achieved by adjusting the mixture ratio of two gases with differing thermal conductivities to control the heat transfer across an insulating gas jacket between the heat source (fuel fissions and gamma heating of capsule materials) and the relatively cold reactor coolant (52°C). The experiment flow path is shown in Figure 5.

Helium is used as the high (thermally) conductive gas and neon is used as the insulating gas. Neon (versus argon that can provide a wider temperature control band) was selected for the insulating gas in these experiments to avoid the effects of the activated argon gas on the fission product monitors. Computer-controlled mass flow controllers are used to automatically blend the gases (based upon feedback from the experiment thermocouples) to control the graphite holder temperatures, which are analytically coupled to the fuel specimen temperatures.

The temperature measurements are taken with the thermocouples located in each experiment capsule, one of which is designated as the control thermocouple. In the event the control thermocouple fails open (as indicated by a significant increase in resistivity); temperature control for the capsules will automatically be switched over to the designated back-up thermocouple, and it will be designated as the new control thermocouple. The thermocouples typically used at ATR are 1.6 mm sheath diameter Type K, with high-purity magnesia insulation. However, due to the very high thermocouple temperatures (up to 1100°C) coupled with the relatively long irradiation, there was concern for the survivability of the thermocouples. To achieve the best thermocouple survivability possible, a selection of the most promising long-life Type K and Type N thermocouples were purchased and tested in a thermal mock-up of the AGR irradiation conditions. In addition, several INL developmental (molybdenum-niobium) thermocouples were also included in the thermal testing to determine how they would survive the irradiation conditions [3]. The testing was conducted for 4 months, and based upon the test results, the best performing Type N thermocouples were selected for use in the cooler positions in the AGR-1 capsule (away from core center), and the INL developmental thermocouples were selected for use in the higher temperature positions in the capsule (towards core center).

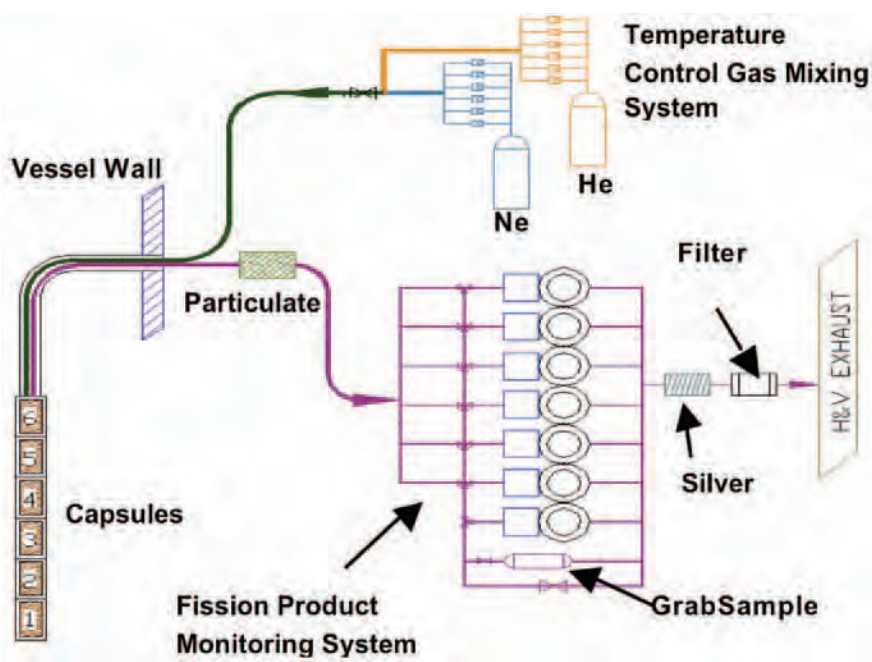

Figure 5. *AGR experiment flow path.*

Fission Product Monitor

To minimize temperature changes and maintain the temperature as constant as possible, the temperature control gas system provides a continuous flow to each specimen capsule. Monitoring this continuous gas flow for fission gases can provide valuable information on the fuel performance during irradiation.

As shown in Figure 5, the outlet gas from each capsule is routed to individual fission product monitors, and the gas flows can be rerouted to an online spare monitor if any monitors experience detector or other failures. There is also the capability to take a grab sample of the effluent gas from each capsule. The fission product monitors consist of a spectrometer for identifying and quantifying the fission-gas nuclides and a gross gamma detector to provide indication when a puff release of fission gases passes through the monitor. The gross gamma detector also provides the release timing. With the combination of a gross gamma detector and a spectrometer being continuously on-line, the gross

gamma detector results can be scanned quickly to determine which portions of the voluminous spectrometer data need to be closely scrutinized. A puff release of fission gases typically indicates when a TRISO fuel coating failure may have occurred. Through identification and quantification (with uncertainties) of the isotopes, the spectrometer can be used to determine the isotopic release-to-birth ratio (with uncertainties) of the fission gases being detected. The determination of the release-to-birth ratios can establish whether a new TRISO fuel coating failure has occurred or if the fission products are merely being released from an existing failure or uranium contamination on the outside surface of the fuel particles. These details can be very important in the qualification of fuel especially in small TRISO particle fuels, where a few random particle failures are anticipated and need to be tallied very accurately to support statistical qualification of the fuel. The system was designed and response modeled to detect and quantify each individual fuel particle failure up to and including a very unlikely 250 fuel particle failures.

AGR-1 and AGR-2 Experiment Missions and Differences

The irradiation of AGR-1 was completed in early November 2009, and the irradiation of AGR-2 started in June 2010. Before discussing the differences in these two experiments, the similarities between them should be explained. As indicated earlier, these two experiments are both being irradiated in the Large B irradiation positions in ATR, though on opposite sides of the ATR core (shown in Figure 4). The irradiation of AGR-2 on the west side instead of the east side of the ATR core is being done to maximize the use of the planned power levels in the ATR to achieve the irradiation goals of AGR-2. Since the experiments will be utilizing the same type of irradiation positions, the experiment capsule designs will be essentially identical. AGR-2 will also use the same temperature control and fission-product monitoring systems designed and installed for AGR-1. However, with AGR-2 located on the opposite side of the ATR core, some simple mirror imaging of the capsule features was necessary. The two fuel stacks in AGR-2 facing toward the ATR core will be on the opposite side of the capsules compared to the fuel stacks facing towards the core in the cross section of AGR-1 (e.g., right side versus left, shown in Figure 2). The routing of the lead-out from the experiment capsules to the reactor vessel wall will also be reversed, and the connections to the control and monitoring systems will be moved from the east side to the west side of the reactor vessel for connection to the test train.

There are four major differences between AGR-1 and AGR-2. The first significant difference is the purpose or missions for the two experiments (as defined in Reference 1). The primary mission for AGR-1 was to provide a shakedown of the experiment capsule/test-train design. This shakedown or test of the experiment design was to be performed using early laboratory-scale fuel with different coating variants. Irradiation of baseline fuel as well as fuel with different coating variants could provide data on fuel irradiation performance to support further development of the fuel to be used in the later AGR irradiations. In fulfilling its shakedown mission, AGR-1 has provided some lessons learned in the design, assembly and operation that are being incorporated into the design and irradiation of AGR-2. Alternatively, the primary mission for AGR-2 is to test production-scale fuel versus the laboratory-scale fuel used in AGR-1. In this capacity, AGR-2 will provide valuable feedback, both during irradiation and from post irradiation examination to support further development and fabrication of the fuel to be used in the actual fuel qualification irradiations planned as AGR-5 and AGR-6.

The second major difference between AGR-1 and AGR-2 is the fuel types and sources in the two experiments. The fuel irradiated in AGR-1 was exclusively uranium oxycarbide (UCO)-type fuel fabricated on a laboratory scale and included several different variants in the TRISO coating used on the fuel particles. As indicated earlier, the fuel to be irradiated in AGR-2 will be fabricated on a production scale, but it will also include both UCO and uranium dioxide (UO_2)-type fuel. In addition, the two different fuel types will

also have different fuel kernel and particle sizes, enrichment levels, burnup and temperature requirements, etc. Since there are many differences in the details for the fuel and irradiation requirements for AGR-1 and AGR-2, they will be provided in the following subsections.

The third major difference between AGR-1 and AGR-2 is the sources of the fuel. As part of the Generation IV (GEN IV) International Forum, two capsules in AGR-2 were offered to two other GEN IV countries, France and South Africa, to irradiate fuel in support of their gas reactor development programs. The fuel in one capsule contains fuel for the Pebble Bed Modular Reactor (PBMR) program in South Africa, and a second capsule contains fuel fabricated in France as part of their VHTR program. However, the fuel and irradiation details provided in the following subsections only encompass the NGNP/AGR program fuels since the fuel and irradiation details for the French and South African fuel are beyond the scope of this article and are protected under their irradiation agreement with INL.

The final major difference between AGR-1 and AGR-2 is the operating temperatures for the UCO fuel. The decision was made in late 2009 to increase the operating temperature in one of the three UCO-fueled capsules to obtain early data on the UCO fuel performance at slightly elevated operating temperatures. This data will be available for use in early licensing discussions for the NGNP and to determine if any final fuel production adjustments will be necessary prior to the fabrication of the fuel for the qualification irradiations planned as AGR-5 and AGR-6.

AGR-1 Fuel and Irradiation Details

As indicated earlier, the AGR-1 experiment contains exclusively UCO type fuel, which has an LEU enrichment level of 19.8%. The fuel was fabricated into 350 μm nominal diameter fuel kernels, which were then covered with the TRISO coatings to make 780 μm nominal diameter fuel particles. Approximately 4,150 fuel particles with a mean total uranium content of approximately 0.9 grams were used to make up each fuel compact. Compacts containing baseline fuel, fabricated to the baseline process parameters, as well as three fuel variants with different coatings and process development variations, were included in the experiment. Since all of the fuel in AGR-1 had the same enrichment, the boron carbide concentration used in the graphite holder for the top and bottom capsules was different than the concentration used in the other four capsules to compensate for the chopped cosine shaped vertical neutron flux profile in the ATR core. As previously noted, the irradiation time for the AGR-1 experiment was essentially determined by the neutron flux rate in the Large B position and the average burnup goal of 18% FIMA for all fuel compacts with a minimum of 14% FIMA for each fuel compact [4]. The temperature requirements for AGR-1 were to maintain a time-average volume-average temperature of 1150 +30/-75°C during the irradiation while staying below a time-average peak temperature of 1250°C and a maximum instantaneous peak temperature of 1400°C

AGR-2 Fuel and Irradiation Details

In contrast with AGR-1, the AGR-2 experiment contains both UCO and UO_2 type fuels, which are different in many ways besides the fuel type (enrichment, fuel kernel and particle size, particles/compact, etc.). In addition, the UCO type fuel is also different in enrichment, kernel size, etc., from the UCO fuel irradiated in the AGR-1 experiment. These fuel changes have resulted in other changes in the capsule design that are identified below.

The UCO fuel type was fabricated from 14.0% enriched LEU into 425 μm nominal diameter fuel kernels, which after being covered with the TRISO coatings result in 870 μm nominal diameter fuel particles. Approximately 3150 fuel particles are used to make up each fuel compact with an approximate mean total uranium content of 1.3 grams. Unlike AGR-1, only one type or baseline UCO fuel was included in the experiment. The burnup requirements for this fuel solidified just prior to final assembly of the experiment and insertion in the ATR due to several considerations, including the time available for the irradiation and PIE to be completed to obtain the data prior to development of the fuel for the latter experiments. Furthermore, one of the capsules with this fuel type will be located at the edge of the test train, which will be exposed to a lower neutron flux and, therefore, result in lower fuel burnup compared to the burnup levels in the other capsules containing this fuel type. To account for this lower flux rate, the burnup goal for this fuel type has tentatively been set at 10% FIMA for the majority of the fuel compacts with a minimum compact average burnup of 7% FIMA. The temperature requirements

for this fuel were also finalized just prior to the experiment insertion in ATR. The capsule time-average peak temperature for the high temperature capsule was set at ≤1400°C, and the capsule time-average peak temperature in the other two UCO capsules remained at the same ≤1250°C value used for the UCO fuel in AGR-1. The capsule time-average volume-average temperature was set at ≥1150°C for the high temperature capsule and ≥1000°C for the other two UCO capsules. The tolerance band on the time-average volume-average temperatures was replaced with a simple minimum value based upon the operating experience of AGR-1. Controlling the capsule temperatures to meet a tolerance band on the time-average volume-average temperatures while also trying to keep the time-average peak temperature as high as possible proved to be extremely difficult.

The UO_2 fuel type was fabricated from 9.6% enriched LEU into 510 μm nominal diameter fuel kernels, which result in 950 μm nominal diameter fuel particles after the TRISO coatings are applied. Approximately 1,520 fuel particles are used to make up each fuel compact, with an approximate mean total uranium content of 1.0 gram. There will be only one capsule of this fuel type irradiated for the AGR program, which means only baseline fuel compacts (e.g., no fuel variant type compacts) will be included in the experiment. As with the UCO fuel, the burnup requirements for this fuel were difficult to finalize. Along with being a different fuel type, there are also similar limitations on irradiation and PIE schedules. However, the burn-up requirements were finally set at 10% FIMA for the compact average burnup goal for a majority of the fuel compacts and a minimum of 7% FIMA in each fuel compact. The temperature requirements for this fuel were also finalized, with the same the capsule instantaneous peak temperature of 1800°C used for the UCO fuel. However, the irradiation temperatures will be lower than those used for the UCO fuel because fuel temperatures in a pebble bed are lower than in prismatic gas reactors. The tentative temperatures are a capsule time-average volume-average temperature of ≥900°C and a capsule time-average peak temperature of ≤1150°C.

The different fuel types with widely different enrichments, fuel particles per compact, burnup requirements, etc., presented a whole new set of challenges in the design of the AGR-2 capsules and their incorporation into a single test train. However, some of these differences were used to help offset the effects of other differences to result in a fairly efficient design and use of the ATR core space. One key parameter used in this optimization was the placement of the different fuel types and enrichment levels in the vertical neutron flux profile of the ATR core. This variable was utilized by placing the low enriched UO_2 fuel at the center of the core, where the neutron flux is highest, and placing the higher enriched UCO fuel towards the edges of the test train, in the slightly lower neutron flux rates. This vertical placement scheme helped to balance the effects of the different enrichments (with their associated different burnup requirements) and thereby achieve the required uniform irradiation time for the experiment. Since the experiment utilizes active monitoring and control, it is not possible to remove individual capsules at different irradiation times without reconstitution of the test train in a hot cell facility, which was determined to be cost prohibitive for this program. The other variable used to help offset the effects of fuel loading and burnup requirements was the boron concentration in the graphite holder. The boron concentration is approximately 25% less for the lower enriched UO_2 fuel than the concentration used in the UCO capsules located within a higher neutron flux region of the test train. In the same way, the boron concentration in the outermost UCO capsule, located in the slightly lower neutron flux region, is approximately 15% less than the UCO fuel capsule located in the higher flux region.

AGR-1 Experiment Irradiation Experience

A variety of tests were conducted prior to the AGR-1 test-train fabrication and assembly, including the high temperature thermocouple testing mentioned earlier and testing of the gas leakage through the very tight slip fit between the through tubes and the capsule bottom heads [5]. Development and testing was also conducted on various capsule assembly processes (clearances, welding, brazing, etc.) to ensure the assembly of the test train could be accomplished as designed. Assembly of the experiment, along with the installation of the fission product monitors and the modifications to tailor the existing temperature control system to the experiment needs, was completed in September 2006. The experiment was then inserted in the ATR in mid-December 2006, and final flow testing of the temperature control and fission product-monitoring systems was performed. Irradiation of the experiment was initiated in late December 2006, and the irradiation was completed in November 2009.

The performance and sensitivity of the

fission product monitor system (FPMS) was excellent. The extremely low levels of fission gases (peak release-to-birth ratios of <3 X 10^{-8}) from the anticipated low level uranium contamination on the outside of the fuel were measured and recorded by the FPMS. The ability to measure these very low fission gas levels in the temperature-control exhaust gas demonstrated both the sensitivity of the system as well as the integrity of the fuel. A validation of the sensitivity of this system is its ability to detect activated gases resulting from approximately 5 cc (or less) of air introduced into the system during gas bottle changes in the temperature-control system.

As originally anticipated, there were multiple thermocouple failures. By the end of the irradiation, 10 of the 18 thermocouples had failed, including all thermocouples in half of the experiment capsules. However, temperature control of all capsules was maintained using the remaining thermocouples and the reactor physics and thermal analysis models that were benchmarked against the thermocouple readings early in the irradiation. The model predictions and statistical analysis of the data were used to update the thermocouple control temperature set points to account for the nuclear transmutation and drift in the thermocouples. Based upon the Type N thermocouple experience in AGR-1, coupled with careful placement of the thermocouples in lower-temperature, but well-characterized, areas in the graphite and a 50% increase in the diameter of the type N thermo-elements, the decision was made to utilize only Type N thermocouples in AGR-2. However, it must be noted that the INL developmental thermocouples performed very well in AGR-1 and are anticipated to be utilized in future NGNP experiments where their significantly higher-temperature capability is needed.

AGR-1 Experiment Results

The AGR-1 experiment burnup and fast fluence results are shown by irradiation cycle in Table 1, and by capsule in Tables 2 and 3. As shown in Table 1, AGR-1 was irradiated for 620 ATR Effective Full Power Days (EFPDs). It achieved a peak fuel burnup of slightly over 19.6% FIMA and a peak fast neutron fluence 4.39 X 10^{25} n/m^2. When the experiment was removed from the ATR in early November 2009, it had achieved the 14% FIMA minimum burnup in 85% of the fuel compacts and the 18% FIMA burnup goal in over 35% of the fuel compacts. No fuel particle failures and only low levels of fission gases from uranium contamination were detected throughout the irradiation.

Table 1. *Preliminary AGR-1 irradiation summary.*

ATR Operating Cycle	Cumulative EFPDs	Compact Minimum Burnup (% FIMA)	Compact Peak Burnup (% FIMA)	Compact Minimum Fast* Fluence (x 10^{25} n/m^2)	Compact Peak Fast* Fluence (x 10^{25} n/m^2)
1	47	0.38	1.14	0.15	0.32
2	98	0.87	2.77	0.33	0.68
3	149	1.44	4.59	0.50	1.02
4	196	2.04	6.37	0.65	1.33
5	232	2.52	7.63	0.75	1.55
6	264	3.10	9.07	0.87	1.79
7	312	4.02	10.93	1.04	2.13
8	364	5.11	12.78	1.23	2.53
9	413	6.32	14.48	1.42	2.90
10	470	7.65	16.05	1.64	3.33
11	514	8.77	17.21	1.81	3.65
12	566	10.23	18.50	2.00	4.00
13	620	11.51	19.61	2.21	4.39

** Fast neutron flux defined as E > 0.18 MeV.*

Table 2. *Preliminary AGR-1 capsule burnup results.*

Capsule	Average Burnup (% FIMA)	Minimum Burnup (% FIMA)	Peak Burnup (% FIMA)
1	15.3	13.4	17.2
2	17.8	16.0	19.1
3	18.7	17.1	19.6
4	18.3	16.5	18.5
5	16.6	14.3	18.4
6	13.3	11.5	15.0

Table 3. *Preliminary AGR-1 capsule fast fluence results*

Capsule	Average Fast* Fluence (10^{25} n/m^2)	Minimum Fast* Fluence (10^{25} n/m^2	Peak Fast* Fluence (10^{25} n/m^2)
1	3.06	2.56	3.43
2	3.85	3.42	4.12
3	4.18	3.82	4.39
4	4.09	3.69	4.32
5	3.61	3.16	3.91
6	2.71	2.21	3.08

** Fast neutron flux defined as E > 0.18 MeV.*

Temperature plots of the preliminary data from Capsules 1, 2, and 3 are shown in Figure 6, and the preliminary temperature data for Capsules 4, 5, and 6 are shown in Figure 7. Initially, the experiment design temperatures could not be achieved due to the boron content in the graphite holder. However, as anticipated, as the boron started to burn out in the graphite, the temperatures of the fuel compacts achieved the design temperatures in all but the bottom capsule (Capsule 1) by the end of the second ATR irradiation cycle (e.g., within the first 100 days of irradiation). The bottom capsule achieved the design temperature during the fourth irradiation cycle.

The experiment achieved and passed through the peak heat generation in the fuel at approximately 250 to 300 EFPDs. The desired temperatures in the fuel became harder to achieve as the fuel continued to deplete; however, the unique operating characteristics of the ATR, as well as replacing the leakage gas into the capsules with neon instead of helium, helped to overcome the reduced heat generation within the fuel and allow continued operation at or close to the desired temperatures.

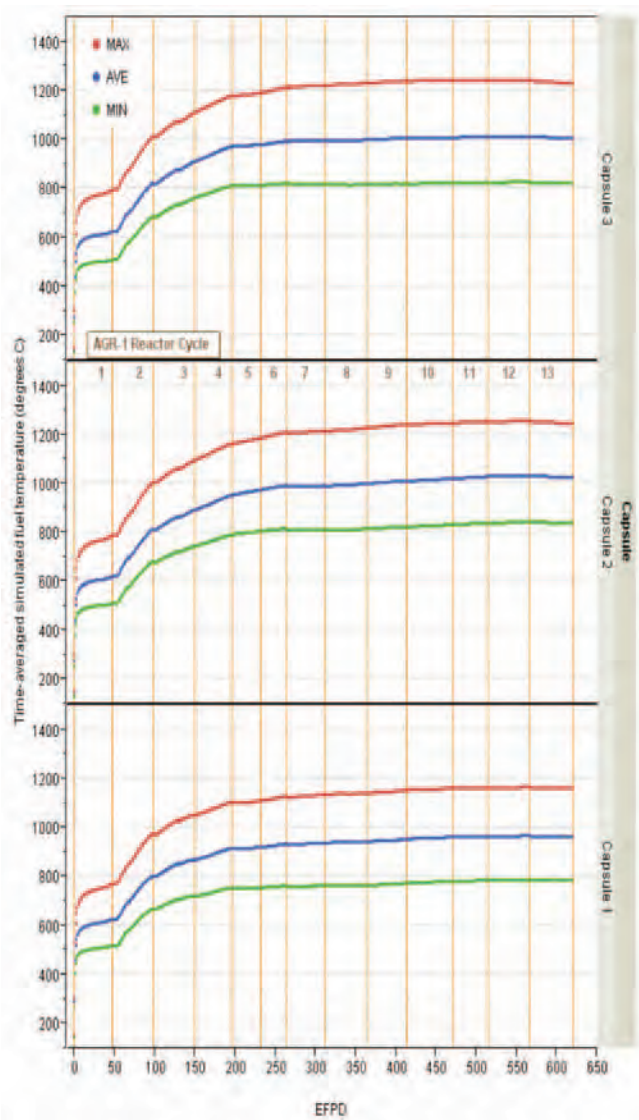

Figure 6. *Preliminary AGR-1 capsule temperatures for Capsules 1, 2, and 3.*

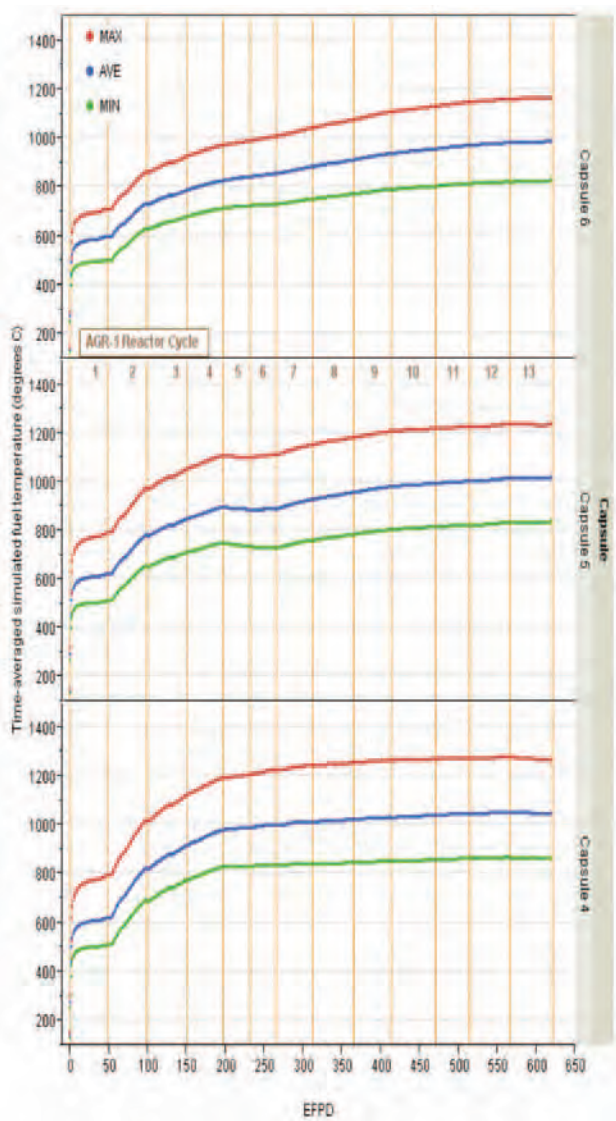

Figure 7. *Preliminary AGR-1 capsule temperatures for Capsules 4, 5, and 6.*

Detailed analyses of the experiment as well as analysis and testing of the fission product monitors indicated a single fuel-particle failure would result in a fission-gas release being detected at the monitor equal to approximately two orders of magnitude greater (e.g., 10^{-6} versus 10^{-8}) than the fission gas levels from the uranium contamination measured by the fission product monitoring system. Release-to-birth rate ratios (R/B) were calculated for many of the short-lived fission gases, and the preliminary results are shown in Figure 8. The values in the figure demonstrate the excellent performance of the fuel throughout the irradiation without a single particle failure being detected.

Conclusions

Development and irradiation of the AGR-1 experiment has provided valuable insights and lessons learned as it completed its primary mission as a shakedown of the experiment design and operating characteristics as well as the temperature-control and fission-product monitoring systems. These insights and lessons learned have been incorporated into the design of

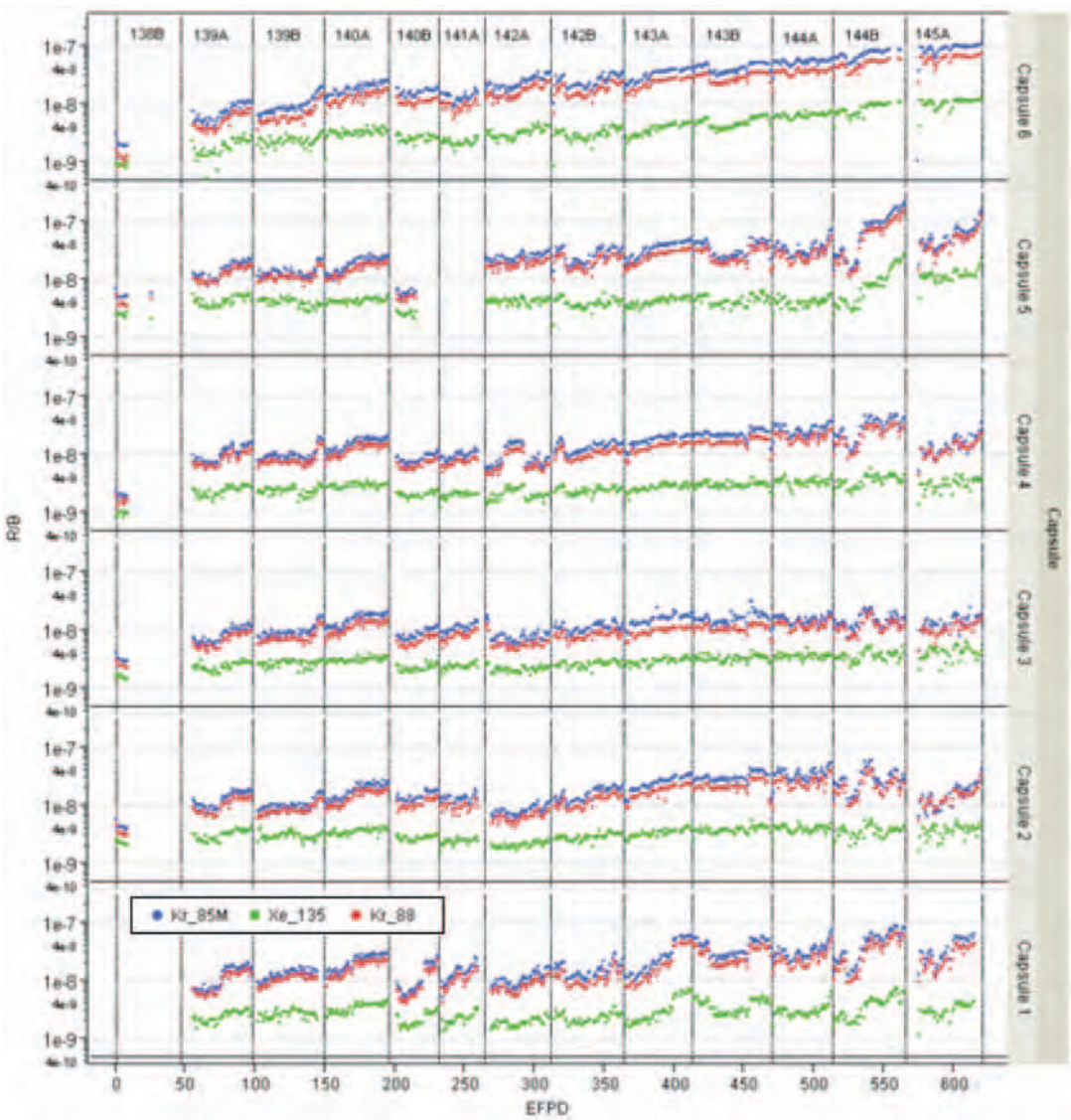

Figure 8. *Preliminary AGR-1 R/B for Capsules 1 through 6.*

AGR-2 and will continue to benefit the NGNP program during the irradiation of AGR-2 and later experiments. A valuable added bonus of the experiment is the data gained on the irradiation performance of the fuel developed by the AGR program. It is anticipated that AGR-2 will provide additional valuable data on the irradiation performance of UCO at both the anticipated operating temperature as well as increased temperatures. AGR-2 will also provide valuable irradiation data on UO_2 fuel. The results of these experiments can then be used to support qualification of particle fuel for use in high temperature gas reactors.

Post-Irradiation Examination

The post-irradiation examination of the coated-particle fuel form is focused primarily on verifying the performance of the fuel during normal irradiation conditions and during off-normal accident scenarios. Here fuel performance refers to the ability of the fuel to maintain coating integrity and retain fission products within the coated particles. As AGR-1 is the first irradiation of its kind in the NGNP program and involves a complex, multi-capsule, instrumented lead experiment containing four types of fuel, the PIE will also seek to investigate the performance of test train and components. Accordingly, the main objectives of the AGR-1 PIE campaign are to:

- Assess the overall performance of the test train and components and provide data to verify the test train thermal analyses
- Evaluate the fission-product retention of the fuel during the irradiation and during post-irradiation accident tests
- Characterize the compacts and individual particles to assess the condition of the matrix material, kernels, and coatings and document any concerns.

For this first irradiation experiment, the NGNP program would like to demonstrate the following for at least one of the fuel types [6]:

- Low in-reactor fission-gas release (release-to-birth ratio [R/B] $\leq 4 \times 10^{-6}$) as measured during irradiation by sweep-gas analysis
- Low release during irradiation (as measured during PIE) of iodine and fission metals (e.g., isotopes of strontium, silver, cesium, and europium)
- Little or no kernel migration
- Minimal corrosion and good structural integrity of the coatings
- Compact matrix stability and integrity
- Minimal fission-product release from fuel compacts under high temperature accident conditions (at least 1600°C in an inert gas atmosphere).

These performance measures will provide confidence that the fuel fabrication has met the standards of high quality fuel, the UCO concept is controlling CO pressure buildup and the amoeba effect, and the UCO-based fuel has satisfactory iodine and metallic fission product retention under normal operation and accident conditions. It will also confirm the program's thinking with regard to the coating properties that are critical for good irradiation performance. AGR-1 PIE will provide important data for the program to help understand the relationship between fuel processing, properties, and performance. This will support the selection of a reference fuel design for subsequent fuel-qualification irradiation planned for the future.

INL has been leading an effort for the last several years to develop a state-of-the-art PIE capability for coated particle fuel in the U.S. national laboratory complex, as the existing capabilities have significantly atrophied since previous programs nearly 2 decades ago. This includes capabilities for high temperature accident testing, compact deconsolidation and leach-burn-leach testing, irradiated particle visual examinations and gamma spectrometry, and detailed dimensional measurements of fuel and capsule components. The post-irradiation examination of the AGR-1 experiment is currently in progress. This section will discuss the PIE capabilities developed at INL and present some initial results of the early AGR-1 PIE activities.

AGR-1 test train inspection

The AGR-1 irradiation test train was shipped to the Hot Fuels Examination Facility (HFEF) at the Materials and Fuel Complex for PIE in March 2010. The test train was loaded into the main hot cell, visually inspected, and then examined by gamma spectrometry to get an initial indication of the condition of the interior capsule components. Complete axial gamma scans of the test train were performed using the HFEF Precision Gamma Scanner. The test train was scanned in a vertical orientation using a 7/8-inch wide by 0.05-inch high collimator slit oriented horizontally (perpendicular to the test train) with a 0.05-inch vertical step size. Three different rotational orientations were used so that each scan included only a single compact stack (due to the

cross-sectional layout of the capsules, only a portion of each compact stack was scanned). The gross gamma results for fuel Stack 3 are shown in Figure 9.

The fuel compacts and interior components of the test train (e.g., capsule heads, Nb gas lines, hafnium shrouds) could be easily resolved from the gross and isotopic scans. Based on the gap between the bottom compact in each capsule and the capsule base, it was concluded that no axial displacement of the compacts had taken place (within the linear resolution of the method). In addition, the non-fueled gap immediately above the Capsule 4 graphite holder and fuel compacts was examined in detail with long count times (1–2 hours) in an attempt to observe fission products that might have migrated from the fuel (e.g., Cs-137, Ag-110m). No fission products were observed in this region above the level of background.

Test capsule disassembly and component dimensional measurements

Following the non-destructive test train exams, the test train and capsules were disassembled to remove the fuel compacts and other components of interest. Due to the complexity of the test capsules and the desire to avoid damage to the fuel compacts and graphite parts, specialized tools have been designed to perform the in-cell disassembly of the AGR-1 experiment. The system consists of a tubing lathe for making circumferential cuts to the test train shell and a series of tools mounting to a sliding rail system to facilitate disassembly operations while minimizing handling of the compacts with the remote manipulators (Figure 10). Initial experience with disassembly of the AGR-1 capsules has presented several challenges due to minor damage to the capsule components during the 3-year irradiation and the need to extract the fuel compacts without damage. This information will be used as valuable feedback to the design of future AGR irradiation experiments to help facilitate disassembly as much as possible.

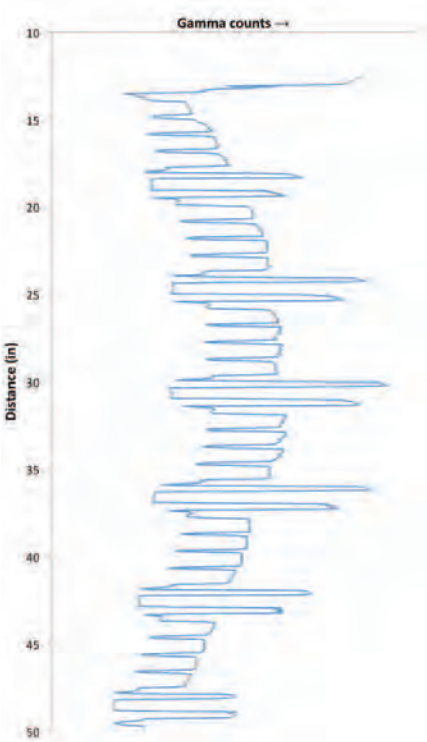

Figure 9. *Gross gamma scan results for AGR-1 fuel Stack 3, showing the location of some interior components of interest.*

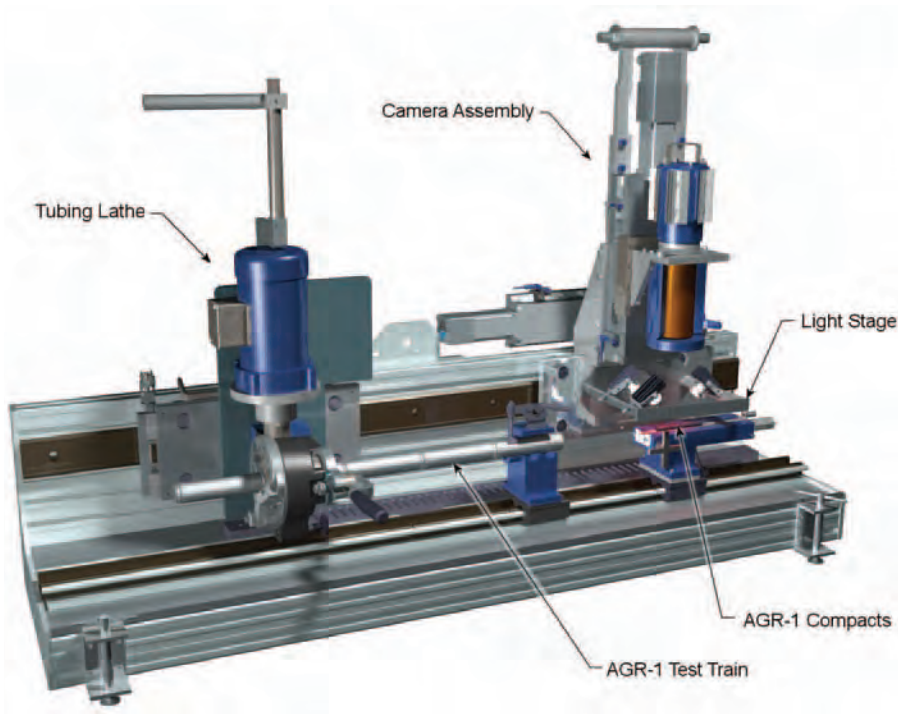

Figure 10. *Drawing of the integrated AGR-1 test train disassembly and metrology system.*

An important characteristic of the fuel compacts and graphite fuel holders in the AGR-1 capsules is the amount of irradiation-induced shrinkage that has occurred during the experiment. This will affect the temperature control gas gaps between the compacts and graphite holder and the graphite holder and the outer metal capsule shell. Therefore, reliable information about dimensional changes of the components is needed to refine the thermal calculations used to predict fuel temperatures during the irradiation. To accomplish this during PIE, a non-contact photo-visual inspection system was designed so that digital images could be taken of the fuel compacts and graphite holders, from which low-uncertainty (combined uncertainties of less than 0.001 inch) dimensional measurements could be made. The system consists of a 6.6 mega pixel digital camera coupled with a 0.31x telecentric lens for image acquisition (Figure 10). Both components are shielded with tungsten alloy for in-cell work based on estimates of the radiation dose expected during their operational life and measurements of the radiation dose-to-failure for each component. Components are illuminated using red light-emitting diodes that minimize chromatic aberration in the acquired images and have good service life in the radiation field of the hot cell. The system is integrated with the disassembly table so that images of the fuel compacts and graphite fuel holders are acquired concurrently with capsule disassembly activities.

An image of an irradiated AGR-1 compact from Capsule 4 is shown in Figure 11. The compact is imaged on two roller bars that allow complete rotation of the compact to inspect the entire circumference and make diameter measurements at multiple orientations. As shown in Figure 11, the digital images provide a high degree of detail for inspection purposes, and the irradiated compacts photographed to date exhibit very little damage. Prior to acquiring dimensional data from the images the digital camera is calibrated using a National Institute for Standards and Technology (NIST)-traceable chrome-on-glass line grid (0.05-mm line widths with 1-mm spacing) to define the pixel pitch of the image sensor. Images are then processed for dimensions by measuring between defined points at the edge of the imaged components using image analysis software. The method is validated prior to analyzing the AGR-1 components by performing measurements on precision-machined carbon steel standards that represent the fuel compacts and the graphite fuel holders and have been characterized to within ±0.00015 inch using NIST-traceable instruments.

Preliminary dimensional data for irradiated AGR-1 compacts indicate shrinkage varying among capsules and often along the length of the individual compacts. Diametrical dimensional change for the compacts from Capsules 1, 4, and 6 is in the range of -0.9 to -1.5%, with an average value of -1.1%. Length change is in the range of -0.2 to -0.9%, with an average of -0.6%. Measurement of compact dimensions from the remaining capsules is currently in progress.

Preliminary data on the graphite holders from Capsules 1 and 6 indicate diametrical dimensional change between -0.4 and -0.8%, and an average length change of -0.3%. However, preliminary data on the Capsule 3 and 5 graphite holders indicate significant expansion (quantitative values are not yet available). This change from graphite holder shrinkage on the ends of the test train (Capsules 1 and 6) to expansion in the center capsules (Capsule 2–5) is believed to be due, in part, to the difference in the type of graphite used and possibly the higher thermal and fast neutron fluence in the center of the test train. Capsules 1 and 6 used a graphite containing 5.5% boron as a burnable poison while the remaining capsules used a graphite containing 7% boron.

Figure 11. *Irradiated fuel compact from AGR-1 Capsule 4.*

Gamma spectrometry of fuel compacts

The irradiated AGR-1 compacts will be characterized with gamma spectroscopy to determine inventories of key fission products (e.g., Ag-110m, Cs-137) and to determine the burnup by measuring the ratio of specific fission products (e.g., Cs-134/Cs-137). The compact fission product inventories are of particular importance because of the need to determine fractional releases during high temperature accident testing. Burnup measurements from spectroscopy data will be compared with values determined from destructive measurements based on the American Society for Testing and Materials (ASTM) E321-96 procedure and with calculated values based on physics models.

Gamma spectra will be acquired by scanning the compacts in axial slices using a 7/8-inch-wide collimator with a slit height and step size of 0.1 inch. The compacts will be gamma scanned along the entire axial length so that the entire compact volume is counted, and the total compact inventories will be determined by summing the results from each axial slice. This activity will also include gamma counting the non-fueled end caps (visible in Figure 1, for example) on selected compacts to provide information on the inventory of fission products released from the particles during irradiation (e.g., Cs-137) and deposited in the compact matrix.

The fuel compacts will be placed in individual aluminum containers, which will, in turn, be placed together in an aluminum tube that will be positioned in front of the gamma detector collimator for counting. Several calibrated 20 mCi Eu-152 sources will be used as standards during the data acquisition and will allow the instrument to be calibrated for gamma energies across a large range (about 0.3 to 1.4 Mev). These sources were extensively characterized using calibrated spectrometers so that the absolute inventories are known to within ±3%. These standards are placed in aluminum containers with identical dimensions as those containing the irradiated compacts. Figure 12 shows the Cs-137 data from four of the Capsule 1 compacts. Work is currently underway to utilize the in-service calibrations and appropriate geometrical corrections to process the acquired spectra into radionuclide activities.

Capsule fission product inventories

A key component of the evaluation of AGR-1 fuel performance will be to determine the extent of metallic fission product release from the fuel compacts during the irradiation. This may occur as diffusive release through intact coatings (especially in the case of silver) or from particles with damaged SiC layers. While online fission product monitors are used to assess the release of Kr and Xe isotopes during the experiment, there is no means of assessing the release of fission products such as Ag, Cs, Sr, and Eu in real time. Instead, these will be determined by measuring the radionuclide inventories of the various capsule components, including the graphite fuel holders and the metal capsule parts (e.g., the capsule shell), during PIE.

The graphite holders will be quantitatively gamma counted using spectrometers in the Analytical Laboratory to determine the inventory of fission products including Ag-110m, Cs-137, and Eu-154. The spectrometer will be calibrated with a Eu-152 source. Fission products on metal capsule parts will first be stripped using an acid treatment, and the leach solution will then be analyzed using radiochemical methods for the fission products of interest.

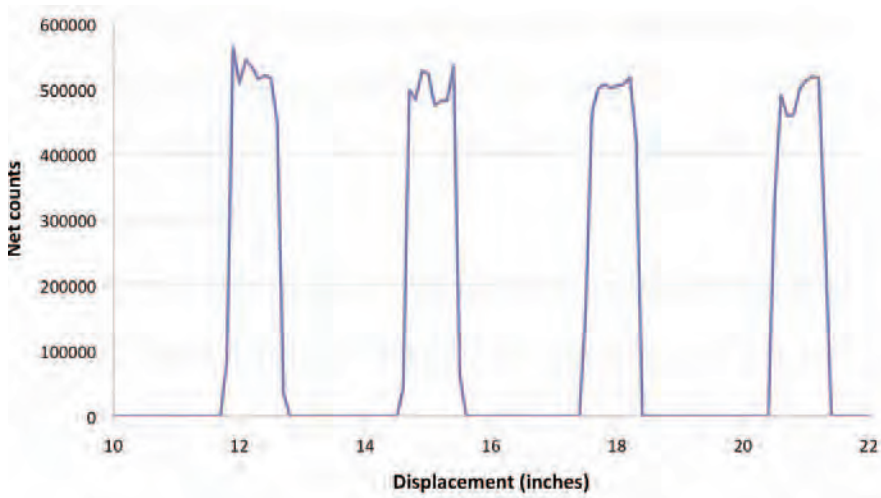

Figure 12. *Cs-137 counts for the four Stack 3 compacts from Capsule 1. Compacts have been removed from the irradiation capsule and placed in aluminum storage containers during acquisition of the gamma spectra.*

The results will be combined to produce a mass balance for each capsule that will describe the magnitude of fission product release from the fuel during the irradiation as well as the distribution of the various fission products in the different capsule components and location.

High temperature accident testing

A critical measure of coated particle fuel quality, and an important aspect of fuel qualification, is the ability to retain fission products during high-temperature accident scenarios in which core temperatures could reach 1600°C or more. At these temperatures, certain fission products can have significant mobility and are capable of diffusing through coating layers and into the core structural materials and beyond. Cesium release is particularly sensitive to flaws in the SiC layer, while krypton release tends to be lower due to holdup by intact pyrocarbon layers. Silver diffuses relatively rapidly through intact SiC and has consequences for reactor maintenance. In addition, reaction of certain fission products, such as palladium, with the SiC layer is significantly accelerated at these temperatures and can jeopardize the integrity of the coating. Measurements of accident performance have historically been carried out during post-irradiation fuel testing by heating fuel elements in pure helium to temperatures in the range of 1600 to 1800°C while monitoring releases of the fission gas Kr-85 as well as condensable fission products such as silver, cesium, and strontium [9, 10].

The NGNP fuel program is initiating an extensive campaign of fuel accident testing to evaluate fuel performance and provide verification of fuel performance code predictions. Testing on the AGR-1 fuel compacts will focus on a comparison of performance among the four fuel types and on determining the effect of irradiation conditions (burnup, fast fluence, and irradiation temperature) on fuel accident performance. This effort includes the development of a dedicated furnace and fission-gas monitoring system at INL that will be installed in the HFEF main cell, an alpha-gamma shielded facility with an inert argon atmosphere.

The Fuel Accident Condition Simulator (FACS) furnace is designed to heat fuel specimens at temperatures up to 2000°C in pure helium while monitoring the release of volatile fission metals and fission gases (see Figure 13). The furnace has tantalum hot zone components and is heated using a graphite resistance element. The power to the heating elements is supplied at 28V and has a maximum ouput of 850 amps. The fuel specimen is heated inside an 85-mm-diameter tantalum flow tube and is supported on a tantalum holder that sits atop a tantalum tube inserted from the bottom of the furnace. The fuel-specimen temperature is monitored with a Type C (W-Re) thermocouple housed within the tantalum tube that supports the sample holder, with the hot junction located about 12 mm below the specimen. The hot zone

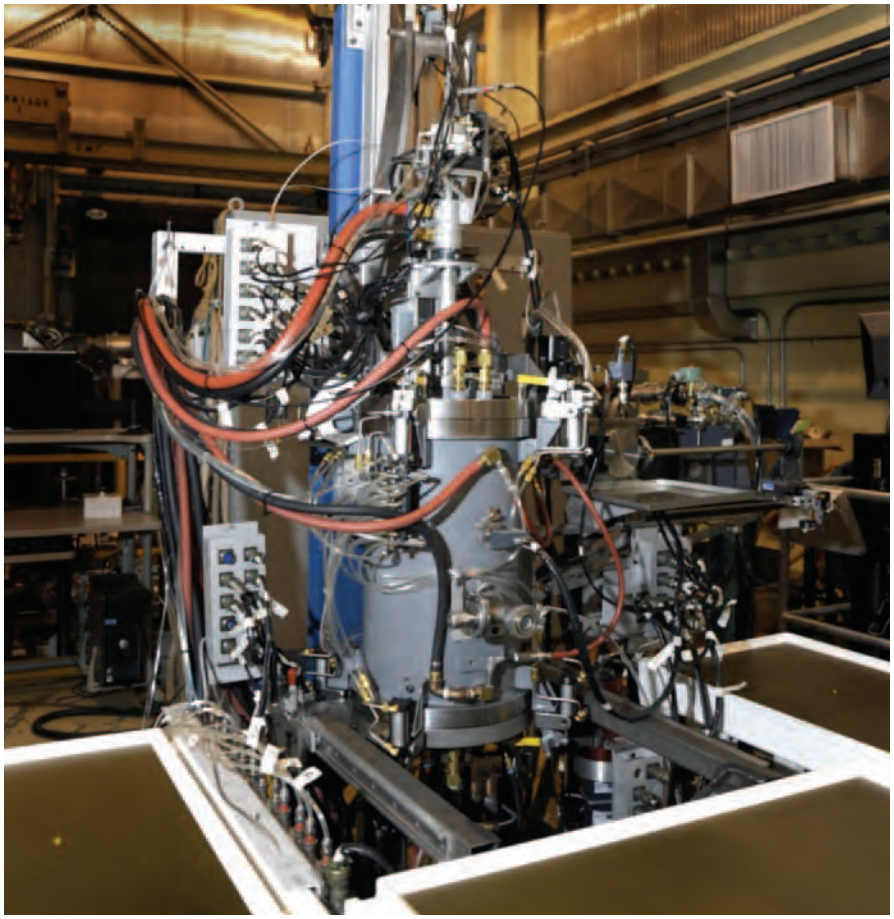

Figure 13. *Fuel Accident Condition Simulator (FACS) furnace during remote qualification testing.*

can accommodate samples up to approximately 75 mm in diameter. Special sample holders have been designed to accommodate the 25 mm long x 12.3 mm diameter AGR compacts, although any specimen geometry can be accommodated through design of a custom tantalum holder.

The furnace main chamber is double-walled water-cooled stainless steel. Both the top and bottom flanges are water-cooled stainless steel and can be removed from the main chamber for sample loading or maintenance operations as needed. Flange and chamber movements are all performed using a dedicated lift motor and are controlled at the main computer console. The water-cooled cold finger is of aluminum construction and holds a 35-mm-diameter plate on the end by means of a mechanical lock using a rotary actuator. The temperature at the base of the cold finger where the condensation plate is attached is monitored using a Type J thermocouple. Figure 14 depicts a cut-away view of the furnace system. Condensate plates are introduced to the furnace through a separate transfer chamber that is purged with helium prior to opening a gate valve to the main chamber. With the cold finger elevated above the furnace hot zone, a cradle located at the end of a positioning arm is moved horizontally beneath the cold finger and the old plate is deposited on the cradle. A new plate on the cradle is then positioned beneath the cold finger and acquired using a mechanical locking action. The entire condensate plate exchange operation is performed automatically by computer control. The operator must only remove the used plate from the cradle once it has been retracted into the transfer chamber and place a fresh plate on the cradle to be placed on the cold finger during the next exchange cycle.

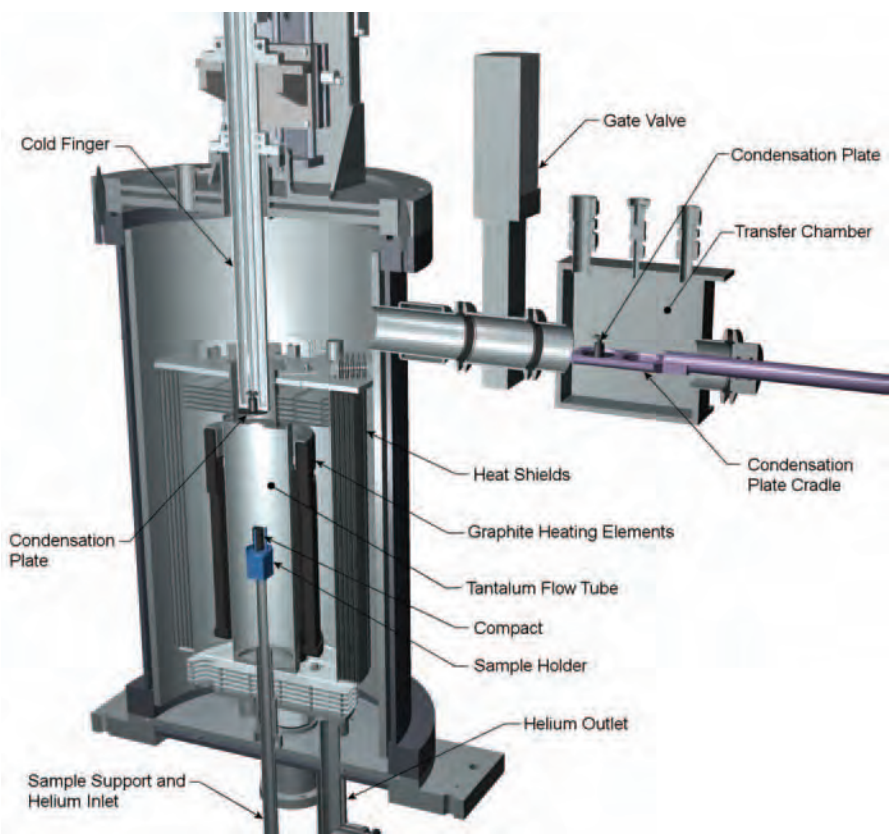

Figure 14. *Three-dimensional cut away diagram of the FACS main chamber and interior components; inset shows sample stage and hot zone detail.*

Condensation plates that are removed from the furnace during operation will be packaged in clean plastic containers and sent to the analytical chemistry laboratory for analysis. This will consist of gamma counting of the plates to measure the inventory of major fission products (e.g., Cs-137, Ag-110m) followed by acid leaching to remove fission products and aqueous radiochemical analysis of Sr-90 (which decays with no gamma emissions) and I-131. Strontium is analyzed by first separating it from the other fission products using an ion-exchange resin, recovering the separated material, and measuring the activity by liquid scintillation. Iodine is quantified by separation, recovery, and either scintillation, gamma spectrometry, or inductively coupled plasma mass spectrometry.

The system has six separate water circuits for cooling the critical components during high temperature operation, including the cold finger and the furnace chamber (see Figure 15). In addition, there are several gas lines to supply pressurized argon to the pneumatic components. A vacuum pump is connected to the main chamber and the transfer chamber, which can be evacuated independently by appropriate control of values on the vacuum lines.

Prior to starting a test, the main chamber is evacuated and filled with ultra-high-purity helium. The helium sweep gas is introduced to the furnace from the bottom and injected into the hot zone beneath the specimen at a rate of 500–1000 mL/min, then flows toward the condensation plate at the end of the cold finger.

The helium is then swept from the furnace, through particulate and moisture filters, and is carried to the fission gas monitoring system (FGMS) for analysis of the Kr-85, Xe-133, or other radioactive noble gases. This system is located outside of the hot cell and consists of dual liquid-nitrogen-cooled charcoal traps to contain the noble gases, each with a high-purity germanium detector and adjustable collimator (Figure 16). A valve manifold allows the gas flow to the cryo-traps to be configured as necessary. If a failure of the primary trap occurs or the trap becomes saturated with fission gas, the helium flow can be routed to the second trap and the test continued without interruption. A schematic diagram of the FGMS is shown in Figure 17. The fission-gas monitoring system has the capability of purging the primary charcoal-traps at the end of a furnace cycle and recapturing the noble gasses in a separate portable cold-trap. These gases can then be further analyzed with other detection systems if desired. Each trap-detector assembly contains its own primary set of control electronics and can be controlled individually or in sync by the FGMS control software. The FGMS control software was developed at INL and automatically controls the temperature of the cold traps and initiates spectral acquisition. Measurements will run for a set period of time, determined by experimental staff based on FACS conditions. The control software saves the spectra, showing spectral information and gross detector count rates as a function of time. This feature allows for quick determination of fission-gas release from the heated fuel elements. Once the acquired spectral data is stored the FGMS analysis program will determine the concentrations of fission gasses present in the cold traps. This data is then stored for further programmatic use.

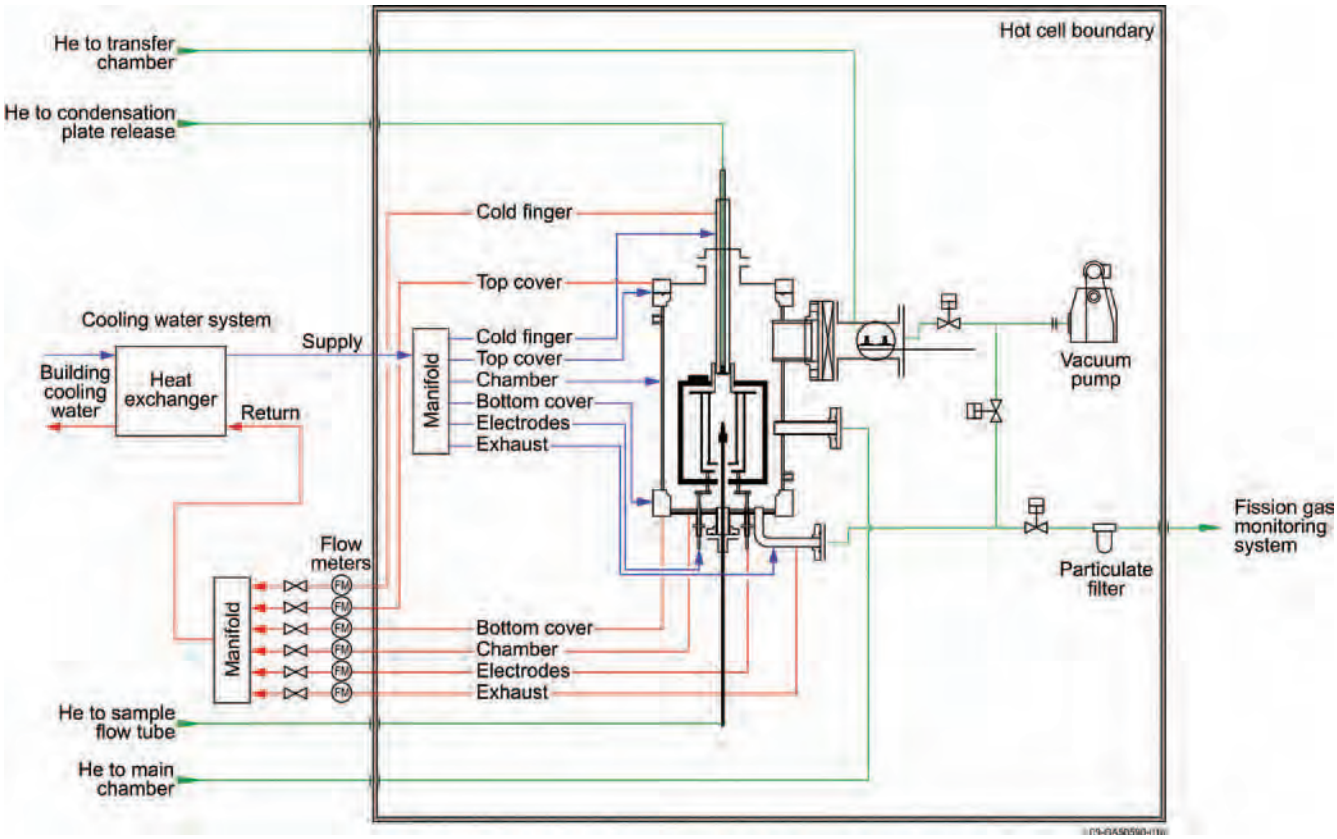

Figure 15. *Schematic of FACS cooling water and helium supply system.*

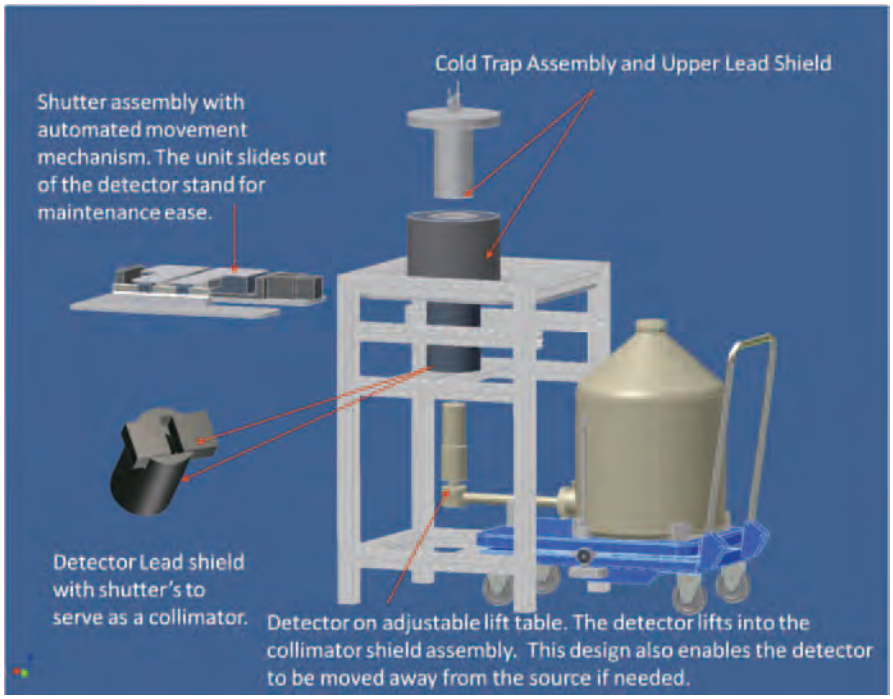

Figure 16. *A cold trap and detector assembly from the FACS Fission Gas Monitoring System (FGMS).*

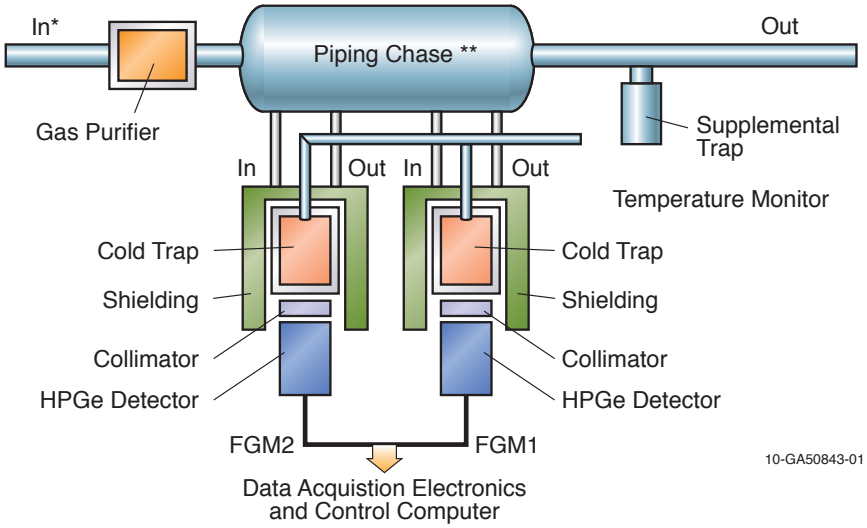

* Fission gas leaving the furnace and the hot cell.

** The piping chase is support for the inlet and outlet gas lines for the fission gas and the LN supply

Figure 17. *FGMS schematic.*

The helium sweep gas enters the liquid-nitrogen-cooled cold trap assembly located within the upper lead shield where it is accumulates and is viewed by the high-purity-germanium (HPGe) detector. The FGMS control software processes the acquired spectra and determines the fission gas concentrations. In the event of a rapid release of fission-gas from the fuel, the system is equipped with an automated tungsten collimator to minimize recovery time of the HPGe detector.

Compact deconsolidation and particle inspection

Compacts will be electrolytically deconsolidated to obtain individual particles for subsequent analysis and as the first step in the "leach-burn-leach" procedure (discussed below). The deconsolidation process involves submersing the bottom of the compact in an electrolyte solution of concentrated nitric acid and applying an electric current (~7 volts at ~1–1.5 amps to maintain a power of about 7–10 watts) via an anode attached to the top of the compact and a cathode suspended in the electrolyte. The compact is retained in a quartz tube with a perforated bottom plate. Application of an electric current results in the electrolytic oxidation and disintegration of the carbonaceous compact matrix, allowing individual fuel particles to fall through the perforated plate into the electrolyte. Particles can then be collected and separated from any fines or larger matrix debris by sieving. A system for performing deconsolidation on the irradiated AGR-1 compacts has been tested and installed in the Analytical Laboratory hot cells.

Once fuel particles are deconsolidated, various exams are performed to assess the condition of the irradiated fuel and the

level of fission-product retention. Low magnification examination of particles will be performed using a custom microscope and particle manipulator system (Figure 18). This system consists of a Leica Z16APO modular microscope with a variable magnification lens and a digital camera for particle imaging and a vacuum needle used to pick up individual particles. The horizontally mounted camera and microscope are shielded with tungsten plates to prolong life in the hot cell. Particles are imaged on a glass slide from below using a 45 degree oriented mirror. The microscope and lens provide a minimum field of view at the glass slide of approximately 1.6 mm. Figure 19 shows an image taken of several surrogate particles on a glass slide and a single particle captured by the vacuum needle. The assembly containing the viewing slide is mounted on an x-y-z translation stage, while the vacuum needle assembly is mounted on a separate translational stage with z-axis travel. This allows particles to be repositioned in the field of view and the vacuum needle lowered to select a specific particle. The vacuum needle can then be raised and the main stage assembly moved to position a receptacle for the particle (e.g., a glass vial) beneath the needle. This system will be used to perform initial visual examination on large batches of particles, to select specific particles, and to load particles into glass vials for subsequent analyses.

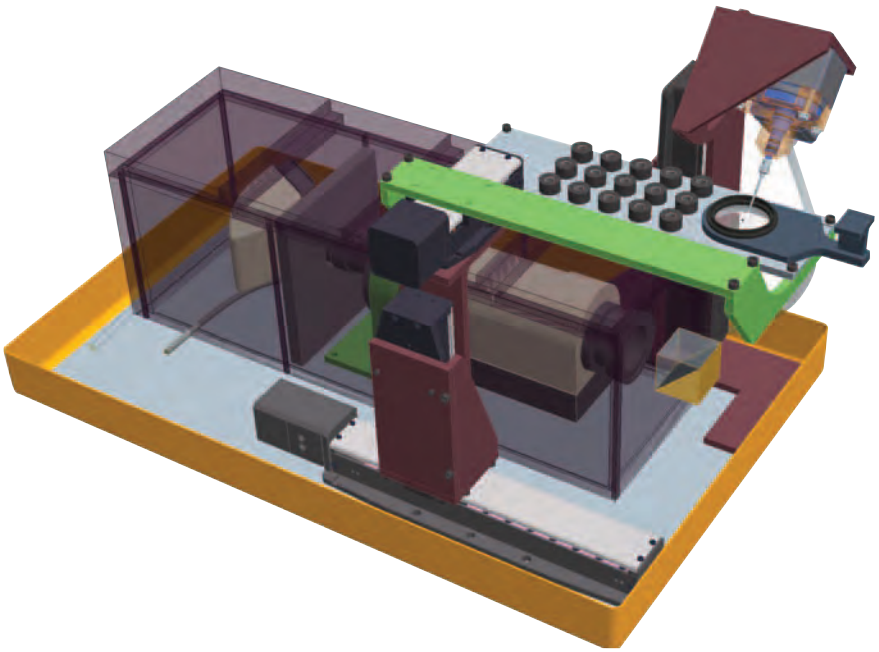

Figure 18. *Irradiated particle handling and inspection system.*

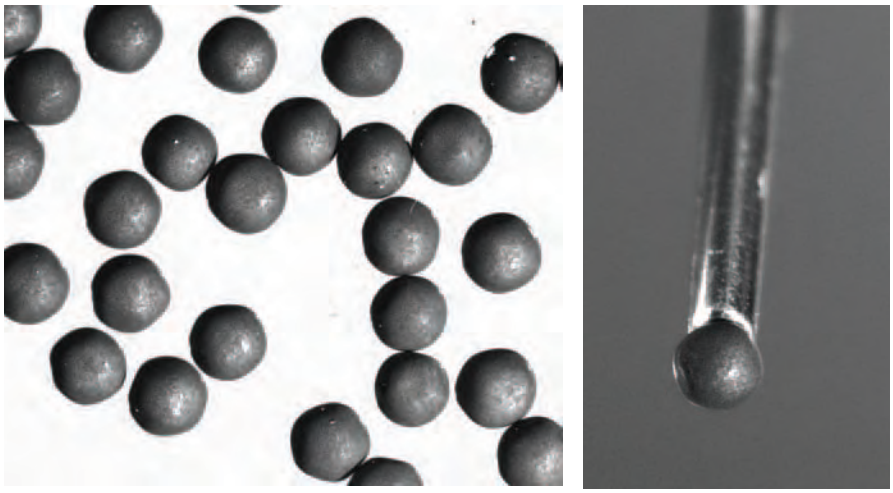

Figure 19. *Image of surrogate particles (~800 micron diameter) imaged with the microscope system (left) and a single particle captured by the vacuum needle (right).*

Leach-burn-leach

One method for detecting failed coating layers in large batches of particles is the "leach-burn-leach" (LBL) procedure. The method involves a preliminary concentrated nitric acid leach on a batch of deconsolidated particles, often performed as a follow-on step after compact deconsolidation and using the same acid electrolyte solution. Particles in the batch that have cracks penetrating all of the dense coating layers (IPyC, SiC, and OPyC) will be infiltrated during this step, and the uranium oxycarbide kernels will be dissolved by the acid. Analysis of the leachate solution reveals the dissolved uranium and the number of exposed kernels can be quantified based on the uranium concentration. Next the particles are placed in a furnace and heated to 750°C in air, which results in oxidation and removal of all exposed carbon layers. If particles have intact SiC layers, then only the outer

pyrolytic carbon layer will be removed. If cracks in the SiC layer exist, then the inner pyrolytic carbon and buffer layers will also be burned off, leaving the kernel exposed. A subsequent acid leach of the particles will remove the exposed kernels and, as before, an assay of the leachate solution will reveal the number of exposed kernels based on the measured uranium inventory. The exposed kernels in the post-burn leach correspond to particles with failed SiC layers but intact pyrocarbon.

In addition to quantifying coating failure fractions, this method will also be used to look at the inventory of fission products that have been released from particles but retained in the compact matrix. This is accomplished by analysis of the pre-burn leach solution for selected fission products (e.g., Ag-110m, Cs-137, Sr-90). This is expected to be most effective if there are no particle failures (i.e., complete through-coating failures) that would result in large fission-product inventories from the kernels to mask the smaller inventory retained in the matrix.

Equipment for performing LBL experiments on deconsolidated particles is located in the Analytical Laboratory hot cells along with the compact deconsolidation hardware.

Particle gamma spectrometry

Gamma spectrometry will be used to determine fission product inventories in individual irradiated particles, which allows the degree of fission product release to be measured. To accommodate variations in kernel size and burnup, this is best accomplished in practice by looking at the ratio of the fission products of interest to one that is known to be relatively immobile within the fuel kernel. An example is cerium, which forms the stable oxide in both uranium oxide and oxycarbide kernels, while some of the fission products of interest for this analysis include Ag-110m, Cs-137, and Eu-154. Thus, a relatively low Cs-137/Ce-144 ratio would indicate a particle that has experienced high Cs release, perhaps revealing a failed SiC coating. This information can be utilized in several ways in the post-irradiation fuel examination. For example, the Ag-110m release fractions among a batch of particles can be compared to determine the distribution of values, and selected particles can be examined in more detail to evaluate the SiC coating microstructures (e.g., grain size, grain orientation, quantity, and types of defects) that may have contributed to increased release rates. The method can also be used to screen a large number of particles (several thousand) based on the Cs-137/Ce-144 ratio to find a single failed particle that can then be analyzed microscopically in detail to determine the cause of the failure. All of these results will provide information linking the coating fabrication processes and properties to fuel irradiation performance.

At INL, particle gamma spectrometry will be accomplished by selecting individual particles using the particle handling and inspection microscope system (Figure 17) and placing them in glass vials. Each vial can then be counted in the Analytical Laboratory hot cell gamma spectrometer for the prescribed period of time and saved for subsequent analysis if warranted.

Microscopy

Fuel specimens will be characterized by microscopic methods both after irradiation and after high-temperature post-irradiation heating tests. Optical and electron microscopy will be used to characterize compact and particle cross sections. Of particular interest are kernel and coating microstructures, coating damage such as cracks or fission product corrosion, coating interactions, and kernel migration. Elemental analysis (wavelength dispersive spectroscopy) will be used to examine kernel microstructures and phase heterogeneity and migration of fission products in the various coating layers, including corrosion of the SiC layer by palladium or other fission products. Additional SiC microstructure information such as grain orientation will be obtained from electron backscatter diffraction analysis (EBSD). Information on SiC microstructure will be of particular interest for explaining any observed differences in silver release from the fuel particles. Detailed analysis of coating microstructures and coating interface phenomena will be explored using transmission electron microscopy (TEM) or atom probe tomography. Focused ion beam (FIB) sample preparation methods will be used to prepare TEM (Figure 20) and atom probe specimens.

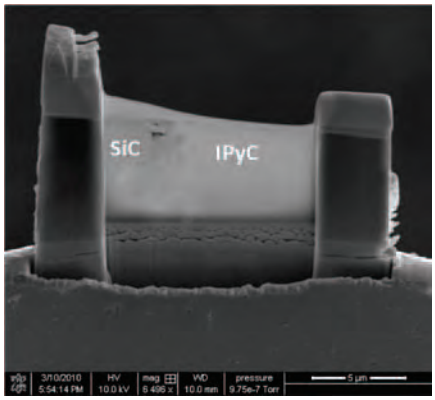

Figure 20. *TEM specimen of the IPyC-SiC interface of a surrogate-coated particle prepared using the focused ion beam.*

Summary

State of the art capabilities exist at INL for irradiation testing of TRISO fuel in multi-capsule instrumented test trains in the ATR. The AGR-1 irradiation experiment was a very successful demonstration of NGNP TRISO fuel performance, reaching peak burnups in excess of 19% FIMA with zero particle failures out of 300,000 particles and extremely low fission gas release-to-birth ratios. The AGR-2 experiment has been assembled, and irradiation is expected to begin in mid-2010.

PIE capabilities at INL for coated particle fuel have recently been renovated to enable detailed fuel performance evaluations. The PIE for the AGR-1 experiment is currently underway and will focus on evaluating differences in performance for the various AGR-1 fuel types. This will include an examination of fission product releases and particle failure fractions during irradiation and during post-irradiation high-temperature accident testing and detailed characterization of kernel and coating microstructures and fission product migration within the particles.

Acknowledgments

This work was supported by the United States Department of Energy (DOE) under DOE Idaho Field Office Contract Number DE-AC07-05ID14517.

References

1. Petti, David, Richard Hobbins, and James Kendall, Eds., Technical Program Plan for the Advanced Gas Reactor Fuel Development and Qualification Program, Idaho National Laboratory Report INL/EXT-05-00465, Rev. 2, July 2008.

2. Barnes, Charles M., W.C. Richardson, DeWayne Husser, and Matthias Ebner, "Fabrication processes and product quality improvements in Advanced Gas Reactor UCO kernels," HTR2008-58039, Proceedings of the 4th International Topical Meeting on High Temperature Reactor Technology, HTR2008, Washington, DC USA, September 28–October 2, 2008.

3. Rempe, J. L., et al., "Evaluation of specialized thermocouples for high-temperature in-pile testing," Proceedings of the International Congress on Advances in Nuclear Power Plants, Reno, NV, USA, June 4–8, 2006, Paper 6068, 2006.

4. Maki, J. T., "AGR-1 Irradiation Experiment Test Plan," Idaho National Laboratory Report INL/EXT-05-00593, August 2005.

5. Grover S. B., and D. A. Petti, "Initial irradiation of the first advanced gas reactor fuel development and qualification experiment in the Advanced Test Reactor," Proceedings of Global 2007 Advanced Nuclear Fuel Cycles and Systems, Boise, ID, USA, September 9–13, 2007, Paper 177457, 2007.

6. Demkowicz, Paul, "AGR-1 Post-Irradiation Examination Plan," PLN-2828, Rev. 1, March 2010.

7. Gontard R. and H. Nabielek, "Performance Evaluation of Modern HTR TRISO Fuels," HTA-IB-05/90, 1990.

8. Schenk, W., G. Pott, and H. Nabielek, "Fuel Accident Performance Testing for Small HTRs," Journal of Nuclear Materials, 171, 1990, pp. 19–30.

PAUL DEMKOWICZ, received a Bachelor's degree in Ceramic Engineering from the University of Washington and MS and PhD degrees in Materials Science and Engineering from the University of Florida. He has worked at the Idaho National Laboratory for seven years studying the performance of advanced reactor fuel, and his present focus is on coated particle fuel development, post-irradiation examination, and high temperature performance testing. He is currently the technical lead for fuel post-irradiation examination for the Next Generation Nuclear Plant project.

S. BLAINE GROVER (B.S., 1978, Nuclear Engineering, Idaho State University; Registered PE) has been involved in designing irradiation experiments and associated support systems for the ATR during almost all of his 30-year tenure at the INL. He is currently the technical lead for the ATR irradiation experiments in support of the DOE Next Generation Nuclear Plant (NGNP) program, which includes both fuel and material irradiation testing. Mr. Grover also supports developing new irradiation experiment programs and external customers for the ATR, as well as assisting the ATR NSUF.

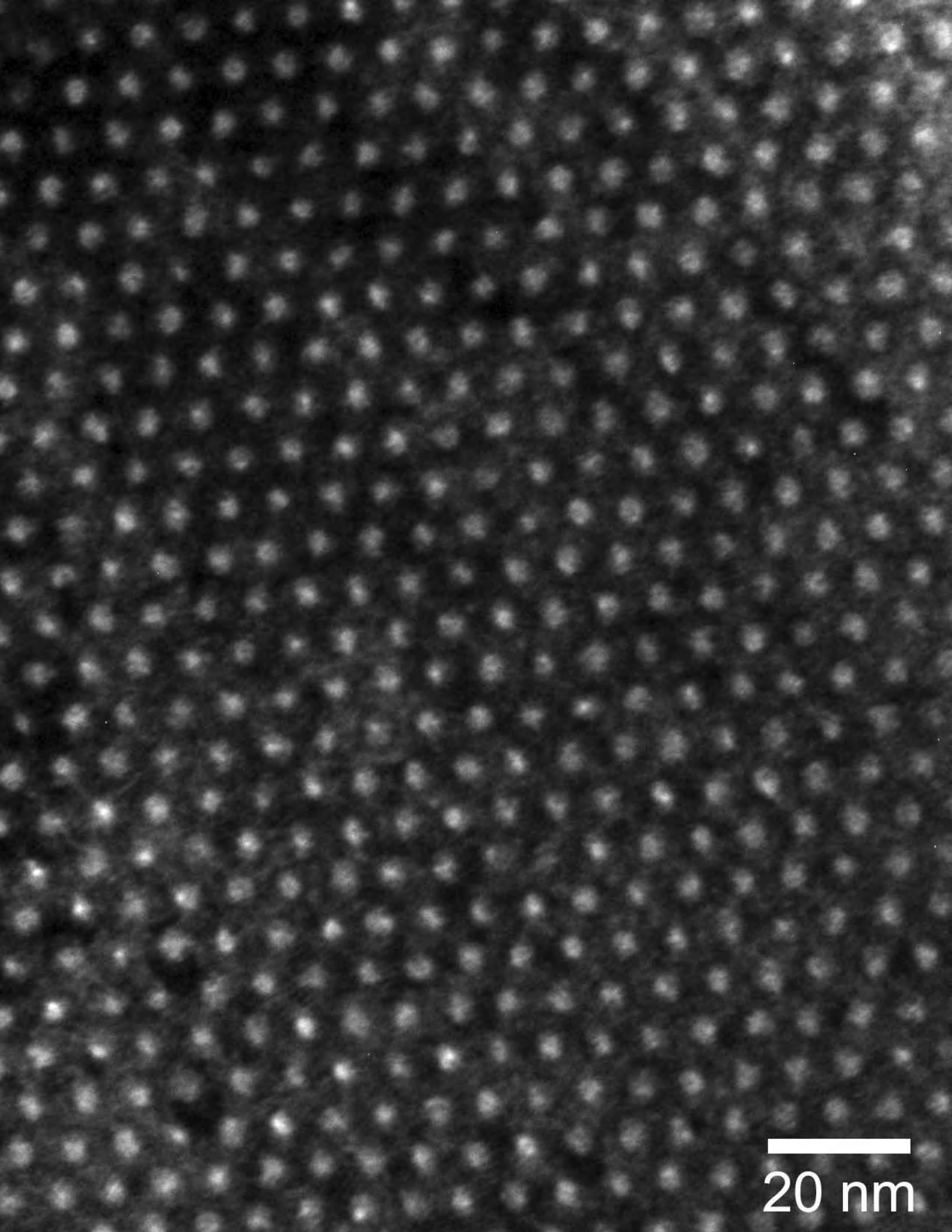
20 nm

TEM Characterization of the Irradiated Dispersion Fuel

J. Gan, D. D. Keiser, Jr., D. M. Wachs, A. B. Robinson, B. D. Miller, T. R. Allen (University of Wisconsin)

Introduction

Plate-type dispersion fuels are widely used for the research and test reactors. The fuel plate, typically about 1.5 mm thick, has three layers, with each at a thickness of approximately 0.50 mm. The top and bottom layers are cladding made of 6061 Al. In a low-enriched uranium (LEU) U-Mo fuel being developed to replace high-enriched uranium (HEU), the middle layer has atomized U(Mo) fuel particles dispersed in a matrix of pure Al or Al alloy. A schematic cutoff view of the dispersion fuel plate is shown in Figure 1. The development of U-Mo dispersion fuels is a part of a global effort on nuclear non-proliferation, and these LEU fuels are being developed by the U.S. Reduced Enrichment for Research and Test Reactors (RERTR) program [1]. A big part of the development of LEU fuels has involved using the Advanced Test Reactor (ATR) at Idaho National Laboratory (INL) to test different fuel types to investigate irradiation performance.

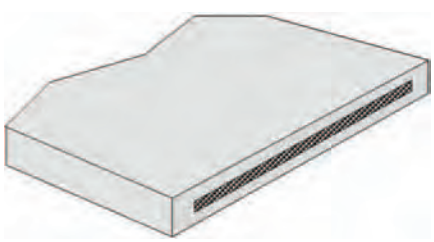

Figure 1. *A schematic of cutoff view of a dispersion fuel plate showing U(Mo) fuel particles dispersed in Al alloy matrix in the middle layer.*

The RERTR-6 experiment with 19.7% enriched uranium fuels was the first to test dispersion fuels with Si-containing Al alloy matrices [2]. Silicon is added to the matrix of a U-Mo dispersion fuel to enable the formation of a stable U-Mo/matrix interaction layer that is expected to behave well during irradiation. Similar interaction layers in U-7Mo dispersion fuels with only Al as the matrix do not exhibit good irradiation performance [3]. Transmission electron microscopy (TEM) characterization of the layers in an irradiated U-7Mo/Al dispersion fuel showed that the interaction layer that was present around the U-7Mo fuel particles was amorphous, without stable gas bubbles [4].

In order to investigate the performance of U-7Mo/matrix interaction layers in an irradiated U-7Mo/Al-2Si fuel plate, TEM characterization was performed on a sample taken from fuel plate R2R010, which was irradiated in ATR as part of the RERTR-6 experiment. Characterization of the same fuel plate using scanning electron microscopy (SEM) was reported by Keiser [5].

Experiment

For the RERTR-6 experiment, fuel plates were tested to medium burn-up under moderate neutron flux and temperature conditions. The calculated peak temperature for the plate R2R010 at fuel-plate midplane was 109°C, as determined using the PLATE fuel performance code [6]. A TEM sample was prepared from a 1.0-mm-diameter cylindrical sample (length ~1.4 mm) taken from the high-flux side of the fuel plate in a hot cell by a punching method described elsewhere [7]. The local irradiation conditions for the sample taken from this side of R2R010 resulted in average fission density, average

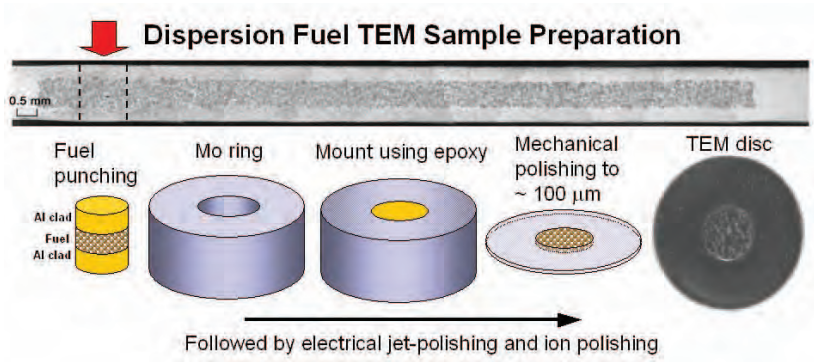

Figure 2. *Schematics of TEM sample preparation from dispersion fuel plate.*

fission rate, and peak heat flux values of approximately 4.5×10^{27} f·m^{-3}, 3.8×10^{20} f·m^{-3}·s^{-1}, and 1.48×10^{6} W·m^{-2}, respectively [5]. In INL's Electron Microscopy Laboratory, the sample was glued inside a 3.0-mm-diameter Mo ring using epoxy and mechanically wet-polished from both sides down to ~100 μm thickness inside a glove-box. The disc sample was followed by jet electropoling and, finally, ion polishing to perforation. Figure 2 shows the major steps in TEM sample preparation. The finished TEM sample was then characterized using a JEOL2010 TEM operated at 200 KV.

Characterization of the U-7Mo fuel particles

It was observed that the U-7Mo fuel particle remains in crystalline gamma phase (bcc) after irradiation. TEM bright-field images and the selected-area diffraction (SAD) pattern of a U-7Mo particle in the R2R010 sample are presented in Figure 4, showing the bubble superlattice at different magnifications with bcc metal oriented at zone [011]. A slightly under-focus in the bright-field imaging enhances the contrast of these three-dimensionally-ordered bubbles. The average size and standard deviation of the fission gas bubbles were measured to be ~3.5 ± 0.4 nm. The plane spacing for "A" and "B" for bubble superlattice measured from bright-field image are 5.75 nm and 6.55 nm, respectively. The corresponding plane spacing estimated from the satellite spots are 5.88 nm and 6.39, respectively. The plane spacing measured from bright-field image and the satellite spots are consistent within less than 2.5% relative error. Bubble superlattice is observed as a general microstructural feature in all transparent crystalline areas in U-7Mo fuel particles. The oxide rings in the SAD pattern are evident. The intensity of the oxide rings varies depending on the location, tilt, and orientation of the U-7Mo fuel particle. Morie fringes as a result of surface oxides are visible in the images at high magnification.

Bubble superlattice imaged with U-7Mo oriented at zone [001], the SAD pattern showing the corresponding satellite spots, and a schematic showing structural relationship between bcc base metal and fcc superlattice of fission-gas bubbles are shown in Figure 5. The plane "C" spacing measured from the bright-field image and estimated from the SAD satellite spots are 5.72 nm and 5.53 nm, respectively. The plane spacing measured from bubble images for "A" and "C" is in excellent agreement (5.75 nm vs. 5.72 nm). Some relatively large fission-gas bubbles (>100

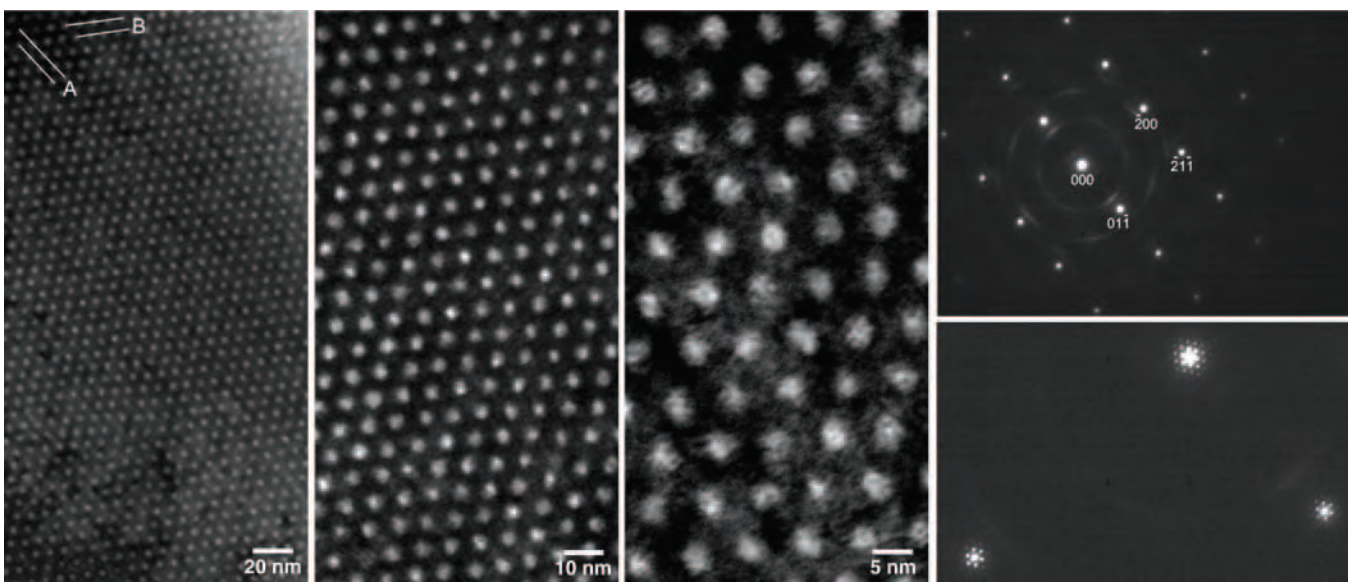

Figure 3. *TEM images showing the superlattice of fission gas bubbles observed in a U-7Mo particle of bcc structure orientated at zone [011]. The selected area diffraction (SAD) patterns showing rings due to oxides formed at the U-7Mo fuel particle from sample preparation. An enlarged view of the SAD pattern showing the satellite spots due to the bubble superlattice.*

nm) were observed in some areas of U-7Mo particles. Based on SEM analysis that has been performed on irradiated RERTR-6 fuel plates, relatively large fission gas bubbles can be observed at the grain boundaries of U-7Mo particles [8].

Characterization of the U-7Mo/ matrix interaction layer

A TEM micrograph showing the interaction layer between the Al-2Si matrix and the U-7Mo fuel particle is presented in Figure 5 (a). The SAD pattern in the inset shows that the interaction layer is amorphous. Measurements of the diffuse ring radii from ten different locations in the sample indicate an average nearest neighbor distance of approximately 0.251 ± 0.002 nm. Compositional analysis was performed in different areas of the interaction layers to determine the variability of the Si content within the layers. Figure 5 (b) shows the areas within the interaction layer where compositional analysis was performed. Tables 1 and 2 enumerate the results of this analysis. From this data, it can be seen that there is fluctuation in the Si content within the interaction layer, along with the U, Mo, and Al. The highest concentrations measured in the interaction layer for U, Mo, Al, and Si were approximately 19, 9, 90, and 12 at%, respectively. These values appear reasonable regardless of the effect of high radiation background on the EDS detector.

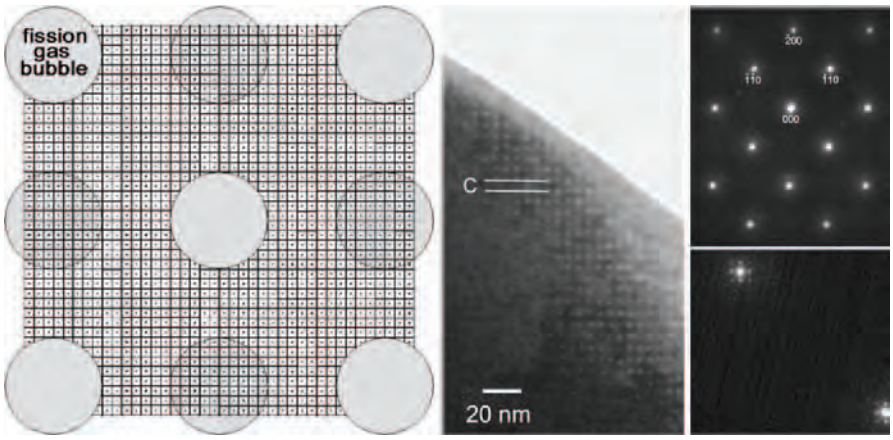

Figure 4. *Superlattice of fission gas bubbles observed in U-7Mo fuel particle of bcc structure oriented at zone [001]. An enlarged view of SAD pattern showing the satellite spots as a result of bubble superlattice. A schematic showing structural relationship between bubble superlattice and bcc base metal oriented at zone [001].*

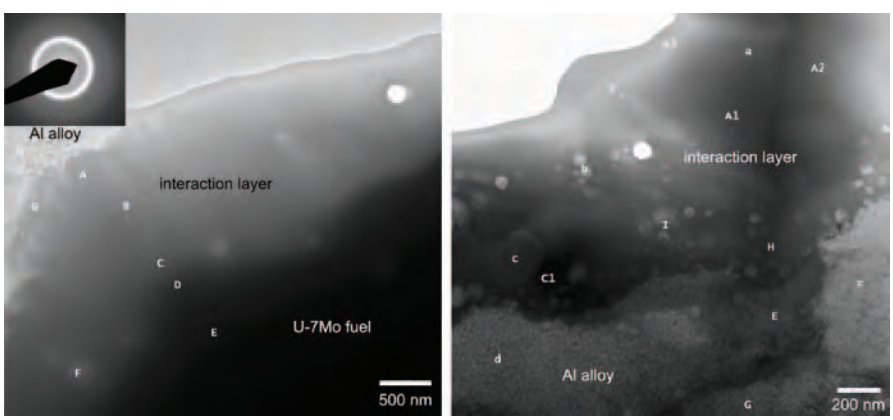

Figure 5. *TEM micrograph shows (a) the fuel, interaction layer, and Al alloy matrix with labels indicating where the EDS measurements were performed (see Table 1). The inset on (a) shows the SAD of FMI indicating its fully amorphous character; (b) shows locations near the interface of interaction layer and Al-alloy matrix where composition analysis was performed (see Table 2).*

***Table 1**. Measured compositions, in at.%, at various locations shown in Figure 5 (a).*

Spot	Al	Si	Mo	U
A	77.8	11.4	1.9	8.9
B	66.9	12.1	4.7	16.3
C	68.7	5.1	6.9	19.3
D	40.1	3.8	12.1	44.0
E	20.9	0	23.9	56.7
F	50.7	4.4	8.8	36.0
G	84.1	7.3	0	9.7
H	93.7	6.0	0	0.2

***Table 2.** Measured at.% at various locations in the interaction layer shown in Figure 5 (b).*

Spot	Al	Si	Mo	U	Zr
A1	78.2	9.9	2.5	9.4	—
A2	74.5	9.2	5.5	10.7	—
A3	75.4	8.9	4.8	10.9	—
b	79.6	8.4	3.0	8.9	—
c	93.8	4.7	0.7	0.7	—
C1	85.5	5.5	3.0	3.4	2.6
d	91.2	7.2	0.7	0.2	0.8
E	91.6	5.2	1.1	0.2	1.7
F	91.8	6.3	0.6	0.3	1.0
G	90.6	7.8	0.6	0.2	0.8
H	87.9	6.8	2.2	0.4	2.7
I	89.7	5.6	2.1	2.6	—
J	82.8	4.2	3.3	9.7	—

Discussion

With respect to the observed crystallinity of the γ-phase U-7Mo particles and the presence of an ordered superlattice structure of fission gas bubbles, the TEM characterization results from this work showed good agreement with what was reported for irradiated U-7Mo dispersion fuel samples by Van den Berghe et al. [4]. Overall, the U-7Mo remained γ-phase and did not become amorphous during irradiation. The average size of the fission gas bubbles in bubble superlattice in U-7Mo fuel was ~3.5 nm. The good agreement between the plane spacing measured from bright field image and that estimated from the satellite spots verifies that the observed satellite spots are the result of bubble superlattice that is coherent with a U-7Mo bcc structure. The relationship between crystalline orientation of fuel particle, the image of bubble superlattice, and the satellite spots from SAD patterns of zone [011], [001], and [111] indicates that bubble superlattice has an fcc structure oriented parallel to U-7Mo bcc lattice. Bubble superlattice constant is estimated to be ~ 11.5 nm, two times the plane "A" spacing in Figure 4, as expected. Although radiation-induced superlattices of voids and helium bubbles are observed from many works [9-14], the first observation of a fission gas bubble superlattice was only reported very recently [4].

The concentration of the three dimensionally ordered fission gas bubbles is estimated to be 2.63×10^{24} bubbles/m^3 and a volume fraction of approximately 6.0%. Considering the fission density in this work is three times that reported by Van den Berghe et al. [4], the larger bubble size (3.5 nm vs. ~2 nm) and volume fraction (6.0% vs. 1.4%) of the bubble superlattice in this work is likely due to the difference in fission density. The observed finely distributed bubble superlattice is believed to play an important role in the delay of the breakaway swelling. Fission gas retention in U-7Mo solution or lattice defects is expected to be small due to insolubility of Xe and Kr atoms. The formation of a stable bubble superlattice and a uniform growth of bubble size is probably the most effective mechanism to accommodate production of the insoluble Xe and Kr fission gaseous atoms in the U-7Mo fuel particles without causing severe fuel swelling.

Considering that the bubble superlattice constant is 33.5 times that of U-7Mo bcc structure, the nucleation mechanism for fission-gas bubble superlatice is not clear and is expected to be more complex than bubble nucleation in random distribution. Once nucleated, the bubble superlattice appears stable, and bubble size grows as fission density increases. The stable bubble superlattice and lack of bubble coalescence suggest that the surface energy is not a controlling factor in the development of the bubble superlattice in U-7Mo fuel particles. It is believed that small bubbles can maintain high gas pressure and store gas more efficiently than large ones [15].

The presence of large fission-gas bubbles (> 100 nm) in U-7Mo fuel particles suggests that the capacity of fission gas retention in the stable bubble superlattice may be reaching to its limit at the specified fission density. As the fission density further increases, it is anticipated that the large fission bubbles will continue to form and grow while the superlattice structure of fine fission-gas bubbles will be destroyed

before the interlinking of bubbles occurs. A sophisticated modeling of the evolution of bubble superlattice is needed to fully account for the effect of microstructural development on fuel swelling behavior.

The Si-rich interaction layers that originated between the U-7Mo particles and the Al-2Si matrix during fuel fabrication and contained crystalline phases [16] have become amorphous during irradiation. This is analogous to the irradiated U-7Mo/Al dispersion fuel reported by Van den Berghe et al. [4] where the interaction layer was also found to be amorphous. The estimated average distance of the nearest neighbors from the diffuse ring in Figure 5 is 0.251 nm, slightly higher than the value of 0.239 nm reported in [4]. The ~5% increase in the average nearest neighbor distance may be related to the cluster expansion by the presence of Si or by the more effective trapping of individual fission gas atoms in the amorphous interaction layer promoted by Si participation.

The EDS measurements from this work and previous work on SEM characterization of the same fuel sample with element mapping indicate the presence of Xe gas in the interaction layers [5]. One speculation is that these fission gases may have been retained in the layer as individual gas atoms or very small fission-gas bubbles (< 2 nm) up to moderate burnup. For irradiated U-7Mo dispersion fuels with pure Al as the matrix, the fission-gases seem to have a greater tendency to migrate through the interaction layer during irradiation to the interaction layer/matrix interface where they can agglomerate into large pores that can ultimately interconnect and cause failure of a fuel plate.

Although the EDS signal for a highly radioactive TEM sample has a high background noise, it was found that composition information can still be extracted from this sample of high β-ray and relatively low γ-ray radioactivity. The EDS measurements suggest that the areas of the interaction layers with the fewest observable fission-gas bubbles were also the most enriched in Si. The presence of Si in the amorphous interaction layer seems to affect certain properties of the material (e.g., viscosity) such that there is a propensity of the layer to retain the fission gases. Si atoms in the interaction layer may possibly occupy the relatively open volume sites. Another possibility is that Si may enhance the bonds between the atoms in the cluster. Both of these effects are likely to reduce the mobility for fission-gas atoms. Hofman [17] proposes that for U-Si fuels, which also go amorphous during irradiation, the additional Si bonds in U_3Si_2, relative to U_3Si, results in an improvement in irradiation performance. These additional bonds reportedly have a large effect on the amount of free volume in the material, which affects the diffusion property of the fuel and hence the fission-gas diffusivity and swelling behavior. For the U_3Si_2, which behaves well during irradiation, the increase in free volume during amorphization is negligibly small, and for U_3Si, which behaves poorly during irradiation, the increase in free volume during amorphization is relatively large. This means that just because a material goes amorphous, it is not guaranteed that there will be a large swelling increase unless there is a significant increase in free volume.

For the case of the Si-containing interaction layers in fuel plate R2R010, the Si may be having a similar effect as it did for the U-Si fuels. For areas of the interaction layers where the Si content is relatively high, the amount of free volume increase is small when the material goes amorphous during irradiation, and for cases where the Si content is relatively low, the free volume increase is larger, and the fission gas bubbles become increasingly mobile and can grow to relatively large sizes. In the R2R010 punchings that were analyzed using SEM [5], it was actually observed that the fission-gas bubbles significantly increased in size in some interaction layer regions where the Si concentration was relatively low. This would suggest that the properties of the interaction layer had changed because of the lower amount of Si (perhaps the larger free volume), which probably resulted in a lower viscosity of the amorphous material, an increase in the mobility of fission gases, and an increase in growth of the bubbles. Due to small thickness of interaction layer (typically several mm) and the submicron-scale local fluctuation of Si content, nanohardness measurements on the interaction layers of a SEM sample from the same irradiated fuel plate may be needed to verify the Si effect on viscosity.

Conclusions

Based on TEM characterization of a U-7Mo/Al-2Si dispersion fuel plate irradiated to moderate burnup in the RERTR-6 experiment, the following conclusions can be drawn:

1. U-7Mo fuel particles irradiated to medium burnup retain their crystallinity and contain small fission gas bubbles distributed on a three-dimensionally ordered superlattice. The bubble superlattice has an fcc structure coherent with the U-7Mo bcc lattice.

2. The Si-rich interaction layers that originally developed around U-7Mo particles during fuel plate fabrication become amorphous during irradiation. These layers exhibit stable irradiation behavior.

Acknowledgments

Acknowledgment is given to the INL Hot Fuel Examination Facility staff for producing the punching sample from fuel plate R2R010. This work was supported by the U.S. Department of Energy, Office of Nuclear Materials Threat Reduction (NA-212), National Nuclear Security Administration, under DOE-NE Idaho Operations Office Contract DE-AC07-05ID14517. Accordingly, the U.S. Government retains a nonexclusive, royalty-free license to publish or reproduce the published form of this contribution, or allow others to do so, for U.S. Government purposes.

This information was prepared as an account of work sponsored by an agency of the U.S. Government. Neither the U.S. Government nor any agency thereof, nor any of their employees, makes any warranty, express or implied, or assumes any legal liability or responsibility for the accuracy, completeness, or usefulness of any information, apparatus, product, or process disclosed, or represents that its use would not infringe privately owned rights. References herein to any specific commercial product, process, or service by trade name, trademark, manufacturer, or otherwise, does not necessarily constitute or imply its endorsement, recommendation, or favoring by the U.S. Government or any agency thereof. The views and opinions of authors expressed herein do not necessarily state or reflect those of the U.S. Government or any agency thereof.

References

1. D. Wachs, D. Keiser, M. Meyer, D. Burkes, C. Clark, G. Moore, J. Jue, M. R. Finley, T. Totev, G. Hofman, Proc. of GLOBAL 2007, Boise, ID, September 9-13, 2007
2. C. R. Clark, S. L. Hayes, M. K. Meyer, G. L. Hofman and J. L. Snelgrove, Transaction of RRFM 2004, Munich, Germany, March 2004. http://www.euronuclear.org/pdf/RRFM-2004-Transactions.pdf, p41
3. H. J. Ryu, J. M. Park, C. K. Kim, Y. S. Kim, and G. L. Hofman, „J. Of Phase Equilibrium and Diffusion, Vol. 27, No. 6 (2006) 651-658.
4. S. Van den Berghe, W. Van Renterghem, A. Leenaers, J. Nucl. Mater., 375 (2008) 340-346.
5. D. D. Keiser, Jr., A. B. Robinson, J. F. Jue, P. Medvedev, M. R. Finley, Proceedings of RRFM 2009, Vienna, Austria, March 23-25, 2009, http://www.euronuclear.org/meetings/rrfm2009/transactions/rrfm09-transactions.pdf, p99
6. Y. S. Kim, H. J. Ryu, G. L. Hofman, S. L. Hayes, M. R. Finley, D. M. Wachs, G. S. Chang, RERTR 2006, Cape Town, South Africa, http://www.rertr.anl.gov/RERTR28/PDF/S15-1_Kim.pdf
7. J. Gan, D. D. Keiser, D. M. Wachs, B. D. Miller, T. R. Allen., Hot Laboratories and Remote Handling Conference (HOTLAB 2008), Kendal, England, September 22-23, 2008.
8. D. D. Keiser, Jr., J. F. Jue, J. Gan, A. B. Robinson, B. D. Miller, RERTR 2008, Washington D. C.
9. K. Krishan, Invited Review Article: "Ordering of Voids and Gas Bubbles in Radiation Environment", Radiat. Eff., 66, (1982) 121-155
10. P. B. Johnson and D. J. Mazey, J. Nucl. Mater., 93 and 94 (1980) 721-727.
11. P. B. Johnson, A. L. Malcolm, and D. J. Mazey, Nature, 329 (September 24, 1987) 316-318.
12. P. B. Johnson and D. J. Mazey, J. Nucl. Mater., 218 (1995) 273-288.
13. F. E. Lawson and P. B. Johnson, J. Nucl. Mater., 252 (1998) 34-42.
14. P. B. Johnson and F. E. Lawson, Nucl. Instrum. Methods Phys. Res., Sect. B, 243 (2006) 325-334.
15. G. L. Hofman, J. Nucl. Mater., 140 (1986) 256-263.
16. D. D. Keiser, Jr., J. Gan, J. F. Jue, and B. D. Miller, "Electron Microscopy Characterization of an As-Fabricated Research Reactor Fuel Plate Comprised of U-7Mo Particles Dispersed in an Al-2Si Alloy Matrix", Submitted to Materials Characterization.
17. G. L. Hofman and Y. S. Kim, Nucl. Engr. and Tech., 37 (2005) 299-308.

JIAN GAN (BS, 1982 in Physics, Fudan University in China; MS, 1992 in Physics, Central Michigan University; and PhD, 1999 in Nuclear Engineering, University of Michigan) is a research scientist in the Fundamental Fuel Properties Department at INL. He has been actively working in the research on irradiation effects in materials and nuclear fuels for more than 15 years, with a focus on investigating microstructural development under irradiation using transmission electron microscopy.

DENNIS D. KEISER, JR. (B.S., 1987, and M.S., 1989, Metallurgical Engineering, University of Idaho; and Ph.D., 1992, Materials Engineering, Purdue University) is a member of the Fuel Performance Department at Idaho National Laboratory. He has over twenty years of experience researching different issues related to the performance of nuclear fuels and materials. His current research relates to the development of low-enriched fuels for application in research and test reactors, to developing a better understanding of the diffusion behavior of fuel and cladding components in irradiated fuels, and to determining the microstructural development of fuels and materials during irradiation.

DANIEL M. WACHS (BS, 1995, Mechanical Engineering, MS, 1997, Nuclear and Mechanical Engineering, Oregon State University; PhD 2000, Mechanical Engineering, University of Idaho) is a member of the Fuel Performance and Design Department at the INL. He is currently the National Technical Director for the RERTR Fuel Development Program. His current research interests and technical background include irradiation testing of nuclear fuel and materials, thermal-hydraulic testing and analysis, and reactor system component design for research reactors and liquid metal cooled fast reactors.

ADAM ROBINSON (BS, 2004; MS, 2006 Nuclear Engineering; MS, 2006, Material Science, Oregon State University) is a nuclear fuels engineer in the Fuel Performance and Design Department at INL. His research for the past 4 years has focused on the post irradiation examination of high density metallic fuel for research and test reactors as part of the Global Threat Reduction Initiative.

BRANDON D. MILLER (BS, Mechanical Engineering , 2003, Idaho State University, MS, Nuclear Engineering 2007, University of Wisconsin-Madison) is a research scientist in the Basic Fuels Properties and Modeling Department at the INL. His research efforts over the past 3 years have been focused on irradiation effects on the microstructure of nuclear fuels using transmission electron microscopy.

The Steady State Swelling Rate Of Ferritic And Ferritic/Martensitic Alloys

B.H. Sencer

Ferritic and ferritic/martensitic steels play a significant role as structural components in some nuclear reactors or accelerator-driven neutron generation devices. The effects of irradiation on these components are usually deleterious to the material properties. As a result, radiation degradation including embrittlement, corrosion, and dimensional instability arising from phase changes, creep, and void swelling are prominent features of any design or safety analysis.

It is well known that ferritic/martensitic steels develop much less void swelling than do austenitic steels during neutron or charged particle irradiation. The prevailing assumption is that the steady-state swelling rate of body-centered cubic (BCC) steels is inherently much lower than that of face-centered cubic (FCC) steels by at least a factor of ten or more. However, it is shown here that that this perception is incorrect, with BCC steels having steady-state swelling rate perhaps only a factor of two to four lower. The irradiation creep compliance of the two types of alloys also differs by only a factor of about two. Additionally, the lower swelling observed in BCC steels seems to be a consequence of a much longer transient regime prior to the onset of steady-state swelling.

This critique will focus on a series of papers that established this misperception. Some independent research was performed to demonstrate some support for the revised concept.

Introduction

Void swelling has been a subject of intense interest, especially for fast breeder reactors operating at high temperatures and high neutron-induced damage rates. At the current time, for instance, it is usually assumed that the steady-state swelling rates of BCC and FCC iron-based alloys are different, perhaps by a factor of 10–20, and must therefore reflect some microscopic property dependent on their different crystal structures. In fact, however, the confidence underlying this assumption has recently been eroding. In particular, the perception that the generic BCC crystal structure confers an immunity on all BCC metals and alloys against the high swelling rates characteristic of FCC metals and alloys was recently called into doubt when various vanadium binary alloys were found to swell at large rates, sometimes in excess of those observed in FCC systems [1,2]. This suggests that chemical and segregation processes can easily overwhelm crystallographic influences or, perhaps even more importantly, that the crystallographic influence was not as large as previously envisioned.

This paper will show that the differences in steady-state swelling rates of iron-based FCC and BCC alloys are not so large, with the observed difference in swelling reflecting primarily the influence of composition, microchemical evolution, dpa rate, and temperature history to dominate the duration of the transient regime of swelling.

Background and Literature Review

Both austenitic and ferritic/martensitic steels play a significant role as structural components in some type of nuclear reactors or accelerator-driven neutron generation devices. One of the effects of irradiation on these components is the dimensional instability that is caused by void swelling. Hence, understanding and predicting the void swelling becomes an important need.

An approach to predict swelling in austenitic stainless steels has been proposed by Garner based on results obtained for simple Fe-Ni-Cr ternary alloys [3]. The ternary alloy results can be interpreted to establish that the steady state swelling rate is ~1%/dpa and that swelling differences among various irradiation alloys and conditions arise from differences in the onset of swelling. Swelling incubation time is increased with increases in nickel content or temperature and with decreases in chromium content.

Ferritic and ferritic/martensitic alloys also appear to be attractive as nuclear materials due to their high swelling resistance. The maximum swelling rate of ferritic/martensitic alloys has been proposed by Gelles to be 0.06%/dpa over the temperature range 400–450°C. Gelles generated data on Fe-Cr alloys ranging from 3 to 18% Cr. According to Gelles, the swelling rate of ferritic alloys is dependent on both composition and temperature. He found

that a major influence of the chromium level lies in the duration of the incubation period, with peak swelling arising as a consequence of the highest swelling rate occuring at ~10% Cr. The formation of the α' phase was thought by Gelles to be associated with the reduction in swelling at higher Cr levels.

The following section will focus on the swelling of pure iron and simple binary Fe-Cr alloys, as observed by researchers other than Gelles.

Swelling of pure iron and Fe-Cr alloys

If Cr additions influence the transient regime of swelling, it would be useful to observe swelling of pure iron. For that reason, by extrapolating downward from the 3% Cr level used in the studies reviewed in this critique paper, it would be reasonable to conclude that pure iron would have low swelling and, therefore, a low swelling rate. This conclusion is probably misleading, however, even though it would require another inflection point in the swelling behavior in the 0–3% Cr range to yield significant swelling for pure iron.

There was one charged particle bombardment experiment that included both Fe and Fe-Cr alloys. The results of this Ni+ ion bombardment experiment are shown in Figure 1, and, at first glance, appear to support the assumption of low swelling in pure Fe. Johnston et al. [4], however, were rather concerned that the use of Ni+ instead of Fe+ ions may have distorted the result since this deposited a Gaussian distribution of nickel with a maximum concentration of 2.7%, peaking just 200 nm behind the position of peak damage. A smaller amount, 1.5% Ni, was deposited at the peak damage region, but it is expected that the irradiation would have somewhat broadened this profile. Whatever the time-averaged nickel distribution over the irradiated volume, it was not insignificant, and there was some concern that it would have a strong effect on the swelling.

To investigate the effect of the deposited nickel, a second and more limited series of Fe-2Ni-Cr alloys were irradiated by Johnston. In going from ~2% final deposited nickel to ~4% total nickel there was a dramatic drop in swelling, as also shown in Figure 1. This implies that the addition of the first 2% Ni by deposition probably had a large effect to reduce swelling and raised the possibility that both Cr and Ni additions may strongly depress the swelling of pure iron.

The possibility of suppression of swelling in pure iron by Cr addition may be explored by examining several other experiments. Little and Stow showed that after neutron irradiation to 30 dpa of annealed pure iron and various Fe-Cr

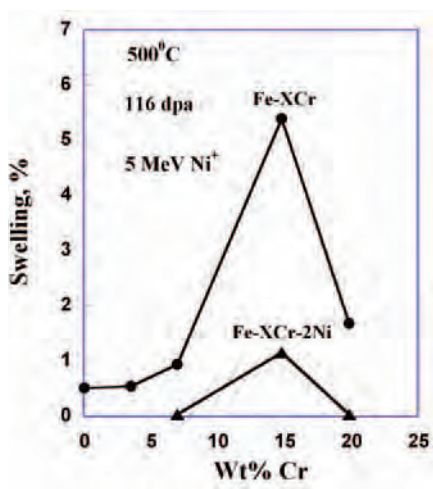

***Figure 1**. Influence of composition on ion-induced swelling of Fe-Cr alloys [4].*

alloys, the first 1% Cr addition depressed swelling strongly, as shown in Figure 2 [5]. The maximum swelling of annealed iron was not large, only ~1% at 30 dpa, but it illustrated the inflection behavior in the 0–3% range that was suggested earlier. The typical increase of swelling at Cr levels above 1% that was observed in other experiments was also observed in this study.

A similar inflection and suppression behavior was demonstrated by Horton et al. in "triple-beam" (D2+, He+, Fe+) irradiation to 10 dpa of annealed Fe and two Fe-Cr alloys at 800K, but the levels of swelling were small (0.22% in Fe, 0.0% in Fe-5Cr, and 0.16% in Fe-10Cr) [6]. In a related study to higher doses, Horten and Bently produced ~2.5% swelling in Fe-10Cr at 100 dpa and 850K [7], demonstrating that binary alloys could eventually reach significant levels of swelling during ion bombardment.

Another more graphic suppression result was provided by Ohnuki et al., who irradiated pure Fe and Fe-13Cr at 525°C to 118 dpa with 200 KeV C+ ions [8]. This produced large swelling, 14%, in Fe, but only <0.5% in Fe-13Cr. In this case, it appears that Fe can be induced to swell easily if the conditions are favorable. However, Ohnuki noted that there was considerable carbon addition during the irradiation leading to extensive formation of Fe_3C precipitates, suggesting that carbon can accelerate swelling at such high temperatures. This critique paper will demonstrate this possibility in the Experimental Breeder Reactor II (EBR-II) irradiation of Fe-12Cr and Fe-12Cr-0.1C alloys at 482–593°C and dpa levels of 74-131 dpa [9]. Swelling jumped from

0–1% to 6–10% simply by adding 0.1% C. This behavior strongly suggests the abrupt termination and shortening of a long transient period. Together, these results imply that both pure iron and Fe-Cr alloys have potentially high intrinsic swelling rates that are camouflaged by long transient regimes.

In general, most irradiations of annealed pure Fe by either neutrons or charged particles have yielded relatively small amounts of swelling and, therefore, do not admit the possibility of high steady-state swelling rates [10–14]. Neutron-induced swelling at relatively low exposure appears to peak at ~400°C [14], as shown in Figure 3, indicating a possible temperature dependence of the duration of the transient regime. While the temperature dependence appears to be pronounced in this latter study, it would take only a slight dependence at low dpa levels to produce such a sharp peak with temperature in these data.

There was an indication in an electron irradiation study by Kitajima et al. [11] that swelling at low temperatures can be significantly increased by cold-working. This is an important and previously overlooked clue since the effect of cold-working has not been studied in most pure metals, especially those with BCC structure.

In a study published recently by Porollo et al. [15], pure iron and various Fe-Cr alloys were irradiated in the BR-10 fast reactor, with the specimens in the ~10% cold-worked condition reaching dpa levels of 5.5–7.1 dpa at 400°C. As shown in Figures 4 and 5, pure cold-worked iron swelled ~3% at 6.2 dpa as confirmed by microscopy. As might be expected, the addition of 2% Cr to iron led to a dramatic suppression in swelling, but unexpectedly produced a large increase in the loop density. There was also a small peak in the swelling at 12% Cr, in agreement with the results of other studies.

The latter experiment suggests that cold-working of pure Fe led to an average swelling rate of 0.5%, only one-half that typical of FCC Fe-Cr-Ni alloys. If any transient was involved, the post-transient rate would be >0.5%/dpa. Such a finding begs for confirmation, and the group led by Porollo plans to examine in the near future a second discharge of this experiment at ~20 dpa.

Another experiment by Agapova et al. in the BOR-60 fast reactor at 460°C and ~37 dpa yielded 1.5% swelling in annealed pure iron and 1.0% swelling in 10% cold-worked iron [16]. In this higher-temperature case, cold-working did not accelerate swelling.

All of this suggests the possibility that the steady-state swelling rates of Fe and Fe-Cr alloys may eventually approach the rate of Fe-Cr-Ni alloys, at least within a factor of two. If this is the case, the large differences in total swelling for FCC and BCC alloys must be a consequence of the transient regime being much longer in the BCC metals. Johnston alluded to this possibility when he noted that Ni+ ion irradiation of Fe-15Cr yielded a large transient regime (≥100 dpa) with ~6 and ~21% swelling at 116 and 240 dpa, respectively [4]. This yields an average swelling rate of 0.12%/dpa between the two dpa levels, which "are not sufficient data points to say that a steady-state swelling rate has been achieved." This is a particularly important observation when it is considered that the steady-state swelling rates developed in 3 to 5 MeV Ni+ ion-bombardment experiments are known to be suppressed by approximately a factor of five due to the injected interstitial effect [17].

This conclusion concerning the injected interstitial effect was reached in an extensive comparison experiment between three ion bombardment groups (including Johnston's group) where it was shown that the Ni+ ion-induced swelling rate in annealed Fe-15Cr-25Ni was reproducible by all groups, but was only 0.2%/dpa [18]. This implies that the swelling rate of 0.12%/dpa in Fe-15Cr, observed by Johnston at 116–240 dpa, is at about half of that observed in the comparable FCC alloy. Although the swelling rate appears to be suppressed in both alloys by the injected interstitial effect, these results are again consistent with a possible difference of only a factor of two in the steady-state swelling rates of the two crystal structures.

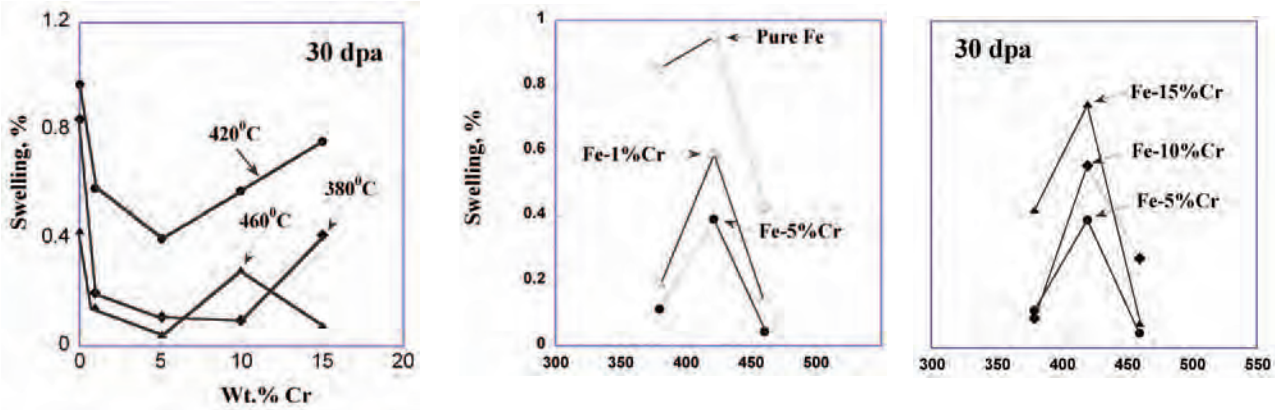

Figure 2. *Effect of chromium level and irradiation temperature of neutron-induced swelling of Fe-Cr alloys at 30 dpa in the DFR fast reactors [5].*

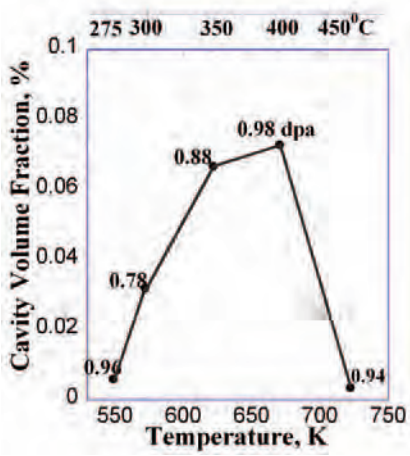

Figure 3. *Temperature dependence of pure iron at ~1 dpa in the ORR reactor [6].*

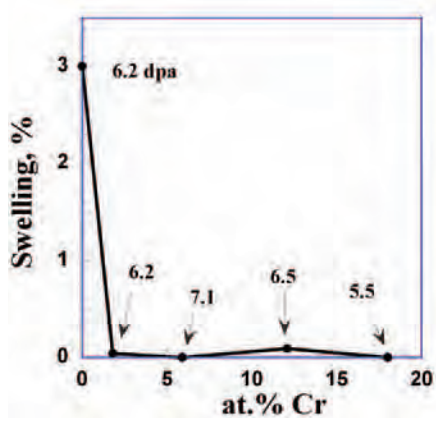

Figure 4. *Swelling observed in 10% cold-worked pure iron and from cold-worked Fe-Cr alloys in the BR-10 fast reactor at 5.5–7.1 dpa [15].*

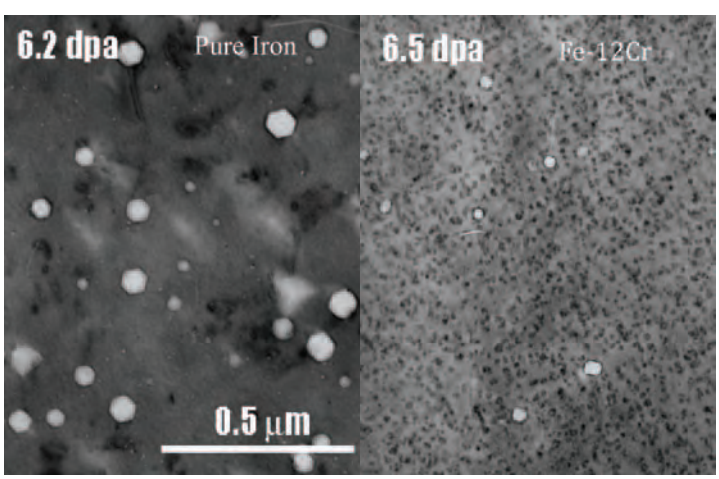

Figure 5. *Microstructure of pure iron and Fe-12Cr at ~6 dpa and 400°C [15].*

Irradiation creep

An increasing amount of irradiation creep data on ferritic steels, especially HT9, has recently become available [19–21]. There has also been better resolution of the influence of important variables such as crystal structure, helium/dpa rate, displacement rate, thermomechanical treatment, and composition on irradiation creep [19–26]. In summary, when the two most important creep coefficients, B_o (describing creep in absence of swelling) and D (describing swelling-enhanced creep) are evaluated from data on various commercial and developmental alloys, it appears that the D coefficient is essentially equal for FCC and BCC steels at ~0.6 x 10^{-2} MPa^{-1}, reflecting the crystal-independent physical relationship between creep and swelling, but the B_o coefficient of BCC steels appears to be about one-half that of FCC steels at ~0.5 x 10^{-6} MPa^{-1} dpa^{-1}. This conclusion is not as well supported as the conclusions drawn from comparison of the swelling rates, but it does imply once again that the defect production and aggregation mechanisms in BCC iron-based alloys may be only a factor of two different in net efficiency to create microstructural alteration with consequent changes in dimension. In general terms, both swelling and creep appear to be telling the same story concerning the effect of crystal structure in iron-based alloys.

Critique of swelling rate in Ferritic/Martensitic steel

The fact that ferritic and ferritic/martensitic (FM) steels develop much less swelling than austenitic steels during neutron or charged particle irradiation is a well-accepted assumption. The prevailing perception is usually that the steady-state swelling rate of BCC steels is inherently much lower than that of FCC steels by at least a factor of ten or more. An approach to predict swelling in austenitic stainless steels was proposed by Garner based on irradiation results for simple Fe-Ni-Cr ternary alloys [27]. There exists a near-universal steady-state swelling rate (~1%/dpa) for Fe-Cr-Ni alloys. The steady-state swelling rate of ferritic/martensitic steels was proposed by Gelles and coworker to be 10-20 times smaller than that of FCC Fe-Cr-Ni alloys ($\dot{S}_{\alpha/Martensite} \ll \dot{S}_{\gamma}$) [28-32]. The primary basis for this perception arises only from swelling data on binary Fe-Cr alloys published by Gelles et al. from irradiation conducted first in EBR-II [28-30] and later in FFTF [30,31]. Specimens of Fe-6, 9, and 12 wt.%Cr alloys were examined by transmission electron microscopy following irradiation at 400°C to 3.6×10^{22} n/cm^2, at 425°C to 4.3×10^{22} n/cm^2 and at 450°C to 2.8×10^{22} n/cm^2. As shown in Figure 6, the swelling rates in EBR-II of Fe-Cr alloys at 400-450°C appear to be low and to be dependent on both composition and temperature. The peak swelling rate occurs for the 12Cr specimen, and the maximum swelling rate was ~0.06%/dpa [28-30]. Based only on FFTF data at 200 dpa (6.98×10^{22} n/cm^2, E>0.1MeV) at 420°C for Fe-9Cr [33], Gelles concluded the maximum average rate in FFTF was ~0.1%/dpa, not significantly larger than that observed in EBR-II, but still ten times smaller than that of FCC alloys over the same dpa range.

It is important to note here, however, that the dpa assignments for the BCC Fe-Cr alloys irradiated at 400, 425, and 450°C are incorrect. This error was recently discovered in another related experiment [3]. Figures 7 and 8 show the impact of correcting the dpa levels, with the magnitude of the correction being different at each irradiation temperature. The maximum average swelling rate at 425°C is observed to dramatically increase.

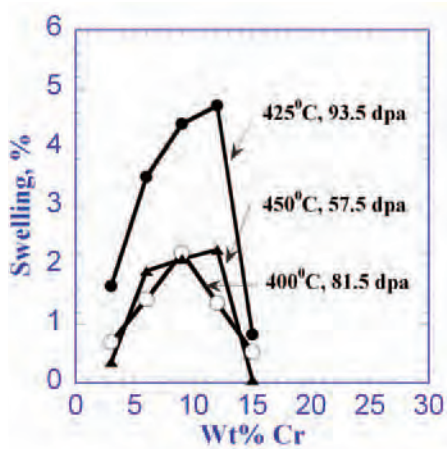

- Originally assigned dpa levels are too large.

T, °C	dpa
400	81.5→35.1
425	93.5→48.3
450	57.5→34.8

Figure 7. *Dependence of swelling reported by Gelles in Fe-Cr alloys on chromium level, temperature, and dpa in EBR-II for Fe-Cr alloys, showing corrections of dpa assignments [3].*

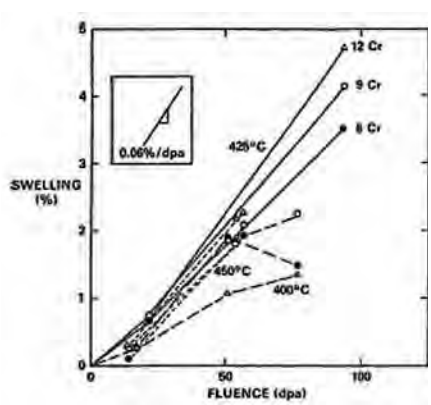

Figure 6. *Published data of Gelles on the swelling of Fe-Cr binary alloys in EBR-II [28-30].*

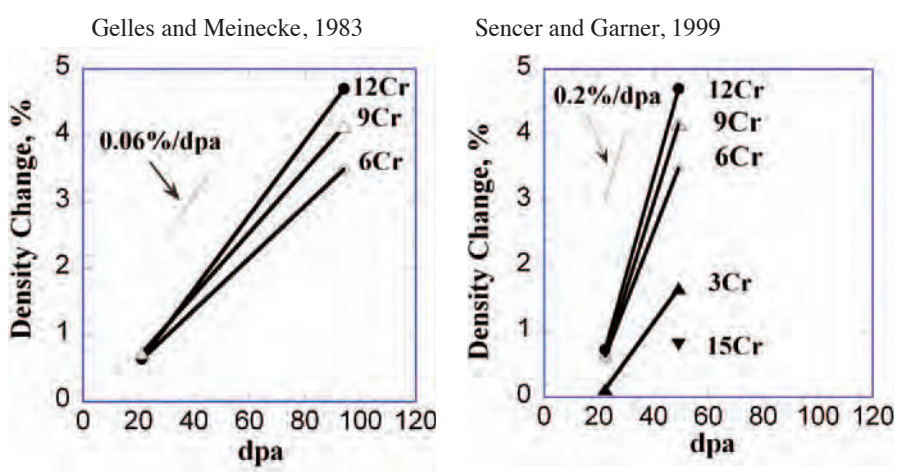

Figure 8. *Impact of dpa corrections on average swelling rate of Fe-Cr alloys at 425°C.*

Following the better-established trends observed in the EBR-II data on FCC Fe-Cr-Ni alloys, which were in the same experiment, the data can be grouped over a range of Cr levels and all three lower temperatures in Figure 9a and at higher temperatures in Figure 9b. It is now apparent that the swelling behavior of the BCC Fe-Cr alloys series closely parallels the behavior of FCC Fe-Cr-Ni alloys in the same experiment [27]. All data appear to behave as if they belong to one alloy being irradiated at one temperature. It is not clear, however, if the steady-state swelling rate has been reached in this experiment. The steady-state swelling rate is at least 0.2%/dpa and may be higher. At least one more datum would be required at higher exposure to assess the possibility that the rate was not still increasing.

Similar Fe-Cr data generated by Gelles et al. [31–33] in Fast Flux Test Reactor Facility Materials Open Test Assembly (FFTF-MOTA) to doses in the range 15–200 dpa are shown in Figure 10. The compositional dependence of swelling is essentially the same at all exposure levels. When plotted in comparison with the EBR-II data as shown in Figure 11a, it immediately becomes clear that while the transient regime in FFTF is much longer than in EBR-II, the post-transient behavior is remarkably similar, with the maximum swelling rates at least 0.2%/dpa. Notice that the major influence of chromium level lies in the duration of the incubation period with peak swelling arising as a consequence of the shortest transient regime at ~10% Cr. The formation of the α' phase is thought to be associated with the reduction in swelling at higher Cr levels [30, 33]. The question then arises whether commercial ferritic/martensitic

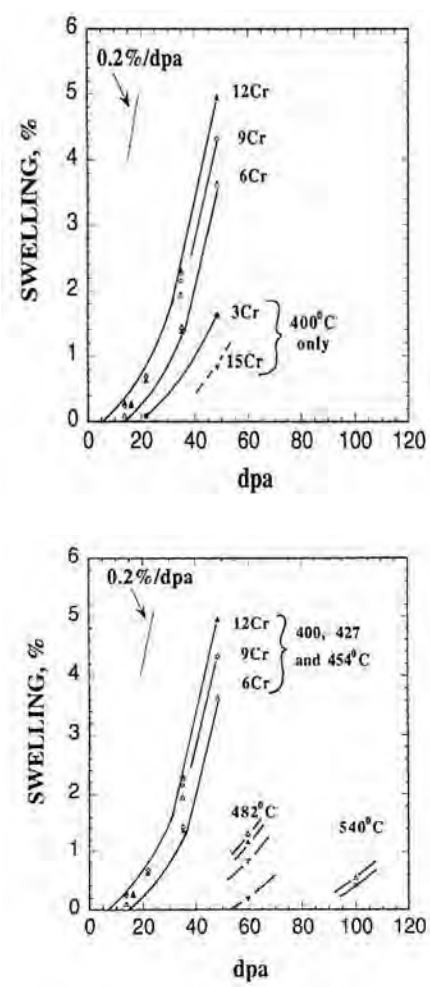

Figure 9. *Revised compilation of Fe-Cr data from EBR-II at all available temperatures, showing behavior similar to that observed in Fe-Cr-Ni alloys.*

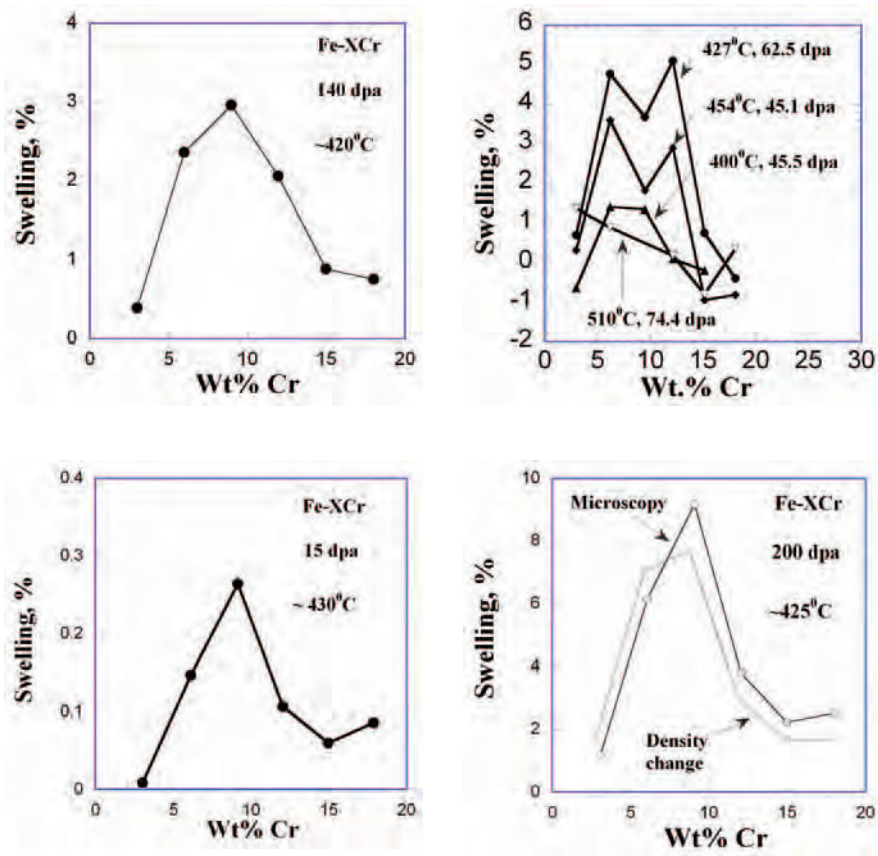

Figure 10. *Swelling of Fe-Cr alloys irradiated in FFTF-MOTA under active temperature control [31–33].*

stainless steels will also exhibit the same behavior as the Fe-Cr binaries. In general, most reported exposures for commercial steels never exceed 100–150 dpa and data usually exist at only one or two exposure levels. Therefore, the best comparison to answer this question is the swelling observed by Toloczko, Garner, and Eiholzer in HT9 (with 12% Cr) using pressurized tubes at ~400°C in FFTF-MOTA [19]. Seven dpa levels were involved in this experiment. These tubes resisted swelling for a long time, but swelled from ~1 to ~3% at 208 dpa over a stress range of 0–200 MPa [18] as shown in Figure 12. The alloy 9Cr-1Mo was also irradiated in this experiment and reached 2–3% swelling at 208 dpa. As shown in Figure 11b, both of these swelling ranges are relatively consistent with the Fe-(9, 12) Cr behavior shown in Figure 18a, with some additional influence of solutes to extend the transient. The dependence of swelling in HT9 on applied stress is yet another indication of the inherent instability associated with the end of the transient regime. Similar creep tube studies were conducted by Toloczko and Garner on various heats of HT9 irradiated side-by-side at ~400°C to 165 dpa [20,21]. These steels exhibited a heat-to-heat variability in the onset of swelling with an abrupt increase in swelling rate in the more swelling-prone heats at ~100 dpa, behavior which also agrees with that of comparable Fe-Cr alloys in FFTF and shown in Figure 11. The foregoing discussion thus leads us to the conclusion that typical solute-bearing ferritic/martensitic steels can exhibit long transient regimes of swelling, especially when irradiated under well-controlled temperature conditions, but eventually they will also swell at an accelerated rate of 0.2%/dpa and possibly greater.

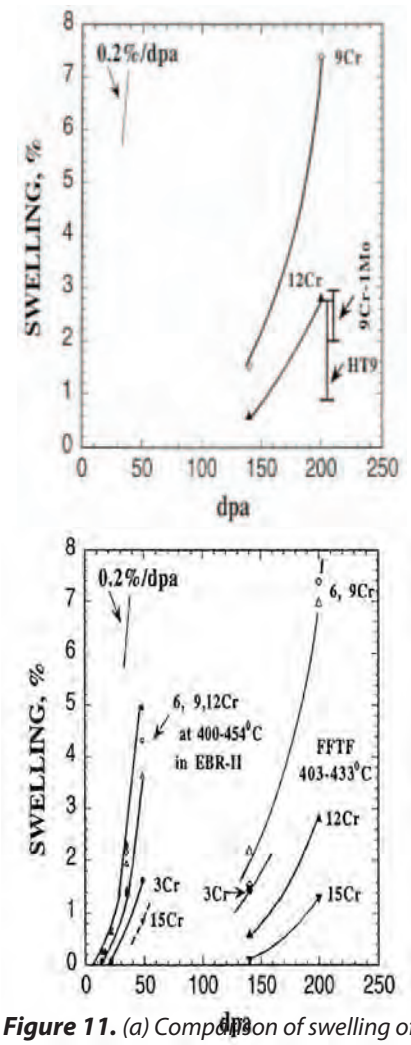

Figure 11. *(a) Comparison of swelling of Fe-Cr alloys in EBR-II and FFTF-MOTA. (b) Swelling observed in HT9 and 9Cr-1Mo in FFTF-MOTA [19–21].*

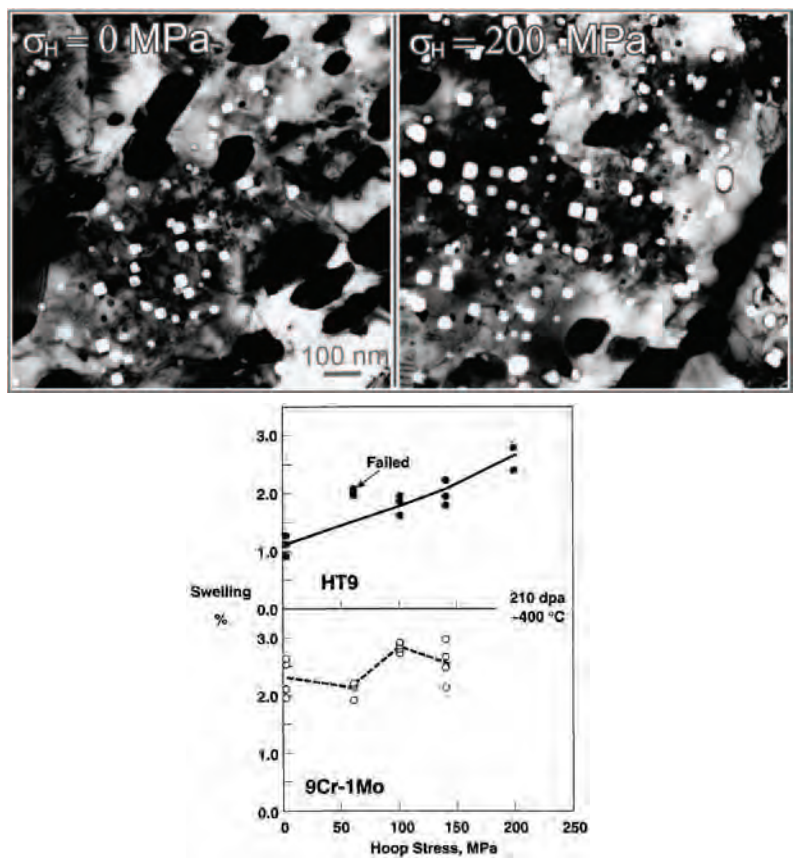

Figure 12. *(a) Voids observed in HT9 pressurized tubes irradiated in FFTF to 208 dpa at ~400°C; (b) Swelling observed in both HT9 and 9Cr-1Mo as a function of applied stress [19].*

New supporting data

As shown earlier, ferritic or ferritic/martensitic (FM) alloys exhibit at low temperatures (~<450°C) a steady state swelling rate of ~ 0.2%/dpa, according to our new analysis. It would be useful to have additional data to confirm this conclusion. In addition, it has been assumed that no significant swelling occurs at higher temperatures and little data has been collected at these temperatures. The following explores the evidence that will help determine if 0.2%/dpa is a valid estimate and also whether swelling occurs in ferritic alloys at higher temperatures. Therefore, the main objective of this section is to show that at high temperature (>450°C) ferritic alloys also swell, perhaps also at a steady state swelling rate of ~0.2%/dpa after a long period of transient regime. The available data on carbon and/or molybdenum modified ferritic alloys will also be reviewed to support the objective. These data come from two sources. The first is new data generated by Sencer and Garner from previously unanalyzed experiments in EBR-II. The second is from previously published data on solute-modified ferritic alloys by Gelles et al. [28-30].

The swelling behavior of FM alloys over a wide range of temperature is shown in Figure 13a and 13b as a function of %Cr addition after irradiation in the EBR-II reactor. These are previously unpublished data. Dose levels of 35 to 131 dpa were achieved in this experiment. The data in 4.1a were obtained in one experimental series where all specimens were in the reactor for the same time period. Each capsule operated at a given temperature and an associated dpa rate, reaching a dpa exposure that was specific to the temperature. The data shown in Figure 13b were obtained from a similar set of capsules that remained in the reactor for a longer period. Once again, the dpa rate and dpa level were specific to a given temperature. The temperature ranged from 400 to 650°C.

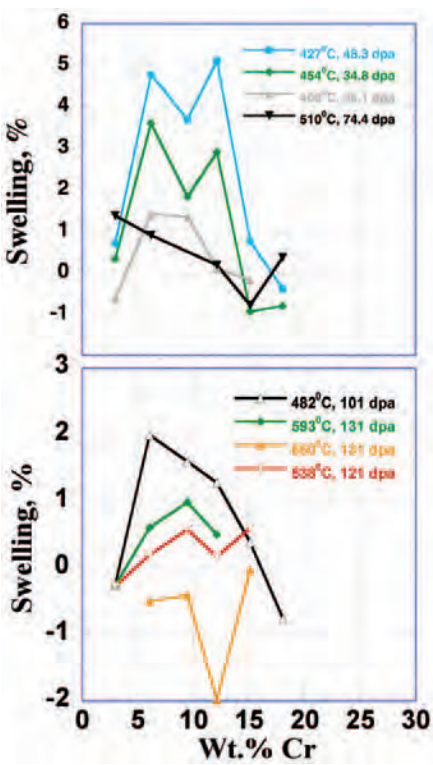

Figure 13. Swelling of simple binary ferritic alloys as a function of %Cr level. These are new data by Sencer and Garner that were not previously analyzed or published.

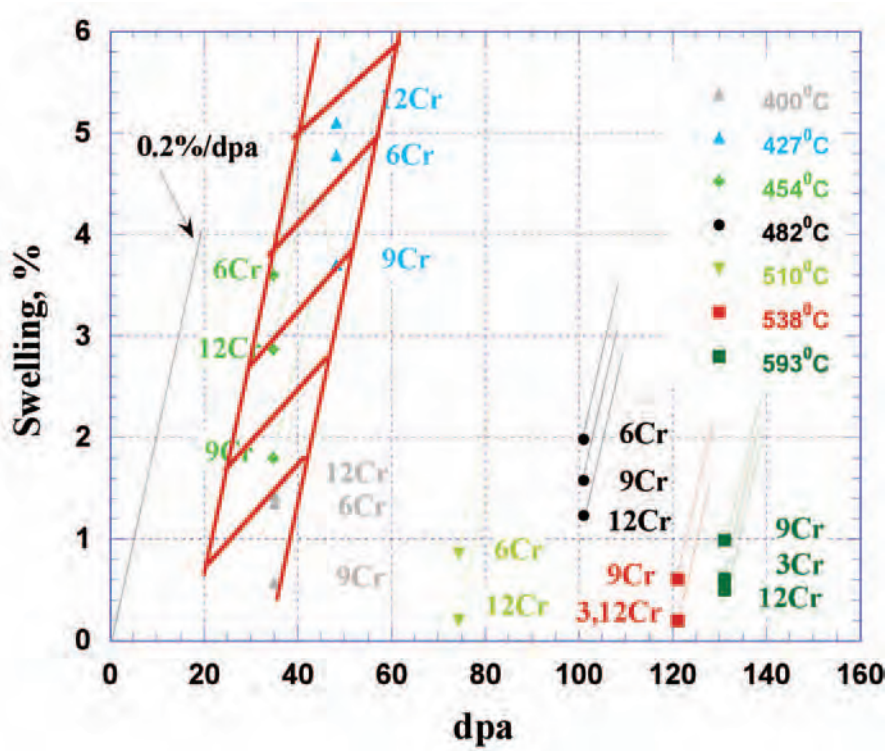

Figure 14. Swelling of ferritic alloys over a wide range of temperature as a function of dpa by Sencer and Garner, excluding the 6500C data, which exhibits negative swelling arising from the formation of the a' phase. These are the same data shown in Figure 13. Based on trends observed in section 3, it is assumed that swelling eventually proceeds at ~ 0.2%/dpa, at least for swelling in excess of 1%.

The sometimes M-shaped swelling behavior with Cr content is believed to be the result of the packing order of specimens in the small tubes containing the specimens, which spanned a fluence gradient along the packet (similar behavior was sometimes observed by Gelles, as shown in Figure 10.). This speculation cannot be confirmed, however. One can replot the swelling data of Figure 13 as a function of dpa as shown in Figure 14. The effects of flux and temperature on swelling can be seen in Figure 14.

Note that the data at 400 and 452°C can be described by a band with average slope of ~0.2%/dpa, which is similar to that observed in the revised data of Gelles in Section 3. Trend lines of slope 0.2%/dpa were drawn through the data at higher temperatures, based on the assumption that a similar swelling rate will eventually develop at these temperatures. There is no support at present for this speculation.

In general, the transient duration increases with temperature (see Figure 14), but there are several exceptions. The 454°C series and the 510°C series appear to be out of place with respect to the received temperature dependence, with smaller than expected transients. However, based on earlier data, it is expected that lower dpa rates lead to earlier swelling. As shown in Figure 15 and 16, the lower flux received at these two temperatures may possibly account for the earlier swelling, somewhat overwhelming the effect of the higher temperature.

Both carbon-modified and molybdenum-modified alloys were also included in the new data set. These alloys were included in the same irradiation packets as the Fe-Cr binary alloys. Carbon addition up to 0.2% suppresses swelling at relatively low temperatures (see Figure 17a). However, at higher temperatures, as seen in Figure 17b, carbon addition up to 0.1% dramatically increases swelling. Further addition of carbon up to 0.2% then suppresses the swelling again. Carbon addition appears to shorten the incubation period at higher temperatures so strongly that swelling levels approaching 10% were reached in this experiment. The high-temperature behavior of single binary alloys with and without carbon addition is shown in Figure 18 as a function of the dpa level. The assumed swelling rate of 0.2% is not so unreasonable in this case, since the average swelling rate over the entire irradiation dose is >0.1%/dpa at 510°C.

The swelling behavior of Fe-12Cr-0.1C alloys with molybdenum addition is shown in Figure 19. At low temperatures molybdenum addition somewhat suppresses the swelling (see Figure 19a), but at high temperatures, a strong suppression of swelling with molybdenum addition can also be seen in Figure 19b. A comparison of these new or current data with those of Gelles is shown in Figure 20, 21, and 22, indicating general agreement in data trends.

Molybdenum addition to Fe-12Cr-0.1C alloy at low temperatures and low dpa levels shows a complex swelling behavior as shown in Figure 23. Molybdenum addition suppresses swelling in ferritic alloys by extending the transient regime, but post-transient swelling rates on the order of 0.2%/dpa do not appear to be unreasonable (see Figure 24).

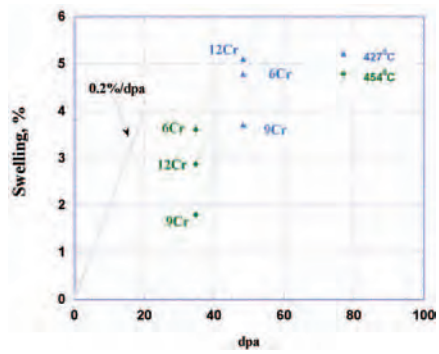

Figure 15. *Combined influence of temperature and flux on the swelling behavior of simple Fe-XCr binary ferritic alloys.*

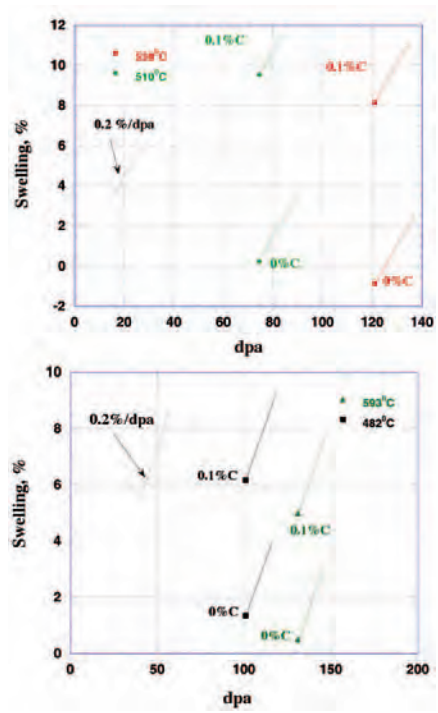

Figure 16. *Combined influence of temperature and flux effects on the swelling behavior of simple Fe-XCr binary ferritic alloys.*

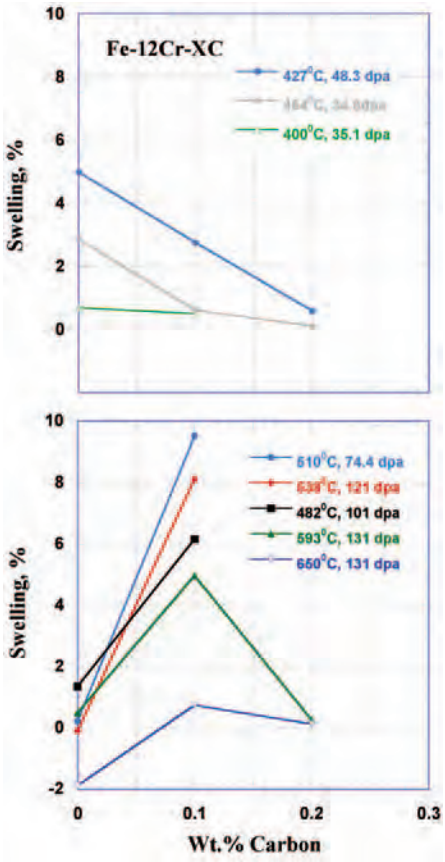

Figure 17. *Effect of carbon addition on swelling of simple Fe-12Cr binary alloys. These are new data by Sencer and Garner.*

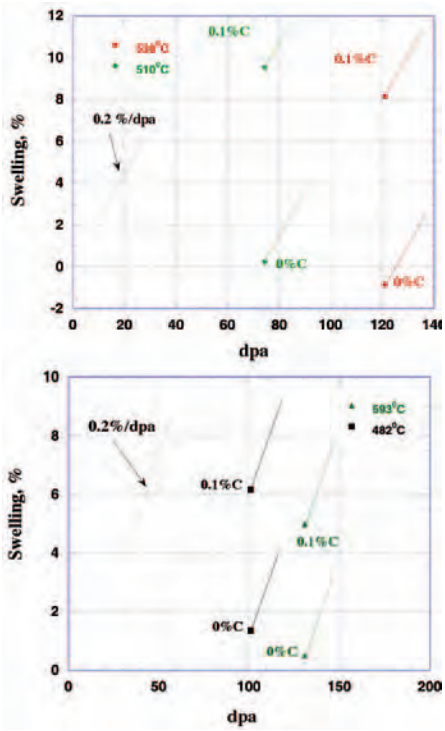

Figure 18. *Swelling behavior with carbon addition to simple Fe-Cr binary alloys.*

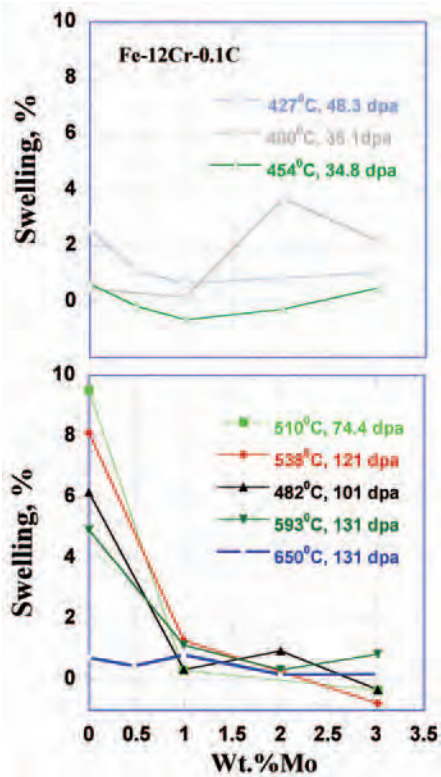

Figure 19. *Effect of molybdenum on swelling of Fe-12Cr-0.1C alloys. These are new data by Sencer and Garner.*

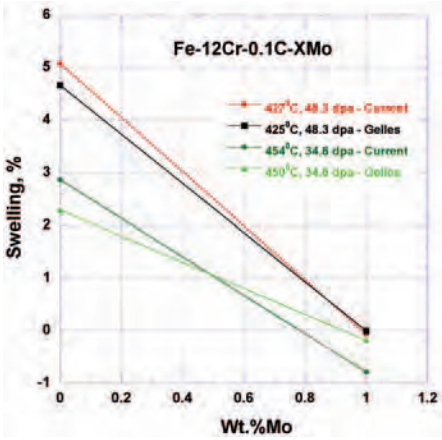

Figure 20. *Comparison of swelling of molybdenum modified alloys as observed by Gelles [28,30] and the current study, both sets of specimens which were irradiated side-by-side.*

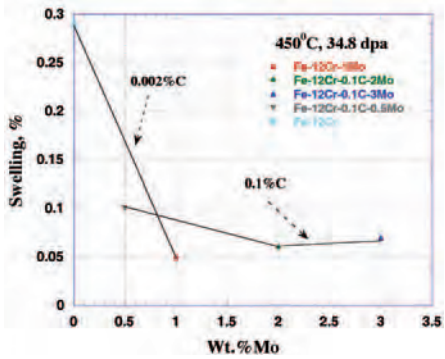

Figure 21. *Swelling of carbon-modified alloys as a function of molybdenum addition at 4500C, as observed by Gelles [28,30], showing the same general trends as observed in Figure 19.*

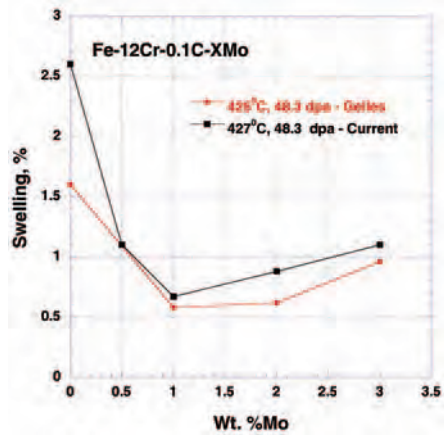

Figure 22. *Comparison of swelling behavior of a function of molybdenum as observed by Gelles [28,30] and the current study in side-by-side irradiation.*

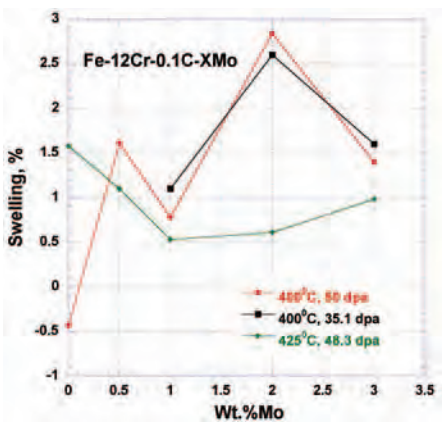

Figure 23. *Swelling behavior of molybdenum-modified alloys at low temperatures, as observed by Gelles [28-30].*

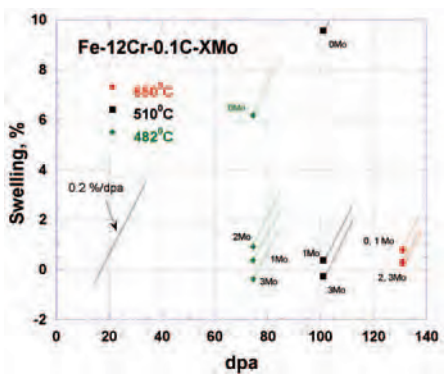

Figure 24. *Swelling behavior of Fe-Cr alloys at high temperatures from the current study.*

Discussion

Not only do the foregoing results have the potential to affect ongoing microstructural modeling efforts at many laboratories, but there are potentially strong engineering and design consequences of these conclusions as well.

The realization that BCC steels can eventually swell at rather high rates, with the primary swelling resistance residing in the transient regime rather than in the steady-state swelling rate, requires that a larger degree of uncertainty must be allowed for the onset of swelling in previously uncharted irradiation environments. This consideration is well illustrated by the large difference in transient duration in the not-so-isothermal irradiation conducted in EBR-II materials tests or FFTF fuel-pin tests as compared to the nearly-isothermal tests conducted in FFTF-MOTA. It is important to remember that most operating reactor systems experience fluctuations

in power and, thereby, temperature. This uncertainty is also foreshadowed by the heat-to-heat variability observed in the swelling of HT9 at 400°C and 165 dpa [20,22].

It is also important to note that these irradiations in FFTF proceed at higher dpa rate than those conducted in EBR-II. The transient regime of swelling has often been observed to be dependent on dpa rates.

There are other possible ramifications of the results of this study. First, the data indicate that there exists a significantly larger resistance to void nucleation in BCC alloys, and that the origin of this resistance is sensitive to alloy composition and, therefore, also to microchemical evolution. Microchemical evolution in FCC systems has been shown to be sensitive to many environmental factors, such as temperature history, applied stresses, helium and hydrogen generation rates, as well as dpa rates. The study of such "history effects" and their ability to accelerate swelling has led to the formulation of a general principle that "the longer the transient regime of swelling, the greater the possibility and magnitude of potential decreases in transient duration and thereby acceleration of swelling" when new test environments are explored. The abrupt termination of long transients, as shown in several of the preceding figures, is another indication of the inherent instability of such systems.

Second, since the resistance to swelling lies primarily in void nucleation, the onset of swelling in BCC steels may be much more sensitive to the high levels of helium and hydrogen generated in light-water moderated reactors, fusion reactors, or spallation neutron environments [34], the latter two of which are currently unexplored territory with respect to temperature, flux, and stress history. The majority of all high fluence data on BCC steels has been developed in fast reactors that have low He/dpa ratios. Gelles provided some support for this possibility in a comparison of HT9 irradiated in EBR-II and High-Flux Isotope Reactor (HFIR) where, in the latter reactor, the early onset of void growth was attributed to higher helium levels [20,29].

Whereas it was previously perceived that the steady-state swelling rates of iron-based ferritic and ferritic/martensitic steels were perhaps ten to twenty times smaller than that of iron-based FCC steels, it now appears that the difference may be as small as a factor of two to four. Due to long transient regimes of swelling in BCC alloys, this possibility has not been previously recognized. In addition, well-controlled materials irradiation tests will tend to yield conservatively low amounts of swelling compared to tests where the temperature history is more typical of normal reactor operation.

It appears that differences in BCC and FCC alloys in irradiation creep rates in the absence of void swelling also support only a factor of perhaps two in defect production efficiency to induce dimensional change by creep. Therefore, efforts to model the kinetics of defect production and aggregation in FCC and BCC alloys must incorporate this smaller than originally perceived difference in steady state swelling and creep rates.

Conclusions

When the previously published (and corrected) data are combined with the new supporting data, the following conclusions can be drawn.

1. At relatively low temperatures, simple binary ferritic alloys swell with a steady swelling rate of ~0.2%/dpa and possibly higher. This is much longer than previously assumed for these alloys by the radiation damage community.

2. At higher temperatures, if one waits long enough (up to ~130 dpa in the current experiment) swelling commences, often a long transient regime, at rates that may be similar to those at lower temperatures. This is contrary to the prevailing wisdom concerning the lack swelling of ferritic alloys at such higher temperatures.

3. Carbon addition up to 0.2% suppresses swelling at low temperatures (<454°C). However, at high temperatures (> 482°C), carbon initially increases swelling dramatically, although further addition of carbon up to 0.2%C suppresses the swelling. Carbon shortens the incubation period so strongly at higher temperatures that swelling levels approaching 10% were reached in the new experiment reported in this critique. This implies that swelling rates are again relatively large, perhaps reaching 0.2%/dpa or greater.

4. Molybdenum addition in general suppresses swelling in ferritic alloys. Commercial ferritic/martensitic alloys usually incorporate both Mo and C in their composition, with Mo acting to produce the longer transient regime, on the order of ≥100 dpa, observed in these steels.

References

1. H. Matsui, D. S. Gelles and Y. "Kohno in Effects of Radiation on Materials," 15th International Symposium, ASTM STP 1125, 1992, pp. 928–941.

2. F. A. Garner, D. S. Gelles, | H. Takahashi, S. Ohnuki, H. Kinoshita and B. A. Loomis, J. Nucl. Mater., 191–194 (1992) 948–951.

3. F. A. Garner and C. A. Black, Proc. 19th ASTM Symp. on Effects of Radiation on Materials, Seattle, WA, June 16–18, 1998, in press.

4. W. G. Johnston, T. Lauritzen, J. H. Rosolowski, and A. M. "Turkalo, in Effects of Radiation on Materials," 11th Conf., ASTM STP 782, 1982, pp. 809–823.

5. E. A. Little and D. A. Stow, J. Nucl. Mater., 87 (1979) 25–39.

6. L. L. Horten, J. Bentley and W. A. Jesser, J. Nucl. Mater., 103 and 104 (1981) 1085–1090.

7. L. L. Horten and J. Bentley, Proc. Topical Conf. on Ferritic Alloys for Use in Nuclear Energy Technologies, AIME, 1984, pp. 569–578.

8. S. Ohnuki, H. Takahashi and T. Takeyama, J. Nucl. Mater., 103 and 104 (1981) 1121–1126.

9. B. H. Sencer and F. A. Garner, to be submitted to the ICFRM-9 Symposium in Colorado Springs, October 1999.

10. E. Kuramoto, N. Yoshida, N. Tsukuda and K. Kitajima, J. Nucl. Mater., 103 and 104 (1981) 1091–1096.

11. K. Kitajima, K. Futagami and E. Kuramoto, J. Nucl. Mater., 85 and 86 (1979) 725–729.

12. K. Farrell and J. T. Housten, "Title," J. Nucl. Mater., 35 (1970) 352–355.

13. G. L. Kulcinski, B. Mastel and J. L. Brimhall, "Radiation Effects 2," (1969) 57–59.

14. L. L. Horten, J. Bentley and K. Farrell, J. Nucl. Mater., 108 and 109 (1982) 222–233.

15. S. I. Porollo, A. M. Dvoriashin, A. N. Vorobjev and Yu. V. Konobeev, J. Nucl. Mater., 256 (1998) 247-253.

16. N. P. Agapova, V. S. Ageev, I. N. Afrikanov, N. I. Budylkin, V. A. Krasnoselov, E. G. Mironova, V. D. Onufriev, Z. E. Ostrovsky, V. I. Prokhorov and Yu. N. Sokursky, Proc. of Alushta '78 Conference on Reactor Material Science, 1978, pp. 297-320 in Russian.

17. F. A. Garner, J. Nucl. Mater., 117 (1983) 177–197.

18. F. A. Garner and seventeen co-authors, in Proc. Workshop on Correlation of Neutron and Charged Particle Damage, CONF-760673, Oak Ridge, TN, June 8-10, 1976, p. 147.

19. M. B. Toloczko, F. A. Garner and C. R. Eiholzer, J. Nucl. Mater., 212–215 (1994) 604–607.

20. M. B. Toloczko and F. A. Garner, J. Nucl. Mater., 233-237 (1996) 289-292.

21. F. A. Garner and M. B. Toloczko, Proc. 18th Symp. on Effects of Radiation on Materials, Sun Valley, June 1996, in press.

22. F. A. Garner, "Materials Science and Technology: A Comprehensive Treatment," Chapter 6 in vol. 10A in Nuclear Materials, Part 1, 1994, pp. 419-543.

23. F. A. Garner and M. B. Toloczko, J. Nucl. Mater., 206 (1993) 230-248.

24. M. B. Toloczko, F. A. Garner and R. J. Puigh, Proc. 19th ASTM Symp. on Effects of Radiation on Materials, Seattle, WA, June 16-18, 1998, in press.

25. F. A. Garner, M. B. Toloczko and M. L. Grossbeck, J. Nucl. Mater., 258–263 (1998) 1718–1724.

26. M. B. Toloczko, F. A. Garner, J. Standring, B. Munro and S. Adaway, J. Nucl. Mater., 258–263 (1998) 1606–1612.

27. F. A. Garner, "Dependence of Swelling on Nickel and Chromium in Fe-Ni-Cr Ternary alloys," Damage Analysis and Fundamental Studies Quarterly Progress Report 4-6/1983, DOE/ER-0046/14, pp.133.

28. D. S. Gelles and R. L. Meinecke, "Alloy Development for Irradiation Performance Semiannual Progress Report," DOE/ER-045/11, 1984, pp. 103–107.

29. D. S. Gelles and L. E. Thomas, Proc. Topical Conf. on Ferritic Alloys for use in Nuclear Energy Technologies, AIME, 1984, pp. 559–568.

30. D. S. Gelles, J. Nucl. Mater., 108–109 (1982) 515–526.

31. D. S. Gelles, Effects of Radiation on Materials: 14th Inter. Symp., Vol. 1, ASTM STP 1046, 1989, pp. 73–97.

32. Y. Katoh, A. Kohyama and D. S. Gelles, J. Nucl. Mater., 225 (1995) 154–162.

33. D. S. Gelles, J. Nucl. Mater. 225 (1995) 163–174.

34. F. A. Garner and L. R. Greenwood, "Incorporating Plasma Science and Plasma Technology," Radiat. Eff. Defects Solids, 144 (1998) 251–286.

DR. BULENT H. SENCER (BS, 1991 Metallurgical Engineering, distinguished, Technical University of Istanbul, in Turkey; MS, 1995, Materials Science, University of Southern California; Ph.D., 2000, Materials Engineering, New Mexico Institute of Technology,) is a staff member in the Nuclear Fuels and Materials Department at INL since 2007. Prior, he was a graduate research fellow in the Materials Resources Department at the Pacific Northwest National Laboratory, postdoctoral fellow at the University of Michigan in the department of Nuclear Engineering and postdoctoral research associate in the Materials Science and Technology Division (MST-8) at the Los Alamos National Laboratory. Dr. Sencer has experience with fast reactor, LWR, high-energy proton (LANSC) and light/heavy-ion irradiated materials. His current research is developing a better understanding of the thermal and the irradiation-assisted diffusion behavior between fuel and clad constituents under selective ion irradiation.

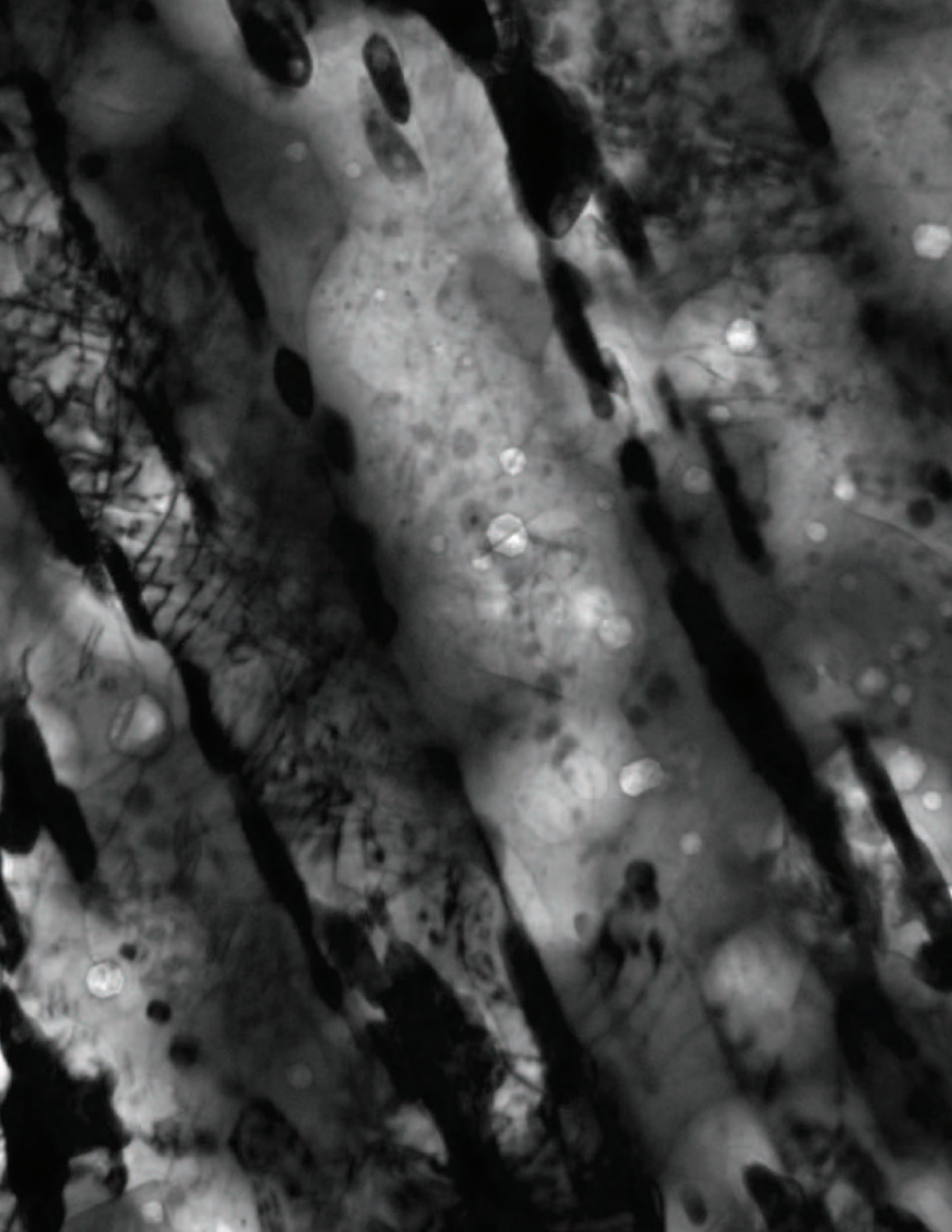

Microstructural Evolution of an HT9 Fuel Assembly Duct Irradiated in FFTF to 155 Dpa at 443ºC

B. H. Sencer, J. R. Kennedy, J. I. Cole, S. A. Maloy (LANL) and F. A. Garner (PNNL)

The majority of data on the irradiation response of ferritic/martensitic steels has been derived from simple free-standing specimens irradiated in experimental assemblies under well-defined and near-constant conditions, while components of long-lived fuel assemblies are more complex in shape and will experience progressive changes in environmental conditions. To explore whether the resistance of HT9 to void swelling is maintained under more realistic operating conditions, the radiation-induced microstructure of an HT9 ferritic/martensitic hexagonal duct was examined following a 6-year irradiation of a fuel assembly in the Fast Flux Test Reactor Facility (FFTF). The calculated irradiation exposure and average operating temperature of the duct at the location examined were ~155 dpa at ~443°C. It was found that dislocation networks were contained predominantly a/2<111> Burgers vector. Surprisingly, for such a large irradiation dose, type a<100> interstitial loops were observed. Additionally, a high density of precipitation occurred. These two microstructural characteristics may have contributed to the rather low swelling level of 0.3%.

Introduction

Ferritic-martensitic steels provide attractive alternatives to the use of austenitic stainless steels for fission, fusion, spallation, and fast reactor applications. This is in part a consequence of their generally greater resistance to neutron irradiation-induced swelling and creep and their reasonably acceptable high temperature strength [1–12], although these attributes are somewhat sensitive to alloy composition and processing history.

The ferritic-martensitic alloy HT9 has been investigated in the United States for application to fast, fusion, and spallation neutron driven devices. This alloy has shown great promise, especially with respect to its resistance to swelling and excellent compatibility with sodium. To date, however, all reported swelling and creep data on this alloy have been derived from very simple, free-standing experimental specimens irradiated under rather well-defined conditions in material test assemblies [13–23].

It is known that the swelling of austenitic stainless steels is sensitive to "history effects" such that materials subjected to reactor-relevant changes in neutron flux, temperature, and stress state often reach much higher swelling levels than is reached in identical material irradiated under constant irradiation conditions [24].

To confirm that HT9 also does not lose a large fraction of its swelling resistance under the variable irradiation conditions characteristic of long-term operation of a relatively complex component in reactor, it was decided to examine a fuel assembly from the FFTF fast reactor that employed this alloy for fuel pin cladding, wire wrap, and the hexagonal duct that encased the fuel pin assembly.

This fuel assembly was designated ACO-3 and reached a maximum exposure of 155 dpa. This first published report on this duct addresses the swelling and associated microstructure of the duct at the position of maximum displacement dose.

Experimental details

The composition of the heat of HT9 used to construct the ACO-3 hexagonal duct is given in Table 1. The duct was subjected to a heat treatment involving 1040°C for 30 min/air cooling followed by 760°C for 1 hr/ and air cooling, producing a fully tempered microstructure. The duct was 367 cm long (12 ft), hexagonal in cross section, with a span of 60 mm across each face and a wall thickness of 3.0 mm.

The ACO-3 assembly was included in a partial core loading of FFTF known as the Core Demonstration Experiment (CDE) that was designed to be an aggressive demonstration of a fuel system using HT9 for cladding, wrapping wire, and duct [25] for fuel assemblies, lead fuel assemblies, and reflector assemblies. The fuel cladding

started irradiation at peak cladding temperatures as high as 660°C in some subassemblies and, to maintain operation at this high temperature, the CDE ensemble was progressively moved inward in the FFTF core as burn-down of the fuel progressed [26, 27]. Thus, there were both slowly declining and abruptly increasing changes in both neutron flux and temperature. In general, the pressure differences across the duct wall and, thereby, the applied stresses were low enough to be ignored.

As shown in Figure 1 and Table 2 the ACO-3 subassembly was one of the CDE assemblies and was irradiated in three positions of the FFTF fast reactor during Cycles 7 to 12B, accumulating an exposure of 1524.2 equivalent full power days (EFPDs) over a 6-year period, as shown in Table 3. The first position was in Row 6, and the second and third positions were in Row 3 in equivalent positions but on opposite sides of the core.

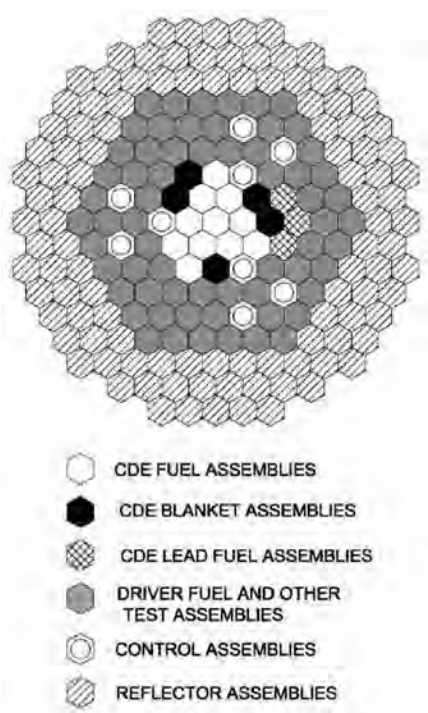

Figure 1. *Initial core loading of CDE subcore in FFTF [25].*

The fuel in the subassembly reached a peak fast fluence of 38.9 x 10^{26} n/m^2, E > 0.1 MeV. In each core position, the same duct face of the ACO-3 assembly was always oriented towards the core center. During Cycles 7 and 8, the reactor ran at 400 MWth while in the remaining irradiation cycles, the reactor operated at 291 MWth. Therefore, the integrated history of the duct experienced a range of exposure conditions over a 6-year period, providing a good test of the swelling

Table 1. *Chemical composition of HT9 in wt%.*

	Fe	Cr	Ni	Mo	Mn	C	Ti	V	W	Si	Al
HT9*	bal.	11.8	0.51	1.03	0.50	0.21	<0.01	0.33	0.24	0.21	0.03

**heat 84425, with S=0.003, P=0.008, N=0.006.*

Table 2. *Irradiation dates and subassembly location of the ACO-3 duct irradiated in FFTF.*

Irradiation Cycle	Cycle Segment	Irradiation Dates	In-Core Location Code	Relative Posn in Core	Handling Socket Orientation Mark
7	7A 7B 7C	8/17/85 — 12/07/85 12/09/85 – 12/13/85 12/16/85 – 1/03/85	1609	Periphery	Towards Core Center
8A	8A	2/6/85 – 4/25/86	1609	Periphery	Towards Core Center
9A	9A.1 9A.2	9/10/86 – 10/13/86	1304	Near Center	Towards Core Center
9B	9B	3/04/87 – 6/20/87	1304	Near Center	Towards Core Center
10A	10A.1 10A.2 10A.3 10A.4	11/18/87 – 1/26/88 2/10/88 – 2/23/88 2/25/88 – 3/04/88 3/07/88 – 5/08/88		Near Center	Towards Core Center
10B	10B	6/11/88 – 10/17/88	1304	Near Center	Towards Core Center
10C	10C.1 10C.2 10C.3	11/09/88 – 1/08/89 1/16/89 – 1/20/89 1/24/89 – 3/13/89	3303	Near Center	Towards Core Center
11A	11A.1 11A.2 11A.3	5/03/89 – 5/16/89 5/21/89 – 6/02/89 6/14/89 – 9/18/89	3303	Near Center	Towards Core Center
11B.1	11B.1	1/04/90 – 4/08/90	3303	Near Center	Towards Core Center
11B.2	11B.2	5/29/90 – 10/27/90	3303	Near Center	Towards Core Center
11C	11C	12/20/90 – 3/19/91	3303	Near Center	Towards Core Center
12A	12A.1 12A.2	5/27/91 – 7/21/91 7/30/91 – 9/22/91	3303	Near Center	Towards Core Center
12B	12B.1 12B.2	11/21/91 – 1/15/92 1/26/92 – 3/19/92	3303	Near Center	Towards Core Center

resistance of HT9 under realistic operating conditions.

Estimated dose and temperature profiles at the conclusion of the ACO-3 irradiation are shown in Figure 2. The conversion factors used to calculate dose from fast fluence were taken from analyses performed on dosimetry packets from Materials Open Test Assemblies (MOTAs) located in comparable positions in the FFTF core. In the central core region, where the specimens extracted for this study were located, the conversion factors ranged between 4.1 to 4.5 dpa per 10^{26} n m^{-2} (E > 0.1 MeV), depending on the core power level, the local flux distribution, and the surrounding assemblies in each core loading.

As shown in Figure 2 the total dose attained in the mid-core region was ~155 dpa. Microstructural examination was conducted on a specimen located at the core center plane, which experienced the maximum neutron exposure at a time-averaged temperature of ~443°C. Both sides of the duct face were in contact with flowing sodium, and the temperature gradient across the duct was estimated to be less than 5°C. While the displacement dose is considered to be accurate within ±5%, the variations in temperature over the lifetime have not yet been estimated. Since this component is a duct, however, the variations in temperature are probably within ±10ºC, a situation quite different from that of the fuel cladding, where the temperatures are driven by the instantaneous local fission rate.

The microscopy specimens used in this study were prepared by punching 2.3 mm discs. TEM samples were prepared by conventional jet electropolishing methods in 5% perchloric acid, 95% methanol, at - 40°C and 65 A. 2.3 mm discs glued on to 3 mm washer. TEM examinations were conducted with JEOL 2010 and TECHNAI G2 F30 electron microscopes. An unirradiated archive duct was available to determine the starting microstructure.

Table 3. *Incremental and Cumulative EFPD for the ACO-3 duct irradiated in FFTF.*

Irradiation Cycle	Cycle Segment	Incremental EFPD	Cumulative EFPD
7	7A	105.1	105.1
	7B	3.3	108.4
	7C	14.4	122.8
8A	8A	54.9	177.7
9A	9A.1	29.4	207.1
	9A.2	108.3	315.4
9B	9B	106.4	421.8
10A	10A.1	66.3	585.8
	10A.2	20.3	606.1
	10A.3	5.8	611.9
	10A.4	59.4	671.3
10B	10B	126.7	798.0
10C	10C.1	56.9	854.9
	10C.2	2.9	857.8
	10C.3	47.0	904.8
11A	11A.1	11.3	916.1
	11A.2	10.5	926.6
	11A.3	94.6	1021.2
11B.1	11B.1	85.5	1106.7
11B.2	11B.2	132.7	1239.4
11C	11C	81.5	1320.9
12A	12A.1	52.8	1373.7
	12A.2	48.6	1422.3
12B	12B.1	50.3	1472.6
	12B.2	51.6	1524.2

Results

Preirradiation microstructure of HT9

Prior to irradiation, the microstructure of unirradiated HT9 contains a duplex structure of martensite and ferrite. Large blocky carbides with a strong contrast in bright field images were observed on the martensite lath boundaries. Carbides distributed on or near subgrain boundaries are shown in Figure 3.

Irradiated HT9

Detailed analysis of the microstructure examination revealed that dislocation loop, network dislocations, precipitates, and cavities had developed in the HT9 alloy irradiated at 443°C to 155 dpa with well-developed precipitate arrays

decorating subgrain lath boundaries, non-uniform void arrays within laths, and fine precipitates on boundaries and within laths in Figure 4a. In addition to the small fine precipitation, large bulky carbides with strong contrast in bright-field images were observed on grain and lath boundaries, as seen in Figure 4b. It also appears, comparing Figure 3 and Figure 4b, that there is an enhancement in carbide density on or near the subgrain boundaries after irradiation. The HT-9 developed void structures typical of martensitic steels. These void structures consisted of void arrays between lath boundaries and void-free regions on, and adjacent to, the boundaries.

In the dislocation analysis, it is assumed that the network dislocations contain only a<100> and (a/2)<111> components. Network segments in 200 dark-field image are not observable in 011 image, while another population of a<100> dislocations is imaged. Hence most must be a<100> dislocations. Weakly imaged dislocations in 200 contrast are mostly (a/2)<111> dislocations since they are also visible in 110 contrast, as seen in Figure 5a and 5b. In these dark-field images, the electron beam is z=<001> zone. Dislocation pinning at cavity surfaces is often observed. The 200 contrast reveals 1/3 of a<100> dislocations and all of (a/2)<111> dislocations, while the 110 contrast images 2/3 of a<100> dislocations and 1/2 of (a/2)<111> dislocations. Therefore, the density of each type of dislocation is calculated from the quantification results of a pair of 200 and 110 micrographs. The total network dislocation density ((a/2)<111>+a<100>) is estimated to be ~$3x10^{15}$ m^{-2}, and a/2<111> dislocation density is estimated to be ~$2.2x10^{15}$ m^{-2}, indicating the network dislocation structure is predominantly (a/2)<111> type. In Figure 5, loops are predominantly a<100> type, but their number density is relatively low. Figure 6 also shows loops, presented together with loop size distribution. The mean loop size is estimated to be ~18 nm. Loop number density is estimated to be ~ 5 x 10^{20} m^{-3}.

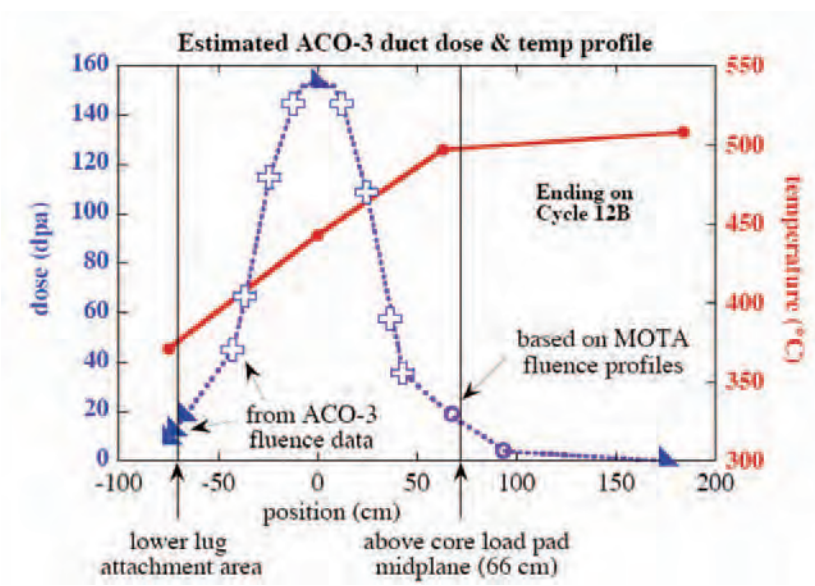

Figure 2. *Irradiation conditions that were experienced by the ACO-3 duct. Determination of dose levels was augmented using dosimetry measurements conducted in Materials Open Test Assemblies (MOTA) irradiated in comparable positions in FFTF.*

Another feature found in the microstructure of irradiated HT9, as shown in Figure 7, is radiation-enhanced precipitation, previously identified as G-phase by Gelles and Thomas [28] or as η phase by Maziasz and Klueh [29] and α' precipitates [4, 15, 16]. Figure 8a shows a bright-field TEM image of G-phase and α' precipitates while Figure 8b shows precipitate dark-field image of G-phase. Comparison of Figure 8a and Figure 8b reveals that not all precipitates are imaged in Figure 8a. The smaller precipitates do not appear in Figure 8b are expected to be chromium-rich α' precipitates. The mean G-phase precipitate size is ~20 nm in diameter within the laths, but somewhat larger on subgrain boundaries. Irradiation hardening found in HT-9 can be partially attributed to this phase. The α' precipitates have a cube-on-cube relationship with the matrix and form by precipitation of chromium with the same body-centered cubic structure as the matrix and only a slightly larger (<1%) lattice constant. Hence α' precipitates can only be imaged in bright-field TEM images.

Cavities thought to be voids are shown in Figure 9 at 155 dpa with a mean cavity size of ~28 nm. The highest swelling was measured as high as 1.2% in isolated regions. Estimated mean void swelling is ~0.3%, based on a measured cavity number density of ~2.5 x 10^{20} m^{-3}. Void swelling measurements were conducted as recommended in Gelles, Claudson, and Thomas's article [30]. The spatial distribution of cavities was quite uniform within the matrix, although grain boundaries and

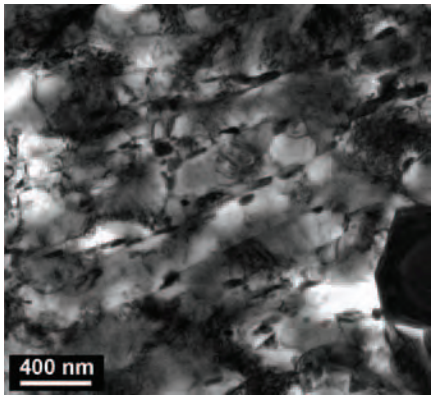

Figure 3. *Microstructure of HT9 alloy prior to neutron irradiation. The martensite transformation has occurred, and carbides have formed during tempering.*

adjacent regions were usually free of cavity formation. Since void size distribution extended to small sizes, steady-state void populations had, at best, only just been achieved. In some cases, voids were in linear arrays, indicating that heterogeneous nucleation on dislocations played a role.

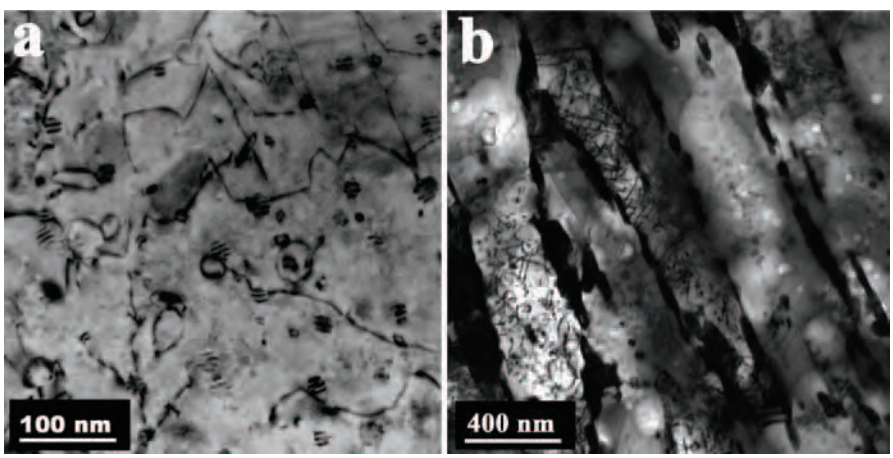

Figure 4. *(a) TEM image showing dislocation loop, network dislocations, precipitates, and cavities, g= 110. (b) TEM image showing carbides on lath boundaries.*

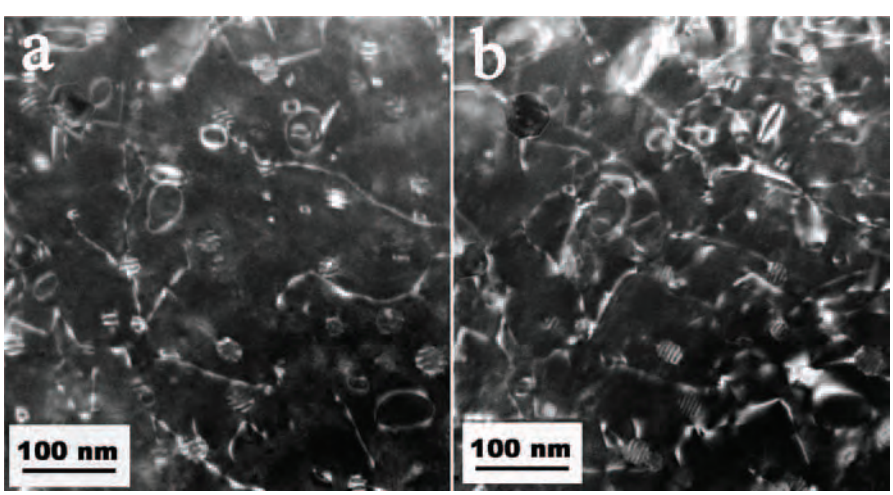

Figure 5. *TEM dark-field images of (a) g= 110 and (b) g= 200 are from the same region in irradiated HT9 at 155 dpa.*

Discussion

It is clear that even under non-constant irradiation conditions, the alloy HT9 displays a remarkable resistance to void swelling. While the crystal structure of BCC iron and iron-based ferritic alloys is thought to convey immunity against the high swelling rates characteristic of FCC iron-base alloys [4], it has been shown that under some conditions (e.g., cold-working, low dpa rates) pure iron can develop relatively high swelling rates [31–33].

More importantly, the Fe-12Cr binary alloy from which HT9 is based has been shown to swell at a steady-state rate of ~0.2%/dpa [34] where data have been generated to doses as high as 30 dpa in DFR [35], 50–100 dpa in EBR-II [36] and 140–200 dpa in FFTF [37, 38]. The onset of swelling of Fe-12Cr has also been shown to be accelerated by lower temperatures, lower dpa rates, and carbon addition (at least at some higher temperatures) [34]. It has also been demonstrated that HT9 and 9Cr-1Mo appear to be swelling at rates comparable to that of pure binary alloys Fe-12Cr and Fe-9Cr, but to begin swelling after a somewhat longer transient regime [34]. The onset swelling of HT9 in FFTF was observed to be accelerated by application of stress [20, 34]. It also appears that the swelling of Fe-Cr binary alloys is sensitive to the helium/dpa ratio [39].

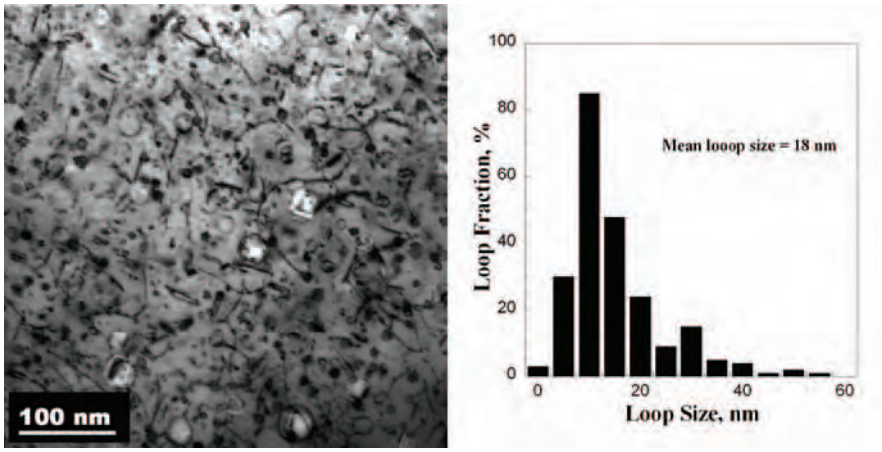

Figure 6. *Bright-field TEM images (g=110) showing dislocations, small and large loops, precipitates and voids, together with loop size distribution.*

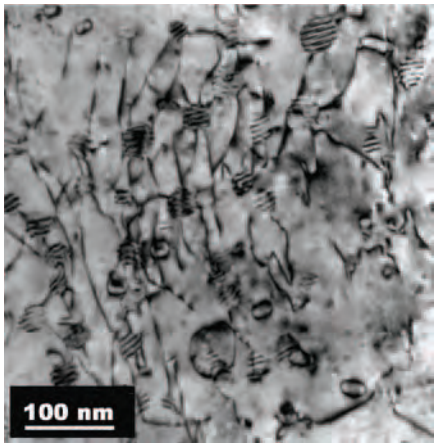

Figure 7. *Bright-field TEM image, g=110, of both G-phase and chromium-rich precipitates.*

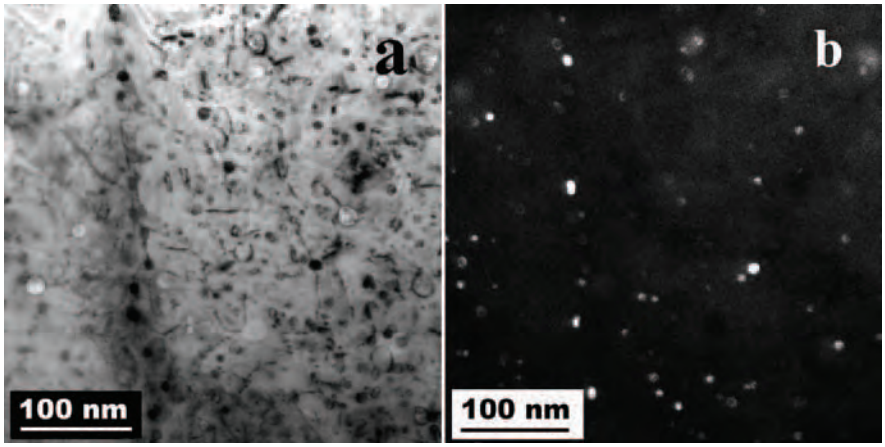

Figure 8. *(a) Bright-field TEM image of both G-phase and chromium-rich precipitates, near void imaging condition (b) Precipitate dark-field TEM image of G-phase.*

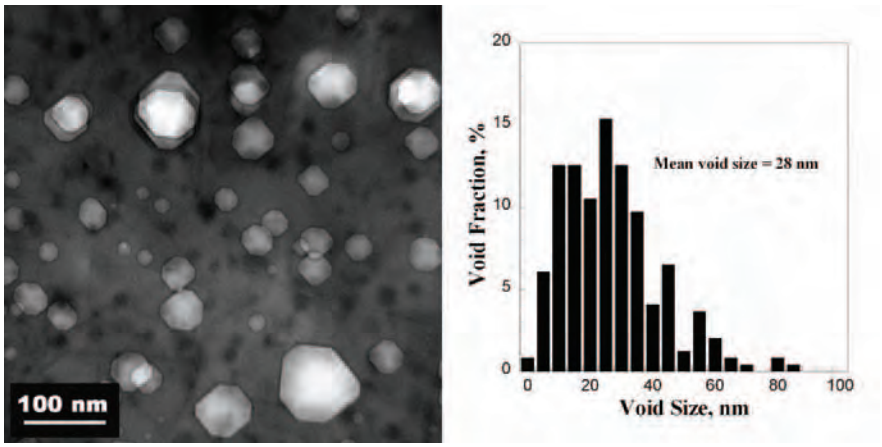

Figure 9. *TEM void image and void size distribution.*

It should be noted that most measurements of swelling of HT9 cited earlier were determined from either diameter changes of zero-stress creep tubes or from density change measurements. This observation is significant in that both diameter change and density change contain contributions from phase changes. These previous studies have shown, however, that the combined swelling and phase-related density change behavior of HT9 is somewhat sensitive to heat-to-heat variability, minor compositional changes, as well as irradiation temperature and dpa rate.

Actual measurements of void volume per se were made only in references 14, 16, and 20. Most significantly, if we ignore the difference between the two specimens, the current measurement of 0.3% swelling at 155 dpa and 443°C and the stress-free swelling of ~1% at 208 dpa and ~400°C [20, 34], the swelling rate is beginning to approach the anticipated 0.2%/dpa rate, at least in the 400–450°C temperature range. The acceleration of swelling at 208 dpa by stress from ~1% to ~2.5% [20] indicates that the swelling rate is obviously beginning to further increase, implying that the terminal rate of ~0.2%/dpa may have been reached at a dose level below 208 dpa.

From this current study alone it cannot be stated confidently whether the observed swelling of 0.3% still lies in the transient regime of swelling. It may be noted that a broad void size distribution, which includes small sizes, is usually an indication that steady-state swelling has not been achieved. Most importantly, the somewhat complex temperature and flux history over its 6-year lifetime did not appear to significantly impact the swelling resistance of the HT9 duct.

How might the exceptional swelling resistance of HT9 arise in FFTF? Most likely there are a number of factors, both environmental and material in nature. In high-flux reactors, such as FFTF, it is suspected that the transient regime of swelling for Fe-Cr alloys is extended at higher dpa rates as was demonstrated in comparison of swelling in FFTF and lower flux EBR-II [34]. This effect of higher dpa rate to delay the onset of steady-state swelling is well established for Fe-Cr-Ni FCC alloys [40–44], but only one study confirms that a similar phenomenon occurs in BCC iron-base alloys such as EP-450 [44].

Additionally, higher flux reactors frequently have mixed oxide fuels rather than metal fuels. As a consequence, the neutron spectra are softened, and the He/dpa ratio is reduced in oxide cores, making void nucleation more difficult [39]. Also, as noted earlier, the duct in FFTF did not experience any significant stresses.

Additionally, there are some microstructural features that may contribute to the swelling resistance of HT9. Two features stand out at present. These are the nature of the precipitate evolution and of the dislocation/loop population produced by irradiation.

The HT9 ferritic/martensitic alloy developed a high density of small precipitates that were identified to be G-phase and chromium rich α', consistent with previously published results [15, 16]. The α' precipitates are typically of spheroidal geometry and in a size range resolvable by electron microscopy. If they are assumed to act like a perfect sinks, which would have very high point defect-capture efficiency and could absorb a number of point defects of either kind, they would be a strong swelling suppressor. However, since α' is cube-on-cube precipitation of chromium with the same body-centered cubic structure as the matrix and only a slightly larger (<1%) lattice constant, the precipitates are unlikely to be very effective sinks. Future work on the precipitations remains to be explored.

The other microstructural feature is the presence of predominantly a<100> type interstitial dislocation loops. The interstitial loops are sensitive to chromium content [16]. The presence of a high density of such loops at this high dose is rather surprising, especially in the presence of a dislocation network. Also point defects are highly mobile at 443°C, and the possibility of interstitial clustering is extremely weak. Perhaps there is some interaction between continuous nucleation of interstitial loops and the precipitations that promotes the loop nucleation and/or stabilizes the nucleated loops. This could be supported by the coincidence of conditions for high density loop development and precipitation, especially chromium-rich precipitates.

Conclusions

An HT-9 duct was irradiated in three positions in FFTF over 6 years at ~443°C reaching ~155 dpa. The duct experienced both slowly declining and two abrupt changes in neutron flux and temperature. Examination by transmission electron microscopy showed that HT-9 retained its swelling resistance in spite of the somewhat complex flux and temperature history, reaching only about 0.3%. Based on this study only, it cannot be determined whether the transient regime of swelling is still in progress or the steady-state swelling rate is being approached.

Acknowledgements

This research is supported by the Advanced Fuel Cycle Initiative (AFCI). The authors are indebted to M. B. Toloczko of Pacific Northwest National Laboratory for the information describing the irradiation conditions of the AC03 duct, as presented in Figure 2 and Tables 2 and 3 and to W. Witherspoon, who led the retrieval of this duct. A special acknowledgment is given to F. Goldner at the Department of Energy (DOE) for making all this happen. We also thank T. Romero for remotely cutting the TEM specimens from the duct and J. Gan for sample preparation. We also acknowledge the staff of the University of Nevada, Las Vegas, for the use of their electron beam facility.

References

1. Proceedings of the Topical Conference on Ferritic Alloys for use in Nuclear Energy Technologies, AIME, 1984, p. 559.
2. E. A. Little and D. A. Stow, J. Nucl. Mater., 87(1979) 25.
3. R. W. Powell, D. T. Peterson, M. K. Zimmerscheid, J. F. Bates, J. Nucl. Mater., 103 and 104 (1981) 969.
4. G. R. Odette, J. Nucl. Mater., 155–157 (1988) 921.
5. R. L. Klueh, K. Ehrlich, F. Abe, J. Nucl. Mater., 191–194 (1992) 116–124.
6. A. G. Ioltukhovsky, V. P. Kondrat'ev, M. V. Leont'eva-Smirnova, S. N. Votinov, V. K. Shamardin, A. V. Povstyanko, T. M. Bulanova, J. Nucl. Mater., 233–237 (1996) 299–304.
7. A. Hishinuma, A. Kohyama, R/ L. Klueh, D. S. Gelles, W. Dietz, K. Ehrlich, J. Nucl. Mater., 258–263 (1998) 193–204.
8. B. van der Schaaf, D. S. Gelles, S. Jitsukawa, A. Kimura, R. L. Klueh, A. Moslang, G. R. Odette, J. Nucl. Mater., 283–287 (200) 52–59.
9. R. L. Klueh, D. S. Gelles, S. Jitsukawa, A. Kimura, G.R. Odette, B. van der Schaaf, M. Victoria, J. Nucl. Mater., 307–311 (2002) 455–465.
10. S. Jitsukawa, A. Kimura, A. Kohyama, R.L. Klueh, A. A. Tavassoli, B. van der Schaff, G.R. Odette, J. W. Rensman, M. Victoria, C. Petersen, J. Nucl. Mater., 329–333 (2004) 39–46.
11. A. Kimura, R. Kasada, A. Kohyama, H. Tanigawa, T. Hirose, K. Shiba, S. Jitsukawa, S. Ohtsuka, S. Ukai, M. A. Sokolov, R. L. Klueh, T. Yamamoto, G. R. Odette J. Nucl. Mater., 367–370 (2007) 60–67.
12. D. S. Gelles, "Development of Martensitic Steels for high Neutron Damage Applications," J. Nucl. Mater., 239 (1996) 99.
13. D. S. Gelles, "12Cr-1Mo steel for Fission and Fusion Applications", in Proc. ASM Intern. Conf. on Ferritic Steels for High Temperature Applications, Warren, PA, October 1981, p.197.
14. D. S. Gelles and L. E. Thomas, "Effects of Neutron Irradiation on Microstructure in Experimental and Commercial Ferritic Alloys," Proc. Of the Topical Conf. on Ferritic Alloys for Use in Nuclear Energy Technologies, AIME, Snowbird, Utah, June 1983, p. 559.
15. D.S. Gelles, DOE/ER-0046/24 (1986) 43.
16. D. S. Gelles, J. Nucl. Mater., 233–237 (1996) 293–298.
17. F. A. Garner and D. S. Gelles, "Neutron-Induced Swelling of Commercial Alloys at Very High Exposures," in Effects of Radiation on Materials: 14th International Symposium, Volume 2, ASTM STP 1046, N. H. Packan, R. E. Stoller and A. S. Kumar, Eds., American Society for Testing and Materials, Philadelphia, 1990, pp. 673–683.
18. R. J. Puigh and F. A. Garner, "Irradiation Creep Behavior of the Fusion Heats of HT9 and Modified 9Cr-1Mo Steels," in Effects of Radiation on Materials: 14th International Symposium, Volume 2, ASTM STP 1046, N. H. Packan, R. E. Stoller and A. S. Kumar, Eds., American Society for Testing and Materials, Philadelphia 1990, pp. 527–536.
19. F. A. Garner and R. J. Puigh, J. of Nucl. Mater., 179–181 (1991) 577–580.
20. M. B. Toloczko, F. A. Garner, C.R. Eiholzer, J. Nucl. Mater. 212–215 (1994) 604.

21. M. B. Toloczko, F. A. Garner, J. Nucl. Mater. 233–237 (1996) 289–292.

22. M. B. Toloczko and F. A. Garner, "Variability of Irradiation Creep and Swelling of HT9 Irradiated to High Neutron Fluence at 400-600°C," ASTM STP 1325, Effects of Radiation on Materials: 18th International Symposium, R. K. Nanstad, M.. Hamilton, F. A. Garner and A. S. Kumar, Eds., American Society of Testing and Materials, 1999, pp.765–779.

23. M. B. Toloczko, B. R. Grambau, F. A. Garner and K. Abe, "Comparison of Thermal Creep and Irradiation Creep of HT9 Pressurized Tubes at Test Temperatures from ~490°C to 600°C," Proceedings of Symposium on Effects of Radiation on Materials, 20th International Symposium, ASTM STP 1405, S. T. Rosinski, M. L. Grossbeck, T. R. Allen, and A. S. Kumar, Eds., American Society for Testing and Materials, West Conshohocken, PA, 2001, pp. 557–569.

24. F. A. Garner, Chapter 6: "Irradiation Performance of Cladding and Structural Steels in Liquid Metal Reactors," Vol. 10A of Materials Science and Technology: A Comprehensive Treatment, VCH Publishers, 1994, pp. 419–543.

25. J. J. Laidler and R. J. Jackson, Trans. ANS, Vol. 49, p. 90.

26. R. D. Leggett, and L. C. Walters, J. Nucl. Mater., 204 (1993) 23–32.

27. R. B. Baker, F. E. Bard, R. D. Leggett, A. L. Pintner, J. Nucl. Mater., 204 (1993) 109–118.

28. D.S. Gelles, L.E. Thomas, Proceedings of the Topical Conference on Ferritic Alloys for use in Nuclear Energy Technologies, AIME, 1984, p. 559.

29. P. L. Maziasz and R. L. Klueh, "Void Formation and Helium Effects in 9Cr-1MoVNb and 12 Cr-1MoVW Steels Irradiated in HFIR and FFTF at 400°C," to be published in proceedings of the 14th International Symposium on the Effects of Radiation on Materials, held June 27–29, 1988 in Andover, Massechusetts.

30. D. S. Gelles, R. M. Claudson and L. E. Thomas, in: Electron Microscopy, 1990, Vol. 4, (San Francisco Press, San Francisco, 1990) pp. 844–845.

31. S. I. Porollo, A. M. Dvoriashin, A. N. Vorobyev, Yu. V. Konobeev, J. Nucl. Mater., 256 (1998).

32. A. M. Dvoriashin, S. I. Porollo, Yu. V. Konobeev and F. A. Garner, J. Nucl. Mater., 283–287 (2000) 157–160.

33. N. I. Budylkin, E. G. Mironova and V. M. Chernov, V. A. Krasnoselov, S. I. Porollo and F. A. Garner, J. Nucl. Mater., 375 (2008) 359–364.

34. F. A. Garner, M. B. Toloczko, B.H. Sencer, J. Nucl. Mater., 276 (2000) 123-142.

35. E. A. Little and D. A. Stow, J. Nucl. Mater., 206 (1993) 324.

36. B.H. Sencer and F.A. Garner, J. Nucl. Mater., 283–287 (2000) 164.

37. Y. Katoh, A. Kohyama, D. S. Gelles, J. Nucl. Mater., 225 (1995) 154–162.

38. D. S. Gelles, J. Nucl. Mater., 225 (1995) 163–174.

39. F. A. Garner, D. S. Gelles, L. R. Greenwood, T. Okita, N. Sekimura and W. G. Wolfer, J. Nucl. Mater. 329–333 (2004) 1008–1012.

40. T. Okita, N. Sekimura, T. Sato, F. A. Garner and L. R. Greenwood, J. Nucl. Mater., 307–311 (2002) 322–326.

41. T. Okita, W. G. Wolfer, T. Sato, N. Sekimura and F. A. Garner, "Influence of Composition, Helium Generation Rate and Dpa Rate on Neutron-Induced Swelling of Fe-15Cr-1Ni-0.25Ti Alloys in FFTF at ~400°C," 11th International Conference on Environmental Degradation of Materials in Nuclear Power Systems – Water Reactors, 2003, pp. 657–663.

42. F. A. Garner, N. I. Budylkin, Yu. V. Konobeev, S. I. Porollo, V. S. Neustroev, V. K. Shamardin, A. V. Kozlov, "The Influence of DPA rate on Void Swelling of Russian Austenitic Stainless Steels," 11th International Conference on Environmental Degradation of Materials in Nuclear Power Systems – Water Reactors, 2003, pp. 647–656.

43. N. I. Budylkin, T. M. Bulanova, E. G. Mironova, N. M. Mitrofanova, S. I. Porollo, V. M. Chernov, V. K. Shamardin and F. A. Garner, J. Nucl. Mater., 329–333 (2004) 621–624.

44. A. M. Dvoriashin, S. I. Porollo, Yu. V. Konobeev and F. A. Garner, J. Nucl. Mater., 329–333 (2004) 319–323.

DR. BULENT H. SENCER (BS, 1991 Metallurgical Engineering, distinguished, Technical University of Istanbul, in Turkey; MS, 1995, Materials Science, University of Southern California; Ph.D., 2000, Materials Engineering, New Mexico Institute of Technology) is a staff member in the Nuclear Fuels and Materials Department at INL since 2007. Prior, he was a graduate research fellow in the Materials Resources Department at the Pacific Northwest National Laboratory, postdoctoral fellow at the University of Michigan in the department of Nuclear Engineering, and postdoctoral research associate in the Materials Science and Technology Division (MST-8) at the Los Alamos National Laboratory. Dr. Sencer has experience with fast reactor, LWR, high-energy proton (LANSC) and light/heavy-ion irradiated materials. His current research is developing a better understanding of the thermal and the irradiation-assisted diffusion behavior between fuel and clad constituents under selective ion irradiation.

J. RORY KENNEDY (BS, 1982, Colorado State University; MS, 1983; and PhD, 1987, Inorganic Chemistry, Northwestern University) is Manager of the Basic Fuel Properties and Modeling Department at the INL. He has been investigating the synthesis and structure/property relations of materials for over 20 years. Over the last 12 years, his interests have been directed to the fabrication and characterization of materials associated with the nuclear fuel cycle, with emphasis on advanced nuclear fuels.

JAMES I. COLE (BS, 1989, MS, 1992, PhD 1996, Materials Science, Washington State University) is a Materials Scientist in the Fuel Performance and Design Department at the INL. His research efforts over the last 10 years have focused on radiation effects in reactor structural materials, cladding and structural materials development for advanced reactor systems, and the study of chemical interactions between fast reactor fuels and cladding materials.

STUART MALOY has been a Technical Staff Member at Los Alamos National Laboratory for 20 years and is the co-deputy director and core materials technical leader for the Fuel Cycle Research and Development's Advanced Fuels campaign at LANL. He also serves as Program Manager for Advanced Nuclear Energy Systems at LANL. He has a Bachelors ('89) Masters ('91) and PhD ('94) in Materials Science from Case Western Reserve University. He has applied his expertise to characterizing and testing the properties of metallic and ceramic materials in extreme environments, such as under neutron and proton irradiation at reactor-relevant temperatures. This includes testing the mechanical properties (fracture toughness and tensile properties) of Mod 9Cr-1Mo, HT-9, 316L, 304L, Inconel 718, Al6061-T6 and Al5052 after high-energy proton and neutron irradiations using accelerators and fast reactors. Characterization of materials after testing includes using transmission electron microscopy to analyze defects such as dislocations, twins and second phases, using high resolution electron microscopy to characterize defects at an atomic level and nanoscale mechanical testing. Stuart has >100 peer reviewed technical publications and numerous presentations.

FRANCIS "FRANK" A. GARNER (B. Sc., 1963 Chemical Engineering, D. Sc., 1970 Nuclear Engineering, Materials Science emphasis, University of Virginia) operates Radiation Effects Consulting, LLC, and also serves as Chief Consulting Scientist for TechSource Incorporated in support of USDOE programs. Previously, he joined Advanced Reactors Division, Westinghouse Electric Company, then transferred to Westinghouse Hanford Company before beginning work at Battelle's Pacific Northwest National Laboratory (as a result of the DOE-directed Hanford consolidation). Dr. Garner's studies on the response of structural alloys to neutron and charged-particle radiation have led to significant revisions of the nuclear community's perception of materials issues involving void swelling, irradiation creep, embrittlement, transmutation and radiation-enhanced corrosion. Early studies on liquid metal fast breeder reactors broadened into the fusion reactor field, and then turned to materials issues of light-water and heavy water reactors, as well as accelerator-driven spallation neutron sources. This research impacts worldwide development and application of alloys for fast breeder and fusion reactors, and his theoretical work on void swelling and irradiation creep in light water reactors has proven important in plant life extension.

10-50559 • INL/MIS-10-20524